UNIVERSITY FEDERICO II OF NAPLES

Department of Chemical Sciences

PhD Course in Chemical Sciences

XXIX cycle

PhD Thesis in Organic Chemistry

Design, synthesis and characterization of multifunctional therapeutic and diagnostic agents

Student: Dr. Claudia Riccardi

Tutor: Prof. Daniela Montesarchio

Supervisor: Prof. Filomena Sica

Contents

Chapter 1

Introduction

Chapter 2

Ruthenium(III)-based complexes

Chapter 3

NOTA chelators

Chapter 4

Aptamers as targeting ligands

Chapter 5

Multifuctional systems

Chapter 6

Summary

My PhD program has been focused on the development of multifunctional systems for potential applications in theranostic nanomedicine, which aims at simultaneously providing the diagnosis and treatment of a disease. For the construction of these tools, different kinds of nanoparticles (NPs) have been investigated, selected as optimal nanoplatforms for the *in vivo* delivery of drugs and diagnostic agents thanks to their capacity to incorporate multiple functional units into their coating.

Main goal of my research has been the derivatization of these scaffolds with both therapeutic and diagnostic agents, as well as with active targeting ligands. In detail, the compounds here studied are:

- new **ruthenium(III)-based complexes**, as anticancer agents.
- suitable derivatives of the macrocycle NOTA, as **chelators of ^{68}Ga radioisotope**, used in PET imaging.
- **oligonucleotide aptamers**, as the thrombin binding aptamer (**TBA**) and the nucleolin-targeting **AS1411**.

All these decorations have been *ad hoc* designed and synthesized with suitable tethers so to allow their attachment onto specific nanoparticles (*i.e.*, gold NPs, streptavidin-coated silica NPs, superparamagnetic NPs, liposomes or niosomes). In consideration of the kind of chosen derivatization, different recognition schemes can be exploited (*i.e.* hydrophobic or electrostatic interactions, covalent bonds, selective recognition).

Following this general strategy, a small library of decorated multifunctional NPs, differing for the nature of the NP core, Ru(III)-complex, oligonucleotide sequence and ^{68}Ga chelator, has been prepared. These systems have been tested *in vitro* as theranostic agents towards targeted pathologies, as cancer and clotting disorders.

Despite many Ru(III)-based compounds, in particular NAMI-A and KP1019 - currently in advanced clinical trials - display better antitumor activity and pharmacological profile than other metal-based drugs, they are poorly stable in aqueous media. So, new amphiphilic nucleolipids have been recently proposed by the research group of prof. D. Montesarchio as innovative carriers to transport in cell Ru(III)-compounds. Following this strategy, a novel nucleolipid-based Ru(III)-complex, named **LipThyRu**, has been here prepared. Then, in order to expand the repertoire and chemical diversity of the available amphiphilic Ru(III)-complexes, biocompatible scaffolds alternative to nucleosides, *i.e.* trifunctional α-amino acids, have been also exploited to serve as carriers for the Ru(III) metal core. Within this approach, two new aminoacyl lipidic Ru(III)-complexes, *i.e.* **TUGluRu** and **TOTyroRu**, have been synthesized.

As far as the imaging agents are concerned, a mini-library of novel lipophilic derivatives of NOTA, designed as ^{68}Ga chelators in PET analyses, has been prepared. The synthesized analogs differ for their hydrophobic tail, *i.e.* an oleic acid, a lipoic acid or a biotin residue (**NOTA-OL**, **NOTA-Lip** and **NOTA-Bio**, respectively), which ensures the subsequent anchoring of NOTA on differently decorated nanoplatforms.

Two active targeting agents have been investigated: the 15-mer **thrombin-binding aptamer** (**TBA**) - able to inhibit the activity of human thrombin, a protein with key roles in coagulation processes - and **AS1411**, an oligonucleotide targeting nucleolin, which is a ubiquitous, multifunctional protein involved in cell survival, growth and proliferation, overexpressed on the outer membrane of cancer cells.

In a first study, a new tris-conjugated TBA (named tris-mTBA) has been prepared, characterized in solution using UV, CD and fluorescence spectroscopy and then immobilized onto silica NPs commercially available as Sicastar®. This aptamer has been equipped with a biotin tag at the 5'-end, allowing its incorporation onto streptavidin-coated Sicastar® NPs, and further conjugated with a dansyl group and a β-cyclodextrin at the 3'- and 5'-end, respectively. This represents an efficient host-guest system useful to monitor the NP functionalization and the correct aptamer folding onto the nanoparticles, thanks to the fluorescence enhancement of the dansyl probe observed when it is inserted in the hydrophobic cavity of β-cyclodextrin.

Sicastar® NPs have been thus functionalized with the tris-mTBA and characterized using DLS, SLS, gel electrophoresis and fluorescence analysis. DLS experiments nicely demonstrated that the tris-mTBA inhibited human α-thrombin ca. 10-fold more efficiently than unmodified TBA. Notably, under the same experimental conditions, the tris-mTBA/Sicastar® NPs completely blocked thrombin activity, which was restored upon addition of the TBA antidote, *i.e.* its complementary sequence.

In a successive study, with the aim of exploiting AS1411 as an active targeting agent for multifunctional, theranostic nanoplatforms, a set of AS1411 derivatives have been selected (*i.e.*: 5'-stearyl-AS1411, 5'-cholesteryl-C6-AS1411 and 5'-cholesteryl-TEG-AS1411) with lipophilic tails at their 5'-end allowing their subsequent insertion into liposomes or lipid coated-NPs.

The solution behavior of the AS1411 derivatives has been investigated using different techniques, in comparison with the unmodified aptamer. In particular, CD, CD-melting, UV-melting, gel electrophoresis and size exclusion chromatography analysis have been carried out to get information on their secondary structure and the thermal stability of their preferred conformations.

This study was carried out in two different solutions, mimicking the extracellular and intracellular media, and at different oligonucleotide concentrations; special attention was devoted to the investigation of possible effects due to the nature of the lipophilic tail, or of the specific linker, on the overall structure and conformation of the aptamers.
All these experiments consistently showed a high polymorphism for AS1411 and its derivatives, which are able to form form higher order G4 structures or large aggregates, particularly at high concentrations.

These decorations (Ru complexes, aptamers and NOTA chelators) have been then combined on suitable platforms, realizing to date mainly two multifunctional systems: DOTAP-based liposomes, functionalized with TUGluRu and NOTA-OL, and niosome-based formulations, decorated with LipThyRu and AS1411.

DOTAP-based liposomes functionalized with TUGluRu and NOTA-OL represent a good model for the realization of theranostic nanoparticles, offering several advantages, such as the possibility of monitoring their half-life, distribution, and tissue release. DOTAP/TUGluRu (70:30), DOTAP/NOTA-OL (95:5) and DOTAP/TUGluRu/NOTA-OL (65:30:5) systems have been prepared and fully characterized. DLS data indicated that these species form stable, monodisperse vesicles. In cell bioactivity assays, these formulations showed a good antiproliferative activity on MCF-7, C6 and HeLa cancer cell lines, with IC_{50} values in the low μM conc., in turn not evidencing any toxicity on normal human cells even at 250 μM concentration.

Niosome formulations including the nucleolipidic Ru(III)-complex LipThyRu and the nucleolin-selective aptamer AS1411 have been prepared and characterized using several techniques, *i.e.* gel electrophoresis, Zeta potential and DLS measurements. Preliminary cellular experiments on HeLa cells showed a small, but detectable cell viability decrease for the niosome_LipThyRu system, and a relevant antiproliferative effect for the formulation containing both AS1411 and the nucleolipidic Ru(III)-complex, indicating a marked synergic effect for these niosome-based anticancer agents.

Future work, starting from the results obtained in this PhD program, will be directed to incorporating the amphiphilic Ru(III)-complexes (*i.e.*, LipThyRu, TUGluRu, TOTyroRu or previously developed Ru(III) derivatives), the imaging agents (*i.e.*, NOTA chelators) and the targeting agents (*i.e.*, the lipophilic AS1411 derivatives) in combination into various kinds of other nanoplatforms, particularly in superparamagnetic NPs, so to obtain a mini-library of multifunctional systems to be tested *in vitro* and *in vivo* and identify the best anticancer theranostic agents.

Chapter 1

Introduction

1. Theranostic nanomedicine: a single "package" for personalized treatments and diagnosis

The concept of personalized medicine has recently emerged as a promising approach to overcome the limitations of standard diagnostic and therapeutic strategies and obtain tailored treatments, taking into account the inter-individual variability in therapeutic response.[1–5] This therapeutic approach may reduce the undesirable side effects of standard treatments and potentially produce better overall results.[1–5]

Theranostic nanomedicine, which is intended to provide simultaneous diagnosis and treatment of a disease, with early detection, easy monitoring, targeted therapy, minimal toxicity and higher therapeutic efficiency,[1,6] can be a very useful tool to reach this challenging goal. The term theranostics epitomizes the strict interplay of therapy and diagnosis, the pillars of medicine,[7,8] and involves the combination of two activities, *i.e.* the treatment and diagnostic imaging, into a single multifunctional system.[4,5,9–14] The main reason behind the huge enthusiasm for theranostics is its revolutionary approach that promises improved therapeutic outcomes on the basis of specific molecular features of the drug, greater predictive power for possible side effects and new ways to reliably monitor the response to a given treatment.[9,15] These properties are key elements for the development of personalized medicine.[6,9] Thus, theranostic agents are designed as integrated nanosystems allowing both disease detection and drug delivery, which can play major roles in early preclinical studies as well as at a clinical stage of drug development.[2,7,13,15–17]

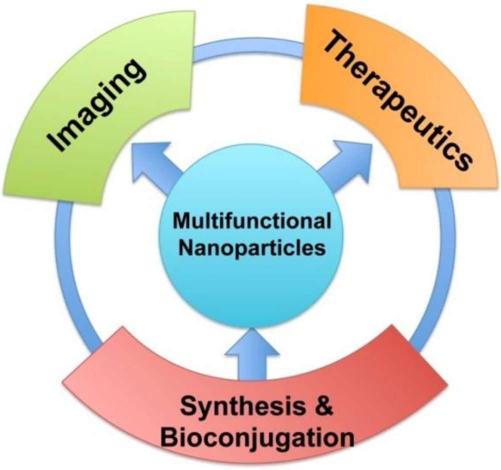

Figure 1. The majority of the known multifunctional nanoparticles are aimed at applications for *in vivo* imaging and therapy. Figure reproduced from Choi and Wang.[18]

In this frame, multifunctional nanoparticles (NPs) are attracting a growing interest as suitable platforms for several biomedical applications - including drug delivery and bio-imaging (Figure 1) - thanks to their ability to exert several advanced functions through incorporation of multiple functional units into a unique system.[2,5,9,18–29] In order to achieve this multifunctionality, typically four components are included: a) a nanoparticle-based platform, b) a diagnostic imaging moiety, c) a targeting ligand, and d) a therapeutic agent.[5] The introduction of suitable targeting ligands may help to increase the target-to-background contrast in imaging techniques and, above all, the local concentration of the drug at the target site, thus reducing or eliminating possible, untoward side effects.[5,7]

Nanomaterial	**Trade Name**	**Application**	**Target**	**Adverse Effects**	**Manufacturer**	**Current Status**
Metallic						
Iron oxide	Feridex	MRI contrast	Liver	Back pain, vasodilatation	Bayer Schering	FDA approved
	Resovist	MRI contrast	Liver	None	Bayer Schering	FDA approved
	Combidex	MRI contrast	Lymph nodes	None	Advanced Magnetics	In Phase 3 clinical trials
	NanoTherm	Cancer therapy	Various forms	Acute urinary retention	MagForce	In Phase 3 clinical trials
Gold	Verigene	In vitro diagnostics	Genetic	Not applicable	Nanosphere	FDA approved
	Aurimmune	Cancer therapy	Various forms	Fever	CytImmune Sciences	In Phase 2 clinical trials
Nanoshells	Auroshell	Cancer therapy	Head and neck	Under investigation	Nanospectra Biosciences	In Phase 1 clinical trials
Semicondutor						
Quantum dot	Qdots, EviTags, semiconductor nanocrystals	Fluorescent contrast, in vitro diagnostics	Tumors, cells, tissues and molecular sensing structures	Not applicable	Life Technologies, eBioscience, Nanoco, CrystalPlex, Cytodiagnostics	Research use only
Organic						
Protein	Abraxane	Cancer therapy	Breast	Cytopenia	Abraxis Bioscience	FDA approved
Liposome	Doxil/Caelyx	Cancer therapy	Various forms	Hand-foot syndrome, stomatitis	Ortho Biotech	FDA approved
Polymer	Oncaspar	Cancer therapy	Acute lymphoblastic leukemia	Urticaria, rash	Rhône-Poulenc Rorer	FDA approved
	CALAA-01	Cancer therapy	Various forms	Mild renal toxicity	Calando	In Phase 2 clinical trials
Dendrimer	Vivagel	Microbicide	Cervicovaginal	Abdominal pain, dysuria	Starpharma	In Phase 2 clinical trials
Micelle	Genexol-PM	Cancer therapy	Various forms	Peripheral sensory	Samyang	For Phase 4 clinical trials

Table 1. Examples of nanomaterials in clinical use. Table reproduced from Chan *et al.*[30]

The success of nanoparticles is certainly due to their distinctive features, such as their easy surface functionalization and high surface area-to-volume ratios, yielding high loading capacities.[7,9,25,30–32]

The nanometric size of these materials precludes their ready clearance through the kidneys, thereby extending their blood circulation depending on their surface functionalization characteristics.[7,33–37] Furthermore, following a precise design, nanoparticles can be engineered to either avoid immune system recognition or specifically inhibit or enhance the immune responses.[38,39] For all these reasons, they could act as a promising "single-entity" scaffold able to yield meaningful information on the pharmacokinetics and biodistribution of a given drug, as well as on the presence of the exact molecular target before, during, and after therapy.[9]

A number of nanostructures, including liposome and nanoparticles-based systems, have been approved for clinical applications, and even more are currently under preclinical or clinical investigations (Table 1).[2,30,40,41]

2. PhD project goals

The studies carried out during my PhD program are fully inserted into the research context focused on the development of multifunctional nanoparticle-based systems for theranostic applications. As schematically represented in Figure 2, the main goal of this research is the incorporation on the same scaffold of both therapeutic and diagnostic agents, as well as of targeting ligands.

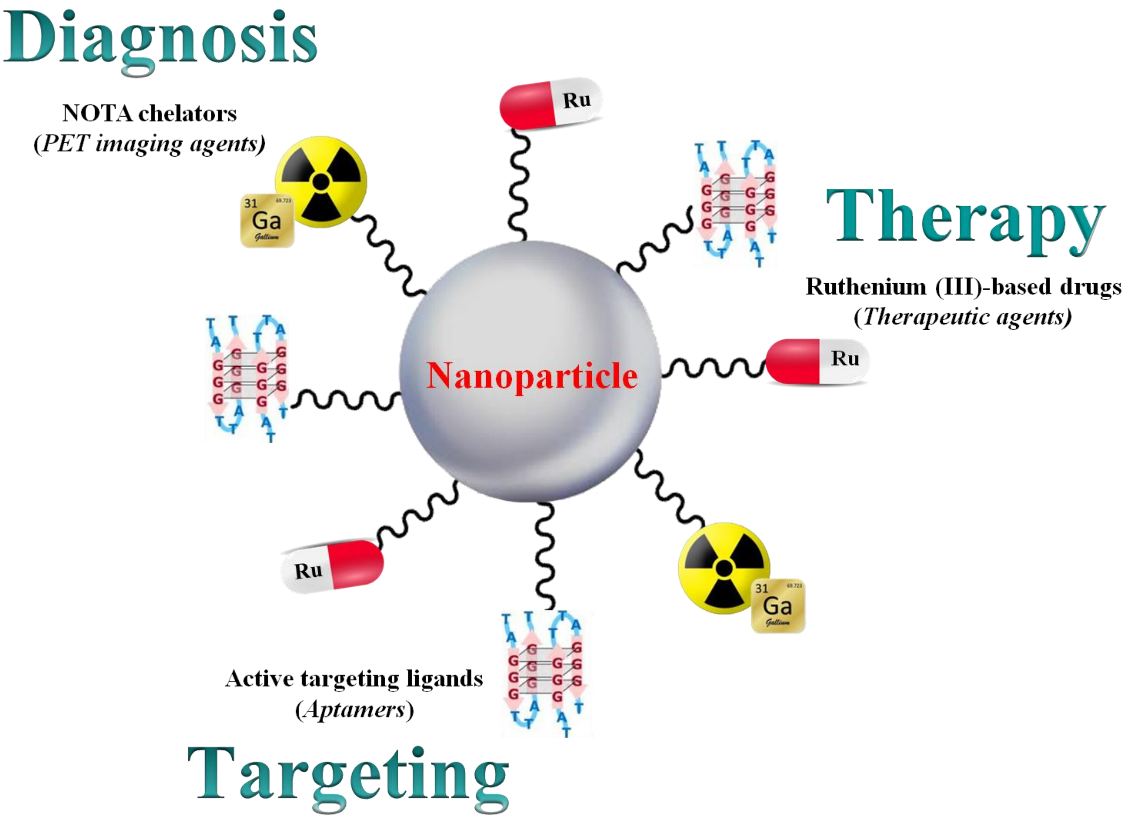

Figure 2. Scheme of an ideal multifunctional nanoparticle-based system for molecular imaging, drug delivery and targeting, based on NOTA chelators, Ru(III)-complexes, and oligonucleotide aptamers, respectively.

In detail, the compounds selected as nanoplatform decorations are:

- new **ruthenium(III)-based complexes**, as promising alternative to Pt-based anticancer agents, inspired to NAMI-A and KP1019 currently in advanced clinical trials[42–45] (see Chapter 2).
- suitable derivatives of the macrocycle 1,4,7-triazacyclononane-1,4,7-triacetic acid (NOTA), as **chelators of ^{68}Ga radioisotope** used in Positron Emission Tomography (PET) imaging, which can provide molecular/functional information on the *in vivo* biodistribution and pharmacokinetics of the drugs[46,47] (see Chapter 3).
- **oligonucleotide aptamers** with well proven pharmacological or active targeting activity, as **TBA** and **AS1411** aptamers (see Chapter 4).

All these decorations have been *ad hoc* designed and synthesized for the functionalization of specific types of nanoparticles (*i.e.*, gold NPs, streptavidin-coated silica NPs, superparamagnetic NPs, liposomes or niosomes).

In consideration of the kind of chosen derivatization, different recognition schemes can be exploited (Figure 3). In the case of a lipophilic tail, we can functionalize liposomes or lipid-coated NPs through hydrophobic interactions. Introducing a disulfur or a thiol-moiety into the starting core scaffold, we can functionalize metal-based NPs as Au-NPs through formation of stable metal-S or Au-S covalent bonds.[48,49] With negatively charged molecules (as aptamers and Ru-based compounds) we can exploit electrostatic interactions to functionalize niosomes. Finally, the exceptionally high affinity of the streptavidin/biotin recognition system (K_d ~ 10^{-15} M)[50] can be exploited for the decoration of streptavidin-coated NPs with molecules labeled with a biotin moiety.
Following this general strategy, a small library of decorated multifunctional NPs, differing for the nature of the platform, Ru(III)-complex, ODN sequence and ^{68}Ga chelator, has been prepared and tested *in vitro* as theranostic agents towards targeted pathologies, as cancer and clotting disorders.

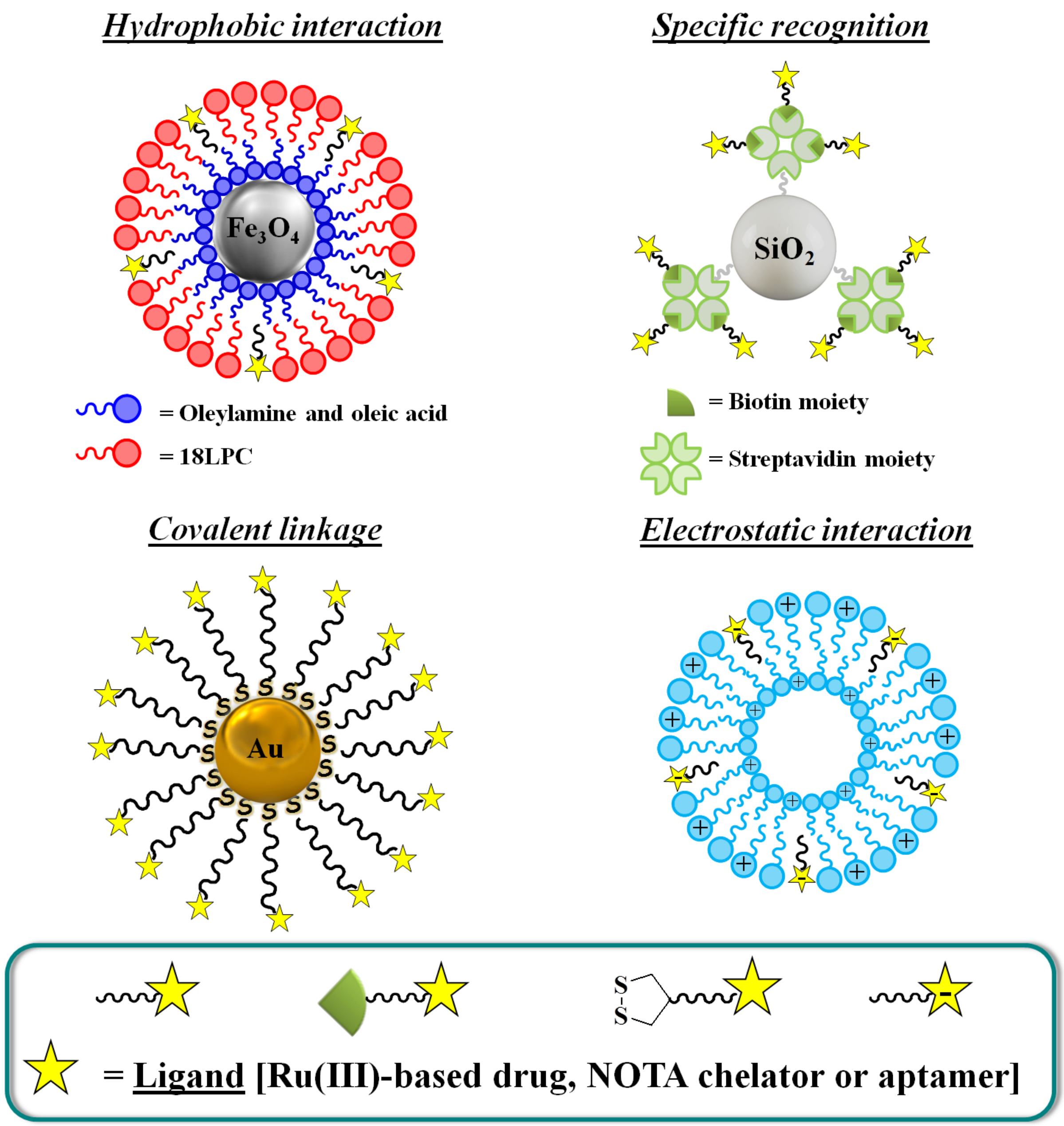

Figure 3. Possible functionalization schemes for nanoparticle surface decoration. By labelling a ligand with a lipophilic tail, we can incorporate it into lipid-coated NPs or liposome platforms (not shown) through hydrophobic interactions. The insertion of a disulfur or of a thiol moiety into a ligand allows its immobilization onto gold NPs through the formation of covalent Au-S linkages. The presence of negative charges in the ligand allows the functionalization of niosome platforms *via* simple electrostatic interactions. The high affinity of the (strept)avidin/biotin recognition can be useful to conjugate (strept)avidin-coated NPs with biotin-labeled ligands.

Chapter 2

Ruthenium(III)-based complexes

1. Ru(III)-complexes: *state of the art*

A major challenge in biomedical research is the discovery of compounds able to selectively inhibit cancer cell proliferation without adversely affecting normal cell growth.[51] To this purpose, transition metal-based compounds have been proposed as potential drugs to treat several human diseases, in particular cancer.[52,53] Based on their wide spectrum of coordination numbers and geometries, metal complexes offer different mechanisms of action that are not accessible with small organic molecules.[53,54]

The interest for this class of chemotherapeutics started in the 60's, with the serendipitous discovery by Rosenberg and co-workers of *cis*-diamminedichloro-platinum(II) or cisplatin. A plethora of platinum compounds have been prepared thereafter and evaluated as potential chemotherapeutic agents, although very few have entered clinical use.[55–59] In fact, the efficacy of treatments based on cisplatin-related derivatives suffers from heavy side effects and resistance phenomena. These unresolved problems in platinum-based anticancer therapy have stimulated further research efforts aimed at the identification of novel antitumoral, non platinum-containing metal species.[53,54] In this context, Ru(III)-complexes have particularly emerged for their remarkable anticancer or antimetastatic properties, generally associated with low systemic toxicity.[60–73]

1.1. Ru(III)-based lead compounds: NAMI-A and KP1019

The interest in ruthenium complexes rapidly increased when it was discovered that some Ru(III)-based derivatives are therapeutically active on solid tumours resistant to cisplatin treatments. In principle, these compounds offer several advantages over antitumor Pt(II) complexes currently used in clinic - *i.e.* a reduced toxicity, different mechanisms of action, prospect of non-cross-resistance[74,75] and wide spectrum of activity.[64,76] Among the available Ru(III)-based compounds, some heterocyclic complexes proved to be the most promising candidate drugs.[61,77] They have the general formula (HB)[Ru(III)B_2Cl_4] - where B is a heterocyclic base - and typically include axial heterocyclic nitrogen donor ligands and equatorial chlorides, with charge compensation provided by protonated nitrogen heterocycles - as is the case of KP1019[43,78–80] (Figure 4), developed by Keppler *et al.* - or sodium ions.

In this context, Alessio, Sava and coworkers analysed the DMSO-containing variants of the above mentioned class, discovering a very active Ru(III)-complex, ImH^+ [*trans*-$RuCl_4$(DMSO)Im]$^-$

(where Im = imidazole), called NAMI-A (Figure 4).[81,82] This compound, together with KP1019, has been introduced in advanced clinical trials.[42–45]

Although the mechanism of action and the main target of these Ru(III)-based drugs have not been unambiguously determined yet, a large amount of valuable data have been obtained on their *in vitro* and *in vivo* behaviour,[83–85] summarized in several reviews.[68,69,71,86,87] In spite of their structural similarity, these Ru(III) derivatives exhibit markedly different anticancer effects.[88–90]

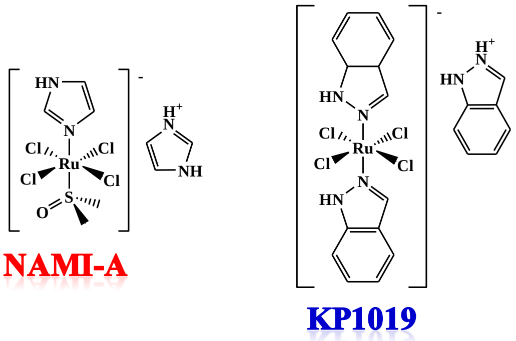

Figure 4. Chemical structures of ImH^+ [*trans*-$RuCl_4(DMSO)Im]^-$ (NAMI-A) and $IndH^+$ $[RuCl_4(Ind)_2]^-$ (KP1019), where Im = imidazole, and Ind = indazole.

NAMI-A shows a remarkable and selective activity against cancer metastases,[91–103] mostly of solid lung tumours, but is not effective in the reduction of primary cancers. ImH^+ [*trans*-$RuCl_4(DMSO)Im]^-$ consists of a pseudo-octahedral complex, in which Ru(III) is coordinated with six ligands: one imidazole, one DMSO and four chloride ions. All these ligands can be replaced by water or hydroxide ions, resulting in a mixture of aquated species - ultimately responsible for the antimetastatic activity.[99] *In vitro* experiments have shown that NAMI-A readily undergoes hydrolysis under physiological conditions;[104,105] in particular, following the mechanism depicted in Figure 5, the chloride ions are the ligands most rapidly substituted by water and/or hydroxide ions.[81,106]

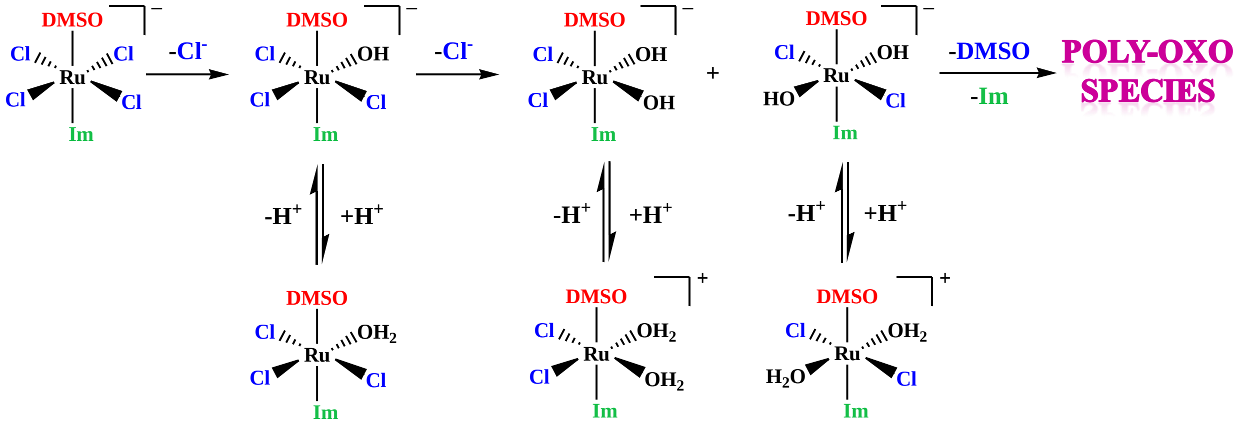

Figure 5. Proposed hydrolysis mechanism for NAMI-A.[81]

The loss of chloride groups is catalysed by the reduction of Ru(III) to Ru(II), which is expected to occur under physiological conditions and is enhanced *in vitro* by traces of biological reductants, such as ascorbic acid or cysteine.[61,107] Overall, NAMI-A hydrolysis is complete within 15-20 min, with both Cl^- and DMSO ligands replaced by water. The nature and rate of the hydrolytic processes in aqueous solution are strongly pH-dependent.[99,108–110] Hydrolysis eventually leads to the formation of polymeric oxo- or hydroxo-bridged species which can precipitate; this phenomenon, which would dramatically limit the therapeutic efficacy of these compounds, is less likely *in vivo* because of the presence of several proteins (including integrins, transferrin and serum albumin) which can form stable adducts with the Ru-complexes, inhibiting the precipitation of insoluble oligomers.[110]

Notably, NAMI-A increases the capsule thickness around the primary tumours and the extracellular matrix around tumour blood vessels, thereby preventing tumour cells from invading surrounding tissue and blood vessels.[61,82,93,111] In addition, NAMI-A is able to inhibit matrix metalloproteinases and induce antiangiogenic effects.[66,111] In contrast to platinum-based drugs, NAMI-A weakly binds to DNA, which suggests that its antimetastatic activity is not primarily related to DNA damage.[112] Lastly, NAMI-A is much less toxic to healthy tissues than cisplatin.[113]

KP1019 is a Ru(III) chlorido-indazole complex showing remarkable antitumor activity at the primary tumour site.[65,114–118] $IndH^+$ $[RuCl_4(Ind)_2]^-$ (where Ind = indazole) is an octahedral complex, in which Ru(III) is coordinated to two indazole ligands and four chloride groups. Biological tests[71,86,119] proved that KP1019 is highly active against colorectal cancer cell lines both *in vitro* and *in vivo.*[62,65,114–116] The efficiency of KP1019 has been associated with its ability to interact with DNA and inhibit its synthesis probably involving different modes of action.[86] Compared with NAMI-A, KP1019 is more readily taken up by cancer cells and is more stable toward hydrolysis.[68,103,110,119,120] Unlike NAMI-A, KP1019 does not have relevant effects on metastatic cells, still showing cytotoxic activity and reducing the cell population by promoting apoptosis[71,120–122] *via* the mitochondrial pathway.[53,86,107] Analysis of the intracellular distribution of Ru in single human cells treated with KP1019 showed that Ru localized in both cytosol and in the nuclear region. In marked contrast, Ru could not be well visualized in cells treated with NAMI-A, indicating that it was not effectively internalized and supporting the hypothesis that its activity is exerted through membrane-binding mechanisms.[123]

In summary, in a very simplified scheme, three main events have been hypothesized to determine the fate of these ruthenium complexes *in vivo*: the *activation by hydrolysis*, the *activation by reduction* and the *high affinity binding to blood plasma proteins*. An interplay between these mechanisms seems to account for the biological effects of these Ru(III)-complexes. For both species, chlorido ligands can be rapidly exchanged with water molecules or hydroxide ions, activating the complex; then, in a second substitution event, the bound aqua ligands are replaced by the target biomolecules.[124] In addition, both these Ru(III)-complexes readily react with biological reductants[117] suggesting that the *in situ* reduction of Ru(III) to Ru(II)[64] species may be relevant for their biological activity,[68,76,107] producing a more reactive form,[64,118] able to interact with proteins[106,112,125–127] and/or to bind nucleic acids.[106,128]

Finally, both these Ru-complexes can tightly interact with plasma proteins, in particular with human serum transferrin (hTf),[88–90,129–132] *i.e.* the iron transport protein in blood responsible for controlling the level of free iron in biological fluids (for a recent review, see for example Harris et al.[133]). General interference with the iron metabolism has been also invoked to explain the anticancer activity of Ru(III)-complexes.[68,88,89,107,123,129]

1.2. AziRu, a pyridine analog of NAMI-A

In 2012, almost simultaneously, two different research groups, Walsby *et al.*[134] and Paduano *et al.*[135,136] revisited a pyridine analogue of NAMI-A, called NAMI-Pyr by the first group and AziRu by the second ones, whose structure had been previously described by Attia *et al.* in 1993.[106]

Compared to NAMI-A, AziRu has a pyridine molecule replacing one imidazole ligand, and sodium replacing imidazolium as the counterion (Figure 6).

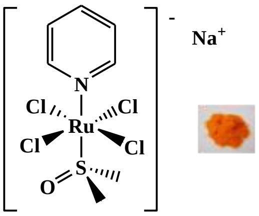

AziRu

Figure 6. Chemical structure of AziRu, along with a picture of a sample of this compound, obtained as a solid orange powder.

In vitro biological experiments have shown very low cytotoxicity for AziRu[135–137] on different cancer cell lines. Thus, AziRu is not cytotoxic *per se* – similarly to NAMI-A – against human cancer cells; however, its IC_{50} value is half that of NAMI-A on MCF-7 breast cancer cells (Table 2), indicating that the structural modifications introduced in NAMI-A allow increasing its antiproliferative activity. One possible reason for this difference lies in the presence of a pyridine ligand in lieu of imidazole, conferring a higher lipophilicity to AziRu, which could determine enhanced non covalent interactions with proteins, particularly with human serum albumin.[134] Indeed, Walsby and co-workers have synthesized and studied a mini-library of Ru(III)-complexes;

their analysis showed that, upon increasing their lipophilicity, reduced solubility has been observed in physiological media for the free complexes, however accompanied by enhancement of non-covalent interactions with the hydrophobic domains of serum proteins, in particular of human serum albumin. Formation of these protein adducts basically improves the solubility of the complexes, also inhibiting the formation of oligomeric species and leading to higher *in vitro* cytotoxicity.[138–140]

	IC_{50} (Mm)			
	MCF-7	**WiDr**	**C6**	**HeLa**
NAMI-A[141]	**620 ± 30**	**-**	**-**	**-**
AziRu[135,137]	**305 ± 16**	**441 ± 20**	**318 ± 12**	**382 ± 19**

Table 2. IC_{50} values (μM) relative to the antiproliferative activity of NAMI-A and AziRu in the indicated cancer cell lines following 48 h of incubation. IC_{50} values are reported as mean ± SEM. (MCF-7: human breast adenocarcinoma cell line; WiDr: human epithelial colorectal adenocarcinoma cell line; C6: tumor rat glioma cells; HeLa: human cervical cancer cells).

Proteins are considered to be the privileged biological targets of Ru(III)-complexes.[142–144] However, it cannot be excluded that the adducts formed with proteins, and mainly albumin and transferrin present in serum, may represent intermediate forms protecting the metal from further degradation[145] and allowing its transport to nuclei; under these circumstances, also DNA could be considered a possible *in vivo* target, in analogy with the mechanism hypothesized for cisplatin.[146]

In this frame, the interaction of AziRu with suitable DNA model systems, both single strand and duplex oligonucleotides, has been investigated in comparison with its analogue NAMI-A using different biophysical methods, including absorption UV-vis spectroscopy, circular dichroism (CD) and electrospray mass spectrometry (ESI-MS) techniques.[147]

UV-vis measurements allowed monitoring over time the ligand exchange processes of these Ru complexes, in the absence and presence of the examined oligonucleotides. CD experiments provided information on the overall conformational changes of the DNA model systems induced by the metal complexes. Treatment with AziRu and NAMI-A did not produce any detectable change in the CD profile of the model, preformed duplex, indicating that – contrarily to cisplatin and other anticancer Pt(II)-complexes – these compounds did not perturb the overall conformation of the studied duplex. Interestingly, CD-melting experiments showed that the ruthenated duplex had in all cases higher T_m values compared to the untreated system, showing however a lower difference of the CD signal intensity at its maximum (264 nm) upon denaturation with respect to the natural duplex. These data indicate the formation of stable ruthenium-duplex adducts, with local, partial loss of some Watson–Crick H-bonding and/or stacking interactions induced by Ru binding.

ESI-MS experiments (Figure 7), carried out on several oligonucleotide/ruthenium complex mixtures, allowed detecting the formation of stable adducts with guanine-containing oligomers for both NAMI-A and AziRu, while no adduct was observed with guanine-free sequences. The obtained results unambiguously demonstrate that both AziRu and NAMI-A are able to selectively interact with DNA model systems at the level of guanines, preferentially targeting a “GG” dinucleotide box. Remarkably, AziRu proved to be far more reactive than NAMI-A, leading to oligonucleotide adducts with a naked Ru^{3+} ion incorporated, while with NAMI-A only $Ru(Im)^{3+}$ (Im = imidazole) fragments were observed. Although very similar in their structures, the two metal compounds thus show a markedly different reactivity with the examined sequences: AziRu reacts with guanine-containing oligonucleotides forming stable adducts in which ruthenium loses all its original ligands, while NAMI-A keeps imidazole in the oligonucleotide-ruthenium complex adduct formation, showing that pyridine is a more labile ligand compared to imidazole. This different behavior in the binding mode with nucleic acids is in good agreement with studies on the interaction with proteins[134,143,144] underlining that, although structurally similar, NAMI-A and AziRu have a quite different reactivity profile towards biologically relevant targets.

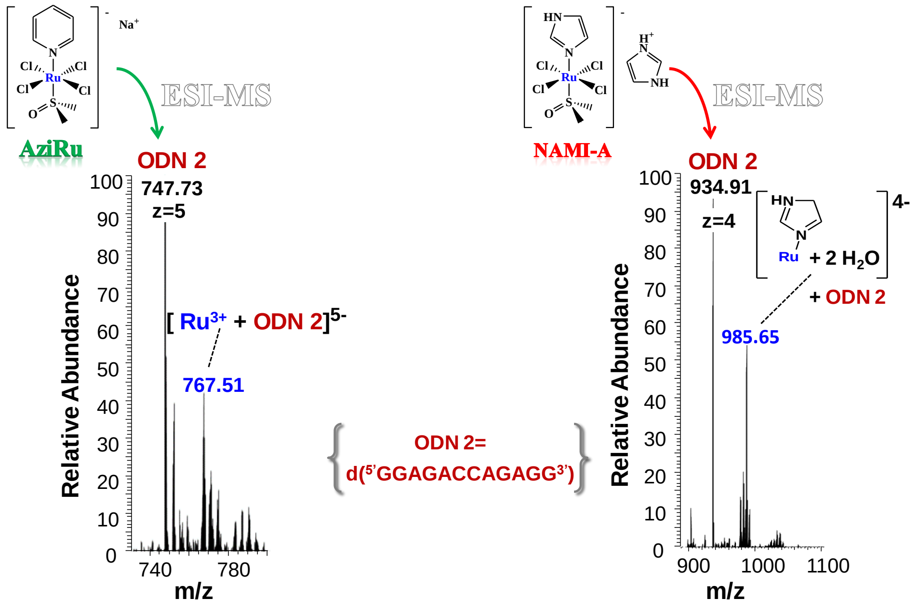

Figure 7. ESI-MS spectrum of the selected ODN **2** (50 µM), incubated with 1 eq of NAMI-A (right) and 1 eq of AziRu (left) in water at 37 °C for 48 h. The analysis was carried out at final concentration of 25 µM in MeOH/H_2O, 1:1 (v/v). Figure adapted from Montesarchio *et al.*[147]

1.3. Design of novel Ru(III)-based complexes

Although in the case of NAMI-A it is generally accepted that the hydrolysis process and formation of oligomer species does not really impair its overall antitumor activity[148] - at least for some tumor cell lines[100] - the premature aquation can deactivate or activate too early most of the administered drug.[146,149] Thus, in order to obtain long-life Ru(III)-based antineoplastic agents, a pro-drug approach, involving the decoration of the ruthenium complex with amphiphilic nanovectors, has been proposed by Paduano *et al.* for the *in vivo* delivery of these compounds.[73,135–137,150–154]

The use of pro-drugs is an established strategy to improve the physico-chemical, biomedical or pharmacokinetic properties of therapeutically relevant compounds. A pro-drug is a chemically modified version of a pharmacologically active agent that must undergo an *in vivo* transformation to release the effective drug. For example, the use of pro-drugs allows overcoming drawbacks such as poor aqueous solubility, chemical instability, insufficient oral absorption, rapid pre-systemic metabolism, inadequate brain penetration and toxicity. A very simplified, representative scheme of the pro-drug concept is shown in Figure 8, in which the barrier depicted can be any physical obstacle (*e.g.*, a cell membrane) that limits the optimal *in vivo* performance of a parent drug. The drug and the carrier are covalently bound *via* a linker that contains chemically or enzymatically cleavable bonds. The 'ideal' pro-drug is based on a non-toxic carrier and, once crossed the barrier, releases the intact therapeutic agent in an almost quantitative manner.

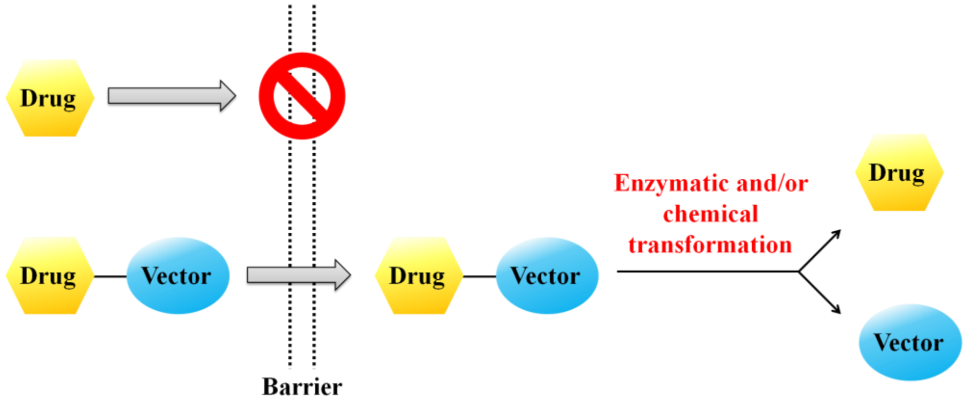

Figure 8. Simplified representative scheme of the pro-drug concept.

1.4. Nucleolipid nanovectors as molecular carriers for Ru(III)-based drugs

As biocompatible carriers for the *in vivo* transport of Ru(III)-based complexes, Paduano and co-workers have selected amphiphilic molecules and in particular nucleolipidic scaffolds[150,151,155] to which the Ru core can be covalently linked.

As well known, self-assembling amphiphiles allow an efficient bottom-up strategy for the formation of aggregates whose size and shape can be easily tuned. Further benefits related to the use of nanostructures in metal-based drug delivery include the possibility to:

- transport higher amount of the metal inside the blood stream;
- obtain "stealth" aggregates, not detected by the human immune system, thus specifically increasing their permanence in the blood;
- produce aggregates selectively captured by specific cancer cell lines by inserting, within the aggregates, targeting molecules, specifically recognized by protein receptors over-expressed in tumor cells;

- tune the shape and size of the aggregates by modifying either their molecular structure or some external physico-chemical parameters, such as pH and ionic strength.[136,151,156] The latter effects may be very useful in a stimuli-responsive approach.[156,157]

Nucleolipids - *i.e.*, hybrid molecules carrying lipid moieties covalently attached to nucleoside scaffolds - are able to mimic the molecular organization of the biological systems, forming a wide variety of supramolecular systems.[158–161] In planning the synthesis of Ru-containing nanovectors, our basic idea was to covalently link the ruthenium complex - *i.e.*, AziRu - to a nucleolipid structure able to spontaneously self-assemble in aqueous media, thus protecting it from chemo-enzymatic degradation in the extracellular environment and prolonging its half-life. To this purpose, several different nucleolipidic carriers have been designed,[151] in principle able to favour the transport of the Ru(III)-complex in an intact form until it reaches the tumour site. Following this concept, once internalized into the cell, the amphiphilic decorations of the nucleolipid scaffold are removed exploiting enzymatic hydrolysis mechanisms, thus releasing a low molecular weight Ru-based compound, able to fully exert its activity. The general design of the functional nucleolipids is schematically described in Figure 9 and involves:

- a thymidine or uridine moiety selected as the central scaffold, allowing high and easy functionalization;
- a pyridyl-methyl group inserted at the N-3 position on the nucleobase as the ligand for the Ru-complexation, thus producing an AziRu-like structure;
- a lipophilic oleoyl or cholesteroxyacetyl group covalently anchored (one in the case of thymidine derivatives, or two in the case of the uridine analogue) at the ribose secondary hydroxyl group(s). These residues, able to induce self-structuring in aqueous solutions, have been chosen due to their structural similarity with lipid membrane constituents and easy availability;
- a hydrophilic oligo(ethylene glycol) chain linked at the 5’-OH ribose moiety; this decoration is expected to optimize the “hydrophilic/lipophilic balance” within the molecule and to increase its circulation time[162] preventing extracellular chemo-enzymatic degradation. In addition, oligoethylene glycols have ‘stealth properties’,[163–165] allowing the attached drug escaping the immune system.

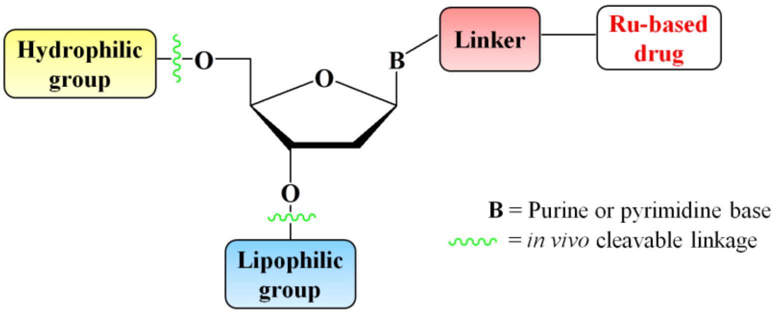

Figure 9. Schematic representation of the general design exploited for the preparation of nucleolipidic nanocarriers of Ru(III)-based drugs.

Based on the design shown in Figure 9, a series of amphiphilic Ru complexes able to form supramolecular aggregates have been prepared. These complexes - named ToThyRu, HoThyRu, ToThyCholRu and DoHuRu - are depicted in Figure 10.

As in the case of NAMI-A and AziRu, also these nucleolipidic complexes tend to be unstable when left in aqueous solutions and form insoluble precipitates, though at a much slower rate than NAMI-A and AziRu, *i.e.* in a period ranging from few hours, in phosphate buffer, to few days, when dissolved in pure water. The hydrolysis results in a change of the solution colour from yellow to green, followed by precipitation of brown particles.[135,136]

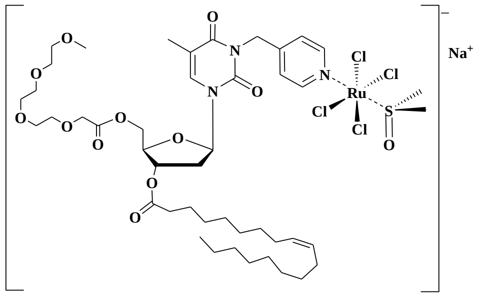

ToThyRu

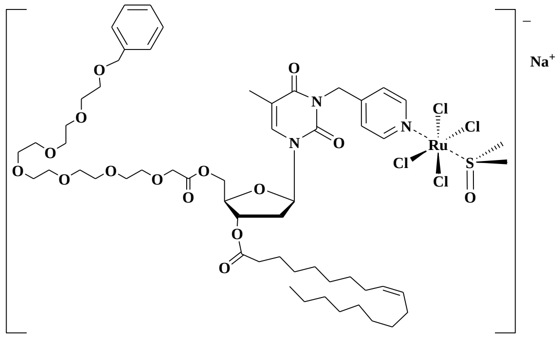

HoThyRu

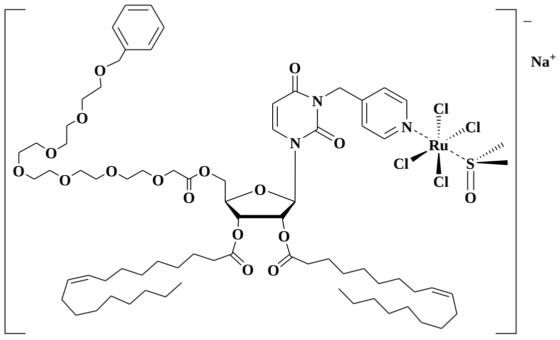

DoHuRu

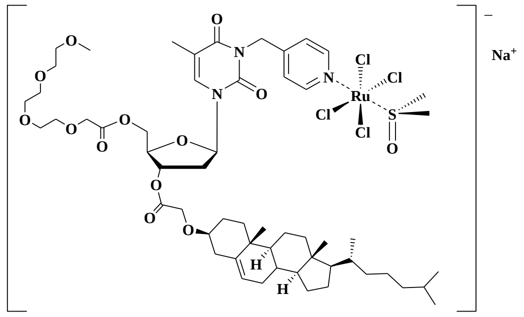

ToThyCholRu

Figure 10. Amphiphilic nucleolipid-based Ru(III)-complexes, described by Paduano *et al.*[135,136]

In order to sensibly reduce the aquation processes, nucleolipidic Ru(III)-complexes have been studied in formulation with biocompatible bi-tailed phospholipids, as the zwitterionic 1-palmitoyl-2-oleoyl-*sn*-glycero-3-phosphocholine (POPC) and the cationic 1,2-dioleoyl-3-trimethylammoniumpropane (DOTAP), depicted in Figure 11. The use of phospholipid formulations allows obtaining Ru complexes stable for months in physiological media, as well as finely modulating the metal amount to be administered *in vivo*. Indeed, bi-tailed phospholipids can adopt an ordered arrangement in aqueous solutions by forming bilayers in which the nucleolipidic Ru complexes can be easily lodged. The various lipid formulations here prepared differ for the lipid in use: in the case of POPC, the main driving forces promoting the formation of stable co-aggregates are hydrophobic interactions, while for DOTAP also electrostatic interactions contribute to stabilize the final co-aggregates. POPC and DOTAP have been chosen as stabilizing agents on the basis of their proved biocompatibility, being among the main components of cell membranes.[136,166]

Effective retardation of the ligand exchange processes in physiological solutions, resulting into formulations stable at r.t. for months, has been observed with the Ru(III)-complex present up to a maximum of 15% in mol in mixture with POPC,[135,136] and up to 50% in mixture with DOTAP.[137,153]

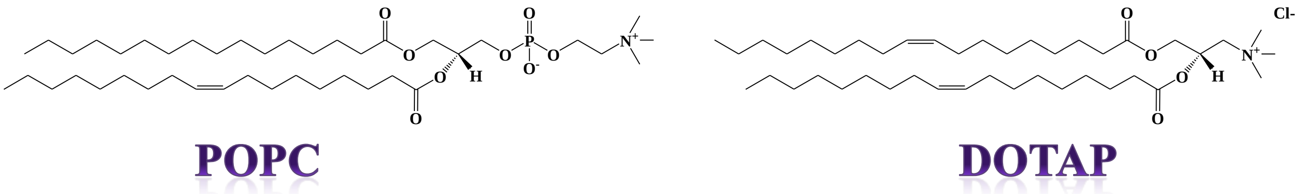

Figure 11. Chemical structures of POPC (1-palmitoyl-2-oleoyl-*sn*-glycero-3-phosphocholine) and DOTAP (1,2-dioleoyl-3-trimethylammoniumpropane).

An in-depth characterization by dynamic light scattering (DLS) and small angle neutron scattering (SANS) - in pure water and in a pseudo-physiological buffer solution - has been performed first on ToThy,[151] HoThy,[151] DoHu,[151] and ToThyChol[136] *i.e.*, the parent nucleolipids, and then on the corresponding nucleolipidic Ru(III)-complexes, as such and in formulation with POPC or DOTAP. ToThy, HoThy, DoHu, ToThyChol nucleolipids showed the desired distinctive features of nanocarriers, being mainly organized as small aggregates *i.e.* rod-like micelles in pure water, and as bigger aggregates, *i.e.* multilayer vesicles, in pseudo-physiological solutions.[136,151]

Notably, DLS analysis showed that under pseudo-physiological conditions all the complexes in POPC formulation (Ru complex/POPC 15:85 molar ratio) form aggregates with a monomodal distribution, having a hydrodynamic radii distribution similar to pure POPC. SANS data allowed confirming that the aggregation is essentially driven by POPC self-assembly.[135,136]

Compared with POPC co-aggregates, liposomes based on DOTAP can tolerate a higher amount of nucleolipidic Ru complex without losing in stability. In fact, stable liposomal DOTAP co-aggregates can contain up to 30% in moles of ToThyCholRu[137] and 50 % in moles of ToThyRu, HoThyRu and DoHuRu.[153] These nanoaggregates form catanionic vesicles which, analysed in a pseudo-physiological solution for more than three months, were found to be perfectly stable at r.t., showing no degradation. The formation of catanionic nanoaggregates has been confirmed also by zeta potential measurements, which proved that the positive surface charge, carried by bare DOTAP vesicles, is partially neutralized upon addition of negatively charged nucleolipidic Ru complexes.[137,153]

Furthermore, to gain insight into their antiproliferative activity, an in-depth bioactivity investigation has been performed first on ToThy,[151] HoThy,[151] DoHu[151] and ToThyChol[136] - *i.e.*, the naked nucleolipids, here used as the carriers - and then on the final formulations ToThyRu/POPC,[135] HoThyRu/POPC,[135] DoHuRu/POPC,[135] and ToThyCholRu/POPC,[136] in comparison with AziRu (see Table 3). Focusing on the cells more sensitive to the ruthenium treatment *in vitro, i.e.* MCF-7 and WiDr, naked nucleolipids showed the absence of significant cytotoxicity effects on both normal and tumor cells;[136,151] while POPC formulations have been found to be at least one order of magnitude more active than free AziRu. Particularly interesting results have been obtained on the MCF-7 human breast cancer cell line for the formulations ToThyRu/POPC and HoThyRu/POPC with IC_{50} values of 9 and 7 μM, respectively, calculated with respect to the ruthenium concentration. To the best of our knowledge, these *in vitro* data show these molecules as among the most promising Ru-based anticancer agents currently described in the literature.[135,136]

	IC_{50} (μM)		
	MCF-7	**WiDr**	**C6**
AziRu	**305 ± 16**	**441 ± 20**	**318 ± 12**
ToThyRu/POPC	**9 ± 4**	**75 ± 4**	**36 ± 8**
HoThyRu/POPC	**7 ± 4**	**40 ± 5**	**81 ± 7**
DoHuRu/POPC	**71 ± 6**	**99 ± 5**	**24 ± 5**
ToThyCholRu/POPC	**70 ± 12**	**165 ± 10**	**-**

Table 3. IC_{50} values (μM) relative to AziRu and to the effective ruthenium concentration carried by ToThyRu/POPC, HoThyRu/POPC, DoHuRu/POPC and ToThyCholRu/POPC liposomes in the indicated cell lines following 48 h of incubation. IC_{50} values are reported as mean ± SEM. (MCF-7: human breast adenocarcinoma cell line; WiDr: human epithelial colorectal adenocarcinoma cell line; C6: tumor rat glioma cells).

The higher *in vitro* cytotoxicity of Ru-complex/POPC formulations, compared to AziRu, suggests that all the nucleolipidic liposomes are able to deliver the active transition metal in a very efficient way, enhancing the effectiveness of the transported anti-cancer drug.[135,136]

Similarly, also DOTAP formulations have been evaluated *in vitro* showing high antiproliferative activity against specific human adenocarcinoma cell types. Remarkably, even the Ru-complex/DOTAP nanoaggregates, tested on a panel of human and non-human cancer cell lines, exhibited IC_{50} values in the low µM range, proving to be 10−20-fold more cytotoxic against MCF-7 and WiDr cells than free AziRu.[137,153] In some cases DOTAP formulations were also found to be more efficient than those in POPC, as shown in Table 4. Indeed, the liposomes formed by the cationic lipid DOTAP may closely interact with the negatively charged cell membrane, further improving the liposome fusion with the plasma membrane. Interestingly, no significant cytotoxicity has been detected on non-cancer cells, as human HaCaT keratinocytes and rat L6 muscle cells.

	IC_{50} (µM)					
	MCF-7	**WiDr**	**C6**	**HeLa**	**L6**	**HaCaT**
AziRu	**305 ± 16**	**441 ± 20**	**318 ± 12**	**382 ± 19**	**> 500**	**> 500**
ToThyRu/DOTAP	**19 ± 8**	**50 ± 11**	**54 ± 8**	**-**	**-**	**-**
HoThyRu/DOTAP	**15 ± 7**	**65 ± 8**	**43 ± 11**	**-**	**-**	**-**
DoHuRu/DOTAP	**13 ± 5**	**41 ± 10**	**34 ± 9**	**-**	**-**	**-**
ToThyCholRu/DOTAP	**13 ± 2**	**23 ± 8**	**-**	**34 ± 4**	**187 ± 1**	**377 ± 2.5**

Table 4. IC_{50} values (µM) relative to AziRu and to the effective ruthenium concentration carried by ToThyRu/DOTAP, HoThyRu/DOTAP, DoHuRu/DOTAP and ToThyCholRu/DOTAP liposomes in the indicated cell lines, following 48 h of *in vitro* treatment. IC_{50} values are reported as mean ± SEM. (MCF-7: human breast adenocarcinoma cell line; WiDr: human epithelial colorectal adenocarcinoma cell line; C6: tumor rat glioma cells; HeLa: human cervical cancer cells; L6: rat muscle cells; HaCaT: keratinocytes cells).

1.5. Interfacing nucleolipidic Ru(III)-complexes with bilayer-coated superparamagnetic nanoparticles: a successful marriage for theranostics

Normally, cancer is diagnosed at a stage of the disease in which some anatomical changes occur in the body in the form of well-defined tumors. Generally, these masses are removed by surgery, but this approach is not applicable to small or hidden tumors. Nanotechnology offers potential solutions for the treatment of various types of cancer, particularly at a very early stage: nanoparticles could protect a drug from recognition by the reticulo-endothelial system (RES) - *e.g.*, if highly PEGylated - and deliver a therapeutic agent in a controlled manner at a target site, so that rate and duration of drug delivery can be therapeutically effective, minimizing the requirement of booster dose.[38,167–169]

The flexibility in obtaining tailor-made nanoparticles with specific features (for example molecular weight, number and types of attached drugs, targeting moieties and even bioresponsive components)[170] makes them suitable drug delivery systems. In this frame, the incorporation of Ru(III)-complexes within nanoparticles can improve their *in vivo* performance by - in principle - increasing their circulation time in the body, decreasing their susceptibility to degradation, limiting recognition by the body's immune system and targeting specific sites. This strategy allows increasing the drug amount which can reach the desired area and reducing the side effects due to drug accumulation in undesired regions.

Remarkably, nanoparticles are very attractive platforms due to their capability to load multiple systems, as therapeutic and diagnostic compounds, thus affording useful theranostic agents.[1,2]

Superparamagnetic Iron Oxide Nanoparticles (SPIONs) are particularly attractive tools, being able to modify the transversal proton relaxation time (T2) of water molecules, resulting into effective contrast agents for *in vivo* Magnetic Resonance Imaging (MRI) analyses.[171,172]

Stable phosphocholine-functionalized SPIONs (18LPC/SPIONs) have been recently prepared exploiting hydrophobic interactions between a suitable phosphocholine, *i.e.* 1-octadecyl-2-hydroxy-*sn*-glycero-3-phosphocholine (18LPC), and an inner amphiphilic layer (oleic acid and oleylamine), covering the surface of the NPs.[173,174]

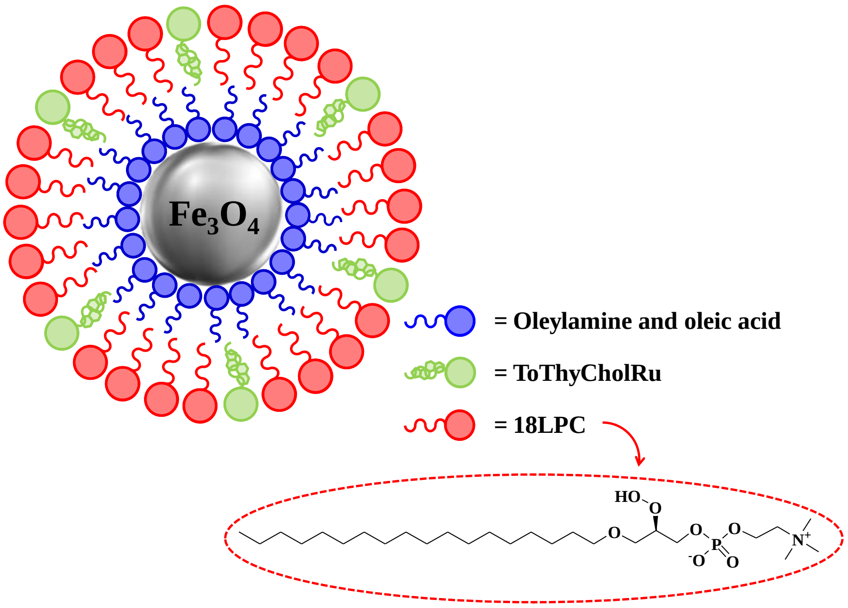

Figure 12. Schematic representation of the system 18LPC-ToThyCholRu/SPIONs.

In this context, 18LPC-SPIONs have been loaded with ToThyCholRu (18LPC-ToThyCholRu/SPIONs),[174] lodged in the external coating layer of the nanoparticle surface, to which it is reversibly bound through hydrophobic interactions (Figure 12). ToThyCholRu is thus easily transported *in vivo* where it can exert its activity. The evaluation of the bioactivity of the

ToThyCholRu-functionalized SPIONs on selected human cancer and non-cancer cells confirmed the potential of the system as an effective theranostic device.[174] Indeed, 18LPC/SPIONs were devoid of significant biological effects, while 18LPC-ToThyCholRu/SPIONs showed relevant selective cytotoxicity against human cancer cells. These results highlighted the possibility to exploit the nucleolipidic Ru(III)-complexes also for the functionalization of properly coated nanoparticles: indeed, all these compounds present a hydrophobic appendage which can be inserted not only within lipid-decorated SPIONs, but also in any other kind of inorganic nanoparticles, provided that they are decorated with a lipophilic layer.

	IC_{50} (µM)				
	MCF-7	**Calu-6**	**A549**	**HaCaT**	**3T3-L1**
cDDP	**22 ± 4**	**45 ± 5**	**36 ± 4**	**272 ± 7**	**> 100**
18LPC-ToThyCholRu/SPIONs	**17 ± 5**	**12 ± 4**	**14 ± 5**	**205 ± 6**	**> 100**

Table 5. Comparison of the IC_{50} values (µM) relative to cisplatin (cDDP) - used as a positive control for cytotoxic effects - and to the effective ruthenium concentration carried by 18LPC-ToThyCholRu/SPIONs in the indicated cell lines following 48 h of incubation.

2. Synthesis and characterization of novel nucleolipid-based Ru(III)-complex LipThyRu

Following the design of the amphiphilic nucleolipids ToThyRu, HoThyRu, DoHuRu and ToThyCholRu (described before in paragraph 1.4),[135–137,153] a novel nucleolipid-based Ru(III)-complex was prepared (Figure 13). This compound was named LipThyRu, following the acronym taken from the main structural motifs present in its molecular skeleton: Lipoic acid-Thymidine-Ruthenium salt.

With a general structure similar to the previously described derivatives, LipThyRu is a thymidine derivative carrying a pyridine-methyl arm at the *N*-3 position of the nucleobase, inserted as anchoring ligand for the Ru(III)-complex; this nucleoside has been further derivatized with a hydrophilic heptaethylene glycol chain at the 5'-position and a lipophilic chain, *i.e.* a lipoic acid residue, at the 3' position. As already discussed for the previously described nucleolipidic compounds, the use of a hydrophilic moiety is intended not only to optimize the "hydrophilic/lipophilic balance" within the hybrid molecule, but also - at a functional level - to prevent extracellular enzymatic degradation by the reticuloendothelial system. On the other hand, the lipophilic component of the nucleolipidic Ru(III)-complex is necessary in our design to ensure its self-assembly in aqueous solution but also to establish specific interactions with suitable nanoplatforms, as liposome or niosome structures, which can thus incorporate it giving stable formulations. If inserted within liposomes, or liposome-coated nanoparticles, the driving force for the nucleolipid encapsulation is simply based on hydrophobic interactions. In the case of niosomes, since these are positively charged carriers, their functionalization process is based on electrostatic attractions with the negatively charged Ru(III)-complex (see chapter 5.2).

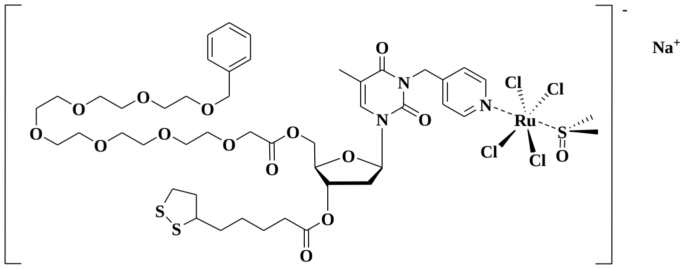

LipThyRu

Figure 13. Structure of the amphiphilic nucleolipidic Ru(III)-complex LipThyRu.

As an additional property, the presence of the lipoic acid disulfide bond in LipThyRu can be exploited to allow its easy immobilization onto gold surfaces, as for instance gold nanoparticles, thanks to the high affinity of sulfur for gold, forming very stable S-Au covalent bonds.

Thus, this nucleolipidic Ru(III)-complex, carrying useful decorations which in principle allow their easy functionalization onto different nanoplatforms, appears as a really versatile tool in the construction of multifunctional nanosystems.

The decoration with the lipophilic and hydrophilic chains on the sugar hydroxyl moieties was performed through simple ester bonds, which are easily formed by classical DCC/DMAP activation of the selected carboxylic acids.[175,176] These chemical linkages are typically stable in neutral solutions and in extracellular media, but are rapidly cleaved within the cell by cellular esterases, releasing the active portion of the molecule.

2.1. Results and discussion

2.1.1. Synthesis and characterization of LipThyRu

The synthesis of target compound LipThyRu was realized by a straightforward and high yielding strategy based on a well-established chemistry, involving the use of easy-to-handle, commercially available reagents (Scheme 1).

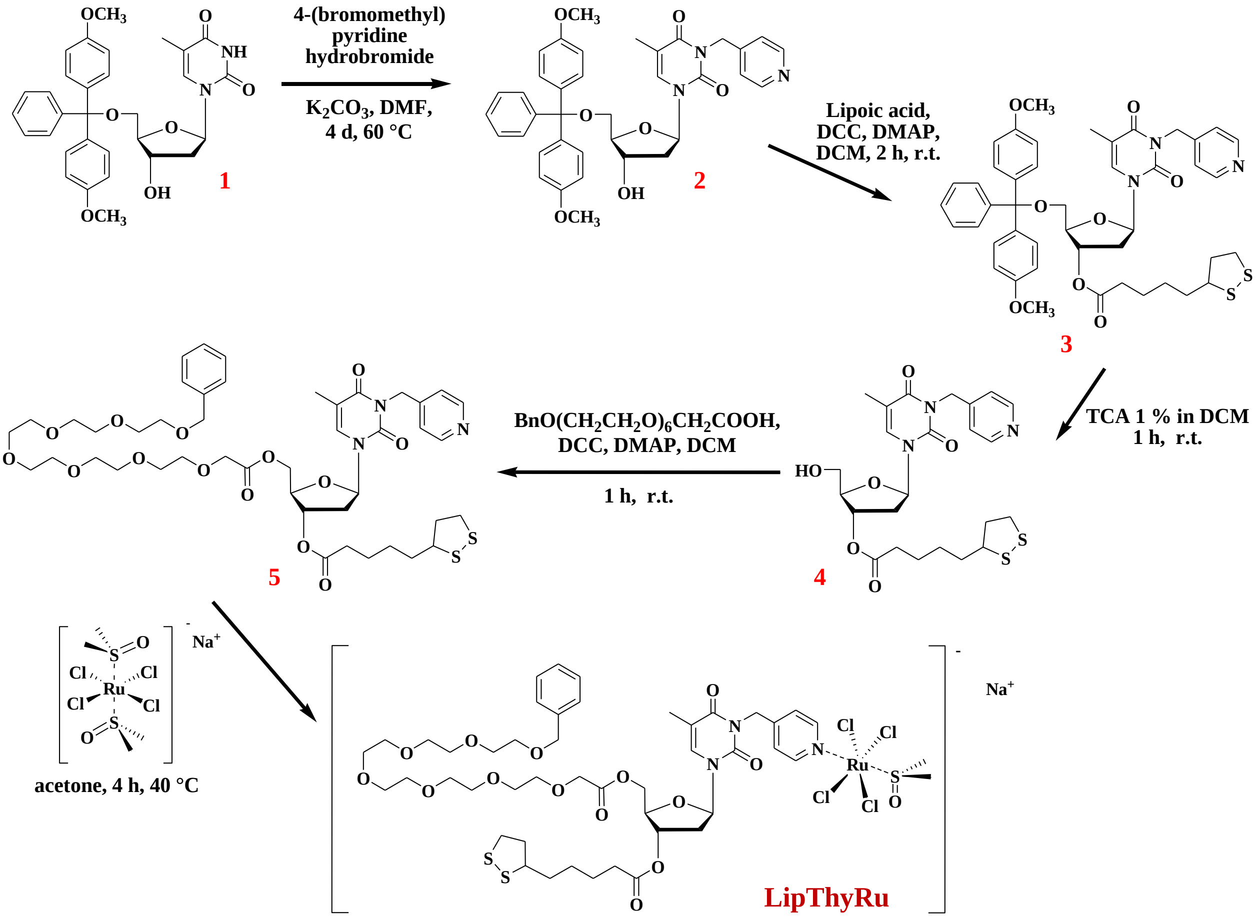

Scheme 1. Synthetic procedure for the preparation of the nucleolipidic Ru(III)-complex LipThyRu.

Insertion of the pyridine moiety on the thymidine scaffold was achieved by treatment of the commercially available 5′-O-(4,4′-dimethoxytriphenylmethyl)thymidine **1** with a slight excess of 4-(bromomethyl)pyridine in DMF in the presence of K_2CO_3 as base. In this reaction, the imide N-3 of thymidine has a relatively acidic proton (pK_a ca. 8) and could be easily deprotonated, thus undergoing a nucleophilic substitution and giving alkylated compound **2** in 59 % isolated yields. Under the used conditions, the less reactive 3’-hydroxyl of the sugar moiety did not compete in the alkylation reaction, remaining available for the next coupling step. This group was then coupled with lipoic acid using DMAP and DCC as condensing agents, affording compound **3** in 77 % yields after chromatographic purification on a silica gel column. The successive DMT removal realized under acidic conditions (1 % TCA in CH_2Cl_2) gave compound **4** in almost quantitative yields (99 %). Next, the condensation with the heptaethylene glycol derivative **8** (BnO-HEG acetic acid) allowed obtaining target nucleolipid **5**.

BnO-HEG acetic acid **8** was synthesized starting from hexaethylene glycol (HEG), elaborated into an acetic acid derivative (Scheme 2), following a straightforward and high yielding procedure. First, a benzylation to selectively cap one OH group was required: this nucleophilic substitution reaction was realized using benzyl bromide (in 1:1 ratio with respect to the starting material) and NaH in THF as solvent, giving alcohol **6** in 65 % yields. The following treatment with *tert*-butyl bromoacetate, in the presence of NaH, provided ester **7** in 86 % isolated yields. After an acid treatment with formic acid, ester **7** was converted into target carboxylic acid **8** in almost quantitative yields (98 %), and finally coupled at the 5’-OH end of **4** to give the desired nucleolipid **5**. The 5’-functionalization was obtained by ester bond formation using the coupling system DCC/DMAP, affording the target compound in 74 % overall yields after silica gel column purification.

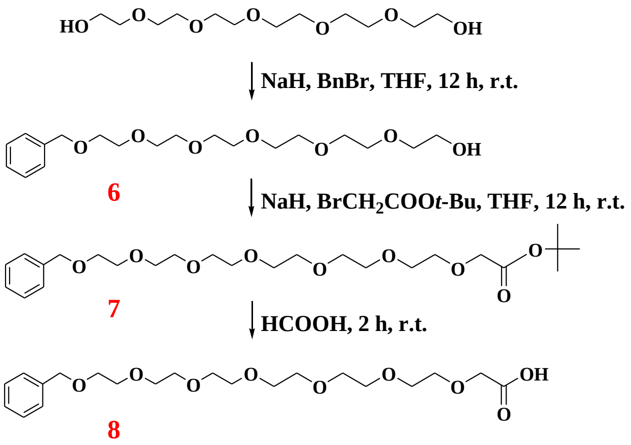

Scheme 2. Synthetic procedure for the preparation of BnO-HEG acetic acid (Bn = benzyl group).

The last step was a ligand exchange reaction between nucleolipid **5** and the Na^+ [*trans*-$RuCl_4(DMSO)_2]^-$ salt prepared in our laboratory following a reported procedure.[106,177] The reaction was performed at 40 °C using acetone as solvent. After 4 h, TLC monitoring showed the complete disappearance of the starting materials and the reaction was quenched removing the solvent under vacuum. Then the crude product, filtered and washed several times with AcOEt, allowed the desired LipThyRu, recovered in 71 % yields. Following this synthetic procedure, LipThyRu was obtained in 24 % overall yields for 5 steps.

All the synthetic intermediates and the final nucleolipid have been characterized by ^1H and ^{13}C NMR spectroscopy, as well as by ESI-MS spectrometry, which in all cases confirmed the identity and purity of the target compounds. Signals observed in the ^1H NMR spectrum of LipThyRu (Figure 14) are particularly diagnostic of the effective complex formation.[81,178] Indeed the presence of the paramagnetic ruthenium(III) ion produces a dramatic upfield shift and a broadening of the protonic signals of pyridine and dimethyl sulfoxide, found at δ = -1.8 and δ =-12.7 ppm, respectively. In the ESI-MS spectrum, recorded in the positive ions mode, the molecular ion shows the expected mass/charge ratio and the characteristic isotopic pattern of ruthenium (Figure 15).

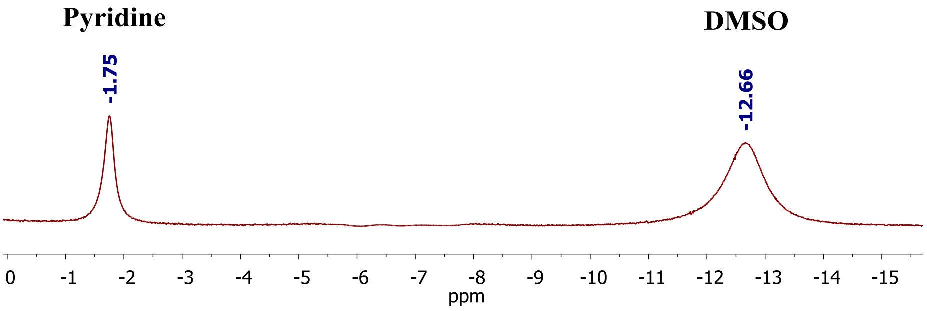

Figure 14. Upfield region expansion of the ^1H NMR spectrum of the nucleolipid-based Ru(III)-complex LipThyRu [400 MHz, $(CD_3)_2CO$].

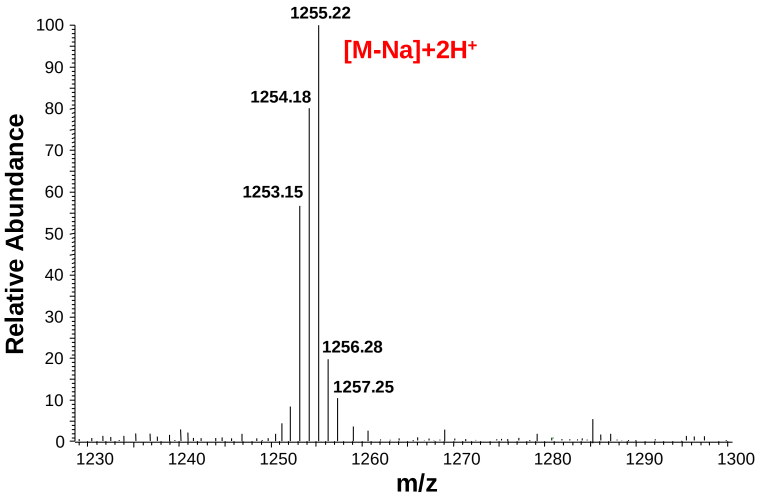

Figure 15. ESI-MS spectrum (positive ions) of LipThyRu.

2.1.2. UV-vis studies: absorbance spectra of LipThyRu

In analogy with NAMI-A and AziRu, also the nucleolipidic Ru(III)-complexes ToThyRu, HoThyRu, DoHuRu and ToThyCholRu showed limited stability in aqueous solutions. In fact, formation of green precipitates, in a period going from few hours in phosphate buffers to few days in pure water, was observed also for these nucleolipidic Ru(III)-complexes, even if somehow retarded compared with the "naked" AziRu or NAMI-A. The degradation process was attributable to the replacement of the ligands of the ruthenium complex by water molecules and/or hydroxide ions, well known for NAMI-A and related analogs.[81,104,105,108] In this frame, also the hydrolysis of LipThyRu complex has been analysed, by monitoring its UV-vis spectra over time. Indeed, UV-vis analysis allows detecting the formation of the aqua-complexes, obtained through the exchange of the chloride or DMSO ligands with water molecules and postulated to be the species effectively reactive with the *in vivo* targets.[64,108,112,118,125–128,178]

The UV-vis-monitored hydrolysis of the new complex LipThyRu was analysed over time in a saline buffered solution mimicking the extracellular physiological conditions (10 mM phosphate buffer/100 mM NaCl pH = 7.3). First of all, the UV-vis spectrum of LipThyRu was recorded immediately after its dissolution in DMSO at 100 μM final concentration, and compared with those of AziRu[147] and Na^+ [*trans*-$RuCl_4(DMSO)_2]^-$ (Figure 16).

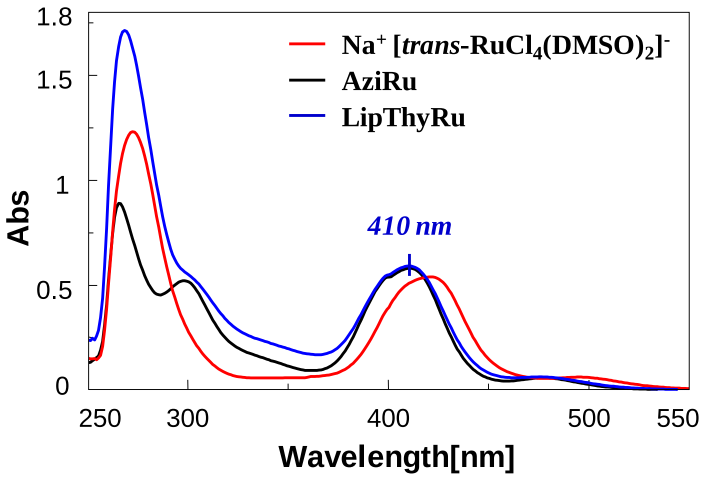

Figure 16. Overlapped UV-vis absorption spectra of Na^+ [*trans*-$RuCl_4(DMSO)_2]^-$, AziRu and LipThyRu (from samples freshly dissolved at 100 μM concentration in DMSO).

The UV-vis spectrum of LipThyRu showed the characteristic band centred at 410 nm, relative to the ligand-to-metal charge transfer transition (LMCT) for the Ru–Cl bond, in addition to overlapped bands in the region 250-350 nm, which can be attributed to the metal, the pyridine portion and the thymine base contributions. Comparing the UV-vis spectra of LipThyRu and AziRu, the presence of the same band at ca. 400 nm confirmed the same ligands arrangement around the Ru(III) nucleus.

Interestingly, this band is slightly blue-shifted with respect to the salt Na$^+$ [*trans*-RuCl$_4$(DMSO)$_2$]$^-$ precursor of both AziRu and LipThyRu – which presents DMSO as apical ligand in lieu of pyridine.

2.1.3. UV-vis-monitored hydrolysis of LipThyRu in a saline phosphate buffer

The hydrolysis of LipThyRu was monitored by UV-vis analysis over time in a saline phosphate buffered solution (10 mM phosphate buffer/100 mM NaCl pH = 7.3), mimicking the extracellular media. The absorption spectra (Figure 17) showed a band centred at 398 nm, attributed to the LMCT, which gradually diminished over time disappearing in ca. 7 h; concomitantly, a decrease of the absorption bands in the region between 250-300 nm was observed.

Since the first monitoring hours, an overall raising of the spectrum baseline was observed, associated with scattering phenomena, probably due to the formation of aggregates, which reached stability after 4 h (Figure 17).

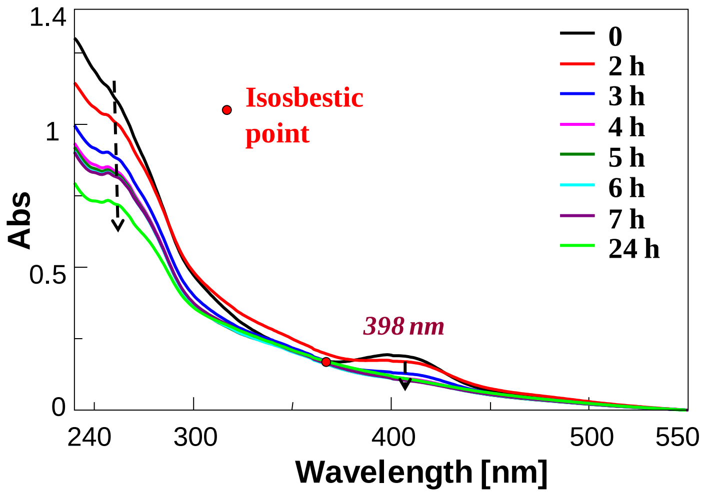

Figure 17. Overlapped UV-vis absorption spectra of LipThyRu at 50 μM concentration in the PBS (saline phosphate buffer) solution, recorded at different times after dissolution (0→24 h). The red circle indicates the isosbestic point.

In Figure 18 the absorbance evolution over time of AziRu under the same conditions is reported for comparison, showing its conversion into a species having a maximum at 349 nm (presumably, by analogy with the hydrolysis of NAMI-A, the mono-aquo complex), successively forming a species with a maximum at 305 nm (presumably, the di-aquo complex).[147]

In analogy with AziRu, the presence of an isosbestic point is evident in Figure 17 for LipThyRu, indicating its transformation into another species within 3.5 h; unlike AziRu, in the saline phosphate buffer LipThyRu was transformed only into the monoaquo-complex and not into a diaquo-complex.

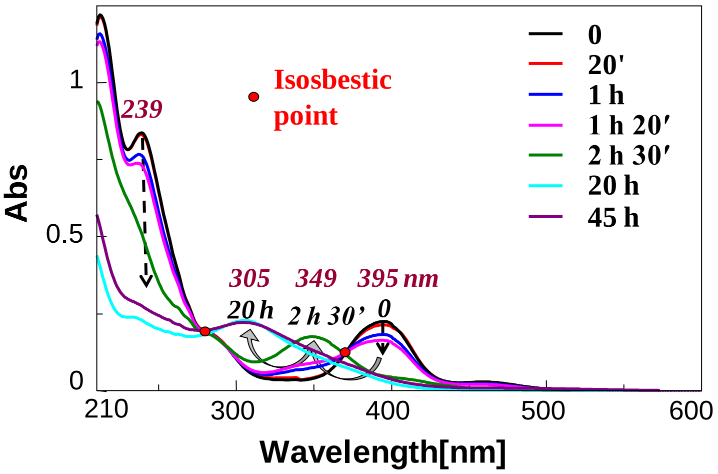

Figure 18. Overlapped UV-vis absorption spectra of AziRu at 50 µM conc. in the saline buffer recorded at different times after dissolution (0→45 h). The red circles indicate the isosbestic points.

Reporting the A_{398} as a function of time (Figure 19) a half-life time ($t_{1/2}$) of 2.5 h is obtained, almost 3.3 times higher than that observed for AziRu ($t_{1/2}$ for AziRu = 45 min[147]). The slower hydrolysis rate of LipThyRu is a clear evidence of the higher stability of the Ru complex when inserted into a nucleolipidic carrier. In summary, LipThyRu showed a slower hydrolysis kinetics than AziRu when analysed in a pseudo-physiological solution, confirming that the presence of the nucleolipid moiety decorating the Ru(III)-complex effectively protects it and retards the aquo-species formation.

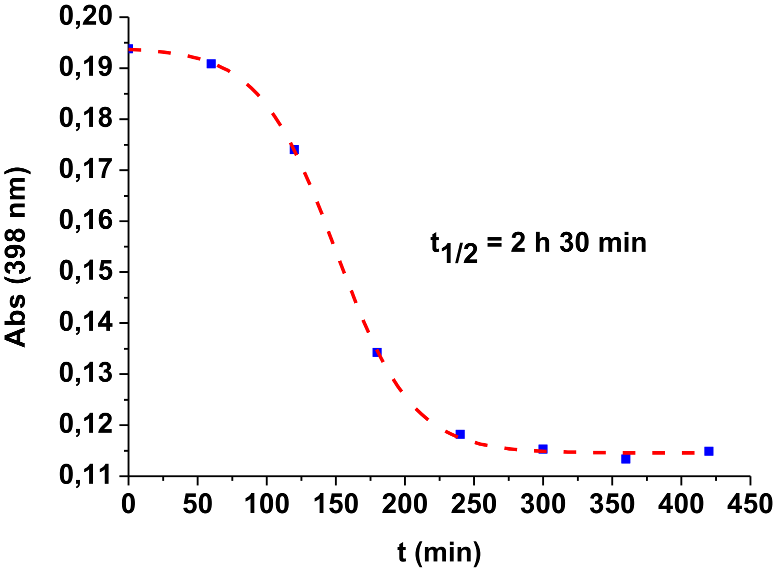

Figure 19. A_{398} values of LipThyRu as a function of the hydrolysis time in a saline phosphate buffer.

3. Synthesis and characterization of novel aminoacyllipidic Ru(III)-complexes TUGluRu and TOTyroRu

In order to expand the repertoire and chemical diversity of available amphiphilic Ru(III)-complexes, we moved to the exploration of biocompatible scaffolds alternative to nucleosides to build novel multifunctional compounds. To this purpose we selected trifunctional α-amino acids to replace the central core of previously described nucleolipidic Ru(III)-complexes, however maintaining the same general design (Figure 9). In fact, these novel aminoacyl derivatives, as their nucleolipidic congeners, incorporate the active principle - *i.e.*, the Ru(III)-complex - into multifunctional scaffolds carrying both hydrophilic and lipophilic portions, in principle able to self-assemble in water to give stable aggregates, and thus obtain a suitable nanocarrier for *in vivo* delivery.

In this optimization process, special attention has been paid to the simplification of the synthetic schemes, trying to reduce the number of purification steps and increase the overall yields, so to obtain the target Ru(III)-complexes in the large amounts required for future *in vivo* studies.

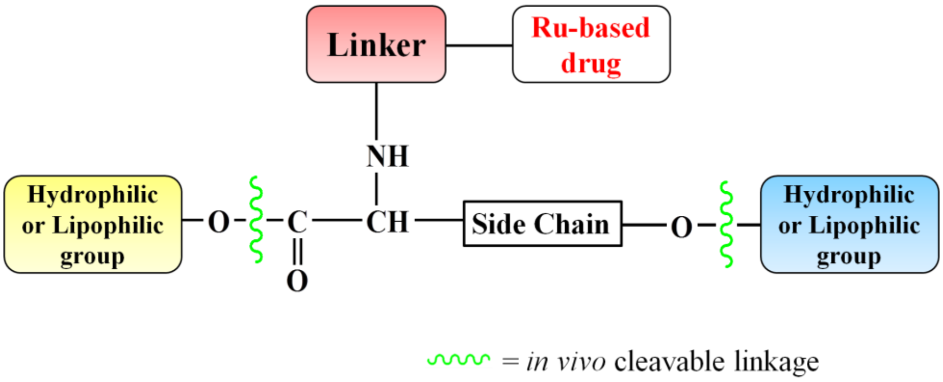

Figure 20. Schematic representation of the general design exploited for the preparation of aminoacyllipidic Ru(III)-complexes.

These novel molecules, described as aminoacyllipidic Ru(III)-complexes, share the general design represented in Figure 20, characterized by:

- a natural trifunctional α-amino acid, selected as the central scaffold;
- a lipophilic group, to induce self-assembly in aqueous solutions and to improve cell uptake of the final compound through the membrane phospholipidic bilayers;
- a triethylene glycol monomethyl ether residue as hydrophilic group. This decoration – as in the case of nucleolipidic Ru(III)-complexes - is expected to optimize the “hydrophilic/lipophilic balance” within the molecule and to increase its circulation time,[162] preventing extracellular chemo-enzymatic degradations. In addition, it is known to have ‘stealth properties’, masking the attached drug from immune system responses;[163–165]

- a pyridine-methyl arm, as the active Ru(III)-complex, inserted through formation of an amide bond with the aminoacyl core, expectedly stable *in vivo*.

Following this general design, two aminoacyllipidic Ru(III)-complexes, named TUGluRu and TOTyroRu (Figure 21) - following the acronym taken from the main motifs present: Triethylene glycol-Undecenyl-Glutammic acid-Ruthenium salt and Triethylene glycol-Oleyl-Tyrosine-Ruthenium salt, respectively - have been successfully synthesized and characterized using both spectroscopic (NMR and UV) and mass spectrometry techniques.

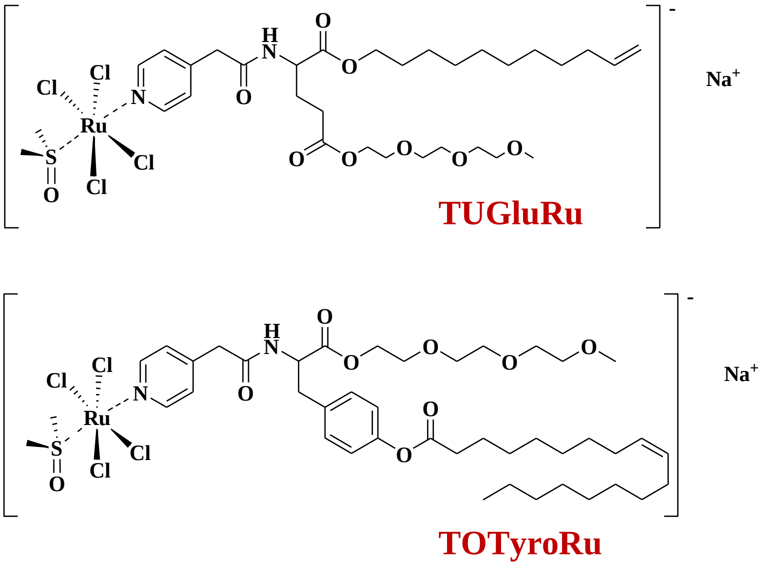

Figure 21. Structure of the novel amphiphilic aminoacyllipid Ru(III)-complexes here prepared.

Following a scheme similar to the one exploited for the nucleolipidic Ru(III)-complexes, we have functionalized the central scaffold with different lipophilic and hydrophilic residues, inserted exploiting ester linkages, *in vivo* cleavable by cellular esterases. The choice of ester bonds as chemical linkages between the aminoacyl core scaffold and the functional appendage has been dictated by both synthetic and functional requirements: these groups are typically obtained easily and in high yields, are stable at neutral pH, but are susceptible of rapid hydrolysis within cells, due to the action of esterases. These cellular enzymes of the class of hydrolases are capable of cleaving the ester bonds in a non-specific manner, thus releasing a small molecular weight Ru-complex once internalized into the cell.

The linker ensuring the attachment of the Ru(III)-complex is also in this design a pyridine derivative, selected as chelating ligand given the high affinity of ruthenium for nitrogen, introduced into the aminoacyl central scaffold through formation of an amide bond, expectedly stable *in vivo*.

For the preparation of the new aminoacyllipidic Ru(III)-complexes, commercially available derivatives of glutammic acid and tyrosine having the same set of protective groups have been selected as starting materials, so to handle a similar general synthetic procedure.

In particular, we focused on protective groups selectively removable in an orthogonal manner, *i.e.* 9-fluorenylmethoxycarbonyl (Fmoc) for the α-NH_2 group, and *tert*-butyl (*t*Bu) for the side chain OH or COOH functions. Fmoc/*t*Bu probably is the most popular "orthogonal" combination of protecting groups used for trifunctional α-aminoacids, relying on the lability to bases of the α-amino protecting group Fmoc, and on the lability to acids of the side chain protecting group *t*Bu ethers/esters. In the Fmoc/*t*Bu strategy, 20 % piperidine in DMF is generally used as the basic solution to remove the Fmoc group and release the free α-amino group, and 90% TFA to remove the *tert*-butyl group in the side chain.

This orthogonal protecting group strategy is well established for the solid phase synthesis of peptides and peptidomimetics, but can be easily extended to our solution syntheses of novel aminoacyllipidic derivatives.

In particular, the α-amino acids here selected have a free, unprotected carboxylic acid group, on which the first functionalization reaction (with a lipophilic or a hydrophilic moiety, respectively in the case of TUGluRu and TOTyroRu) could be directly performed. Next, removal of the acid labile protecting group (*t*Bu) in the side chain allowed performing a coupling of the free COOH or OH groups with a hydrophilic (for TUGluRu) or lipophilic (for TOTyroRu) moiety, respectively.

Finally, after deprotection from the base labile Fmoc protecting group, the α-NH_2 function was exploited for the labeling with a pyridine-containing linker, necessary for successive Ru(III) complexation.

In all the investigated cases, the decorations used for the preparation of the new aminoacyllipidic Ru(III)-complexes are commercially available compounds, which have been used as such, without further synthetic elaboration before use. For both TUGluRu and ToTyroRu triethylene glycol monomethyl ether (TEG-OMe) was used as hydrophilic decoration, already employed in ToThyRu and ToThyCholRu, for which the ability to self-assemble in water to give stable aggregates has been well proved. In particular, the TEG-OMe residue was introduced on the free carboxylic group of Fmoc-protected tyrosine in ToTyroRu and on the side chain carboxylic group of Fmoc-protected glutamic acid in TUGluRu. As the lipophilic components, we selected oleic acid for ToTyroRu - already tested in ToThyRu, HoThyRu and DoHuRu - inserting it on the phenolic OH in the side chain. In the case of TUGluRu, we labeled the free carboxylic COOH with 10-undecen-1-ol. This alcohol has been selected to investigate if, even using a shorter lipophilic chain than that of oleic acid, stable aggregates in water are still obtained. In addition, this functionalization, carrying a terminal alkene, would also allow in principle the coupling with a thiol using a "thiol-ene" click chemistry strategy.[179] Therefore, this type of lipid functionalization could be a powerful strategy to incorporate aminoacyllipidic Ru-complexes in nanoparticles or lipid-based platforms exposing a thiol functionality on their surface. This design - which will be explored in future studies - could improve the conveyance and stability of the drug in physiological environments.

3.1. Results and discussion

3.1.1. Synthesis and characterization of TUGluRu

For the preparation of TUGluRu, the first step was the esterification of commercially available Fmoc-Glu(O*t*Bu)-OH with 10-undecen-1-ol. The reaction was carried out under anhydrous conditions using a little excess of the starting amino acid with respect to the alcohol. HATU/DIPEA was selected as the best coupling system[180] after several attempts with other activation methods (Scheme 3). Desired compound **9**, isolated in 81 % yields after chromatographic purification on a silica gel column, was then treated with formic acid to remove the *tert*-butyl group. The mechanism of this deprotection is based on the release of the stable *tert*-butyl cation, which then rearranges forming isobutylene, a volatile compound which can be easily removed by coevaporating the reaction mixture with dry CH_3CN. The reaction went to completion in 2.5 h and, after this simple work-up, compound **10** could be recovered as a pure species in almost quantitative yields.

Successively, the COOH group in the side chain of **10** was coupled with TEG-OMe, previously coevaporated several times with dry CH_3CN, using HATU/DIPEA as condensing system under anhydrous conditions, yielding compound **11** in 66 % yields after chromatographic purification. This derivative was then treated with a 10 % piperidine solution in CH_3CN to remove the Fmoc protecting group and release the free α-amino group. Amino diester **12**, obtained in almost quantitative yields from TLC analysis of the reaction mixture, was directly reacted, as a crude, with 4-pyridylacetic acid under dry conditions – using HATU/DIPEA as a coupling system – to obtain the final aminoacyllipid derivative **13**.

Desired compound **13** was obtained in 50 % yields (calculated for the two steps, *i.e.* Fmoc removal and 4-pyridyl acetic acid coupling) after chromatographic purification on a silica gel column. This compound was not stable in solution and decomposed over time, partially losing the TEG-OMe residue (probably due to an intramolecular attack of the pyridine ring on the carboxylylate group, which promotes the detachment of the TEG-OMe residue forming a stable six-atom cyclic intermediate). Therefore, in order to perform the last reaction, **13** was further purified and then immediately reacted with the Ru(III) salt to obtain the final target compound TUGluRu. The reaction was performed using a stoichiometric amount of Na^+ [*trans*-$RuCl_4(DMSO)_2]^-$ salt, synthesized according to reported procedures[106,177] (see paragraph 5). The reaction mixture was left under stirring at 40 °C. After 30 h, TLC monitoring showed the formation of a new product, attributed to the desired TUGluRu, recovered as a pure compound by solvent removal under reduced pressure (Scheme 3).

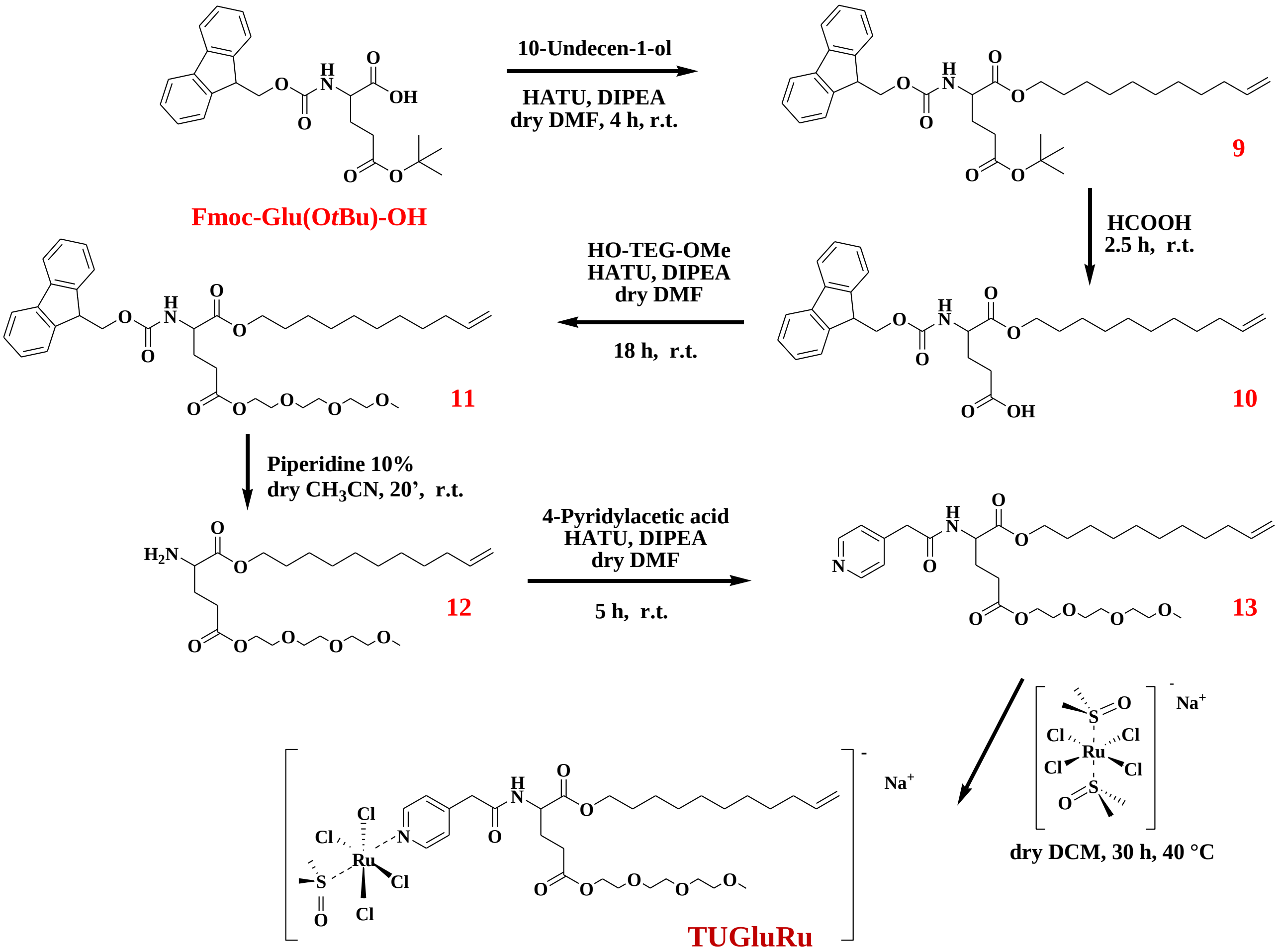

Scheme 3. Synthetic procedure for the preparation of the target aminoacyllipid Ru(III)-based complex TUGluRu.

Following this synthetic scheme, the final aminoacyllipidic Ru(III)-complex TUGluRu was obtained in 6 steps and 27 % overall yields. The characterization of all the synthetic intermediates and of final TUGluRu has been carried out by NMR spectroscopy and MS spectrometry, which in all cases confirmed the identity and purity of the target compounds. The signals observed in the ^{1}H NMR spectrum of TUGluRu (Figure 22) were particularly diagnostic of the effective complex formation, with a dramatic upfield shift and a broadening of the protonic signals of pyridine and dimethyl sulfoxide, found at δ = - 0.90 and δ = -9.51 ppm, respectively.

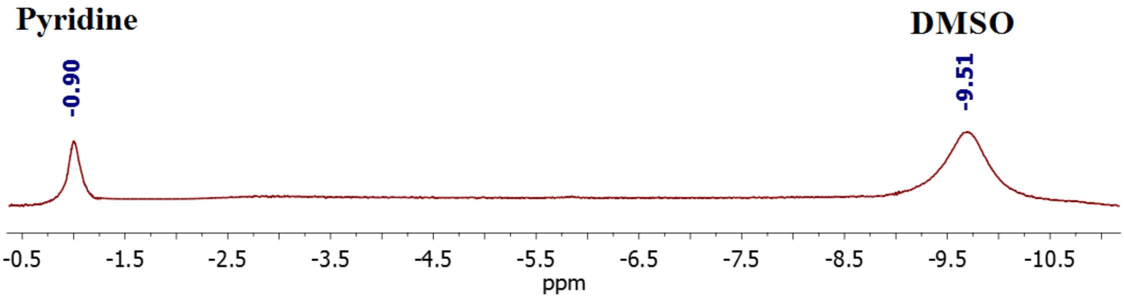

Figure 22. Upfield region expansion of the ^{1}H NMR spectrum of TUGluRu [400 MHz, $(CD_3)_2CO$].

The ESI-MS spectrum of TUGluRu, recorded in positive ions mode, did not show the *m/z* signal corresponding to the molecular ion, but clusters of signals with the typical isotopic pattern of ruthenium were observed. In particular, as shown in Figure 23, the adduct with sodium ($M+Na^+$) was found together with other *m/z* values attributable to ligand exchange species, *i.e.* ($M-2Cl^- +2H_2O$) and ($M-Cl^-+H_2O$).

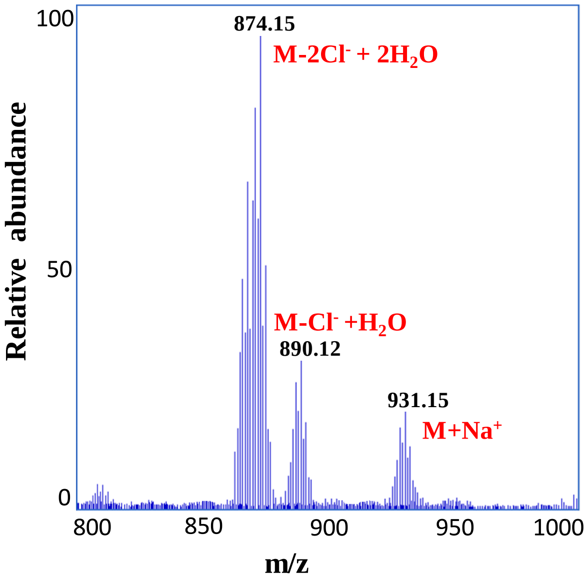

Figure 23. ESI-TOF (positive ions) mass spectrum of TUGluRu.

3.1.2. Synthesis and characterization of TOTyroRu

The synthetic strategy to obtain the aminoacyllipid Ru(III)-complex TOTyroRu is similar to the one previously described to obtain TUGluRu (see paragraph 3.1.1). The only difference resides in the functionalization of the phenolic OH group in the side chain, for which the best results were obtained using a Mitsunobu reaction.[181]

As starting material, the commercially available Fmoc-Tyr(*t*Bu)-OH was selected. Its coupling with the alcohol TEG-OMe using the system HATU/DIPEA as condensing agent gave desired compound **14** (Scheme 4), recovered in 96 % yields after column chromatography. The successive deprotection of the phenol group in the side chain was obtained treating compound **14** with formic acid, affording desired compound **15** in almost quantitative yields and in pure form simply removing the volatile by-product isobutylene through coevaporation with dry CH_3CN.

Successively, the deprotected phenol OH of tyrosine was reacted with oleic acid to obtain the corresponding phenyl ester. First experiments were carried out condensing derivative **15** with oleic acid in the presence of the system HATU/DIPEA as coupling agent. Nevertheless, this reaction proved to be troublesome, providing the desired compound only after a prolonged reaction time (48 h) under heating, and in low yields. Unfortunately, also testing different conditions, our attempts did not result in a significant yield enhancement, due to the low nucleophilicity of phenolic OH groups.

Thus, we were intrigued by the possible application of the Mitsunobu reaction to construct the desired C-O bond and provide phenyl ester **16**. Indeed, various protocols based on the Mitsunobu reaction[182] have been developed for the coupling of alcohols with phenols, amines or carboxylic acids. Hence, we exploited this synthetic strategy, screening a variety of reaction conditions. The best results were obtained on reacting pure compound **15**, oleic acid (1 eq.) and triphenylphosphine (2 eq.) – previously coevaporated three times with dry CH_3CN – in dry THF under stirring at r.t. for 10 min. Then DEAD (2 eq.) was added dropwise and the reaction mixture heated at 65 °C under argon atmosphere. After 24 h, TLC analysis showed the appearance of a new product in the mixture and the reaction was quenched by solvent removal *in vacuo*. The resulting white precipitate of triphenylphosphine oxide was filtered off and the solution was then purified by column chromatography, affording desired compound **16** in 38 % yield. Pure compound **16** was successively treated with a 10 % piperidine solution in dry CH_3CN under argon atmosphere. The obtained free amine **17** was not isolated, but directly treated with 4-pyridylacetic acid in the presence of HATU and DIPEA in anhydrous conditions, so to obtain the final aminoacyllipid **18**. After 17 h, TLC monitoring showed the complete disappearance of the starting materials and the reaction was quenched by taking the mixture to dryness. After work-up, the crude product was purified by column chromatography. The desired compound **18** was obtained in 54 % yields, calculated for two subsequent steps, *i.e.* Fmoc removal and coupling with 4-pyridylacetic acid.

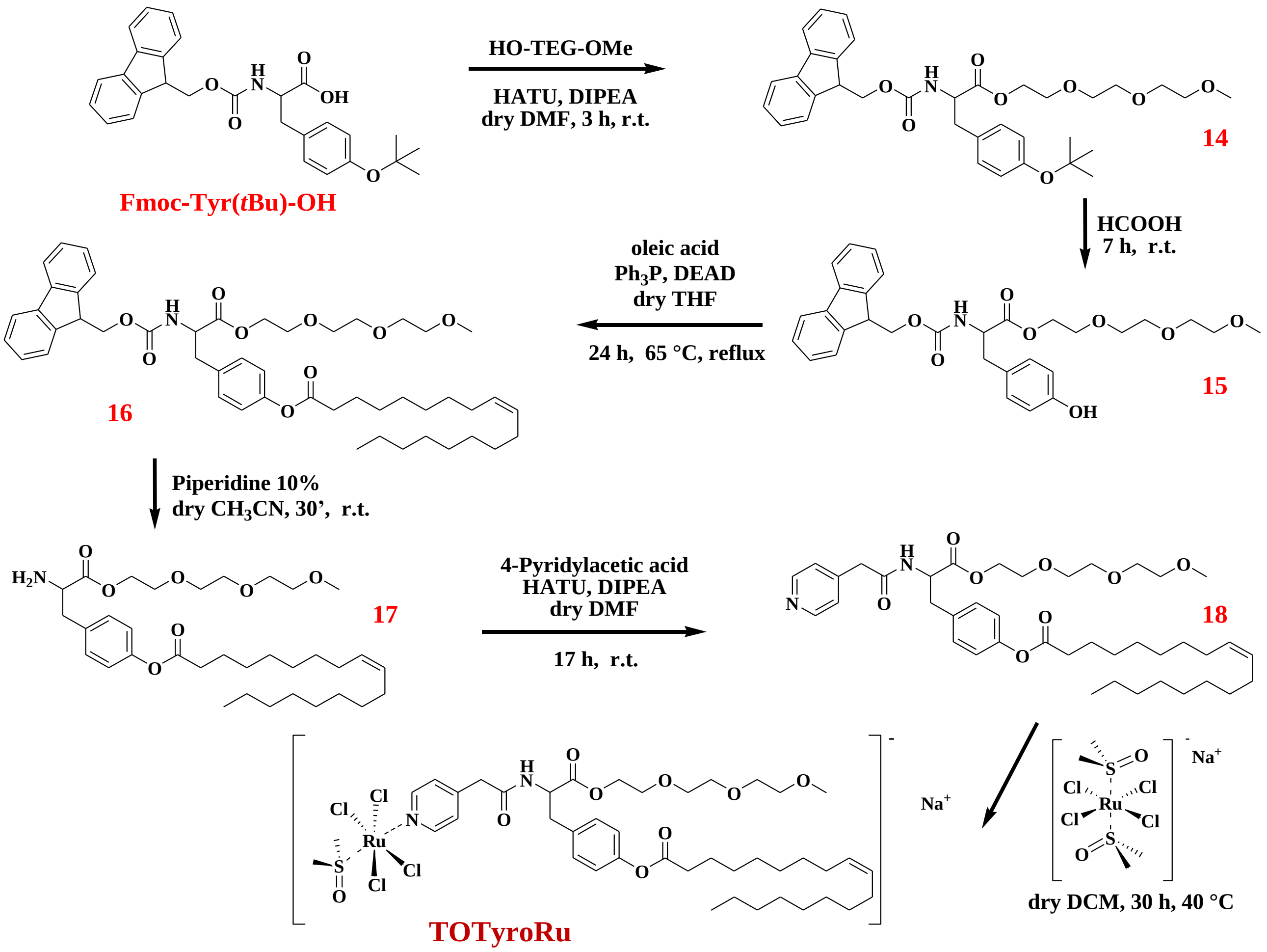

Scheme 4. Synthetic procedure for the preparation of the target aminoacyllipidic Ru(III)-complex TOTyroRu.

The last step of this synthesis was a ligand exchange reaction with a precursor ruthenium salt, prepared using reported procedures[106,177] (see paragraph 5), in which pure compound **18** was treated with stoichiometric amount of Na^+ [*trans*-$RuCl_4(DMSO)_2]^-$ at 40 °C for 30 h (Scheme 4). After solvent removal *in vacuo*, TOTyroRu was recovered as a pure compound in almost quantitative yields.

Following this synthetic scheme, the final aminoacyllipid Ru(III)-complex TOTyroRu was obtained in 6 steps and 20 % overall yields. All the synthetic intermediates and the final ruthenium complex have been characterized by NMR spectroscopy and mass spectrometry. In particular, as already observed for TUGluRu, the ^1H NMR spectrum of TOTyroRu (Figure 24) showed broadened signals, attributable to the presence of the paramagnetic Ru(III) ion. In addition, a dramatic upfield shift of the protonic signals of pyridine and DMSO, to δ = -1.48 ppm, and δ = -9.18 ppm, respectively, was observed, particularly diagnostic of the effective complex formation.[81,178]

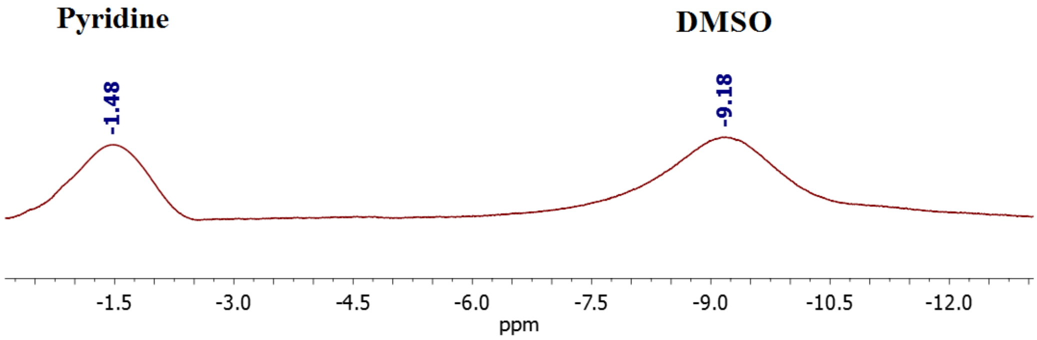

Figure 24. Upfield region expansion of the ^{1}H NMR spectrum of TOTyroRu [400 MHz, $CDCl_3$].

The ESI-MS analysis of TOTyroRu, carried out in the positive ions mode, did not show the *m*/*z* signals corresponding to the target compound. However, a cluster of signals with the typical isotopic pattern of ruthenium have been observed having *m/z* values attributable to the ligand exchange species $M\text{-}Cl^- + H_2O$. (Figure 25). This value is attributable to the aquo-complex of the desired Ru(III) derivative, obtained after a single hydrolysis event. This undesired process, however, can be presumably obtained during the LC-MS experiments, requiring a prolonged contact with the elution aq. solutions, and appears therefore as a MS artefact rather than an effective degradation of the target compound.

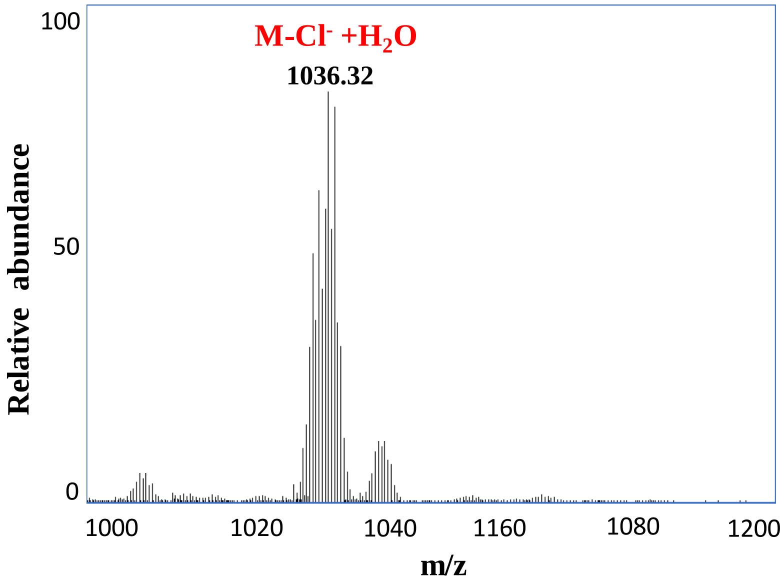

Figure 25. ESI-TOF (positive ions) mass spectrum of TOTyroRu.

3.1.3. UV-vis studies: absorbance spectra of TUGluRu

The solution behaviour of the new complex TUGluRu was first of all analysed by UV-vis absorbance. Thus, the UV-vis spectrum of TUGluRu was recorded at 100 µM concentration in DMSO, and compared with those of AziRu[147] and Na^+ [*trans*-$RuCl_4(DMSO)_2]^-$ under the same conditions (Figure 26).

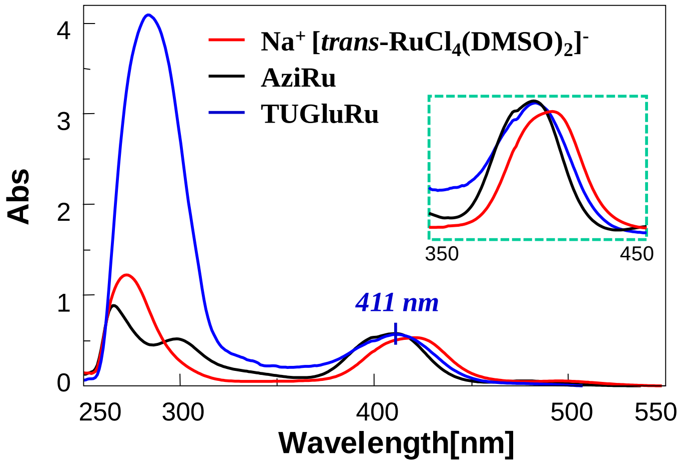

Figure 26. Overlapped UV-vis absorption spectra of Na$^+$ [*trans*-RuCl$_4$(DMSO)$_2$], TUGluRu and AziRu (from samples freshly dissolved at 100 μM concentration in DMSO).

The UV-vis spectrum of TUGluRu showed the characteristic band centred at 411 nm, relative to the ligand-to-metal charge transfer transition (LMCT) for the Ru–Cl bond, in addition to overlapped bands in the region 250-350 nm, which can be attributed to the metal, pyridine and thymidine absorptions. Comparing the UV-vis spectra of TUGluRu and AziRu, the similarity of the band at ca. 400 nm confirmed the same ligands arrangement around the Ru(III) core. Interestingly, this band is slightly blue-shifted with respect to the salt Na$^+$ [*trans*-RuCl$_4$(DMSO)$_2$]$^-$ – precursor of both AziRu and TUGluRu – having DMSO as apical ligand in lieu of pyridine (Figure 26).

3.1.4. UV-vis-monitored hydrolysis of TUGluRu in a saline phosphate buffer

The hydrolysis of TUGluRu was monitored by UV-vis analysis over time in a saline phosphate solution buffered at pH = 7.3 so to mimic pseudo-physiological conditions. The absorption spectra showed a band centred at 392 nm, attributed to the LMCT, which gradually diminished over time disappearing in ca. 3.5 h (Figure 27). In Figure 18 (paragraph 2.1.3.) the absorbance evolution with time of AziRu under the same conditions showed its conversion into a species having a maximum at 349 nm (presumably, by analogy with the hydrolysis of NAMI-A, the mono-aquo complex), successively forming a species with a maximum at 305 nm (presumably, the di-aquo complex). In the case of TUGluRu, the band at 392 nm gradually decreased over time with the concomitant emergence of a new band at 347 nm after 1 h, which reached its highest value after 3.5 h and then started decreasing (Figure 27). Unlike AziRu, in the saline phosphate buffer TUGluRu was only transformed into the monoaquo-complex and did not produce a diaquo-complex. A concomitant decrease of the absorbance intensity in the region 250-300 nm was also observed (Figure 27).

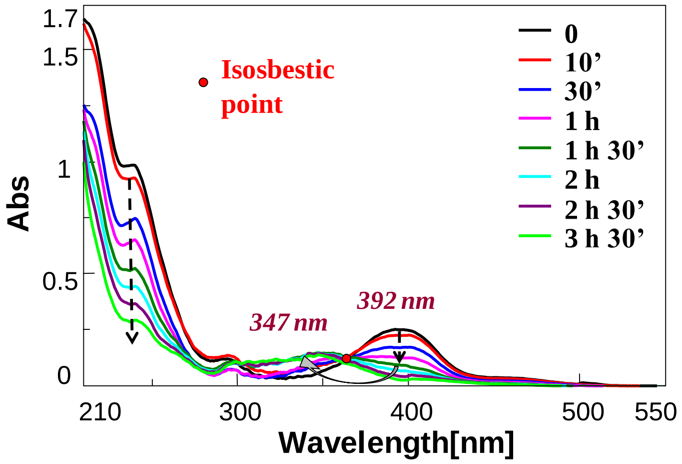

Figure 27. Overlapped UV-vis absorption spectra of TUGluRu at 50 μM concentration in the saline phosphate buffer, recorded at different times after dissolution (0→3.5 h). The red circle indicates the isosbestic point.

In analogy with AziRu, the presence of an isosbestic point is evident in Figure 27 for TUGluRu, indicating its transformation into another species during the initial 3.5 h monitoring. Reporting the A_{392} as a function of time (Figure 28) a $t_{1/2}$ = 105 min is obtained, almost twice higher than observed for AziRu ($t_{1/2}$ for AziRu = 45 min). In the time interval 4-72 h an overall raising of the spectrum baseline was observed, associated with scattering phenomena due to the probable formation of aggregates. In summary, TUGluRu showed a slower hydrolysis kinetics than AziRu when analysed in a pseudo-physiological solution, confirming that the presence of the aminoacyllipid moiety decorating the Ru(III)-complex effectively protects it and retards aquo-species formation.

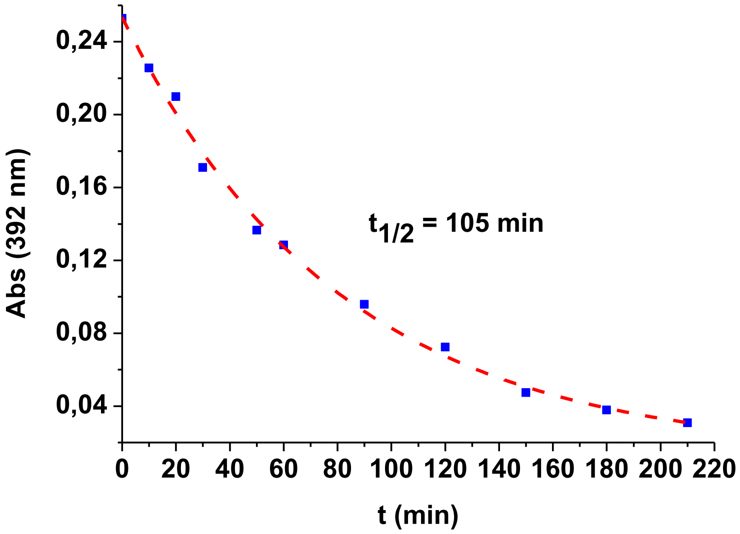

Figure 28. A_{392} values of TUGluRu as a function of the hydrolysis time in a phosphate buffer.

4. Synthesis and characterization of a new Ru(III)-complex, PySSRu, carrying a disulfide bridge

In addition to amphiphilic Ru(III)-complexes, also a new AziRu analog was here prepared, named PySSRu, characterized by a disulfide bridge. In analogy with the design chosen for LipThyRu, this moiety is finalized to anchoring the Ru(III)-based complex onto gold surfaces (*e.g.*, electrodes) in order to study the properties and oxidation kinetics of AziRu-like ruthenium derivatives through combined techniques, including cyclic voltammetry and Raman spectroscopy. The immobilization onto gold platforms can be realized exploiting the high affinity of sulphur for gold, leading to the formation of a stable covalent bond.

The synthetic procedure adopted for the preparation of PySSRu employs simple manipulations and easily available starting materials; with the target PySSRu complex obtained in three reaction steps.

Starting from commercially available 2-(4-pyridinyl)ethanethiol hydrochloride, an acid–base reaction was first performed to convert the hydrochloride salt into 2-(4-pyridinyl)ethanethiol.

Taking into account the pKa values of the pyridinium ion (pKa ca. 5) and the thiol group (pKa ca. 8-9), addition of a base in stoichiometric amount leads to the deprotonation of the pyridinium ion as the exclusive event under the experimental conditions tested.

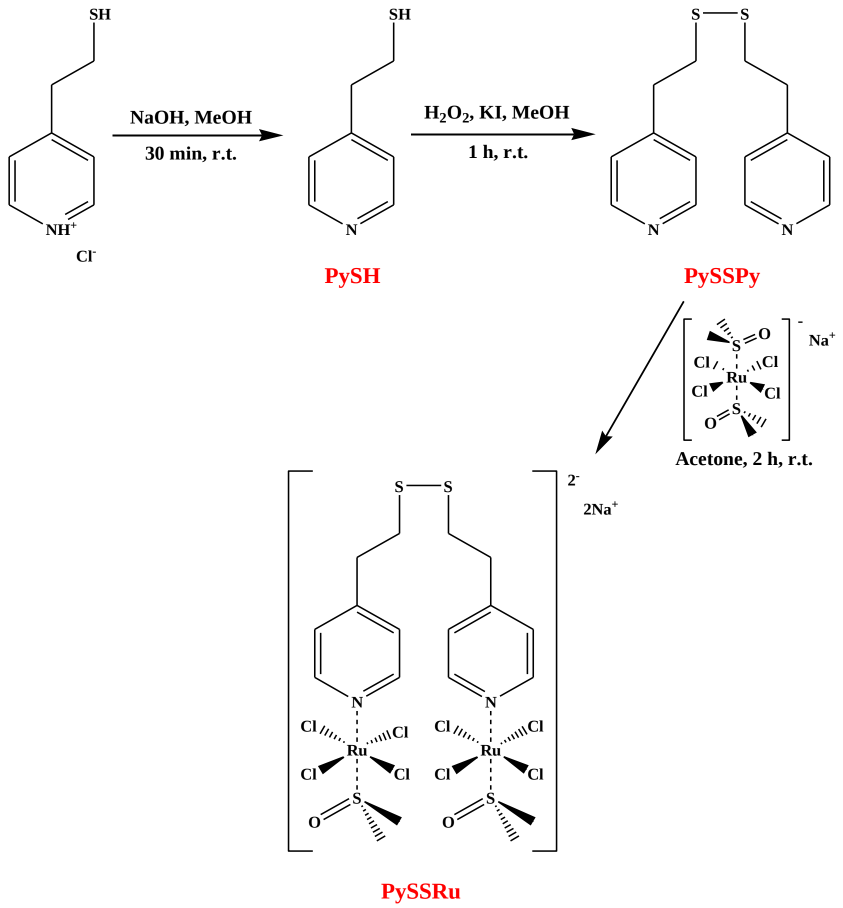

Scheme 5. Synthetic procedure for the preparation of the target compound PySSRu.

The conversion to the desired 2-(pyridin-4-yl)ethanethiol (here called PySH) was thus obtained by addition of 1 eq. of NaOH in MeOH according to Scheme 5, monitored by pH measurements until neutral pH was achieved, indicating that the reaction was complete. Then the solvent was removed *in vacuo* and the crude product extracted with CH_2Cl_2/H_2O. The extraction - necessary to remove NaCl formed during the neutralization reaction - provided pure compound **19** as a yellow oil in 82 % isolated yields.

PySH could not be used for the complexation reaction with the ruthenium salt. Indeed, first of all thiolates are able to strongly coordinate metal ions (including ruthenium) and form stable transition metal-thiolate complexes. Then, thiols can reduce Ru(III) to Ru(II): experimental evidences indicated that the reaction between PySH and the precursor ruthenium salt cannot be realized preserving Ru in its +3 oxidation state. In fact, the reaction mixture immediately turned from dark red to green, diagnostic of the reduction of Ru(III) to Ru(II). Therefore, it was necessary to convert first the thiol group of PySH to disulfide, using a reported oxidation procedure,[183] involving the treatment with hydrogen peroxide (30 wt. % in H_2O solution) as co-oxidant agent, and potassium iodide as catalyst (Scheme 5). The desired compound **20** (PySSPy) was recovered in almost quantitative yields after standard work-up with CH_2Cl_2/H_2O.

The last step (Scheme 5) is the ligand exchange reaction with the precursor ruthenium salt Na^+ [*trans*-$RuCl_4(DMSO)_2$]$^-$, prepared using reported procedures.[106,177] After 2 h, TLC analysis showed the formation of a new product, corresponding to the desired ruthenium complex, with the concomitant complete disappearance of both the starting materials. PySSRu was recovered in 75 % yields after solvent removal under reduced pressure and subsequent precipitation/centrifugation steps from CH_2Cl_2 solutions.

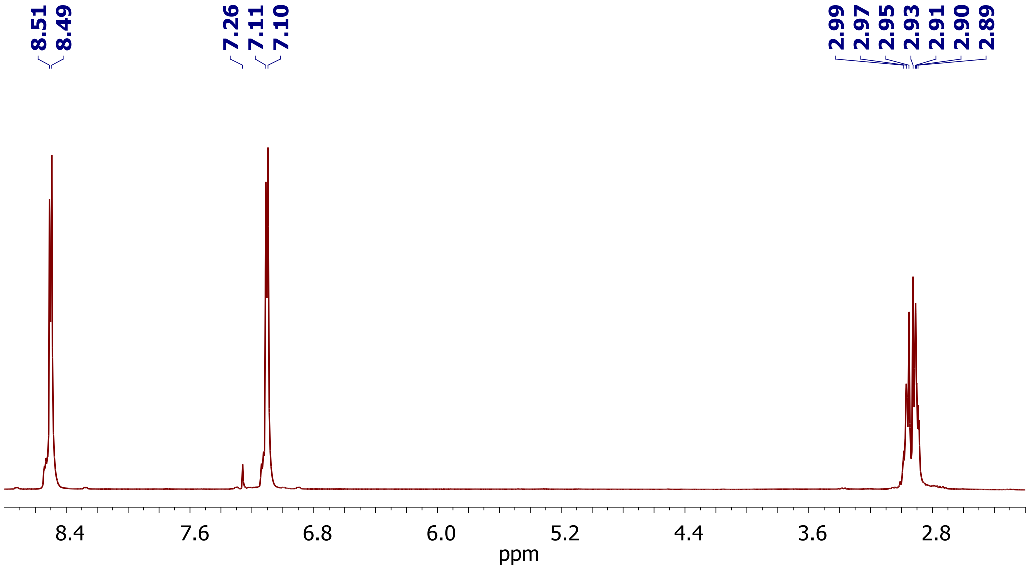

Figure 29. ^{1}H NMR spectrum of PySSPy (400 MHz, $CDCl_3$).

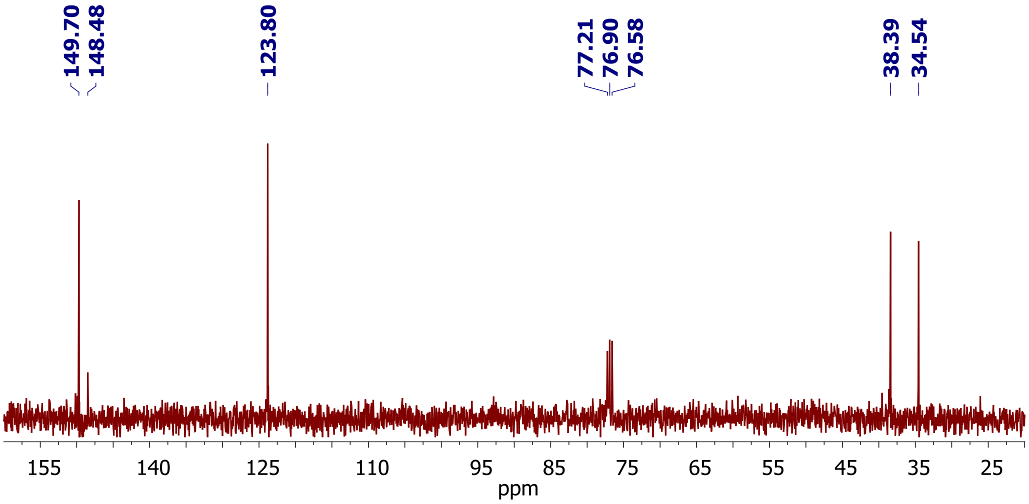

Figure 30. ^{13}C NMR spectrum of PySSPy (100 MHz, $CDCl_3$).

Following this synthetic scheme, the final PySSRu complex was obtained in 3 steps and 62 % overall yields. The identity of the target compounds was then confirmed by ^{1}H and ^{13}C NMR spectroscopy and mass spectrometry data (Figures 29-32).

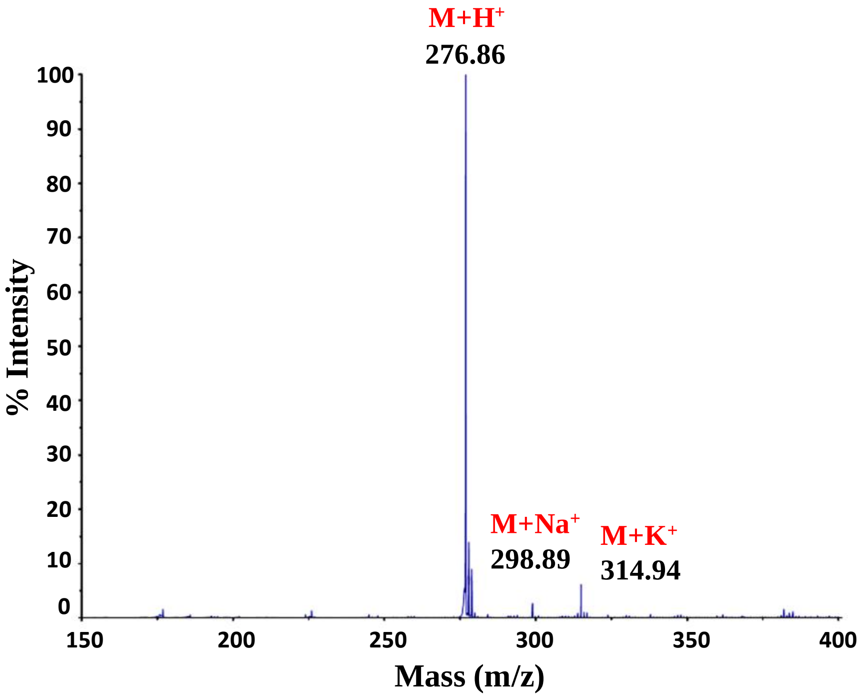

Figure 31. MALDI-TOF spectrum (positive ions) of PySSPy.

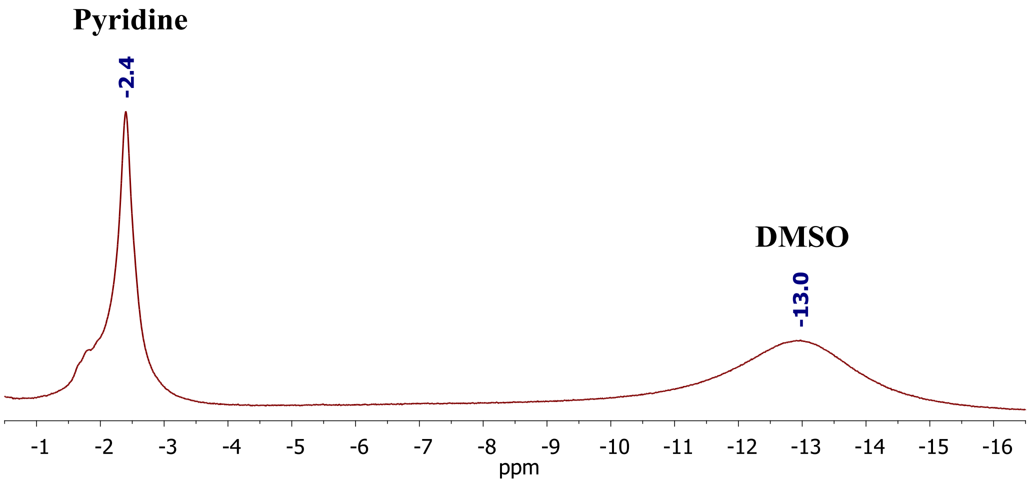

Figure 32. Upfield region expansion of the ^{1}H NMR spectrum of PySSRu (400 MHz, DMSO-d_6).

In analogy with AziRu and all the nucleolipidic and aminoacyllipidic Ru(III)-complexes previously described, the ^{1}H-NMR spectrum of PySSRu was particularly diagnostic of the effective Ru(III)-complex formation,[81,178] with the protonic signals of pyridine and dimethyl sulfoxide at δ = -2.4 and δ = -13.0 ppm, respectively (Figure 32). In addition, in the 7-8 ppm region, free protonic signals of pyridine were not present, demonstrating that the complexation of both pyridine ligands with the ruthenium ion was quantitative.

As a further spectroscopic characterization, the UV and IR spectra of the synthesized compounds were recorded. In particular, UV analysis of PySH, PySSPy and final PySSRu complex (Figure 33) was performed on freshly dissolved samples in CH_3CN at 100 µM final concentration. Both PySH and PySSPy compounds showed a main absorption band centred at 256 nm.

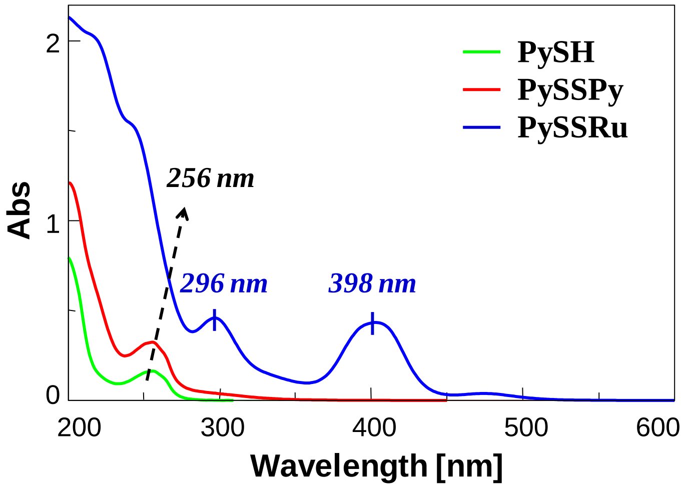

Figure 33. Overlapped UV-vis absorption spectra of the compounds indicated in the legend, from samples freshly dissolved at 100 µM concentration in CH_3CN.

On the contrary, the UV-vis absorption spectrum of the final PySSRu complex showed the characteristic band of Ru(III) ion at 398 nm - attributable to the ligand-to-metal charge transfer transition (LMCT) for the Ru-Cl bond - as well as a band centred at 296 nm, attributed to Ru(III)[106] as well as to pyridine portions. Comparing the UV-vis spectra of PySSRu and that reported for AziRu,[147] the similarity of their bands at ca. 400 nm confirmed the same ligands arrangement around the Ru(III) ion.

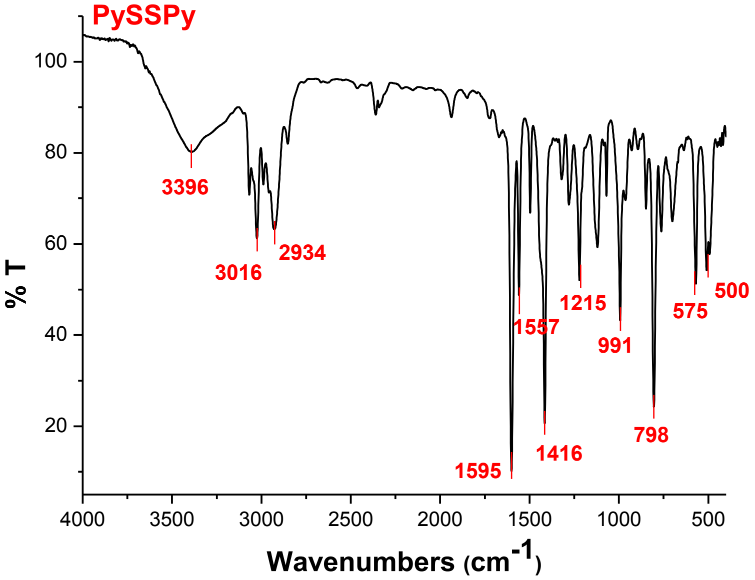

Figure 34. IR spectrum of PySSPy.

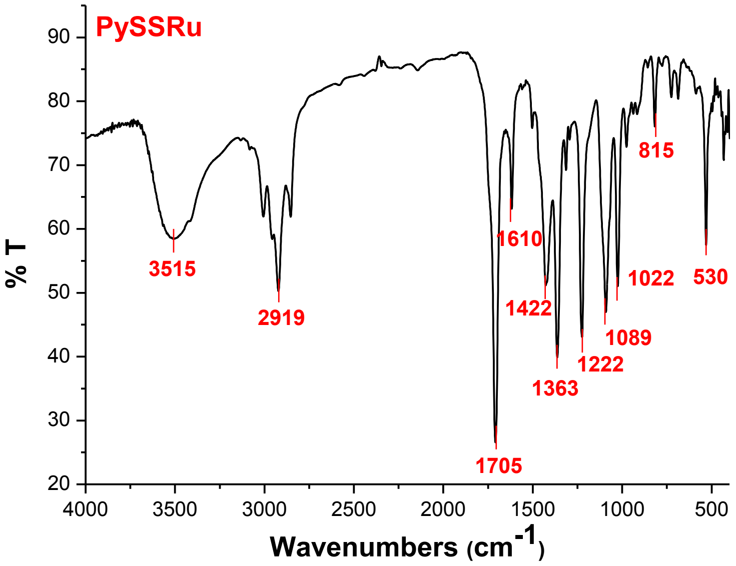

Figure 35. IR spectrum of PySSRu.

5. Synthesis and characterization of the precursor ruthenium salts

The ruthenium complex Na^+ [*trans*-$RuCl_4(DMSO)_2]^-$, or sodium *trans*-bis(dimethyl sulfoxide) tetrachlororuthenate(III), was synthesized using reported procedures[106,177] starting from ruthenium trichloride, as follows.

The commercial hydrated $RuCl_3$ was first partially dissolved in DMSO and then 37 % aqueous HCl was added. The mixture was left at 80 °C under vigorous stirring for 20 min, until complete dissolution of $RuCl_3$. The dense and deep dark solution was then heated at 100 °C for 10 min, gradually turning colour to bright dark red. After cooling, acetone was added and the solution was left at 4 °C overnight to favour precipitation. Dark-red crystals were obtained; these were filtered off, then washed with cold acetone and diethyl ether, and vacuum-dried (Scheme 6).

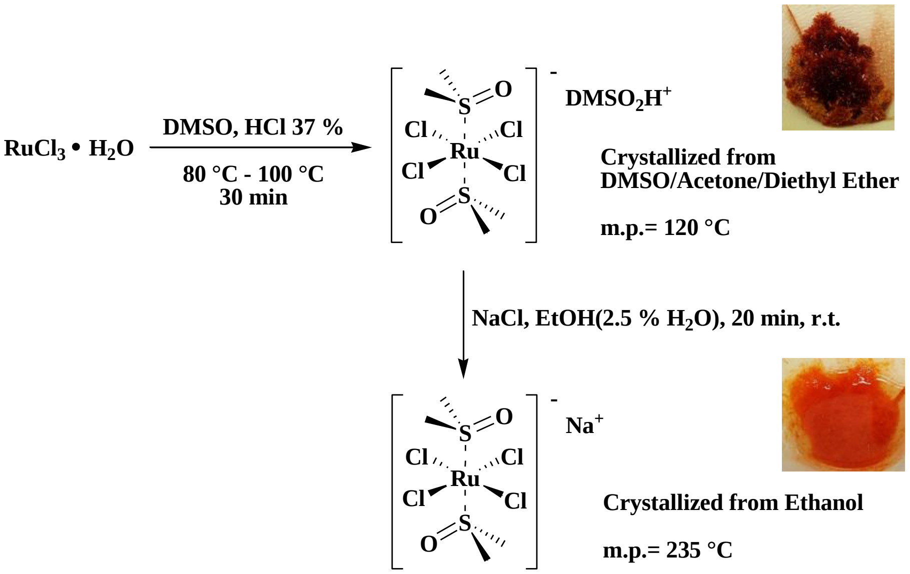

Scheme 6. Synthetic procedure for the preparation of $[(DMSO)_2H]^+$ [*trans*-$[Ru(DMSO)_2Cl_4]^-$ (**21**) and Na^+ [*trans*-$RuCl_4(DMSO)_2]^-$ (**22**) salts starting from commercially available $RuCl_3$, as reported by Attia *et al.*[106,177] On the right, pictures of samples of the two salts.

Compound **21**, *i.e.* hydrogen *trans*-bis(dimethylsulfoxide)tetrachlororuthenate(III) or $[(DMSO)_2H]^+$ [*trans*-$[Ru(DMSO)_2Cl_4]^-$, was obtained in 60 % yields. In this complex, the Ru(III) ion is coordinated to four chlorides in equatorial positions and two DMSO molecules – through the sulfur atom – in apical positions; $(DMSO)_2H^+$ is the cationic counterion.

Afterwards, finely ground $[(DMSO)_2H]^+$ [*trans*-$[Ru(DMSO)_2Cl_4]^-$ was dissolved in a mixture of ethanol and water and then aqueous NaCl solution was added (Scheme 6).

The desired compound rapidly precipitated as light-orange microcrystals, which were filtered, washed with cold ethanol and diethyl ether, and vacuum-dried. In this reaction a change of counterion was realized. Compound **22**, *i.e.* Na^+ [*trans*-$RuCl_4(DMSO)_2]^-$, obtained in 86 % yields, was used in the synthesis of all Ru(III)-complexes described before (paragraphs 2 for LipThyRu, 3 for TUGluRu and TOTyroRu and 4 for PySSRu).

Both Ru(III)-salts **21** and **22** were characterized using spectroscopic techniques (NMR, UV-vis and IR) and melting point measurements.

The ^{1}H NMR spectra of $[(DMSO)_2H]^+$ [*trans*-$[Ru(DMSO)_2Cl_4]^-$ and of Na^+ [*trans*-$RuCl_4(DMSO)_2]^-$ are shown in Figure 36 and 37, respectively. The paramagnetic Ru(III) nucleus severely shifts and broadens the NMR signals of coordinated ligands, not allowing a standard assignment procedure.

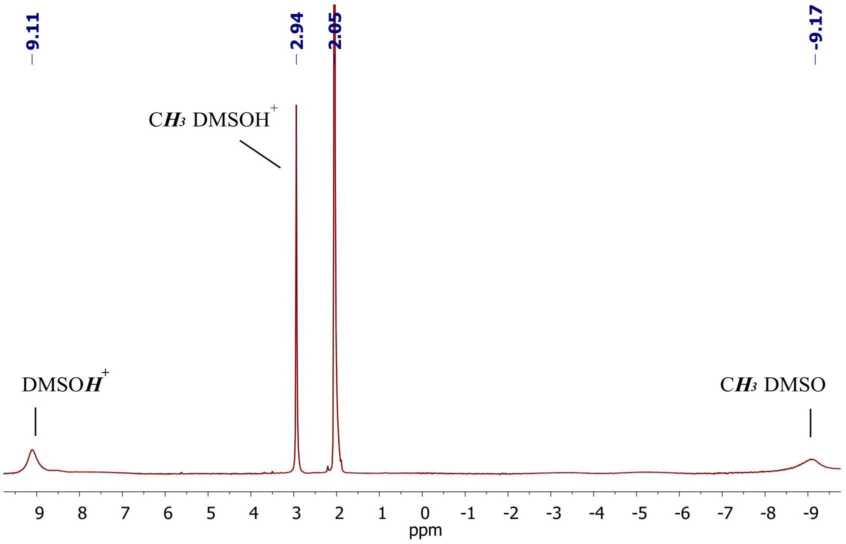

Figure 36. Upfield region expansion of the ^{1}H NMR spectrum of compound **21** [400 MHz, $(CD_3)_2CO$].

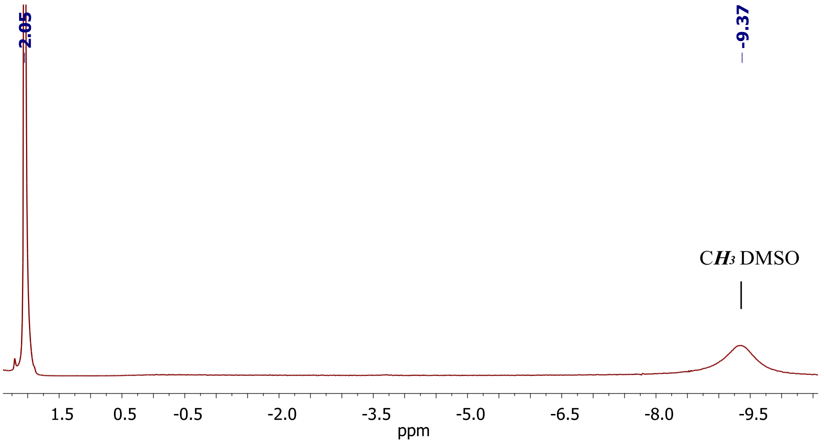

Figure 37. Upfield region expansion of the ^{1}H NMR spectrum of compound **22** [400 MHz, $(CD_3)_2CO$].

In both ^{1}H spectra, a characteristic broad peak of the S-coordinated protonic signals of DMSO is observed in the upfield region, diagnostic of a direct binding to the paramagnetic Ru(III) ion, in agreement with literature data[81,106,177,178]. Furthermore, in Figure 36 the presence of two significant signals at positive *δ*, related to the cationic counterion $(DMSO)_2H^+$, is evident; interestingly, these signals disappear in the spectrum of compound **22** (Figure 37), in which Na^+ is the counterion.

Melting point measurements for **21** and **22** were in good agreement with the values reported in literature[177]. Indeed, for compound **21** a melting range of 118-121 °C was found. For compound **22**, a slow and gradual thermal decomposition was found at high temperatures (>230 °C), in agreement with literature data (235 °C).

Also FTIR-ATR spectra were performed, obtaining signals in agreement with those reported in literature[106,177]. Since the FTIR-ATR spectra of ruthenium salts **21** and **22** were very similar, in Figure 38 only the spectrum of compound **21** was representatively shown.

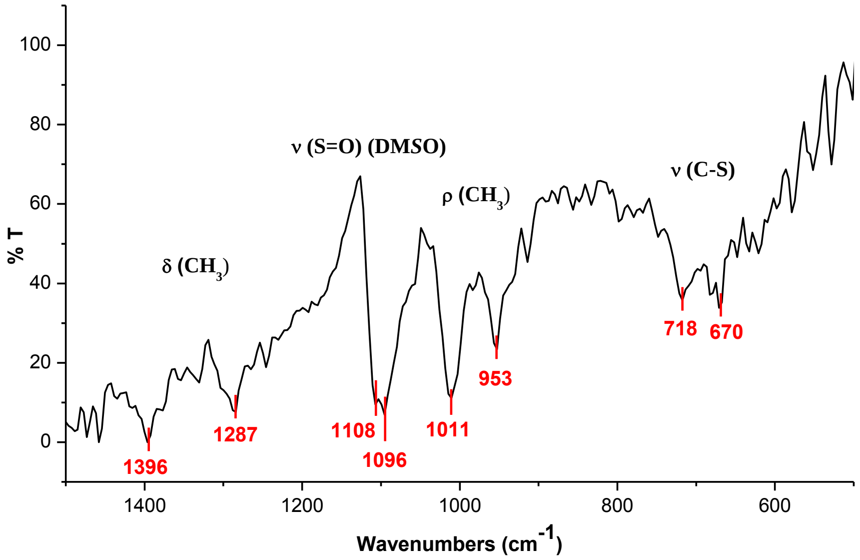

Figure 38. FTIR-ATR spectrum: vibrational frequencies (cm^{-1}) for the main absorption band of compound **21**, *i.e.* $[(DMSO)_2H]^+$ [*trans*-$[Ru(DMSO)_2Cl_4]^-$ (δ = deformation; ν = stretching; ρ = rocking).

$[(DMSO)_2H]^+$ [*trans*-$[Ru(DMSO)_2Cl_4]^-$ and Na^+ [*trans*-$RuCl_4(DMSO)_2]^-$ were further characterized by UV-vis spectroscopy. These compounds were analysed as freshly dissolved 100 μM solutions in DMSO (Figure 39). The UV-vis absorption spectra showed the characteristic band of Ru(III) ion at 421 nm, attributable to the ligand-to-metal charge transfer transition (LMCT) for the Ru-Cl bond, as well as a band centred at 272 nm, which can be attributed to Ru(III).[106,177] The strong similarity of these spectra confirmed for both systems the same arrangement and type of ligands around the ruthenium atom.

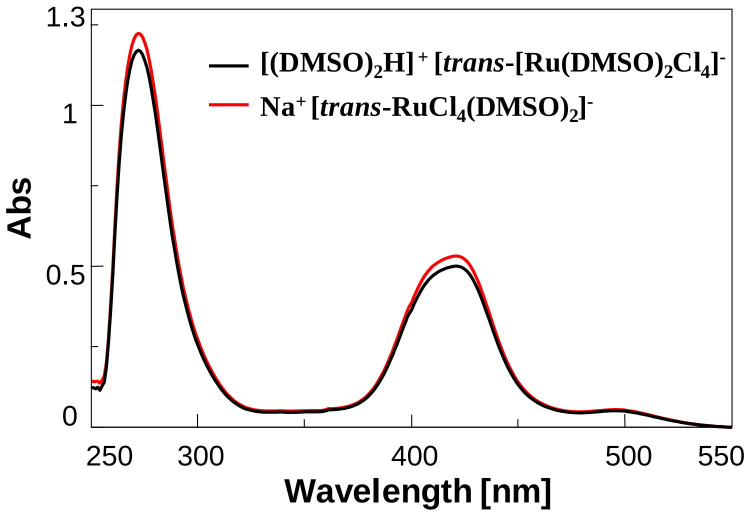

Figure 39. Overlapped UV-vis absorption spectra of compounds $[(DMSO)_2H]^+$ [*trans*-$[Ru(DMSO)_2Cl_4]^-$ (**21**) and Na^+ [*trans*-$RuCl_4(DMSO)_2]^-$ (**22**), from samples freshly dissolved at 100 μM concentration in DMSO.

6. Experimental section

- **Materials and general methods**

All the reagents and solvents were of the highest commercially available quality and were used as received; where anhydrous conditions were required, coevaporations with dry CH_3CN were performed before use. All the esterification reactions were carried out in the presence of activated molecular sieves and under argon atmosphere. TLC analyses were carried out on silica gel plates from Macherey-Nagel (60, F254). Reaction products on TLC plates were visualized by UV-light and then by treatment with an oxidant acidic solution (acetic acid / water / sulfuric acid, 10:4:5, v/v). For the column chromatography purifications, silica gel from Macherey-Nagel (Kieselgel 60, 0.063-0.200 mm) was used.

NMR spectra were recorded on Bruker WM-400, Varian Gemini 200 and Varian Inova 500 spectrometers, as specified. All the *chemical shifts* (δ) are expressed in ppm with respect to the residual solvent signal both for ^1H NMR [$CDCl_3$ = 7.26 ppm, $(CD_3)_2CO$ = 2.05 ppm, MeOD = 3.31 ppm, DMSO-d_6= 2.50 ppm] and ^{13}C NMR ($CDCl_3$ = 76.9 ppm, MeOD = 49.1 ppm). All the coupling constants (*J*) are quoted in Hertz (Hz). Peaks assignments were carried out based on standard ^1H-^1H COSY and HSQC experiments. The following abbreviations were used to explain the multiplicities: s = singlet; d = doublet; t = triplet; q = quartet; m = multiplet; b = broad.

In order to easily identify the proton and carbon signals of the compounds, letters and numbers were assigned to their structures; in particular, in TUGluRu and TOTyroRu derivatives the Fmoc group was identified with the letters “a-h” starting from the oxygen of the carbamic group. The side chain of the amino acid was indicated with progressive numbers starting from the CH-α, to which number 2 was assigned. Then, the lipophilic components (10-undecen-1-ol in TUGluRu and oleic acid in TOTyroRu) were indicated with progressive numbers (1’-11’ or 2’-18’, according to the carbon chain length) starting from the ester oxygen or carbonyl group, respectively. Finally, the numbers 1’’-7’’ were assigned to the protons and carbons of the hydrophilic residue of TEG-OMe, starting from the ester oxygen.

For the ESI-MS analyses, a Waters Micromass ZQ instrument - equipped with an Electrospray source - was used in the positive and/or negative mode.

MALDI-TOF mass spectrometric analyses were performed on a TOF/TOF™ 5800 System in the positive mode, using 2,5-dihydroxybenzoic acid (DHB) as the matrix. For the deposition on MALDI plate, the droplet spotting method was used: the sample - 1 μg/μL in CH_3CN/MeOH, 7:3 (v/v) - was first deposited on the plate followed by DHB deposition - 10 mg/mL in CH_3CN/MeOH, 7:3 (v/v) - and proper mixing before drying the components. The mass spectra were recorded in the range 100-1000 m/z values.

LC-MS analyses were performed on an Agilent 6230B TOF LC/MS instrument, equipped with a 1260 Infinity HPLC analytical system with binary pump coupled with a 6230 time of flight mass spectrometer as detector and an Electrospray source; an Agilent ZORBAX C18 column (1.8 µm, 50 x 4.6 mm) for reverse phase liquid chromatography was used. Stock solutions of the samples were prepared at 2 mg/mL concentration in CH_3CN, HPLC grade. The injections were carried out at the final concentration of 4 ng/µL in CH_3CN/H_2O (1:1, v/v), using a flow rate of 0.4 mL/min. Column elution was performed using H_2O (A) and CH_3CN (B) as eluents; a gradient elution, starting from 5 % B in A and increasing B to 95 % over 5 min, was followed by an isocratic elution at 95 % B in A for 3 min. The ESI/TOF-MS was operated in positive and/or negative ion mode (100-1500 *m*/*z* values).

The UV-vis measurements were performed on a JASCO V-530 UV-vis spectrophotometer equipped with Peltier Thermostat JASCO ETC-505T, by using 1 cm path length cuvette. The spectra were recorded at r.t. in the range 200-600 nm with a medium response, a scanning speed of 100 nm/min and a 2.0 nm bandwidth with the appropriate baseline subtracted.

All the spectra were averaged over 3 scans and each experiment performed in triplicate. All the target compounds were analysed from samples freshly dissolved at 100 µM concentration in CH_3CN or DMSO or at 50 µM concentration in a saline buffered solution (10 mM phosphate buffer/100 mM NaCl pH = 7.3).

The analysis of crystals was carried out on Zeiss Axioskop (Optical microscope), equipped with FP82HT Melting Point Systems used for melting point measurements.

For PySSPy and PySSRu, IR spectra were obtained on a Jasco FTIR-4100 spectrometer in the range 4000-400 cm^{-1}. For the ruthenium salts **21** and **22**, IR spectra were obtained on a Nicolet 5700 FT-IR spectrometer. The solid-state spectra were recorded in the range 1500-500 cm^{-1}. The following abbreviations were used: δ = deformation; ν = stretching; ρ = rocking; m = medium; w = weak; s = strong; br = broad.

- **Synthesis and characterization of LipThyRu**

Synthesis of 3-(4-pyridylmethyl)-5’-O-(4,4′-dimethoxytriphenylmethyl)-thymidine (2)

5’-O-(4,4′-dimethoxytriphenylmethyl)thymidine **1** (121 mg, 0.22 mmol) was dissolved in 8 mL of dry DMF. K_2CO_3 (92.0 mg, 0.67 mmol) and 4-(bromomethyl)pyridine hydrobromide (84.2 mg, 0.33 mmol) were then added to the reaction mixture, left at 60 °C under stirring. After 4 d, TLC analysis indicated the presence of the desired product and the reaction was quenched by removing the solvent under reduced pressure. First, an extraction CH_2Cl_2/H_2O was performed to remove the excess reagents. Then, the crude product was purified by chromatography on a silica gel column using AcOEt/MeOH (97:3, v/v, containing 2 % of TEA), as eluent, giving desired compound **2** in 59 % yield (82.5 mg, 0.13 mmol).

2: oil. R_f = 0.7 (AcOEt/MeOH, 95:5, v/v).

^{1}**H NMR** (400 MHz, $CDCl_3$): *δ* 8.44 (d, *J* = 5.2, 2H, 2x ***H***α Py); 7.56 (s, 1H, ***H***-6); 7.34 (d, *J* = 7.4, 2H, 2x ***H***β Py); 7.35-7.25 (overlapped signals, 9H, aromatic protons of DMT); 6.77 (d, *J* = 8.7, 4H, 4 aromatic protons of DMT), 6.35 (t, *J* = 7.4 and 6.7, 1H, ***H***-1'); 5.05 (s, 2H, -C***H***$_2$Py); 4.52 (m, 1H, ***H***-3'); 4.06 (m, 1H, ***H***-4'); 3.72 [s, 6H, 2x (-OC***H***$_3$) of DMT group]; 3.52-3.40 (m, 2H, ***H***$_2$-5'); 2.50-2.29 (m, 2H, ***H***-2'); 1.43 (s, 3H, C***H***$_3$-Thy).

^{13}**C NMR** (100 MHz, $CDCl_3$): *δ* 163.0 (***C***-4 Thy); 158.4, 144.0, 133.8, 127.9, 127.0 and 113.2 (aromatic carbons of DMT); 150.8 (***C***-2 Thy); 149.8 (2x ***C***α Py); 145.3 (***C***γ Py); 135.0 (***C***-6 Thy); 123.4 (2x ***C***β Py); 110.7 (***C***-5 Thy); 87.0 (quaternary carbon of DMT); 85.0 (***C***-1'); 84.0 (***C***-4'); 74.8 (***C***-3'); 63.5 (***C***-5'); 55.1 [2x (O***C***H$_3$) of DMT]; 43.4 (-***C***H$_2$Py); 37.9 (***C***-2'); 12.2 (***C***H$_3$-Thy).

Synthesis of 3-(4-pyridylmethyl)-3’-O-lipoyl-5’-O-(4,4′-dimethoxytriphenylmethyl)-thymidine (3)

Alkylated compound **2** (70.0 mg, 0.11 mmol) was dissolved in 2 mL of dry CH_2Cl_2 and then DMAP (40.0 mg, 0.33 mmol), lipoic acid (34.0 mg, 0.16 mmol) and DCC (68.0 mg, 0.33 mmol) were sequentially added. After stirring for 2 h at r.t., TLC analysis indicated the complete disappearance of the starting materials. Thus, the reaction mixture was concentrated under reduced pressure; the crude product was purified by chromatography on a silica gel column using $CHCl_3$/MeOH (95:5, v/v, containing 2 % of TEA) as eluent, providing desired compound **3** in 77 % yield (66.0 mg, 0.08 mmol).

3: oil. R_f = 0.8 (AcOEt/MeOH, 95:5, v/v).

^{1}**H NMR** (400 MHz, $CDCl_3$): *δ* 8.53 (d, *J* = 5.2, 2H, 2x ***H***α Py); 7.67 (s, 1H, ***H***-6); 7.39-7.28 (overlapped signals, 11H, 2x ***H***β Py and 9 aromatic protons of DMT); 6.85 (d, *J* = 8.7, 4H, 4 aromatic protons of DMT); 6.45 (dd, *J* = 7.4 and 6.7, 1H, ***H***-1'); 5.45 (m, 1H, ***H***-3'); 5.12 (s, 2H, -C***H***$_2$Py); 4.11 (m, 1H, ***H***-4'); 3.80 [s, 6H, 2x (-OC***H***$_3$) of DMT]; 3.58 (m, 1H, C***H***-S); 3.49 (m, 2H, ***H***$_2$-5'); 3.23-3.11 (m, 2H, C***H***$_2$-S); 2.50-2.46 (m, 3H, ***H***$_2$-2' and C***H***$_2$a-CH$_2$-S); 2.35 (t, *J* = 7.4, 2H, -C***H***$_2$-C=O lipoic residue); 1.95-1.90 (m, 1H, C***H***$_2$b-CH$_2$-S); 1.73-1.46 (m, 6H, 3x C***H***$_2$ lipoic residue); 1.42 (s, 3H, C***H***$_3$-Thy).

^{13}**C NMR** (100 MHz, $CDCl_3$): *δ* 172.6 (***C***=O lipoic ester); 163.0 (***C***-4 Thy); 158.6, 133.8, 129.9, 127.9, 127.8, 127.0 and 113.2 (aromatic carbons of DMT); 150.8 (***C***-2 Thy); 149.8 (2x ***C***α Py); 145.3 (***C***γ Py); 135.1 (***C***-6 Thy); 123.3 (2x ***C***β Py); 110.7 (***C***-5 Thy); 87.0 (quaternary carbon of DMT); 85.0 (***C***-1'); 83.9 (***C***-4'); 75.0 (***C***-3'); 63.5 (***C***-5'); 56.1 (***C***H-S); 55.1 [2x (O***C***H$_3$) of DMT];

43.4 (-***C***H$_2$Py); 40.0 (***C***H$_2$-S); 38.3 (***C***H$_2$-C=O lipoic residue); 37.9 (***C***-2'); 34.7, 28.5, 26.1, 24.5 (overlapped signals, 4 aliphatic carbons of lipoic residue); 12.2 (***C***H$_3$-Thy).

ESI-MS (positive ions): calculated for $C_{45}H_{49}N_3O_8S_2$, 823.3; found *m/z*: 862.49 [M+K$^+$].

Synthesis of 3-(4-pyridylmethyl)-3'-O-lipoyl-thymidine (4)

Compound **3** (237 mg, 0.29 mmol) was dissolved in 2 mL of a 1 % TCA solution in CH_2Cl_2. Upon addition of the acid, the reaction mixture acquired an intense yellow-orange colour, typical of the trityl cation, and was left under stirring at r.t.. After 1 h, TLC monitoring showed the complete disappearance of the starting compound. Thus the reaction was quenched by adding few drops of MeOH until complete decoloration, and finally TEA was added to neutralize the solution. Then the reaction mixture was concentrated *in vacuo* and purified by chromatography on a silica gel column eluted with $CHCl_3$/MeOH (99:1, v/v), giving the desired compound **4** in almost quantitative yields (155 mg, 0.29 mmol).

4: yellow oil. R_f = 0.4 ($CHCl_3$/MeOH, 95:5, v/v).

^{1}H NMR (400 MHz, $CDCl_3$,): δ 8.52 (d, *J* = 5.2, 2H, 2x ***H***α Py); 7.65 (s, 1H, ***H***-6); 7.35 (d, 2H, 2x ***H***β Py); 6.34 (dd, *J* = 7.4 and 6.7, 1H, ***H***-1'); 5.37 (m, 1H, ***H***-3'); 5.12 (s, 2H, -C***H$_2$***Py); 4.10 (m, 1H, ***H***-4'); 3.93 (m, 2H, ***H$_2$***-5'); 3.59 (m, 1H, C***H***-S); 3.22-3.12 (m, 2H, C***H$_2$***-S); 2.48 (m, 1H, C***H$_2$***a-CH$_2$-S); 2.40-2.32 (m, 4H, ***H$_2$***-2', C***H$_2$***-C=O lipoic residue); 1.92 (m, 1H, C***H$_2$***b-CH$_2$-S); 1.68 (m, 4H, 2x C***H$_2$*** lipoic residue); 1.49 (m, 2H, C***H$_2$***-CH-S); 1.42 (s, 3H, C***H$_3$***-Thy).

^{13}C NMR (100 MHz, $CDCl_3$): δ 171.9 (***C***=O lipoic ester); 164.5.0 (***C***-4 Thy); 148.7 (2x ***C***α Py); 144.5 (***C***-2 Thy); 133.7 (***C***γ Py); 122.3 (2x ***C***β Py); 113.7 (***C***-6 Thy); 109.4 (***C***-5 Thy); 85.2 (***C***-1'); 84.2 (***C***-4'); 73.7 (***C***-3'); 61.3 (***C***-5'); 56.1(***C***H-S); 43.4 (-***C***H$_2$Py); 40.1 (***C***H$_2$-S); 38.3 (***C***H$_2$-C=O lipoic residue); 37.9 (***C***-2'); 34.7-24.5 (overlapped signals, 4 aliphatic carbons of lipoic residue); 12.2 (***C***H$_3$-Thy).

ESI-MS (positive ions): calculated for $C_{24}H_{31}N_3O_6S_2$, 521.17; found *m/z*: 522.34 [M+H$^+$]; 972.38 [M+K$^+$].

Synthesis of 3-(4-pyridylmethyl)-3'-O-lipoyl-5'-O-(benzyloxy)hexaethylene glycol acetyl-thymidine (5)

To compound **4** (35.0 mg, 0.07 mmol), dissolved in 1 mL of dry CH_2Cl_2, DMAP (16.4 mg, 0.13 mmol), BnO-HEG acetic acid **8** (43.0 mg, 0.10 mmol) and DCC (28.0 mg, 0.14 mmol) were sequentially added, and the resulting reaction mixture was left under stirring at r.t.. After 1 h TLC analysis indicated the formation of a new product, so the solvent was removed under reduced pressure and the crude product was purified by chromatography on a silica gel column eluted with CHCl$_3$/MeOH (95:5, v/v), giving the desired compound **5** in 74 % yield (48.4 mg, 0.05 mmol).

5: oil. R_f = 0.8 (CHCl$_3$/MeOH, 9:1, v/v).

^{1}H NMR (400 MHz, CDCl$_3$): δ 8.51 (d, *J* = 5.2, 2H, 2x ***H***α Py); 7.30-7.26 (overlapped signals, 8H, ***H***-6, 2x ***H***β Py and 5 aromatic protons of Bn); 6.34 (dd, *J* = 7.4 and 6.7, 1H, ***H***-1'); 5.15 (m, 1H, ***H***-3'); 5.08 (s, 2H, -C$\boldsymbol{H_2}$Py); 4.48 (s, 2H, -C$\boldsymbol{H_2}$Ph); 4.41 (m, 2H, $\boldsymbol{H_2}$-5'); 4.21-4.12 (overlapped signals, 3H, ***H***-4' and -OC$\boldsymbol{H_2}$COO-C5'); 3.72-3.57 [overlapped signals, 25H, 6x (-O-C$\boldsymbol{H_2}$-C$\boldsymbol{H_2}$-O-) and C***H***-S]; 3.23-3.15 (m, 2H, C$\boldsymbol{H_2}$-S); 2.37-2.32 (overlapped signals, 5H, $\boldsymbol{H_2}$-2', C$\boldsymbol{H_2}$-C=O lipoic residue and C$\boldsymbol{H_2}$a-CH$_2$-S); 1.92 (s, 3H, $\boldsymbol{CH_3}$-Thy); 1.90 (m, 1H, C$\boldsymbol{H_2}$b-CH$_2$-S); 1.65 (m, 4H, 2x C$\boldsymbol{H_2}$ lipoic residue); 1.45 (m, 2H, C$\boldsymbol{H_2}$-CH-S lipoic residue).

^{13}C NMR (100 MHz, CDCl$_3$): δ 171.7 (***C***=O lipoic ester); 168.7 (***C***=O HEG ester); 163.0 (***C***-4 Thy); 149.7 (***C***-2 Thy); 148.8 (2x ***C***α Py); 144.2 (***C***γ Py); 137.0 (quaternary carbon of Bn); 132.4 (***C***-6 Thy); 127.2, 126.4 (aromatic carbons of Bn); 122.3 (2x ***C***β Py); 109.7 (***C***-5 Thy); 84.4 (***C***-1'); 80.9 (***C***-4'); 73.2 (***C***-3'); 72.1 (-***C***H$_2$Ph); 70.0, 69.4 (O-***C***H$_2$-***C***H$_2$-OHEG); 68.3 (-O***C***H$_2$COO-C5'); 63.0 (***C***-5'); 55.1(***C***H-S); 42.5 (-***C***H$_2$Py); 49.1 (***C***H$_2$-S); 37.3 (***C***H$_2$-C=O lipoic residue); 35.9 (***C***-2'); 33.4-23.3 (overlapped signals, 4 aliphatic carbons of lipoic residue); 12.1 (***C***H$_3$-Thy).

ESI-MS (positive ions): calculated for $C_{45}H_{63}N_3O_{14}S_2$, 933.38; found *m/z*: 935.28 [M+H$^+$]; 972.38 [M+K$^+$].

Synthesis of LipThyRu

Nucleolipid **5** (46.0 mg, 0.05 mmol) was dissolved in 2.5 mL of acetone and then Na$^+$ [*trans*-RuCl$_4$(DMSO)$_2$]$^-$ (21.0 mg, 0.05 mmol) was added under stirring at 40 °C. After 4 h the reaction, monitored *via* TLC, indicated the complete disappearance of both starting products and the concomitant formation of a more polar product. After removing the solvent under reduced pressure, the obtained solid was exhaustively washed with AcOEt, able to solubilize only the target complex LipThyRu, which was thus recovered in 71 % isolated yields as a pure compound (45.4 mg, 0.03 mmol).

LipThyRu: yellow oil. R_f = 0.3 (CHCl$_3$/MeOH, 9:1 v/v).

^{1}H NMR [400 MHz, (CD$_3$)$_2$CO]: significant signals at δ -1.75 (very broad signal, Py protons); -12.7 (very broad signal, C$\boldsymbol{H_3}$ of DMSO).

ESI-MS (positive ions): calculated for $C_{47}H_{69}Cl_4N_3NaO_{15}RuS_3^+$, 1276.16; found *m/z*: 1255.22 [(M-Na$^+$)+2H$^+$].

- **Synthesis and characterization of BnO-HEG acetic acid**

Synthesis of (monobenzyloxy)hexaethylene glycol (6)

Hexaethylene glycol (2.0 g, 7.10 mmol) was dissolved in 8 mL of dry THF and NaH 60 % p.p. (170 mg, 4.25 mmol) and then benzylbromide (3.37 mL, 22.8 mmol) were sequentially added. The reaction mixture was stirred at r.t. for 12 h, then MeOH (1 mL) was added and the solvent removed *in vacuo*. The crude product was dissolved in $CHCl_3$, filtered on celite and then purified by chromatography on a silica gel column using AcOEt/MeOH (9:1, v/v) as eluent, yielding the desired compound **6** in 65 % yields (1.7 g, 4.60 mmol).

6: oil. R_f = 0.5 (AcOEt/MeOH, 9:1, v/v).

^{1}H NMR (200 MHz, $CDCl_3$): δ 7.34-7.33 (overlapped signals, 5H, aromatic protons of Bn); 4.56 (s, 2H, -C$\boldsymbol{H_2}$Ph); 3.66-3.60 [overlapped signals, 24H, 6x (-O-C$\boldsymbol{H_2}$-C$\boldsymbol{H_2}$-O-)].

^{13}C NMR (50 MHz, $CDCl_3$): δ 138.2, 128.3, 127.7 and 127.6 (aromatic carbons); 73.2 (-**C**H_2Ph); 72.5, 70.6, 70.2 and 69.4 [5x (-O-***C***H_2-***C***H_2-O-) and (-O-***C***H_2-CH_2-OH)]; 61.7 (O-CH_2- ***C***H_2-OH).

ESI-MS (positive ions): calculated for $C_{19}H_{32}O_7$, 372.2; found *m/z*: 373.2 [M+H$^+$]; 395.1 [M+Na$^+$].

Synthesis of *tert*-butyl (monobenzyloxy)hexaethylene glycol acetate (7)

Alcohol **6** (155 mg, 0.42 mmol) was dissolved in 1 mL of dry THF and NaH 60 % p.p. (33.0 mg, 0.83 mmol) and *tert*-butyl bromoacetate (154 μL, 1.01 mmol) were sequentially added. The reaction mixture was stirred at r.t. for 12 h, then few drops of MeOH were added and the solvent removed *in vacuo*. The crude product was dissolved in $CHCl_3$, filtered on celite and then purified by chromatography on a silica gel column eluted with AcOEt, yielding the desired compound **7** in 86 % yields (175 mg, 0.36 mmol).

7: oil. R_f = 0.6 (AcOEt/MeOH, 95:5, v/v).

^{1}H NMR (200 MHz, $CDCl_3$): δ 7.34-7.32 (overlapped signals, 5H, aromatic protons); 4.56 [s, 2H, -C$\boldsymbol{H_2}$Ph]; 4.01 (s, 2H, -C$\boldsymbol{H_2}$COO *tert*-butyl); 3.69-3.64 [overlapped signals, 24H, 6x (-OC$\boldsymbol{H_2}$-C$\boldsymbol{H_2}$-O-)]; 1.46 [s, 9H, 3x (C$\boldsymbol{H_3}$ *tert*-butyl)].

^{13}C NMR (50 MHz, $CDCl_3$): δ 169.6 (***C***=O); 138.3, 128.3, 127.7 and 127.5 (aromatic carbons of Bn); 81.4 (quaternary carbon of *tert*-butyl); 73.2 (-***C***H_2Ph); 70.6 and 69.4 [6x (-O-***C***H_2-***C***H_2-O-)]; 69.0 (-***C***H_2COO-*t*-Bu); 28.1 [3x (***C***H_3 *tert*-butyl)].

ESI-MS (positive ions): calculated for $C_{25}H_{42}O_9$, 486.3; found *m/z*: 509.2 [M+Na$^+$]; 525.2 [M+K$^+$].

Synthesis of (monobenzyloxy)hexaethylene glycol acetic acid (8)

Ester **7** (95.0 mg, 0.19 mmol) was dissolved in 1.5 mL of HCOOH and stirred at r.t. for 2 h. The solvent was then removed *in vacuo* and the residue was coevaporated three times with $CHCl_3$ (3 x 3 mL), yielding the desired compound **8** in almost quantitative yields (82.0 mg, 0.19 mmol).

8: oil. R_f = 0.2 (AcOEt/MeOH, 95:5, v/v).

^{1}H NMR (200 MHz, MeOD): δ 7.36-7.33 (overlapped signals, 5H, aromatic protons); 4.55 [s, 2H, -C***H*₂**Ph]; 4.12 (s, 2H, -C***H*₂**COOH); 3.66-3.62 [overlapped signals, 24H, 6x (-O-C***H*₂**-C***H*₂**-O-)].

^{13}C NMR (50 MHz, MeOD): δ 174.0 (***C***=O); 139.7, 129.4, 129.0 and 128.7 (aromatic carbons); 74.1 (-***C***H_2Ph); 71.7, 71.6 and 70.6 [6x (-O-***C***H_2-***C***H_2-O-)]; 69.1 (-***C***H_2COOH).

ESI-MS (positive ions): calculated for $C_{21}H_{34}O_9$, 430.2; found *m/z*: 431.1 [M+H$^+$]; 453.1 [M+Na$^+$]; 459.1 [M+K$^+$].

- **Synthesis and characterization of TUGluRu**

Synthesis of 2-[(9H-fluoren-9-yl) methoxy] carbonylamino, 5-*tert*-butyl, 1-undec-10-enyl pentanedioate (9)

Commercially available Fmoc-Glu(O*t*Bu)-OH (300 mg, 0.71 mmol) was dissolved in 2.0 mL of dry DMF and then HATU (402 mg, 1.06 mmol), DIPEA (246 µL, 1.41 mmol) and 10-undecen-1-ol (80 µL, 0.42 mmol) were sequentially added. The reaction mixture was stirred at r.t. under argon atmosphere. After 4 h, TLC analysis indicated the presence of one main product in the reaction mixture and the complete disappearance of the starting alcohol. The solvent was removed *in vacuo* and the residue filtered and washed with CH_2Cl_2. The crude product was purified by chromatography on a silica gel column eluted with CH_2Cl_2 containing 2 % of TEA (v/v). The desired compound **9** was obtained in 81 % yields (199 mg, 0.34 mmol).

9: yellow oil. R_f = 0.7 (*n*-hexane/acetone, 8:2, v/v).

^{1}H NMR (400 MHz, $CDCl_3$): δ 7.75 (d, *J* = 7.5 Hz, 2H, C***H***-d Fmoc); 7.59 (t, *J* = 6.4 and 4.0 Hz, 2H, C***H***-e Fmoc); 7.38 (t, *J* = 7.4 Hz, 2H, C***H***-f Fmoc); 7.30 (t, *J* = 7.4 Hz, 2H, C***H***-g Fmoc); 5.85-5.75 (m, 1H, C***H***-10'); 5.62 (bd, *J* = 8.0 Hz, 1H, N***H***); 4.96-4.91 (m, 2H, C***H*₂**-11'); 4.43-4.36 (overlapped signals, 3H, C***H*₂**-a Fmoc and C***H*** α); 4.21 (t, *J* = 7.0 Hz, 1H, C***H***-b Fmoc); 4.14 (t, *J* = 6.6 Hz, 2H, C***H*₂**-1'); 2.36-2.25 (m, 2H, C***H*₂**-4); 2.20-2.14 (m, 1H, C***H***-3a); 2.04-2.00 (m, 2H, C***H*₂**-9'); 1.99-1.93 (m, 1H, C***H***-3b); 1.63-1.51 (m, 2H, C***H*₂**-2'); 1.45 (s, 9H, *t*Bu); 1.28 (overlapped signals, 12H, 6x C***H*₂**-3', 4', 5', 6', 7', 8').

^{13}C NMR (50 MHz, $CDCl_3$): δ 172.0 (overlapped signals, 2x ***C***=O undecenyl ester and ***C***OOtBu); 155.9 (***C***=ONH); 143.8, 143.7 (***C***H-c Fmoc); 141.3 (overlapped signals, ***C***H-h Fmoc); 139.2 (***C***H-10'); 127.7 (***C***H-d Fmoc); 127.0 (***C***H-g Fmoc); 125.1 (***C***H-e Fmoc); 119.9 (***C***H-f Fmoc); 114.1

(***C***H$_2$-11’); 80.8 (quaternary carbon of *t*Bu); 67.0 (***C***H$_2$-a Fmoc); 65.8 (***C***H$_2$-1’); 53.5 (***C***H α); 47.1 (***C***H-b Fmoc); 33.8 (***C***H$_2$-9’); 32.4 (***C***H$_2$-2’); 31.4 (***C***H$_2$-4); 29.4 (3x ***C***H$_3$ of *t*Bu); 29.1, 28.9, 28.5, 28.0 (overlapped signals, 5x ***C***H$_2$-4’, 5’, 6’, 7’, 8’); 27.6 (***C***H$_2$-3); 25.8 (***C***H$_2$-3’).

MALDI-MS (positive ions): calculated for $C_{35}H_{47}NO_6$, 577.34; found *m/z*: 600.25 [M+Na$^+$]; 616.22 [M+K$^+$].

Synthesis of 4-[(9H-fluoren-9-yl) methoxy] carbonylamino-pentandioic acid, 5-(undec-10-enyl) mono ester (10)

Compound **9** (105 mg, 0.18 mmol) was dissolved in 1.0 mL of formic acid and the reaction mixture was stirred at r.t. for 2.5 h. Formic acid was then removed *in vacuo* and the resulting residue was coevaporated three times with dry CH_3CN (3 x 5 mL), yielding the desired compound **10** in almost quantitative yields (95.2 mg, 0.18 mmol).

10: pale yellow oil. R_f = 0.3 (*n*-hexane/acetone, 8:2, v/v); 0.4 (CH_2Cl_2).

^{1}H NMR (400 MHz, $CDCl_3$): *δ* 7.75 (d, *J* = 7.5 Hz, 2H, C***H***-d Fmoc); 7.59 (d, *J* = 7.0, 2H, C***H***-e Fmoc); 7.39 (t, *J* = 7.4 and 7.5 Hz, 2H, C***H***-f Fmoc); 7.30 (t, *J* = 7.4 Hz, 2H, C***H***-g Fmoc); 5.84-5.77 (m, 1H, C***H***-10’); 5.55 (bd, *J* = 8.0 Hz, 1H, N***H***);5.02-4.92 (m, 2H, C***H$_2$***-11’); 4.44-4.37 overlapped signals, 3H, C***H$_2$***-a Fmoc and C***H*** α); 4.21 (t, *J* = 6.8 and 6.9 Hz, 1H, C***H***-b Fmoc); 4.14 (t, *J* = 4.0 and 8.0 Hz, 2H, C***H$_2$***-1’); 2.50-2.41 (m, 2H, C***H$_2$***-4); 2.25-2.20 (m, 1H, C***H***-3a); 2.06-1.95 (overlapped signals, 3H, C***H$_2$***-9’ and C***H***-3b); 1.63-1.61 (m, 2H, C***H$_2$***-2’); 1.37-1.22 (overlapped signals, 12H, 6x C***H$_2$***-3’, 4’, 5’, 6’, 7’, 8’).

^{13}C NMR (50 MHz, $CDCl_3$): *δ* 177.3 (***C***OOH); 171.8 (***C***=O undecenyl ester); 155.9 (***C***=ONH); 143.7, 143.6 (***C***H-c Fmoc); 141.2 (overlapped signals, ***C***H-h Fmoc); 139.1 (***C***H-10’); 127.7 (***C***H-d Fmoc); 126.9 (***C***H-g Fmoc); 124.9 (***C***H-e Fmoc); 119.9 (***C***H-f Fmoc); 114.1 (***C***H$_2$-11’); 67.0 (***C***H$_2$-a Fmoc); 65.9 (***C***H$_2$-1’); 53.1 (***C***H α); 47.1 (***C***H-b Fmoc); 33.7 (***C***H$_2$-9’); 29.7 (CH$_2$-2’); 29.3, 29.0, 28.9, 28.8 (overlapped signals, 5x ***C***H$_2$-4’, 5’, 6’, 7’, 8’); 28.5 (***C***H$_2$-4); 27.5 (***C***H$_2$-3); 25.6 (***C***H$_2$-3’).

MALDI-MS (positive ions): calculated for $C_{31}H_{39}NO_6$, 521.28; found *m/z*: 544.18 [M+Na$^+$]; 560.15 [M+K$^+$].

Synthesis of 5-{2-[2-(2-methoxyethoxy)ethoxy]ethyl}, 1-undec-10-enyl, 2-(9H-fluoren-9-yl)methoxycarbonylamino-pentanedioate (11)

Compound **10** (17.7 mg, 0.03 mmol) was dissolved in 0.7 mL of dry DMF and then HATU (19.4 mg, 0.05 mmol), DIPEA (11.8 μL, 0.07 mmol) and triethylene glycol monomethyl ether (6.52 μL, 0.04 mmol) - previously coevaporated three times with dry CH_3CN (3 x 5 mL) - were sequentially added. The reaction mixture was left at r.t. under stirring and argon atmosphere. After 18 h, TLC analysis indicated the appearance of a new product. The reaction was quenched by removing the solvent under reduced pressure; the resulting crude was filtered and washed several times with CH_2Cl_2. Finally, it was purified by chromatography on a silica gel column using *n*-hexane/acetone (8:2, v/v) as eluent, which provided pure compound **11** with 66 % yields (13.8 mg, 0.02 mmol).

11: oil. R_f = 0.6 (*n*-hexane/acetone, 7:3, v/v).

^{1}H NMR (400 MHz, $CDCl_3$): δ 7.76 (d, *J* = 8.0 Hz, 2H, C***H***-d Fmoc); 7.60 (bd, *J* = 4.0, 2H, C***H***-e Fmoc); 7.40 (t, *J* = 8.0, 2H, C***H***-f Fmoc); 7.31 (t, *J* = 7.3 and 7.1 Hz , 2H, C***H***-g Fmoc); 5.85-5.75 (m, 1H, C***H***-10'); 5.50 (d, *J* = 8.0 Hz, 1H, N***H***); 5.01-4.91 (m, 2H, C$\boldsymbol{H_2}$-11'); 4.42-4.37 (overlapped signals, 3H, C$\boldsymbol{H_2}$-a Fmoc and C***H*** α); 4.24-4.20 (overlapped signals, 3H, C***H***-b Fmoc and C$\boldsymbol{H_2}$-1''); 4.14 (bt, *J* = 4.6 and 6.7 Hz, 2H, C$\boldsymbol{H_2}$-1'); 3.68 (t, *J* = 4.8 and 4.7 Hz, C$\boldsymbol{H_2}$-2''); 3.64-3.52 (overlapped signals, 8H, 4x C$\boldsymbol{H_2}$-3'', 4'', 5'',6''); 3.36 (s, 3H, OC$\boldsymbol{H_3}$); 2.47-2.39 (m, 2H, C$\boldsymbol{H_2}$-4); 2.23-2.21 (m, 1H, C***H***-3a); 2.05-2.00 (overlapped signals, 3H, C$\boldsymbol{H_2}$-9' and C***H***-3b); 1.65-1.58 (m, 2H, C$\boldsymbol{H_2}$-2'); 1.36-1.27 (overlapped signals, 12H, 6x C$\boldsymbol{H_2}$-3', 4', 5', 6', 7', 8').

^{13}C NMR (100 MHz, $CDCl_3$): δ 172.4 (***C***=O TEG ester); 171.7 (***C***=O undecenyl ester); 155.8 (***C***=ONH); 143.7, 143.6 (***C***H-c Fmoc); 141.2 (overlapped signals, ***C***H-h Fmoc); 139.0 (***C***H-10'); 127.5 (***C***H-d Fmoc); 126.9 (***C***H-g Fmoc); 124.9 (***C***H-e Fmoc); 119.8 (***C***H-f Fmoc); 114.0 (***C***H_2-11'); 71.8, 70.4, 68.9 (overlapped signals, 5x ***C***H_2-2'', 3'', 4'', 5'', 6''); 67.0 (***C***H_2-a Fmoc); 65.7 (***C***H_2-1'); 63.6 (***C***H_2-1''); 58.8 (O***C***H_3); 53.3 (***C***H α); 47.1 (***C***H-b Fmoc); 33.6 (***C***H_2-9'); 30.1 (***C***H_2-4); 29.2, 29.0, 28.9, 28.7, 28.4 (overlapped signals, 6x ***C***H_2-2', 4', 5', 6', 7', 8'); 27.5 (***C***H_2-3); 25.6 (***C***H_2-3').

MALDI-MS (positive ions): calculated for $C_{38}H_{53}NO_9$, 667.37; found *m/z*: 690.27 [$M+Na^+$]; 706.24 [$M+K^+$].

Synthesis of 5-{2-[2-(2-methoxyethoxy)ethoxy]ethyl}, 1-undec-10-enyl, 2-aminopentanedioate (12)

Isolated product **11** (42.7 mg, 0.06 mmol) was dissolved in 1.0 mL of a 10 % piperidine solution in CH_3CN. After 20 min under stirring at r.t., TLC analysis indicated the complete removal of the Fmoc group. Then the solvent was removed *in vacuo* and the residue was coevaporated three times with dry CH_3CN (3 x 5 mL), obtaining the desired compound in almost quantitative yields (28.5 mg, 0.06 mmol). Derivative **12** was not isolated, but directly reacted to obtain the final aminoacyllipidic scaffold.

Synthesis of 5-{2-[2-(2-methoxyethoxy)ethoxy]ethyl}, 1-undec-10-enyl, 2-(2-(pyridin-4-yl)acetamido)pentanedioate (13)

Crude product **12** (35.4 mg, 0.08 mmol) was dissolved in 1.0 mL of dry DMF and then HATU (45.0 mg, 0.12 mmol), DIPEA (27.5 μL, 0.16 mmol) and 4-pyridylacetic acid hydrochloride (13.7 mg, 0.08 mmol) were sequentially added. The reaction mixture was left under stirring and argon atmosphere at r.t.. After 5 h, TLC monitoring indicated the formation of a new compound and the reaction was quenched by removing the solvent *in vacuo*. The resulting crude was filtered, washed with CH_2Cl_2 and purified by chromatography on a silica gel column eluted with *n*-hexane/acetone (3:2, v/v). The desired product **13** was obtained in 50 % yields (20.0 mg, 0.04 mmol), calculated for two steps starting from pure **11**.

13: oil. R_f = 0.7 (CH_2Cl_2/MeOH, 93:7, v/v).

^{1}H NMR (400 MHz, $CDCl_3$): *δ* 8.64 (bd, *J* = 17.8 Hz, 2H, 2x ***H***α Py); 7.65 (bd, *J* = 4.3 Hz, 2H, 2x ***H***β Py); 7.14 (d, *J* = 7.5 Hz, 1H, N***H***); 5.83-5.76 (m, 1H, C***H***-10’); 5.00-4.90 (m, 2H, C***H***$_2$-11’); 4.59-4.54 (m, 1H, C***H*** α); 4.26-4.08 (overlapped signals, 4H, C***H***$_2$-1’’ and C***H***$_2$-1’); 3.76 (s, 2H, -C***H***$_2$Py); 3.69-3.62 (overlapped signals, 10H, 5x C***H***$_2$-2’’, 3’’, 4’’, 5’’, 6’’); 3.34 (s, 3H, OC***H***$_3$); 2.47-2.33 (m, 2H, C***H***$_2$-4); 2.25-2.17 (m, 1H, C***H***-3a); 2.08-2.02 (overlapped signals, 3H, C***H***$_2$-9’ and C***H***-3b); 1.63-1.60 (m, 2H, C***H***$_2$-2’); 1.36-1.25 (overlapped signals, 12H, 6x C***H***$_2$-3’, 4’, 5’, 6’, 7’, 8’).

^{13}C NMR (100 MHz, $CDCl_3$): *δ* 172.7 (***C***=O TEG ester); 171.4 (***C***=O undecenyl ester); 168.1 (***C***=ONH); 150.3 (***C***γ Py); 144.8 (2x ***C***α Py); 139.0 (***C***H-10’); 126.4 (2x ***C***β Py); 114.0 (***C***H_2-11’); 71.8, 70.4, 68.9 (overlapped signals, 5x ***C***H_2-2’’, 3’’, 4’’, 5’’, 6’’); 65.8 (***C***H_2-1’); 63.6 (***C***H_2-1’’); 58.8 (O***C***H_3); 52.2 (***C***H α); 42.2 (-***C***H_2Py); 33.6 (***C***H_2-9’); 30.3 (***C***H_2-4); 29.5, 29.3, 29.0, 28.9, 28.7 (overlapped signals, 6x ***C***H-2’, 4’, 5’, 6’, 7’, 8’); 26.6 (***C***H_2-3); 25.6 (***C***H_2-3’).

MALDI-MS (positive ions): calculated for $C_{30}H_{48}N_2O_8$, 564.34; found *m/z*: 587.24 [$M+Na^+$]; 603.21 [$M+K^+$].

Synthesis of TUGluRu

Aminoacyllipid **13** (2.40 mg, 4.22 μmol) was dissolved in 750 μL of dry CH_2Cl_2 and then Na^+ [*trans*-$RuCl_4(DMSO)_2]^-$ (1.78 mg, 4.22 μmol) was added. The reaction mixture was stirred at 40 °C. After 30 h the reaction, monitored *via* TLC, indicated the complete disappearance of both starting products and the formation of a new product, attributed to the desired ruthenium complex, recovered - by simple solvent removal under reduced pressure - in almost quantitative yields (3.82 mg, 4.22 μmol).

TUGluRu: orange powder: R_f = 0.3 (CH_2Cl_2/MeOH, 93:7, v/v).

^{1}H NMR [400 MHz, $(CD_3)_2CO$]: significant signals at *δ* -0.90 (very broad signal, Py protons); -9.51 (very broad signal, C***H₃*** DMSO).

LC-MS (positive ions): calculated for $C_{32}H_{54}Cl_4N_2NaO_9RuS^+$, 907.12; found m/z ($t_R$ = 6.89 min): 874.15 [M-Cl^-+H^+]; 890.12 [M-Cl^-+H_2O]; 931.15 [M+Na^+].

- **Synthesis and characterization of TOTyroRu**

Synthesis of 2-[2-(2-methoxyethoxy)ethoxy]ethyl, 2-[(9H-fluoren-9-yl)methoxy carbonyl]amino-3-(4-(*tert*-butoxy)phenyl)propanoate (14)

Commercially available Fmoc-Tyr(*t*Bu)-OH (117 mg, 0.25 mmol) was dissolved in 1.5 mL of dry DMF and then HATU (145 mg, 0.38 mmol), DIPEA (88.5 μL, 0.51 mmol) and triethylene glycol monomethyl ether (122 μL, 0.76 mmol) - previously coevaporated three times with dry CH_3CN (3 x 5 mL) - were sequentially added. The reaction mixture was left at r.t. under stirring and argon atmosphere. After 3 h, TLC monitoring indicated the presence of a new product in the reaction mixture and the complete disappearance of the starting amino acid. Then the solvent was removed *in vacuo* and the residue was filtered and washed with CH_2Cl_2; the crude product was purified by chromatography on a silica gel column eluted with CH_2Cl_2/MeOH (95:5, v/v) containing 2 % of TEA (v/v). The desired compound **14** was obtained in 96 % yields (146 mg, 0.24 mmol).

14: yellow oil. R_f = 0.7 (CH_2Cl_2/MeOH, 98:2, v/v).

^{1}H NMR (400 MHz, $CDCl_3$): *δ* 7.76 (d, *J* = 7.4 Hz, 2H, C***H***-d Fmoc); 7.56 (bd, *J* = 6.2 Hz, 2H, C***H***-e Fmoc); 7.39 (t, *J* = 7.3 Hz, 2H, C***H***-f Fmoc); 7.31 (t, *J* = 7.3 and 7.1 Hz, 2H, C***H***-g Fmoc); 7.01 (d, *J* = 7.7 Hz, 2H, C***H***-5 Ph); 6.88 (d, *J* = 7.6 Hz, 2H, C***H***-6 Ph); 5.35 (bd, *J* = 7.8 Hz, 1H, N***H***); 4.66 (m, 1H, C***H*** α); 4.45-4.31 (m, 2H, C***H₂***-a Fmoc); 4.27 (m, 2H, C***H₂***-1’’); 4.20 (t, *J* = 6.9 and 6.6 Hz, 1H, C***H***-b Fmoc); 3.74-3.52 (overlapped signals, 10H, 5x C***H₂***-2’’, 3’’, 4’’, 5’’, 6’’); 3.34 (s, 3H, OC***H₃***); 3.11-3.07 (m, 2H, C***H₂***-3); 1.31 (s, 9H, *t*Bu).

^{13}C NMR (100 MHz, $CDCl_3$): *δ* 171.3 (***C***=O TEG ester); 155.4 (***C***=ONH); 154.3 (quaternary carbon 7 of Ph); 143.7, 143.6 (***C***H-c Fmoc); 141.2 (overlapped signals, ***C***H-h Fmoc); 130.3 (quaternary carbon 4 of Ph); 129.7 (***C***H-5 Ph); 127.6 (***C***H-d Fmoc); 126.9 (***C***H-g Fmoc); 124.9 (***C***H-e Fmoc); 123.9 (***C***H-6 Ph); 119.8 (***C***H-f Fmoc); 78.2 (quaternary carbon of *t*Bu); 72.3 (***C***H₂-2’’); 71.7 (***C***H₂-6’’); 70.5, 70.4, 70.3 (overlapped signals, 3x ***C***H₂-3’’, 4’’, 5’’); 68.6 (***C***H₂-a Fmoc); 64.3 (***C***H₂-1’’); 61.6 (O***C***H₃); 58.8 (***C***H α); 47.0 (***C***H-b Fmoc); 38.5 (***C***H₂-3); 28.6 (3x ***C***H₃ of *t*Bu).

LC-MS (positive ions): calculated for $C_{35}H_{43}NO_8$, 605.30; found *m/z* (t_R = 9.37 min, C18 column): 606.37 [M+H^+], 628.37 [M+Na^+]; 644.32 [M+K^+].

Synthesis of 2-[2-(2-methoxyethoxy)ethoxy]ethyl, 2-[(9H-fluoren-9-yl)methoxy carbonyl] amino)-3-(4-hydroxyphenyl)propanoate (15)

Compound **14** (146 mg, 0.24 mmol) was dissolved in 3.5 mL of formic acid. The reaction mixture was stirred at r.t. for 7 h. Formic acid was removed under reduced pressure and the residue coevaporated three times with dry CH_3CN (3 x 5 mL), yielding the desired compound **15** in almost quantitative yields (132 mg, 0.24 mmol).

15: oil. R_f = 0.2 (*n*-hexane/acetone, 7:3, v/v) and R_f = 0.2 (CH_2Cl_2).

^{1}H NMR (400 MHz, $CDCl_3$): δ 7.76 (d, *J* = 7.4 Hz, 2H, C***H***-d Fmoc); 7.58 (d, *J* = 6.4 Hz, 2H, C***H***-e Fmoc); 7.39 (t, *J* = 7.2 and 7.3 Hz, 2H, C***H***-f Fmoc); 7.30 (t, *J* = 7.2 and 7.1 Hz, 2H, C***H***-g Fmoc); 6.96 (d, *J* = 7.8 Hz, 2H, C***H***-5 Ph); 6.76 (d, *J* = 7.9 Hz, 2H, C***H***-6 Ph); 5.43 (bd, *J* = 8.2 Hz, 1H, N***H***); 4.62 (m, 1H, C***H*** α); 4.43-4.36 (m, 2H, C$\boldsymbol{H_2}$-a Fmoc); 4.32 (t, 2H, *J* = 4.5 and 5.7 Hz, C$\boldsymbol{H_2}$-1’’); 4.20 (m, 1H, C***H***-b Fmoc); 3.74 -3.40 (overlapped signals, 10H, 5x C$\boldsymbol{H_2}$-2’’, 3’’, 4’’, 5’’, 6’’); 3.37 (s, 3H, OC$\boldsymbol{H_3}$); 3.09-3.07 (m, 2H, C$\boldsymbol{H_2}$-3).

^{13}C NMR (100 MHz, $CDCl_3$): δ 171.6 (***C***=O TEG ester); 160.9 (quaternary carbon 7 of Ph); 155.4 (***C***=ONH); 143.6, 143.5 (***C***H-c Fmoc); 141.1 (overlapped signals, ***C***H-h Fmoc); 130.3 (***C***H-5 Ph); 127.6 (***C***H-d Fmoc); 126.9 (***C***H-g Fmoc); 126.6 (quaternary carbon 4 of Ph); 125.0, 124.9 (***C***H-e Fmoc); 119.8 (***C***H-f Fmoc); 115.5 (***C***H-6 Ph); 71.8 (***C***H_2-2’’); 71.7 (***C***H_2-6’’); 70.4, 70.3, 70.1 (overlapped signals, 3x ***C***H_2-3’’, 4’’, 5’’); 68.7 (***C***H_2-a Fmoc); 64.5 (***C***H_2-1’’); 58.7 (O***C***H_3); 54.9 (***C***H α); 46.9 (***C***H-b Fmoc); 37.6 (***C***H_2-3).

LC-MS (positive ions): calculated for $C_{31}H_{35}NO_8$, 549.24; found *m/z* (t_R = 7.67 min, C18 column): 550.33 [$M+H^+$]; 572.24 [$M+Na^+$]; 588.30 [$M+K^+$].

Synthesis of 4-{13-[(9H-fluoren-9-yl)methoxy carbonyl]amino}-12-oxo-2,5,8,11-tetraoxatetradecan-14-yl)phenyl oleate (16)

Pure compound **15** (76.0 mg, 0.13 mmol), oleic acid (41.6 µL, 0.13 mmol) and triphenylphosphine (72.8 mg, 0.28 mmol) - previously coevaporated three times with dry CH_3CN (3 x 2 mL) - were dissolved in 5.0 mL of dry THF and stirred at r.t. for 10 min. Then DEAD (43.4 µL, 0.28 mmol) was added dropwise and the reaction mixture was heated to reflux at 65 °C under argon atmosphere overnight. After 24 h, TLC analysis showed the appearance of a new product in the reaction mixture, thus the solvent was removed under reduced pressure. The resulting residue was filtered and washed several times with CH_2Cl_2 and then purified by chromatography on a silica gel column eluting with *n*-hexane/AcOEt (7:3, v/v). The desired compound **16** was obtained in 38 % yields (36.4 mg, 0.05 mmol).

15: oil. R_f = 0.4 (*n*-hexane/AcOEt, 1:1, v/v).

^{1}H NMR (400 MHz, $CDCl_3$): *δ* 7.79 (d, *J* = 7.5 and 7.8 Hz, 2H, C***H***-d Fmoc); 7.60 (bd, *J* = 6.9 Hz, 2H, C***H***-e Fmoc); 7.43 (t, *J* = 7.4 and 7.5 Hz, 2H, C***H***-f Fmoc); 7.34 (t, *J* = 7.4 Hz, 2H, C***H***-g Fmoc); 7.16 (d, *J* = 8.0 Hz, 2H, C***H***-5 Ph); 7.02 (d, *J* = 8.3 Hz, 2H, C***H***-6 Ph); 5.40-5.36 (overlapped signals, 3H, N***H*** and C***H***-9', 10'); 4.71 (m, 1H, C***H*** α); 4.49-4.38 (m, 2H, $C\boldsymbol{H_2}$-a Fmoc); 4.36-4.33 (m, 2H, $C\boldsymbol{H_2}$-1''); 4.31 (m, 1H, C***H***-b Fmoc); 3.65-3.40 (overlapped signals, 10H, 5x $C\boldsymbol{H_2}$-2'', 3'', 4'', 5'', 6''); 3.38 (s, 3H, $OC\boldsymbol{H_3}$); 3.15 (m, 2H, $C\boldsymbol{H_2}$-3); 2.56 (t, *J* = 7.4 and 7.5 Hz, 2H, $C\boldsymbol{H_2}$-2'); 2.04 (overlapped signals, 4H, 2x $C\boldsymbol{H_2}$-8', 11'); 1.80-1.72 (m, 2H, $C\boldsymbol{H_2}$-3'); 1.41 (overlapped signals, 4H, 2x $C\boldsymbol{H_2}$-7', 12'); 1.29 (overlapped signals, 16H, 8x $C\boldsymbol{H_2}$-4', 5', 6', 13', 14', 15', 16', 17'); 0.90 (t, *J* = 6.6 and 6.9 Hz, 3H, $C\boldsymbol{H_3}$-18').

^{13}C NMR (100 MHz, $CDCl_3$): *δ* 172.2 (***C***=O oleic ester); 171.3 (***C***=O TEG ester); 160.9 (quaternary carbon 7 of Ph); 155.6 (***C***=ONH); 143.9, 143.8 (***C***H-c Fmoc); 141.3 (overlapped signals, ***C***H-h Fmoc); 133.2 (quaternary carbon 4 of Ph); 130.4, 130.1 (overlapped signals, 2x ***C***H-9', 10'); 129.7 (***C***H-5 Ph); 127.7 (***C***H-d Fmoc); 127.1 (***C***H-g Fmoc); 125.1 (***C***H-e Fmoc); 121.6 (***C***H-6 Ph); 120.0 (***C***H-f Fmoc); 71.9 ($\boldsymbol{C}H_2$-2''); 70.6, 70.5, 68.8, 68.7 (overlapped signals, 4x $\boldsymbol{C}H_2$-3'', 4'', 5'', 6''); 67.0 ($\boldsymbol{C}H_2$-a Fmoc); 63.1 ($\boldsymbol{C}H_2$-1''); 62.2 ($O\boldsymbol{C}H_3$); 59.0 (***C***H α); 47.2 (***C***H-b Fmoc); 37.5 ($\boldsymbol{C}H_2$-3); 34.4 ($\boldsymbol{C}H_2$-2'); 31.9, 31.8 (overlapped signals, 2x $\boldsymbol{C}H_2$-7', 12'); 29.7, 29.5, 29.3, 29.2, 29.1, 29.0, 28.9 (overlapped signals, 7x $\boldsymbol{C}H_2$-4', 5', 6', 13', 14', 15',16'); 27.2, 26.7 (overlapped signals, 2x $\boldsymbol{C}H_2$-8', 11'); 24.9 ($\boldsymbol{C}H_2$-3'); 22.6 ($\boldsymbol{C}H_2$-17'); 14.1 ($\boldsymbol{C}H_3$-18').

LC-MS (positive ions): calculated for $C_{49}H_{67}NO_9$, 813.48; found *m/z* (t_R = 11.8 min, C18 column): 812.59 [M^+]; 852.59 [$M+K^+$].

Synthesis of 4-(13-amino-12-oxo-2,5,8,11-tetraoxatetradecan-14-yl)phenyl oleate (compound 17)

Isolated compound **16** (36.4 mg, 0.04 mmol) was dissolved in 1.0 mL of a 10 % piperidine solution in dry CH_3CN. After 30 min under stirring and argon atmosphere at r.t., TLC analysis showed the complete removal of the Fmoc group. Then the solvent was removed under reduced pressure and the residue was coevaporated three times with dry CH_3CN (3 x 5 mL), obtaining the desired compound in almost quantitative yields (26.5 mg, 0.04 mmol). Derivative **17** was not isolated, but directly reacted to obtain the final aminoacyllipidic scaffold.

Synthesis of 4-{12-oxo-13-[2-(pyridin-4-yl)acetamido] 2,5,8,11-tetraoxatetradecan-14-yl}phenyl oleate (18)

Crude derivative **17** (26.5 mg, 0.04 mmol) was dissolved in 1.0 mL of dry DMF and then HATU (25.5 mg, 0.07 mmol), DIPEA (15.5 µL, 0.09 mmol) and 4-pyridylacetic acid hydrochloride (7.76

mg, 0.04 mmol) were sequentially added. The reaction mixture was left under stirring and argon atmosphere at r.t.. After 17 h, TLC monitoring showed the complete disappearance of the starting materials and the reaction was quenched by removing the solvent *in vacuo*. The crude product was filtered, washed several times with CH_2Cl_2 and purified by chromatography on a silica gel column using CH_2Cl_2 as eluent. The desired product **18** was obtained in 54 % yields (17.1 mg, 0.02 mmol), calculated for two subsequent steps starting from **16**.

18: oil. R_f = 0.7 (CH_2Cl_2/MeOH, 93:7, v/v).

^{1}H NMR (400 MHz, $CDCl_3$): δ 8.55 (d, J = 5.5 Hz, 2H, 2x ***H***α Py); 7.64 (d, J = 5.5 Hz, 2H, 2x ***H***β Py); 7.15 (d, J = 8.2 Hz, 2H, C***H***-5 Ph); 6.94 (d, J = 8.2 Hz, 2H, C***H***-6 Ph); 5.34-5.29 (overlapped signals, 3H, N***H*** and C***H***-9’, 10’); 4.81-4.77 (m, 1H, C***H*** α); 4.34-4.23 (m, 2H, C$\boldsymbol{H_2}$-1’’); 3.73-3.71 (m, 2H, -C$\boldsymbol{H_2}$Py); 3.69-3.53 (overlapped signals, 10H, 5x C$\boldsymbol{H_2}$-2’’, 3’’, 4’’, 5’’, 6’’); 3.36 (s, 3H, OC$\boldsymbol{H_3}$); 3.16-3.12 (m, 2H, C$\boldsymbol{H_2}$-3); 2.54 (t, J = 7.4 and 7.5 Hz, 2H, C$\boldsymbol{H_2}$-2’); 2.01-2.00 (overlapped signals, 4H, 2x C$\boldsymbol{H_2}$-8’, 11’); 1.48 (m, 2H, C$\boldsymbol{H_2}$-3’); 1.33 (overlapped signals, 4H, 2x C$\boldsymbol{H_2}$-7’, 12’); 1.29 (overlapped signals, 16H, 8x C$\boldsymbol{H_2}$-4’, 5’, 6’, 13’, 14’, 15’, 16’, 17’); 0.88-0.85 (m, 3H, C$\boldsymbol{H_3}$-18’).

^{13}C NMR (100 MHz, $CDCl_3$): δ 172.5 (***C***=ONH); 172.2 (***C***=O oleic ester); 170.9 (***C***=O TEG ester); 162.6 (quaternary carbon 7 of Ph); 149.6 (2x ***C***α Py); 143.1 (quaternary ***C***γ Py); 133.8 (quaternary carbon 4 of Ph); 130.3, 129.9 (overlapped signals, 2x ***C***H-9’, 10’); 122.3 (2x ***C***β Py); 121.6 (***C***H-5 Ph); 121.4 (***C***H-6 Ph); 72.2, 71.6, 70.3, 70.1, 68.6 (overlapped signals, 5x ***C***H_2-2’’, 3’’, 4’’, 5’’, 6’’); 64.3 (***C***H_2-1’’); 61.5 (O***C***H_3); 58.7 (***C***H α); 43.0 (-***C***H_2Py); 36.6 (***C***H_2-3); 34.2 (***C***H_2-2’); 31.7 (overlapped signals 2x ***C***H_2-7’, 12’); 29.6, 29.5, 29.3, 29.2, 29.1, 28.9 (overlapped signals, 7x ***C***H_2-3’, 4’, 5’, 6’, 13’, 14’, 15’, 16’); 27.1, 27.0 (***C***H_2-8’, 11’); 24.8 (***C***H_2-3’); 22.6 (***C***H_2-17’); 14.0 (***C***H_3-18’).

LC-MS (positive ions): calculated for $C_{41}H_{62}N_2O_8$, 710.45; found *m/z* (t_R = 5.56 min, C18 column): 711.57 [M+H$^+$]; 733.51 [M+Na$^+$].

Synthesis of TOTyroRu

Aminoacyllipid **18** (16.5 mg, 0.02 mmol) was dissolved in 750 μL of dry CH_2Cl_2 and then Na$^+$ [*trans*-$RuCl_4(DMSO)_2$]$^-$ (8.48 mg, 0.02 mmol) was added. The reaction mixture was stirred at 40 °C for 30 h. TLC monitoring showed the complete disappearance of the starting reagents and the formation of a new product, attributed to the desired ruthenium complex, recovered in almost quantitative yields after solvent removal *in vacuo* (24.1 mg, 0.02 mmol).

TOTyroRu: orange powder. R_f = 0.3 (CH_2Cl_2/MeOH, 93:7, v/v).

^{1}H NMR (400 MHz, $CDCl_3$): significant signals at δ -1.48 (very broad signal, Py-Ru); -9.18 (very broad signal, $C\boldsymbol{H_3}$ DMSO).
LC-MS (positive ions): calculated for $C_{43}H_{68}Cl_4N_2NaO_9RuS^+$, 1053.23; found *m/z* ($t_R$ = 7.03 min, C18 column): 1036.32 [M-Cl^-+H_2O].

- **Synthesis and characterization of PySSRu**

Synthesis of 2-(pyridin-4-yl)ethanethiol (19, PySH)

Commercially available 2-(4-pyridinyl)ethanethiol hydrochloride (502 mg, 2.86 mmol) and NaOH (114 mg, 2.86 mmol) were dissolved in 13 mL of MeOH, and then left under stirring at r.t.. The reaction, monitored by pH measurements, after ca. 30 min was quenched by solvent removal under reduced pressure and the crude product was extracted with $CHCl_3/H_2O$. The desired compound was recovered in the organic phases, which were dried upon addition of anhydrous Na_2SO_4, filtered and concentrated under reduced pressure. The pure compound **19** was obtained in 82 % isolated yields (327 mg, 2.35 mmol).
19: yellow oil. R_f = 0.8 (CH_2Cl_2/MeOH, 8:2, v/v).
^{1}H NMR (500 MHz, $CDCl_3$,): δ 8.52 (d, *J* = 5.5 Hz, 2H, 2x ***H***α Py); 7.12 (d, *J* = 5.5 Hz, 2H, 2x ***H***β Py); 2.91 (t, *J* = 7.5 Hz, 2H, $C\boldsymbol{H_2}CH_2SH$); 2.79 (q, 2H, $C\boldsymbol{H_2}SH$); 1.38 (t, *J* = 8.0 Hz 1H, S***H***).
^{13}C NMR (125 MHz, $CDCl_3$): δ 149.8 (2x ***C***α Py); 148.3 (***C***γ Py); 123.8 (2x ***C***β Py); 39.2 ($\boldsymbol{C}H_2CH_2SH$); 24.6 ($\boldsymbol{C}H_2SH$).

Synthesis of 1,2-bis[2-(pyridin-4-yl)ethyl]disulfane (20, PySSPy)

Pure product **19** (100 mg, 0.72 mmol) was dissolved in 500 µL of MeOH and then H_2O_2 (90 µL of a 30 wt. % in H_2O solution, 0.80 mmol) and KI (11.6 mg, 0.07 mmol) were sequentially added to the reaction mixture, left under stirring at r.t.. After 1 h, TLC analysis indicated the appearance of a new product, with concomitant disappearance of the starting material. Thus, the reaction was quenched by addition of few drops of H_2O, the solvent was removed *in vacuo* and the crude product was extracted with CH_2Cl_2/H_2O. The desired compound was recovered in the organic phases, which were dried over anhydrous Na_2SO_4, filtered and then taken to dryness, giving compound **20** in almost quantitative yields (98.0 mg, 0.35 mmol).
20: yellow oil. R_f = 0.6 (CH_2Cl_2/MeOH, 95:5, v/v).
^{1}H NMR (400 MHz, $CDCl_3$,): δ 8.50 (d, *J* = 5.5 Hz, 4H, 2x ***H***α Py); 7.10 (d, *J* = 5.5 Hz, 4H, 2x ***H***β Py); 2.99 – 2.89 (m, 8H, 2x $C\boldsymbol{H_2}C\boldsymbol{H_2}S$).
^{13}C NMR (100 MHz, $CDCl_3$): δ 149.7 (2x ***C***α Py); 148.3 (2x ***C***γ Py); 123.8 (2x ***C***β Py); 38.4 ($\boldsymbol{C}H_2CH_2SH$); 34.5 ($\boldsymbol{C}H_2SH$).

MALDI-MS (positive ions): calculated for $C_{14}H_{16}N_2S_2$, 276.08; found *m/z*: 276.86 [$M+H^+$]; 298.89 [$M+Na^+$]; 314.94 [$M+K^+$].

IR: cm^{-1} 1595 (s), 1557 (m) [C=N)]; 1416 (s), 1215 (m) 991 (m), [CH_2]; 798 (s) [C-S]; 575 (m), 500 (m), [S-S].

Synthesis of PySSRu

Pure compound **20** (10.0 mg, 0.04 mmol) was dissolved in 10 mL of dry acetone and then [trans-$RuCl_4(DMSO)_2]^-$ Na^+ (25.3 mg, 0.06 mmol) was added to the reaction mixture, left under stirring at r.t.. After 2 h, TLC monitoring indicated the complete disappearance of both starting materials and the formation of a new product. The desired ruthenium complex PySSRu was recovered in 75 % isolated yields (28.9 mg, 0.03 mmol) by solvent removal under vacuum followed by precipitation/centrifugation in CH_2Cl_2.

PySSRu: orange powder: R_f = 0.3 (CH_2Cl_2/MeOH, 85:15, v/v).

^{1}H NMR (400 MHz, DMSO-d_6): significant signals at δ -2.40 (very broad signal, Py protons); -13.0 (very broad signal, C***H*₃** of DMSO).

IR: cm^{-1} 1705 (s), 1610 (m) [C=N)]; 1422 (s), 1363 (m) 1222 (m), [CH_2]; 1089 (m), 1022 (m) [(S=O) (DM*S*O)]; 815 (s) [C-S]; 530 (m) [S-S].

- **Synthesis and characterization of the precursor ruthenium salts**

Synthesis of hydrogen *trans*-bis(dimethylsulfoxide) tetrachlororuthenate(III): [(DMSO)₂H][*trans*-Ru(DMSO)₂Cl₄] (21)

A 1.5 g amount of hydrated $RuCl_3$ (7.23 mmol) was partially dissolved in 7 mL of DMSO and 1 mL of 37 % aqueous HCl was added. The mixture was left at 80 °C under vigorous stirring until complete dissolution of $RuCl_3$. The dense, deep dark solution was then heated at 100 °C for 10 min. It gradually became more fluid and its color turned to bright dark red. After cooling, 30 mL of acetone were added to the solution, then left at 4 °C overnight. Large dark-red crystals were formed and were filtered off, washed with cold acetone and diethyl ether and vacuum-dried. The desired product **21** was obtained in 60 % yields (2.3 g, 4.34 mmol).

^{1}H NMR [400 MHz, $(CD_3)_2CO$]: significant signals at δ 9.11 (very broad signal, DMSOH^+); 2.94 (very broad signal, CH_3 DMSOH^+); -9.17 (very broad signal, CH_3 DMSO).

M.p.: 118-121 °C.

FTIR-ATR: cm^{-1} 1395.8 (w), 1287.0 (w) [δ (**CH_3**)]; 1108.0 (s), 1096.0 (s) [ν (**S=O**) (**DM*S*O**)]; 1011.4 (s), 953.9 (m) [ρ (**CH_3**)]; 718.0 (w), 670.0 (w) [ν (**C-S**)].

Sodium *trans*-bis(dimethylsulfoxide)tetrachlororuthenate(III): Na^+ [*trans*-$Ru(DMSO)_2Cl_4]^-$ (22)

1.12 g of finely ground $[(DMSO)_2H]$ [*trans*-$[Ru(DMSO)_2Cl_4]$ (2.02 mmol) were dissolved in a mixture of 50 mL of ethanol and 700 µL of water. To the clear solution, NaCl (176 mg, 3.02 mmol), dissolved in 500 µL of water, was added. The desired product rapidly precipitated from the solution as light-orange microcrystals, which were filtered off, washed with cold ethanol and diethyl ether, and vacuum-dried. The target compound was obtained in 86 % yields (735 mg, 1.74 mmol).

^{1}H NMR [400 MHz, $(CD_3)_2CO$)]: significant signals at δ -9.37 (very broad signal, C***H*$_3$** DMSO).

M.p. (slow and gradual thermal decomposition): >230 °C.

FTIR-ATR: cm^{-1} 1395.8 (w), 1287.0 (w) [δ (**CH_3**)]; 1108.0 (s), 1096.0 (s) [ν (**S=O**) (**DM*SO***)]; 1011.4 (s), 953.9 (m) [ρ (**CH_3**)]; 718.0 (w), 670.0 (w) [ν (**C-S**)].

Chapter 3

NOTA chelators

1. Molecular imaging: introduction

In the treatment of diseases and in particular of cancer, it is essential to deliver the therapeutic agents to the target site, at the right time, correct concentration and in a minimally invasive manner.[184–188] On the other hand, also the early diagnosis of the disease is important to identify functional abnormalities which precede morphological changes, and to this aim molecular imaging may contribute to the reduction of morbidity and mortality.[189]

The field of molecular imaging, "*the visualization, characterization and measurement of biological processes at the molecular and cellular levels in humans and other living systems*",[190] has expanded tremendously over the last decade. 'Molecular imaging' is based on the biomedical imaging methods which allow visualizing specific biomarkers or processes in the living body at the molecular level, introducing suitable probes able to measure the expression of these markers at different stages of the disease.[191] This approach presents several advantages over traditional diagnostic methods: it can give whole-body readout in an intact system which is much more relevant and reliable than *in vitro*/*ex vivo* assays; reduce the workload and speed up the drug development process; aid in lesion detection in patients and help in individualized treatment monitoring and dose optimization.[192,193] Non-invasive detection of various molecular markers of diseases can allow for much earlier diagnosis, earlier treatment, and better prognosis that could eventually lead to personalized medicine.[191,194]

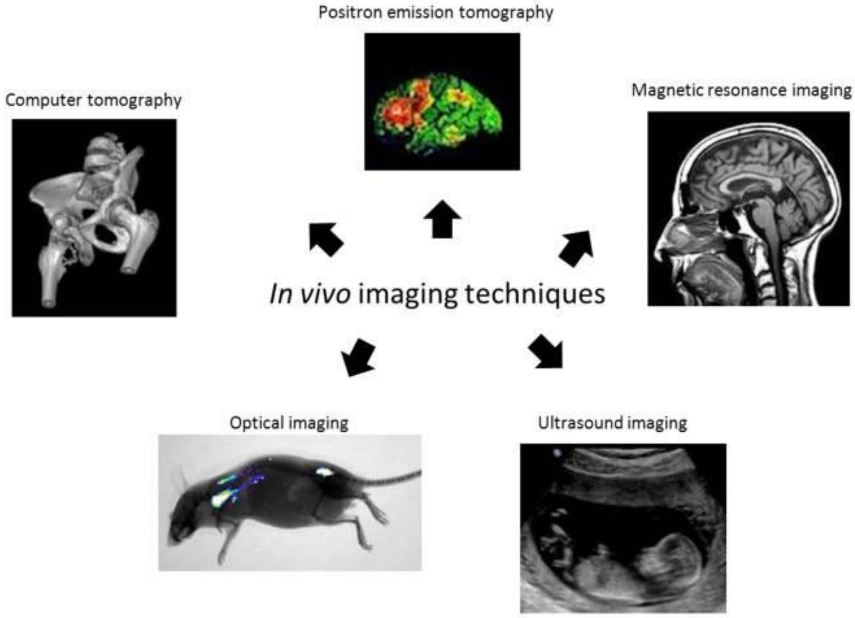

Figure 40. Main *in vivo* imaging techniques. Pictures reproduced from Kizek *et al.*[195]

Imaging techniques are playing an increasingly important role in the investigation of the biodistribution and pharmacokinetics of drugs or drug delivery systems in cancer, and research progresses in medical imaging may be beneficial for the complete health and disease management process.[195] Medical imaging covers many different imaging modalities: X-ray-based methods such as radiography and Computed Tomography (CT), Magnetic Resonance Imaging (MRI), Ultrasound (US), nuclear medicine with Positron Emission Tomography (PET) and Single Photon Emission Computed Tomography (SPECT), and several optical imaging methods (Figure 40).[46,186,195–199] The relative advantages and limitations of these imaging modalities have been elaborately discussed in several recent review articles.[186,197–199]

Among these methods, PET and optical imaging are considered quantitative or semi-quantitative imaging modalities that employ radiotracers or optical tracers to image biodistribution of the labeled drugs or probe loaded delivery systems in the body, while CT and MRI are normally used for anatomical imaging purposes.[200]

PET and SPECT techniques exploit, respectively, positron and gamma emitting radionuclides for the generation of the signal that results in a whole-body scan in a single examination. They provide fast and non-invasive evaluation of physiological and pathological processes, and together with external and internal radiotherapy can be used for theranostic applications, which is considered as the main step towards personalized medicine.[1,8,201,202]

1.1. PET imaging

PET has become an established method for medical research and clinical routine diagnostics because of its ability to diagnose a disease in early stages and monitor therapeutic responses.[197,203,204]

The major application domain of PET analyses is oncology; however, potential has been demonstrated for imaging of myocardial and pulmonary perfusion and ventilation, as well as inflammation and infection. Imaging of general biological properties and processes such as proliferation, apoptosis, hypoxia, glycolysis, and angiogenesis have also been investigated.[205]

In a typical scenario of PET imaging (Figure 41), a suitable compound is radiolabeled with positron-emitting radionuclides such as ^{18}F, ^{64}Cu, ^{68}Ga, or ^{89}Zr and administered to a patient.[197] When the radioactive isotope incorporated into the PET tracer decays, a positron is emitted and immediately collides with an electron. The collision results in annihilation of both particles and release two γ photons (with an energy of 511 keV), which are approximately 180° apart.[206]

The photons can be detected by a ring of detectors configured in the coincidence mode in the PET camera. When a sufficient number of decays have been detected, a computer converts the signal relative to the decay events into a three-dimensional image, which provides information on the spatial distribution of the radioactivity as a function of time in the living subject.[197] In fact, the colour of each pixel is correlated with the radioactivity concentration or some derivative thereof.[206] The major advantage of PET is that it not only enables the *in vivo* visualization of physiological processes at a molecular level in real time, but also quantifies them by measuring the spatial concentration of the radiation source.[205] The widespread opinion is that PET is a costly technique, but indeed the total cost of the otherwise required examinations, hospitalization and risks associated with biopsy - as well as possible false diagnosis leading to futile surgery cost and patient distress - is much higher. In particular, the biopsy results might be misleading since the tumour diagnosis and staging is conducted *ex vivo* on invasively collected tissues. The sampled tissue is commonly heterogenic and thus might not be representative, while PET may provide non-invasively more detailed and accurate information on the heterogeneity of the whole tumour in a single examination.[205]

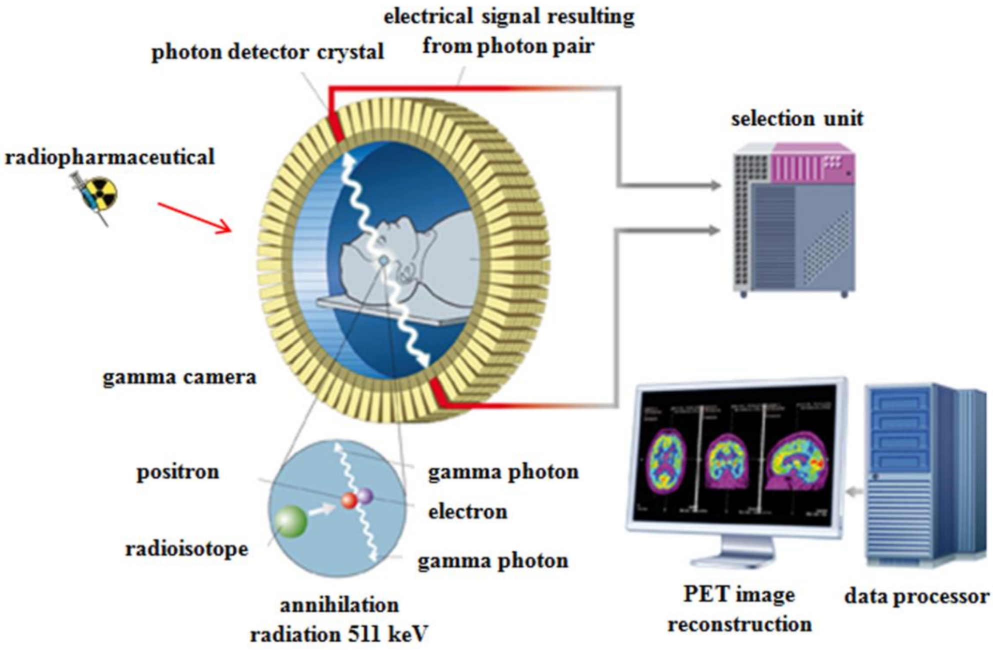

Figure 41. Schematic illustration of a general PET acquisition process.

PET also plays an important role in the process of drug development and evaluation, whereby understanding the mechanism of action of a drug and establishing its optimal dosage regimens and treatment strategies are most crucial.[207–210]

Positron-emitting radionuclides of elements such as C, N, O can replace the stable analogues in drugs and biomolecules, and hence it is possible to synthesize PET probes with the same chemical structure as the parent unlabeled molecules without altering their biological activity.[47] The most common radionuclides relevant for the labelling procedure of radiopharmaceuticals for PET, SPECT, and radiotherapy are presented in Table 6. The majority are metals typically involved in coordination chemistry. Only few radionuclides are produced in generator systems. Factors as their production mode as well as physical and chemical features determine the choice of a radionuclide. Two gallium isotopes, ^{66}Ga ($t_{1/2}$ = 9.5 h) and ^{68}Ga ($t_{1/2}$ = 68 min), decay by β^+-emission and are therefore suitable for PET imaging, ^{67}Ga ($t_{1/2}$ = 78 h) decays by electron capture with concomitant γ-emission and is used for SPECT imaging. Examples of clinically used radionuclides include also ^{11}C, ^{18}F, ^{64}Cu, ^{89}Zr, ^{99m}Tc, ^{111}In, ^{124}I.[47,205] The propagation of PET techniques is greatly stimulated by the widespread use of [^{18}F]-fluorodeoxyglucose ([^{18}F]-FDG) for many indications in oncology. FDG is a non-metabolized glucose analog that is a substrate both for the dedicated glucose transporters on the cell membrane and the cytoplasmic enzyme hexokinase responsible for phosphorylation. After phosphorylation, FDG is not a substrate for further pathways and is effectively trapped in cells.[191,206]

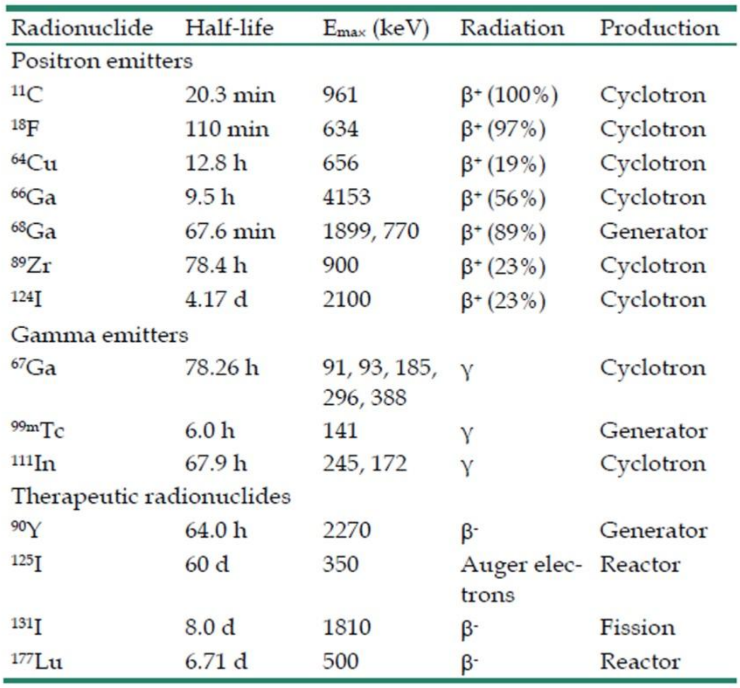

Radionuclide	Half-life	E_{max} (keV)	Radiation	Production
Positron emitters				
^{11}C	20.3 min	961	β^+ (100%)	Cyclotron
^{18}F	110 min	634	β^+ (97%)	Cyclotron
^{64}Cu	12.8 h	656	β^+ (19%)	Cyclotron
^{66}Ga	9.5 h	4153	β^+ (56%)	Cyclotron
^{68}Ga	67.6 min	1899, 770	β^+ (89%)	Generator
^{89}Zr	78.4 h	900	β^+ (23%)	Cyclotron
^{124}I	4.17 d	2100	β^+ (23%)	Cyclotron
Gamma emitters				
^{67}Ga	78.26 h	91, 93, 185, 296, 388	γ	Cyclotron
^{99m}Tc	6.0 h	141	γ	Generator
^{111}In	67.9 h	245, 172	γ	Cyclotron
Therapeutic radionuclides				
^{90}Y	64.0 h	2270	β^-	Generator
^{125}I	60 d	350	Auger electrons	Reactor
^{131}I	8.0 d	1810	β^-	Fission
^{177}Lu	6.71 d	500	β^-	Reactor

Table 6. Selected radionuclides used in clinical PET, SPECT and radiotherapy, their production mode and decay properties.[205]

Despite [^{18}F]FDG is widely used in many cancer forms as a biomarker of the glucose transport, it fails in diagnosis of slowly growing tumours and in differentiating tumours from processes as inflammation, infection, reactive lymph nodes, tuberculosis and sarcoidosis.[211,212]

Many cancer forms rely on glucose for energy production and growth and tend to have enhanced expression of glucose transporters and hexokinase, resulting in an elevated accumulation of FDG when studied with PET *in vivo*. The high uptake in normal organs, particularly in brain and gut, results in poor contrast in those areas and potential failure in lesion detection.[211] Thus alternative imaging agents with specific binding capability to *e.g.* receptors, antigens, enzymes are highly desirable and in this context ^{68}Ga-complexes have particularly emerged.[205]

^{68}Ga can be used for the labelling of small organic compounds, biological macromolecules as well as nano- and microparticles, thus largely expanding the potential of PET.[205,213,214]

1.2. Chemistry of gallium

Gallium is the third element of Group 13 of the Periodic Table and in aqueous solutions the only stable oxidation state of this metal is +3. Its chemistry is largely influenced by pH changes: the optimal pH is 3-5, while at pH >5 it tends to precipitate as $Ga(OH)_3$.[215,216] The isotope ^{68}Ga is a positron emitter with a physical half-life of 67.71 min, which is compatible with the pharmacokinetics of most radiopharmaceuticals of low molecular weight as antibody fragments, peptides, aptamers and oligonucleotides. It can be produced from a generator system where ^{68}Ge is absorbed on a chromatographic column with either inorganic or organic matrix.[213,217,218] The generators are eluted with HCl solutions of various molarity (from 0.05 to 5.5 M, 5-7 mL) offering ^{68}Ga in a cationic form suitable for the subsequent labelling. The generators can be eluted repeatedly during the day.[205] The benefits of ^{68}Ga, in comparison with the other radionuclides mentioned above, can be summarized as follows: it is produced from a long shelf-life and cost-effective generator;[218,219] the half-life of ^{68}Ga permits the production and immediate application of the resulting agents, and the labelling synthesis is amenable to automation and kit-type preparation; in addition, it provides sufficient levels of radioactivity for high quality images, short scanning time (which determines a fast patient examination) and minimized radiation doses for the patient and personnel, also allowing fast dischargement of the patient; finally, it allows repetitive examinations within the same day.[220] Various ^{68}Ga-based imaging agents have already been tested in humans.[8]

The Ga^{3+} ion is classified as a hard Lewis acid, forming thermodynamically stable complexes with ligands that are hard Lewis bases. These are ligands containing oxygen, nitrogen and sulfur donor atoms, such as carboxylate, phosphonate, hydroxamate and amine, but also softer functional groups such as phenolate and thiol groups were found to be appropriate.[218] The hard acid Ga^{3+} can form tetra-, penta-, and hexa-coordinated complexes. The latter ones are the most stable species with octahedral coordination sphere.[213,218]

The coordination reaction requires buffering, first of all, to ensure the suitable pH for the deprotonation of the coordinating positions, and secondly, to maintain Ga^{3+} in solution that might otherwise form $Ga(OH)_3$ and precipitate at pH 3-7.[213] Unlike other PET radioisotopes, like ^{18}F or ^{11}C, ionic Ga^{3+} cannot be directly bound to targeting vectors but must be conjugated to a target vector using a bifunctional chelating agent, such as the macrocyclic chelators NOTA (1,4,7-

triazacyclononane-1,4,7-triacetic acid) and DOTA (1,4,7,10-tetraazacyclododecane-1,4,7,10-tetraacetic acid), which can form within 10 min very stable complexes with Ga^{3+} at pH 3.5 at r.t. in high chelation efficiency (>95%).[221–224] The thermodynamic stability constant of the Ga^{3+} complex with the chelator DOTA is much lower (logK = 21.33)[225] than that of the chelator NOTA (logK = 30.98)[226] due to the larger size of its cavity.

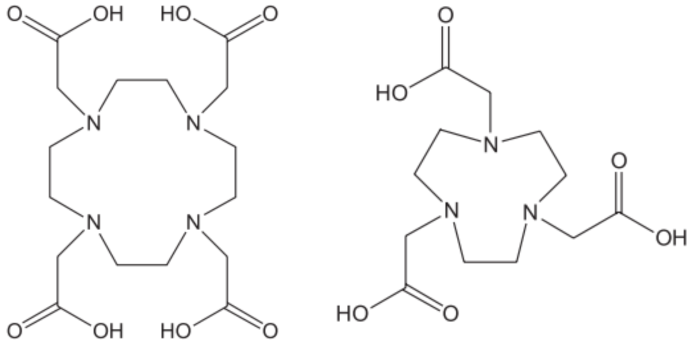

DOTA **NOTA**

Figure 42. Chemical structures of DOTA (left) and NOTA (right) macrocycles.

DOTA has 8 binding sites available for complexing with metals, and NOTA has only 6 (Figure 42); thus, no free binding sites are left on NOTA after gallium complexation, which requires all the 6 binding sites. However, it has been shown that amide oxygen or nitrogen can bind gallium[227] and as a result, various amino acid derivatives conjugated with NOTA have been developed for cancer imaging.[228,229] Remarkbly, different syntheses of bifunctional NOTA derivatives have been reported recently by several groups[230,231] Their approaches included intra- or intermolecular cyclization strategy as key steps, affording NOTA derivatives functionalized on a carbon of the macrocyclic ring. Harsh conditions for deprotection and reduction are required in order to use these compounds for coupling to biomolecules. A bifunctional NOTA derivative, functionalized on the –CH_2- group of one of the acetic acid arms, was proposed for conjugation to proteins.[232]

1.3. Dual-modality imaging with radiolabeled nanoparticles

As mentioned above, various imaging modalities are successfully employed to investigate the anatomic or functional dissemination of tissues in the body. However, no single imaging modality allows overall structural, functional, and molecular information, as each imaging modality has its own unique strengths and weaknesses.[196,233] For example, MRI has high resolution, yet it suffers from low sensitivity; PET imaging has very high sensitivity but relatively poor resolution.[234] The combination of multiple molecular imaging modalities offers the prospect of improved diagnostic and therapeutic monitoring abilities, with remarkable synergistic advantages over any modality alone, overcoming the shortcomings of the individual modalities and providing complementary information, especially *in vivo*, on cellular and molecular functions.[195,233]

For example, with dual function probes for PET/MRI, the high sensitivity of PET can be used as a whole body screen to identify regions of interest, thereby reducing the volume of tissue that needs to be scanned; this reduces scan time required for high-resolution imaging by MRI.[235,236]

The idea of combining imaging technologies moved to the mainstream with the advent of the first successful commercial fused instruments. The first fused PET/CT instrument, developed in 1998 by Townsend and colleagues in collaboration with Siemens Medical, was available commercially in 2001.[236] The next wave of innovation has been in PET/MRI-fused instruments, which have generated much hope for improved patient safety and imaging capability over PET/CT. Although research on PET/MRI instruments was initiated at approximately the same time as PET/CT, the economic and engineering challenges of merging the two modalities slowed development, and the first commercial PET/MRI prototype for a human scale hybrid scanner was not unveiled until 2007.[237]

Multimodality imaging using a small molecule-based probe is very challenging, but nanoparticles (NPs) can be very useful to this purpose.[238] In fact, they can be intrinsically superparamagnetic – as in the case of SPIONs (Superparamagnetic Iron Oxide Nanoparticles) - and therefore useful for MRI imaging[171,172] or having large surface areas they can be used as platforms for the incorporation of multifunctional agents for multimodality molecular imaging.[239–242]

In particular, lipid-based vectors,[243,244] nanoparticles[245] or nanomaterials[246] are being specially investigated due to the fact that the mechanical, chemical, electrical, optical, magnetic, electro-optical and magneto-optical properties of these systems are different from their bulk properties and depend on the particle size.[21,247] Nanoparticle probes can endow imaging techniques with enhanced signal sensitivity, better spatial resolution, and the ability to relay information about biological systems at the molecular and cellular levels.[233,248] In particular, PET radionuclide-labeled nanoparticles have been extensively used in both preclinical and clinical studies as tools to explorethe *in vivo* pharmacokinetics, imaging capability, and theranostic potential of nanoparticles.[31,249–252] Recently, the development of a nanoparticle-based dual-modality diagnostic instrument for PET/MRI has been demonstrated,[234,240–242,252–254] and for this aim iron oxide NPs are considered as favourite platforms.

2. Design, synthesis and characterization of a mini-library of NOTA derivatives

Many novel radio-pharmaceuticals have been recently proposed in the literature to improve tumour identification and localization.[242,255] In this context, we here describe the synthesis and characterization of a mini-library of lipophilic derivatives of NOTA (1,4,7-triazacyclononane-1,4,7-triacetic acid) to be used as ^{68}Ga chelator in PET analyses.[230–232]

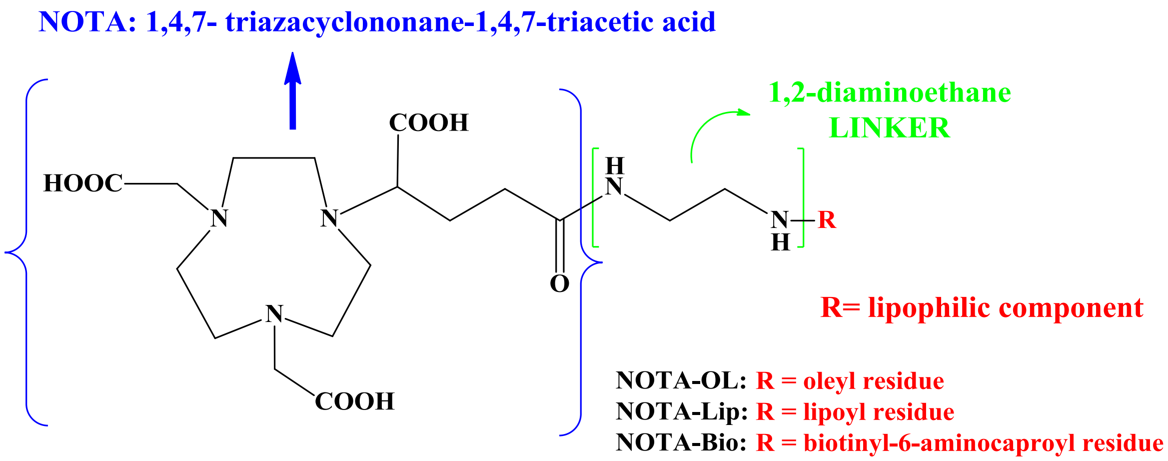

Figure 43. General design used for the preparation of NOTA derivatives.

The here described NOTA analogs (as shown in the general scheme in Figure 43) share a common design, based on a polar NOTA moiety and a flexible linker (1,2-diaminoethane), and differ for the lipophilic component, which is a residue of oleic acid, lipoic acid or a biotin moiety (NOTA-OL, NOTA-Lip and NOTA-Bio, respectively, Figure 44). The lipophilic tails inserted have been chosen for their proven biocompatibility for *in vivo* applications, and for the possibility of subsequent anchoring on differently decorated nanoparticles or nanoplatforms, to be used as PET analysis probes. In the specific case of previously described phosphocholine-decorated SPIONs, the insertion of NOTA-OL in their coating would allow performing bimodal “two-in-one” imaging investigations, *i.e.* MRI and PET analysis.[191,233,236,256,257] Oleic acid has an 18-carbon atoms chain which allows its immobilization onto lipid-functionalized NPs or liposome platforms through hydrophobic interactions. The disulfide bond of lipoic acid, thanks to its high affinity for metals, provides covalent bonds with the surface of metal or metal-oxide NPs. Finally, biotin is useful to functionalize avidin or streptavidin-coated NPs exploiting the exceptionally high affinity of these proteins for biotin. As a successive development of this work, in collaboration with specialized laboratories, we intend to label the NOTA-conjugated nanoparticles with ^{68}Ga in order to obtain the effective labelled probes and evaluate their efficiency as diagnostic agents in animal models.

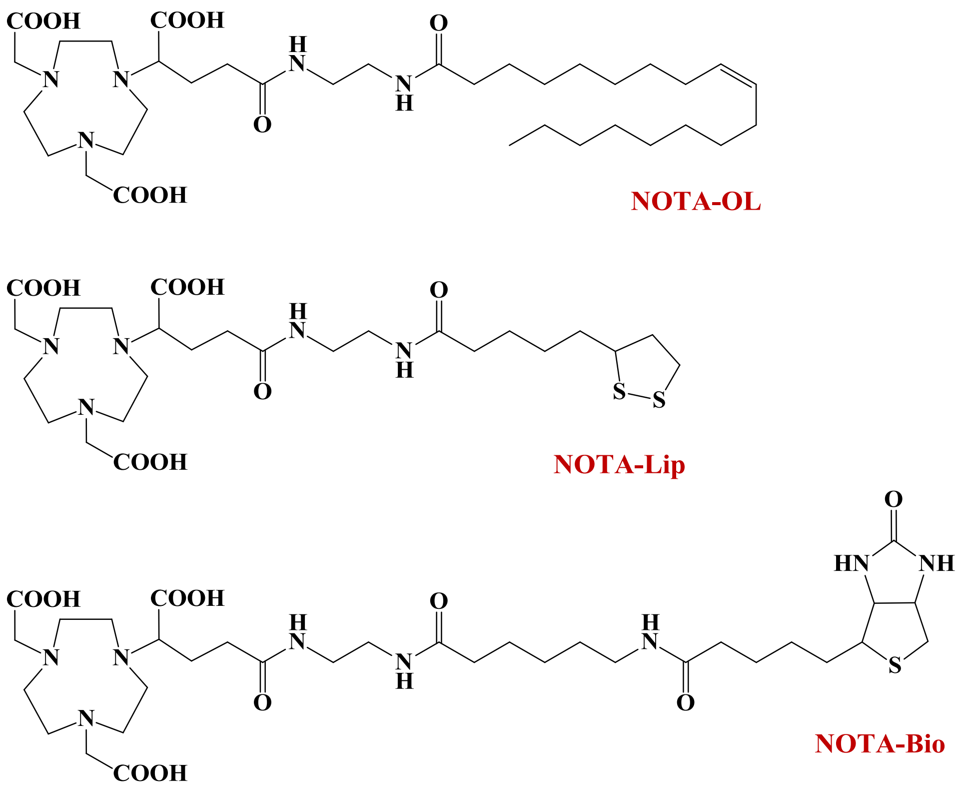

NOTA-OL

NOTA-Lip

NOTA-Bio

Figure 44. Novel NOTA derivatives here realized.

2.1. Results and discussion

2.1.1. Synthesis and characterization of lipophilic NOTA derivatives

The assembly of the three parts of the NOTA derivatives has been based on the formation of amide bonds between NH_2 and COOH groups, which can be easily obtained in high yields using standard condensing agents. Notably, these bonds are chemically stable under a wide range of conditions, and particularly in the acid conditions used in our synthetic plan for the protective groups removal.

For the preparation of all the final NOTA analogs, a similar synthetic protocol has been adopted, differing only for the kind of carboxylic acid used in the second step. In particular, the key intermediate in the preparation of the final derivatives is compound **24**, whose synthesis has been realized starting from commercially available 1,2-diaminoethane (compound **23**). The mono-protection of compound **23** was performed to simplify the successive condensation step: in fact, in all our initial attempts to directly couple **23** with a carboxylic acid (either of the lipophilic component or of the protected NOTA derivative) a very complex mixture was always obtained, with prevalence of dimeric products. For this reason, a 4-monomethoxytrityl (MMT) protective group was introduced at one end of the diamine, so to have a unique reactive amino group available at the other end and thus simplify the successive reaction and related purification. In fact, the MMT moiety presents a high molar absorption coefficient, which allows an easy UV monitoring of the new formed product during the reaction and its chromatographic purification by silica gel column.

The tritylation reaction was hence performed using 4-methoxytriphenylmethyl chloride (MMT-Cl), an excess of 1,2-diaminoethane (20 eq.) and catalytic amounts of DMAP (0.2 eq.) in dry pyridine (Scheme 7). The excess of compound **23** was necessary in order to exclusively obtain the mono-alkylated product and was then removed from the reaction mixture through a CH_2Cl_2/H_2O extraction. Then, desired compound **24** was isolated in 75 % yields *via* a chromatographic purification on a silica gel column. Successively, this was reacted with commercially available carboxylic acids (oleic, lipoic or biotinyl-6-aminocaproic acid) in the presence of DCC (3 eq.) and DMAP (2 eq.) as condensing agents. Pure compound **25**, isolated in a pure form by silica gel column chromatography, was then reacted for 1 h at r.t. with an acidic solution of TCA 2 % in CH_2Cl_2 for the MMT removal. Compound **26** was then conjugated with the macrocycle NOTA using the commercially available, *tert*-butyl protected derivative NODA-Ga(*t*Bu)$_3$ {4-[4,7-bis(2-*tert*-butoxy-2-oxoethyl)-1,4,7-triazonan-1-yl]-5-*tert*-butoxy-5-oxopentanoic acid} in the presence of the condensing system DCC/DMAP under anhydrous conditions. After chromatographic purification on a silica gel column, compound **27** was obtained in a pure form and finally treated with an acidic solution of 10 % TFA in CH_2Cl_2 in order to remove the *tert*-butyl protecting groups. After reaction completion, the solvent was removed under reduced pressure and the crude product coevaporated several times with isopropanol in order to remove acid traces. The use of strong acidic conditions causes the removal of the *tert*-butyl cation, which rearranges by β-elimination forming isobutylene, a volatile compound easily removed by repeated coevaporations with dry solvents.

The complete *tert*-butyl removal from NOTA derivatives was checked by ^1H NMR of the reaction mixture, monitoring the disappearance of the typical signal of the *tert*-butyl protons. The final compound was recovered in almost quantitative yields in all cases (95 %).

Following this synthetic scheme, the final NOTA-OL, NOTA-Lip and NOTA-Bio were obtained in 5 steps in 29, 19 and 32% overall yields, respectively. All the synthetic intermediates and the final NOTA derivatives were characterized using monodimensional (^1H, ^{13}C) and bidimensional (^1H-^1H COSY) NMR, as well as by ESI-MS data. As a representative example, the MS spectrum of NOTA-OL is shown in Figure 45.

For the subsequent immobilization onto liposomes or nanoparticles, NOTA-OL has been further purified by HPLC on C18 analytical column using a linear gradient of B (50 to 100 % in 14 min) in A solutions (Solution A: H_2O 0.1% TFA; Solution B: CH_3OH 0.1 % TFA) and UV detection at λ = 218 nm (t_R = 11.6 min).

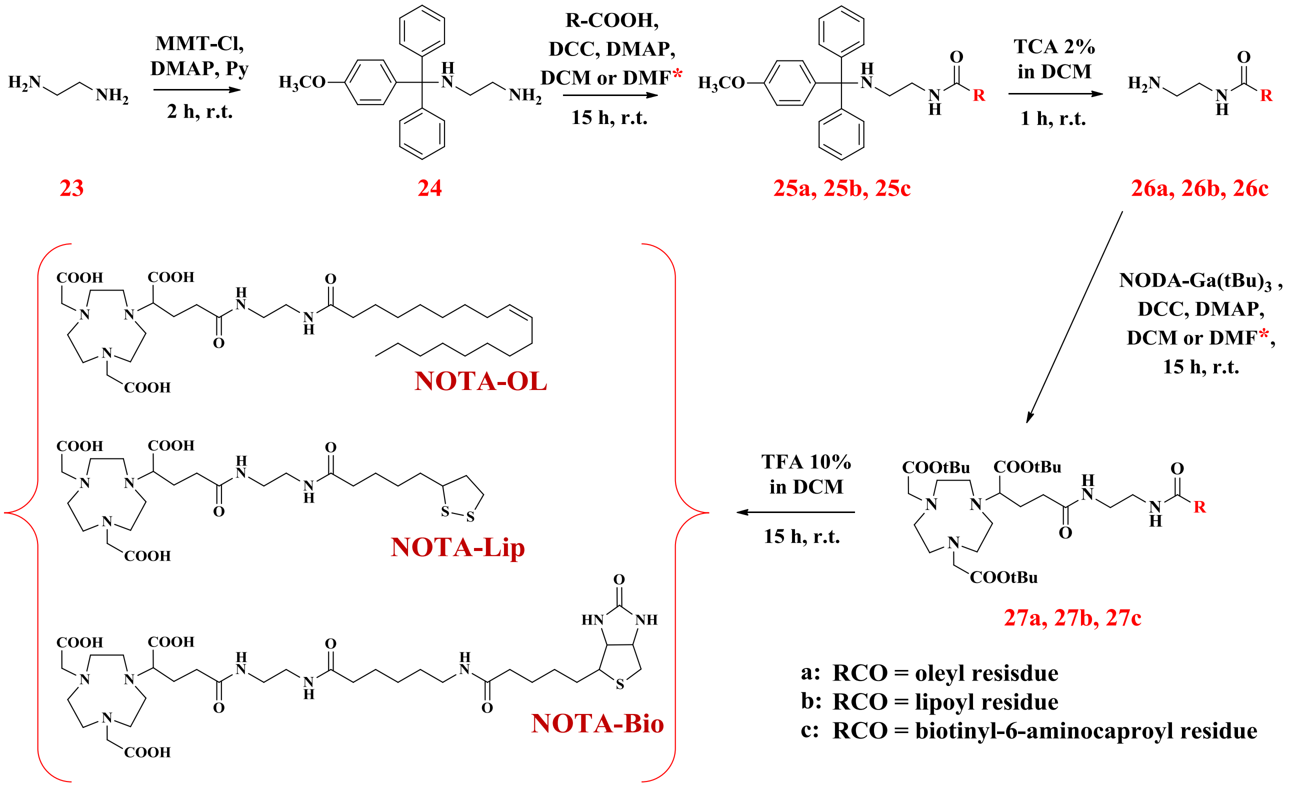

*** DCM in the case of NOTA-OL and NOTA-Lip and DMF in the case of NOTA-Bio**

Scheme 7. Synthetic procedure for the preparation of the NOTA derivatives NOTA-OL, NOTA-Lip and NOTA-Bio.

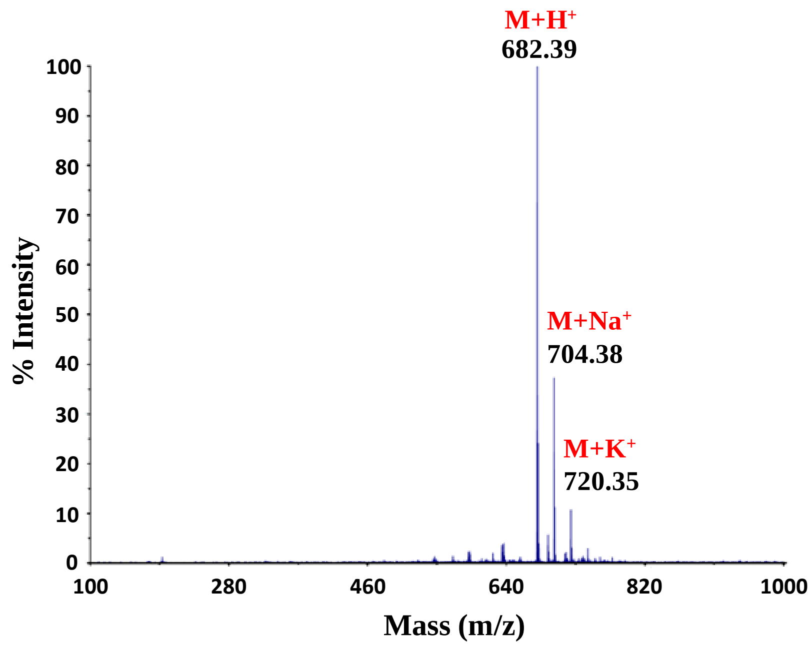

Figure 45. MALDI-TOF spectrum (positive ions) of NOTA-OL.

2.2. Experimental section

- **Materials and general methods**

All the reagents and solvents were of the highest commercially available quality and were used as received. TLC analyses were carried out on silica gel plates from Macherey-Nagel (60, F254). Reaction products on TLC plates were visualized by UV-light and then by treatment with an oxidant acidic solution (acetic acid / water / sulfuric acid, 10:4:5, v/v). For column chromatography, silica gel from Macherey-Nagel (Kieselgel 60, 0.063-0.200 mm) was used.

NMR spectra were recorded on Bruker WM-400, Varian Gemini 200 and Varian Inova 500 spectrometers, as specified. All the *chemical shifts* (δ) are expressed in ppm with respect to the residual solvent signal both for ^{1}H NMR ($CDCl_3$ = 7.26 ppm, MeOD = 3.31 ppm) and ^{13}C NMR ($CDCl_3$ = 76.9 ppm, MeOD = 49.1 ppm). All the coupling constants (J) are quoted in Hertz (Hz). Peaks assignments have been carried out based on standard ^{1}H-^{1}H COSY and HSQC experiments. The following abbreviations were used to explain the multiplicities: s = singlet; d = doublet; t = triplet; q = quartet; m = multiplet; b = broad.

In order to easily identify the proton and carbon signals of the compounds, letters and numbers were assigned to the structures. For MMT and NOTA moieties, the used letters and numbers are shown in accompanying pictures. The lipophilic components (oleyl and biotinyl-6-aminocaproyl residues) were indicated with progressive numbers (1'-18' or 1''-14'', according to the carbon chain length) starting from the carbonyl group.

MALDI-TOF mass spectrometric analyses were performed on a TOF/TOF™ 5800 System in the positive mode, using 2,5-dihydroxybenzoic acid (DHB) as the matrix. For the deposition on MALDI plate, the droplet spotting method was used: the sample - 1 µg/µL in CH_3CN/CH_3OH, 7:3 (v/v) - was first deposited on the plate followed by DHB deposition - 10 mg/mL in CH_3CN/CH_3OH, 7:3 (v/v) - and proper mixing before drying the components. The mass spectra were recorded in the range 200-1000 m/z values.

For the ESI-MS analyses, a Waters Micromass ZQ instrument – equipped with an Electrospray source – was used in the positive and/or negative mode.

HPLC chromatographic analyses and purifications were performed using an Agilent HPLC system, equipped with a UV/vis detector. A Kinetex C18 column (Phenomenex, 250 x 4.60 mm; flow rate 0.8 mL min^{-1}) and UV detection at 218 nm were used for the purification.

- **Synthesis of NOTA-OL**

Synthesis of N-1-[(4-methoxyphenyl)diphenylmethyl]ethane-1,2-diamine (24)

Commercially available 1,2-diaminoethane (1.07 mL, 16 mmol) was dissolved in 3.5 mL of dry pyridine and then MMT-Cl (248 mg, 0.80 mmol) and catalytic amounts of DMAP (19.6 mg, 0.16 mmol) were sequentially added to the reaction mixture, left under stirring at r.t.. After 2 h, TLC analysis indicated the formation of the desired product and the reaction was quenched by addition of few drops of MeOH. The reaction mixture was concentrated *in vacuo*, then the crude product was extracted with CH_2Cl_2/H_2O. The desired compound was recovered in the organic phases, which were dried upon addition of anhydrous Na_2SO_4, filtered and then concentrated under vacuum. The obtained residue was purified by chromatography on a silica gel column eluted with CH_2Cl_2/MeOH (95:5, v/v), containing 2 % of TEA (v/v), necessary to avoid even partial, undesired removal of the MMT protecting group promoted by silica. Target compound **24** was obtained in 75 % yields (200 mg, 0.60 mmol).

24: pale yellow oil. R_f = 0.6 (CH_2Cl_2/MeOH, 9:1, v/v).

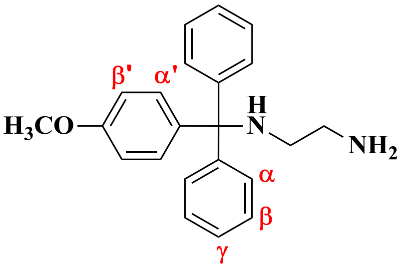

^{1}H NMR (400 MHz, $CDCl_3$): *δ* 7.48 (d, *J* = 7.7 Hz, 4H, 4x ***H***α); 7.39 (d, *J* = 8.6 Hz, 2H, 2x ***H***α'); 7.26 (t, *J* = 7.4 and 7.6 Hz, 4H, 4x ***H***β); 7.17 (d, *J* = 7.1 Hz, 2H, 2x ***H***γ); 6.80 (d, *J* = 8.6 Hz, 2H, 2x Hβ'); 3.74 (s, 3H, -OC***H*₃**); 2.78 (t, *J* =5.8 Hz, 2H, -C***H*₂**NH₂); 2.22 (t, *J* =5.8 Hz, 2H, -C***H*₂**NH MMT).

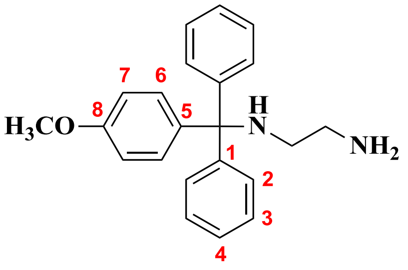

^{13}C NMR (100 MHz, $CDCl_3$): *δ* 157.6 (***C***-8); 146.1 (2x ***C***-1); 138.0 (***C***-5); 129.5 (2x ***C***-6); 128.3 (4x ***C***-2); 127.5 (4x ***C***-3); 125.9 (2x ***C***-4); 112.8 (2x ***C***-7); 69.9 (quaternary carbon of MMT); 54.8 (-O***C***H_3); 46.0 (-***C***H_2NH_2); 42.4 (-***C***H_2NH MMT).

Synthesis of N-2-[(4-methoxyphenyl)diphenylmethylamino]ethyl oleamide (25a)

Commercially available oleic acid (85 µL, 0.27 mmol) was dissolved in 3 mL of dry CH_2Cl_2 and then treated with DMAP (66.7 mg, 0.55 mmol) and DCC (169 mg, 0.82 mmol). After 1 h, compound **24** (99.7 mg, 0.30 mmol) was added to the reaction mixture, which was taken at r.t. under stirring. After 15 h, TLC analysis indicated the complete transformation of oleic acid in a more apolar compound. Thus, the reaction mixture was quenched by addition of MeOH and the solvent was removed under reduced pressure. The crude product was purified by chromatography on a silica gel column using *n*-hexane/AcOEt (8:2, v/v), containing 2 % of TEA as eluent, yielding desired compound **25a** in 59 % yields (96.7 mg, 0.16 mmol).

25a: pale yellow oil. R_f = 0.6 (*n*-hexane/AcOEt 3:2, v/v).

^{1}H NMR (400 MHz, $CDCl_3$): *δ* 7.44 (d, *J* = 7.6 Hz, 4H, 4x ***H***α); 7.35 (d, *J* = 8.6 Hz, 2H, 2x ***H***α'); 7.27 (t, *J* = 7.4 and 7.5 Hz, 4H, 4x ***H***β); 7.19 (d, *J* = 7.1 Hz, 2H, 2x ***H***γ); 6.81 (d, *J* = 8.5 Hz, 2H, 2x Hβ'); 5.98 (bs, 1H, N***H***); 5.35 (s, 2H, C***H***-9', 10'); 3.77 (s, 3H, -OC***H$_3$***); 3.35 (bd, 2H, -C***H$_2$***NH); 2.33 (bt, 2H, -C***H$_2$***NH MMT); 2.18 (t, *J* = 7.5 and 7.6 Hz, 2H, C***H$_2$***-2'); 2.01 (overlapped signals, 4H, 2x C***H$_2$***-8', 11'); 1.66-1.63 (m, 2H, C***H$_2$***-3'); 1.31-1.28 (overlapped signals, 20H, 10x C***H$_2$***-4', 5', 6', 7', 12', 13', 14', 15', 16', 17'); 0.89 (t, *J* = 6.0 and 6.8 Hz, 3H, C***H$_3$***-18').

^{13}C NMR (100 MHz, $CDCl_3$): *δ* 173.3 (***C***=O oleic); 158.0 (***C***-8); 145.6 (2x ***C***-1); 137.5 (***C***-5); 129.9 (overlapped signals, 2x ***C***H-9', 10'); 129.7 (2x ***C***-6); 128.3 (4x ***C***-2); 127.8 (4x ***C***-3); 126.4 (2x ***C***-4); 113.1 (2x ***C***-7); 70.5 (quaternary carbon of MMT); 55.1 (-O***C***H_3); 43.7 (-***C***H_2NH); 39.5 (-***C***H_2NH MMT); 36.8 (***C***H_2-2'); 31.8, 29.6, 29.4, 29.2, 29.0, 22.5 (overlapped signals, 10x ***C***H_2-, 4', 5', 6', 7', 12', 13', 14', 15', 16', 17'); 27.1 (overlapped signals, 2x ***C***H_2-8', 11'); 25.7 (***C***H_2-3'); 14.0 (***C***H_3-18').

ESI-MS (positive ions): calculated for $C_{40}H_{56}N_2O_2$, 596.43; found m/z: 597.97 [$M+H^+$]; 619.79 [$M+Na^+$]; 635.59 [$M+K^+$].

MALDI-MS (positive ions): calculated for $C_{40}H_{56}N_2O_2$, 596.43; found m/z: 347.23 [$M-MMT+Na^+$]; 363.20 [$M-MMT+K^+$].

Synthesis of N-(2-aminoethyl)oleamide (26a)

Compound **25a** (40.1 mg, 0.07 mmol) was dissolved in 2 mL of a 2 % TCA solution in CH_2Cl_2. Upon addition of TCA, the reaction mixture showed an intense yellow-orange colour, typical of the MMT cation. After 1 h, TLC analysis indicated the complete disappearance of the starting material and the appearance of a new, more polar compound. To quench the reaction, MeOH was added until disappearance of the orange colour, and then TEA until neutralization. The crude product was extracted with CH_2Cl_2/H_2O and the residue purified by chromatography on silica gel column using CH_2Cl_2/MeOH (98:2, v/v) as eluent, also containing 2 % of TEA, yielding desired compound **26a** in 98 % isolated yields (22.3 mg, 0.07 mmol).

26a: pale yellow oil. R_f = 0.5 (CH_2Cl_2/MeOH, 8:2, v/v).

^{1}H NMR (400 MHz, $CDCl_3$): *δ* 6.55 (bs, 1H, N***H***C=O oleic); 5.32 (s, 2H, C***H***-9', 10'); 3.27 (bs, 2H, -C***H$_2$***NH oleic); 3.06 (bs, 2H, N***H$_2$***); 2.90 (bt, 2H, -C***H$_2$***NH_2); 2.19 (t, *J* = 7.4 and 7.3 Hz, 2H, C***H$_2$***-2'); 1.98 (overlapped signals, 4H, 2x C***H$_2$***-8', 11'); 1.60 (m, 2H, C***H$_2$***-3'); 1.28-1.19 (overlapped signals, 20H, 10x C***H$_2$***-4', 5', 6', 7', 12', 13', 14', 15', 16', 17'); 0.86 (bt, 3H, C***H$_3$***-18').

^{13}C NMR (100 MHz, $CDCl_3$): *δ* 174.7 (***C***=O oleic); 129.5, 129.4 (overlapped signals, 2x ***C***H-9', 10'); 39.9 (-***C***H_2NH oleic); 36.7 (-***C***H_2NH_2); 36.1 (***C***H_2-2'); 31.5, 29.4, 28.9, 22.3 (overlapped signals, 10x $\boldsymbol{C}H_2$-4’, 5’, 6’, 7’, 12’, 13’, 14’, 15’, 16’, 17’); 26.9 (overlapped signals, 2x $\boldsymbol{C}H_2$-8’, 11’); 25.3 ($\boldsymbol{C}H_2$-3’); 13.8 ($\boldsymbol{C}H_3$-18’).

MALDI-MS (positive ions): calculated for $C_{20}H_{40}N_2O$, 324.31; found m/z: 347.17 [$M+Na^+$]; 363.19 [$M+K^+$].

Synthesis of (Z)-di-*tert*-butyl 2,2'-[7-(1-*tert*-butoxy-5-2-oleamidoethylamino-1,5-dioxopentan-2-yl)-1,4,7-triazonane-1,4-diyl]diacetate (27a)

Commercially available NOTA derivative {4-[4,7-bis(2-*tert*-butoxy-2-oxoethyl)-1,4,7-triazonan-1-yl]-5-*tert*-butoxy-5-oxopentanoic acid} – here indicated as NOTA-(COO*t*Bu)$_3$ - (42 mg, 0.08 mmol) was dissolved in 3 mL of dry CH_2Cl_2; then DMAP (18.5 mg, 0.15 mmol) and DCC (47 mg, 0.23 mmol) were added to the resulting solution. The reaction mixture was left under stirring and argon flow at r.t. for ca. 1 h. After complete activation of the carboxylic group of NOTA, compound **26a** was added in slight stoichiometric excess (31.2 mg, 0.10 mmol). After 15 h the reaction, monitored *via* TLC, indicated the complete disappearance of both starting products and the appearance of a new product. The reaction was quenched by addition of MeOH; the solvent was removed under reduced pressure and the crude product was purified by chromatographic column eluting with $CHCl_3$/MeOH (95:5, v/v). This purification procedure was not satisfactory to completely remove all the impurities and therefore a second chromatographic purification, using a column eluted with AcOEt/MeOH (95:5, v/v), was carried out, affording pure compound **27a** with 68% isolated yields (46.3 mg, 0.05 mmol).

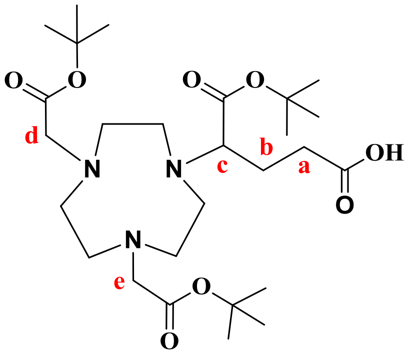

NOTA-(COO*t*Bu)$_3$: ^{1}H NMR (400 MHz, $CDCl_3$): δ 3.41 (overlapped signals, 4H, $C\boldsymbol{H_2}$-d and $C\boldsymbol{H_2}$-e); 3.34 (m, 1H, $C\boldsymbol{H}$-c); 3.05-2.91 (overlapped signals, 12H, -N$C\boldsymbol{H_2}C\boldsymbol{H_2}$N- of macrocycle); 2.51 (m, 2H, $C\boldsymbol{H_2}$-a); 1.96 (m, 2H, $C\boldsymbol{H_2}$-b); 1.44 (s, 27H, $C\boldsymbol{H_3}$ of -*t*Bu).

^{13}C NMR (100 MHz, $CDCl_3$): δ 176.2 ($\boldsymbol{C}$OOH); 171.0, 170.7 (overlapped signals, 3x $\boldsymbol{C}$OO*t*Bu); 81.6, 81.1 (overlapped signals, 3x quaternary carbons of *t*Bu); 68.3 ($\boldsymbol{C}$H-c); 58.5 (overlapped signals, $\boldsymbol{C}H_2$-d and $\boldsymbol{C}H_2$-e); 54.9, 54.3, 52.3 (overlapped signals, -N$\boldsymbol{C}H_2\boldsymbol{C}H_2$N- of the macrocycle); 33.6 ($\boldsymbol{C}H_2$-a); 28.1 ($\boldsymbol{C}H_3$ of -*t*Bu); 24.9 ($\boldsymbol{C}H_2$-b).

27a: yellow oil. R_f = 0.9 (CH_2Cl_2/MeOH, 8:2, v/v).

^{1}H NMR (400 MHz, $CDCl_3$): δ 6.48 (s, 1H, N$\boldsymbol{H}$); 5.33 (s, 2H, $C\boldsymbol{H}$-9’, 10’); 3.75 (m, 2H, -$C\boldsymbol{H_2}$NH oleic); 3.65 (overlapped signals, 4H, $C\boldsymbol{H_2}$-d and $C\boldsymbol{H_2}$-e); 3.38 (overlapped signals, 3H, $C\boldsymbol{H}$-c, -$C\boldsymbol{H_2}$NH oleic); 3.23-2.80 (overlapped signals, 14H, -N$C\boldsymbol{H_2}C\boldsymbol{H_2}$N- of the macrocycle, $C\boldsymbol{H_2}$NH);

2.38 (m, 2H, C***H$_2$***-a); 2.20 (bt, 2H, C***H$_2$***-2'); 1.99 (overlapped signals, 6H, 2x C***H$_2$***-8', 11', C***H$_2$***-b); 1.59 (m, 2H, C***H$_2$***-3'); 1.47 (s, 27H, C***H$_3$*** of -*t*Bu); 1.28-1.26 (overlapped signals, 20H, 10x C***H$_2$***-4', 5', 6', 7', 12', 13', 14', 15', 16', 17'); 0.87 (bt, 3H, C***H$_3$***-18').

^{13}C NMR (100 MHz, $CDCl_3$): δ 174.6 (overlapped signals, ***C***=O NOTA, ***C***=O oleamide); 172.8 (overlapped signals, 3x ***C***OO*t*Bu); 129.8, 129.7 (2x ***C***H-9', 10'); 82.8 (overlapped signals, 3x quaternary carbons of *t*Bu); 63.8 (***C***H-c); 55.9 (overlapped signals, ***C***H_2-d and ***C***H_2-e); 54.3, 53.9, 51.7 (overlapped signals, -N***C***H_2***C***H_2N- of the macrocycle); 39.9 (-***C***H_2NH oleamide); 39.5 (-***C***H_2NH NOTA); 36.4 (***C***H_2-2'); 32.7 (***C***H_2-a); 31.8, 29.7, 29.5, 29.2, 29.1, 22.6 (overlapped signals, 10x ***C***H_2-4', 5', 6', 7', 12', 13', 14', 15', 16', 17'); 27.9 (***C***H_3 of -*t*Bu); 27.1 (overlapped signals, 2x ***C***H_2-8', 11'); 25.6 (***C***H_2-b); 25.3 (***C***H_2-3'); 14.0 (***C***H_3-18').

ESI-MS (positive ions): calculated for $C_{47}H_{87}N_5O_8$, 849.66; found m/z: 850.59 [M+H$^+$]; 883.55 [M+Na$^+$].

Synthesis of NOTA-OL

Compound **27a** (20.1 mg, 0.02 mmol) was dissolved in dry CH_2Cl_2 (1 mL) and then 1 mL of a 10 % TFA solution in $CHCl_3$ was added. The reaction mixture was left under stirring at r. t. and checked by TLC until the disappearance of the starting compound. After 15 h, the crude reaction was concentrated *in vacuo* to remove the solvent. Subsequently, in order to remove even traces of trifluoroacetic acid, the resulting product was coevaporated three times with dry *n*-isopropanol and then taken several hours at the oil pump. In this way, without further purification steps, the final product NOTA-OL was recovered in a pure form with 95% yields (13.1 mg, 0.02 mmol).

NOTA-OL: oil. R_f = 0 (CH_2Cl_2/MeOH, 8:2, v/v).

^{1}H NMR (400 MHz, $CDCl_3$): δ 5.33 (s, 2H, C***H***-9', 10'); 4.01-3.36 (overlapped signals, 5H, C***H$_2$***-d, C***H$_2$***-e, C***H***-c,); 2.97 (overlapped signals, 4H, -C***H$_2$***NH oleamide, -C***H$_2$***NH NOTA); 2.85 (overlapped signals, 14H, -NC***H$_2$***C***H$_2$***N- of the macrocycle, C***H$_2$***-2'); 2.40 (m, 2H, C***H$_2$***-a); 2.01-1.83 (overlapped signals, 6H, 2x C***H$_2$***-8', 11', C***H$_2$***-b); 1.56 (m, 2H, C***H$_2$***-3'); 1.25-1.23 (overlapped signals, 20H, 10 x C***H$_2$***-4', 5', 6', 7', 12', 13', 14', 15', 16', 17'); 0.87 (bt, 3H, C***H$_3$***-18').

^{13}C NMR (100 MHz, $CDCl_3$): δ 175.3 (3x ***C***OOH); 172.0 (***C***=O NOTA); 171.4 (***C***=O oleic); 129.9, 128.2 (overlapped signals, 2x ***C***H-9', 10'); 65.6 (***C***H-c); 56.3 (overlapped signals, ***C***H_2-d and ***C***H_2-e); 53.8, 52.2, 49.4 (overlapped signals, -N***C***H_2***C***H_2N- of the macrocycle); 39.2 (-***C***H_2NH oleamide); 38.5 (***C***H_2-2'); 36.5 (-***C***H_2NH NOTA); 34.6 (***C***H_2-a); 31.8, 29.7, 29.6, 29.4, 29.2, 22.6 (overlapped signals, 10x ***C***H_2-4', 5', 6', 7', 12', 13', 14', 15', 16', 17'); 27.1 (overlapped signals, 2x ***C***H_2-8', 11'); 26.6 (***C***H_2-3'); 24.5 (***C***H_2-b); 14.0 (***C***H_3-18').

MALDI-MS (positive ions): calculated for $C_{35}H_{63}N_5O_8$, 681.47; found *m/z*: 682.39 [M+H$^+$]; 704.38 [M+Na$^+$]; 720.35 [M+K$^+$].

- **Synthesis of NOTA-Lip**

Synthesis of 5-{1,2-dithiolan-3-yl-N-2-[(4-methoxyphenyl) diphenylmethylaminoethyl]} pentanamide (25b)

Commercially available lipoic acid (101 mg, 0.49 mmol) was dissolved in 4.5 mL of dry CH_2Cl_2 and then treated with DMAP (120 mg, 0.98 mmol) and DCC (305 mg, 1.48 mmol). After 1 h compound **24** was added to the reaction mixture in a little stoichiometric excess (179.2 mg, 0.54 mmol). After stirring for 15 h at r. t. TLC analysis indicated the complete transformation of oleic acid into a more apolar product. Thus, the reaction mixture was stopped adding MeOH and the solvent was removed under reduced pressure. The crude product was purified by chromatography on a silica gel column using *n*-hexane/AcOEt (6:4, v/v) as eluent, containing 2 % of TEA, affording desired compound **25b** in 80 % yields (204 mg, 0.40 mmol)

25b: yellow oil. R_f = 0.7 (CH_2Cl_2/MeOH, 95:5, v/v).

^{1}H NMR (400 MHz, $CDCl_3$): δ 7.52 (d, J = 7.6 Hz, 4H, 4x ***H***α); 7.42 (d, J = 8.5 Hz, 2H, 2x ***H***α’); 7.35 (t, J = 7.3 and 7.4 Hz, 4H, 4x ***H***β); 7.27 (d, J = 7.1 Hz, 2H, 2x ***H***γ); 6.89 (d, J = 8.5 Hz, 2H, 2x Hβ’); 5.91 (bs, 1H, NH); 3.85 (s, 3H, -OC***H***$_3$); 3.62 (m, 1H, C***H***-S); 3.43 (q, 2H, -C***H***$_2$NH lipoic); 3.41-3.19 (m, 2H, C***H***$_2$-S); 2.55-2.49 (m, 1H, C***H***$_2$a-CH$_2$-S); 2.39 (t, J = 5.7 and 5.6 Hz, 2H, -C***H***$_2$NH MMT); 2.28 (t, J = 7.1 and 7.2 Hz, 2H, -C***H***$_2$-C=O lipoic); 2.01-1.93 (m, 1H, C***H***$_2$b-CH$_2$-S); 1.81-1.53 (m, 6H, 3x C***H***$_2$ lipoic).

^{13}C NMR (100 MHz, $CDCl_3$): δ 172.6 (**C**=O lipoic); 157.8 (***C***-8); 145.8 (2x ***C***-1); 137.7 (***C***-5); 129.6 (2x ***C***-6); 128.3 (4x ***C***-2); 127.8 (4x ***C***-3); 126.3 (2x ***C***-4); 113.0 (2x ***C***-7); 70.1 (quaternary carbon of MMT); 56.3 (**C**H-S); 55.0 (-O***C***H$_3$); 43.3 (-***C***H$_2$NH lipoic); 40.1 (***C***H$_2$-S); 39.9 (-***C***H$_2$NH MMT); 38.3 (***C***H$_2$-C=O lipoic); 36.5, 34.5, 28.7, 25.3 (overlapped signals, 4 aliphatic carbons of lipoic).

ESI-MS (positive ions): calculated for $C_{30}H_{36}N_2O_2S_2$, 520.22; found m/z: 543.75 [M+Na$^+$].

MALDI-MS (positive ions): calculated for $C_{30}H_{36}N_2O_2S_2$, 520.22; found *m/z*: 271.60 [M-MMT+Na$^+$]; 287.08 [M-MMT+K$^+$].

Synthesis of N-2-aminoethyl-5-(1,2-dithiolan-3-yl)pentanamide (26b)

Compound **25b** (200 mg, 0.38 mmol) was dissolved in 3 mL of a 2 % TCA solution in CH_2Cl_2. Upon addition of TCA, the reaction mixture showed an intense yellow-orange coloration, typical of the MMT cation. After 1 h, TLC analysis indicated the complete disappearance of the starting material and the appearance of a new, more polar compound. To quench the reaction, MeOH was added until disappearance of the orange colour, followed by TEA until neutralization. The crude product was extracted with CH_2Cl_2/H_2O, recovering the desired compound in the aqueous phases. Then the solvent was removed under vacuum and the residue purified by chromatography on a silica gel column using CH_2Cl_2/MeOH (9:1, v/v) as eluent containing 2 % of TEA, giving desired compound **26b** in 58 % isolated yields (53.8 mg, 0.22 mmol).

26b: yellow oil. R_f = 0.4 (CH_2Cl_2/MeOH, 8:2, v/v).

^{1}H NMR (400 MHz, $CDCl_3$): δ 5.93 (bs, 1H, NH); 3.57 (m, 1H, C***H***-S); 3.30 (m, 2H, -C***H₂***NH lipoic); 3.20-3.08 (m, 2H, C***H₂***-S); 2.83 (t, *J* = 5.9 and 5.8 Hz, 2H, -C***H₂***NH_2); 2.50-2.42 (m, 1H, C***H₂***a-CH_2-S); 2.20 (t, *J* = 7.2 and 7.5 Hz, 2H, -C***H₂***-C=O lipoic); 1.97-1.86 (m, 1H, C***H₂***b-CH_2-S); 1.77-1.41 (m, 6H, 3x C***H₂*** lipoic).

^{13}C NMR (100 MHz, $CDCl_3$): δ 172.8 (**C**=O lipoic); 56.3 (***C***H-S); 41.8 (-***C***H_2NH lipoic); 41.2 (***C***H_2-S); 40.1 (-***C***H_2NH MMT); 38.4 (***C***H_2-C=O lipoic); 36.4, 34.5, 28.7, 25.3 (overlapped signals, 4 aliphatic carbons of lipoic).

ESI-MS (positive ions): calculated for $C_{10}H_{20}N_2OS_2$, 248.10; found m/z: 249.24 $[M+H^+]$; 272.16 $[M+Na^+]$.

Synthesis of di-*tert*-butyl 2,2'-7-5-{2-[5-(1,2-dithiolan-3-yl)pentanamido ethylamino]-1-*tert*-butoxy-1,5-dioxopentan-2-yl}-1,4,7-triazonane-1,4-diyl diacetate (27b)

Commercially available NOTA derivative NODA-Ga(tBu)$_3$ (40.1 mg, 0.07 mmol) was dissolved in 3 mL of dry CH_2Cl_2; then DMAP (17.8 mg, 0.15 mmol) and DCC (45.0 mg, 0.22 mmol) were added to the resulting solution. The reaction mixture was left under stirring and argon flow at r. t. for ca. 1 h. After complete activation of the carboxylic group of NOTA, compound **26b** was added to the reaction mixture in slight stoichiometric excess (20.9 mg, 0.08 mmol). After 15 h the reaction, monitored *via* TLC, indicated the complete disappearance of both starting products and the appearance of a new product. So the reaction was quenched by addition of MeOH; the solvent was removed under reduced pressure and the crude product purified by chromatographic column eluting with $CHCl_3$/MeOH (98:2, v/v), affording pure compound **27b** with 58% isolated yields (31.4 mg, 0.04 mmol).

27b: oil. R_f = 0.8 ($CHCl_3$/MeOH, 8:2, v/v).

^{1}H NMR (400 MHz, $CDCl_3$): δ 3.65 (m, 1H, C***H***-S); 3.35-321 (overlapped signals, 9H, -C***H₂***NH lipoic, C***H***-c, C***H₂***-d, C***H₂***-e, C***H₂***-S); 3.04 (overlapped signals, 12H, -NC***H₂***C***H₂***N- of the macrocycle); 2.91-2.74 (overlapped signals, 4H, C***H₂***-a, -C***H₂***NH NOTA); 2.57 (m, 1H, C***H₂***a-CH_2-

S); 1.73-1.13 (overlapped signals, 11H, -C***H*₂**-C=O lipoic, C***H*₂**-b, C***H*₂**b-CH$_2$-S, 3x C***H*₂** lipoic); 1,44 (s, 27H, C***H*₃** of -*t*Bu).

^{13}C NMR (100 MHz, CDCl$_3$): *δ* 172.7 (overlapped signals, ***C***=O NOTA, **C**=O lipoic); 171.1 (overlapped signals, 3x ***C***OO*t*Bu); 80.9 (overlapped signals, 3x quaternary carbons of *t*Bu); 66.4 (***C***H-c); 59.0 (overlapped signals, ***C***H$_2$-d and ***C***H$_2$-e, ***C***H-S); 55.3, 49.9 (overlapped signals, -N***C***H$_2$***C***H$_2$N- of the macrocycle); 41.6 (overlapped signals, -***C***H$_2$NH lipoic, ***C***H$_2$-S); 39.2 (overlapped signals, -***C***H$_2$NH NOTA, ***C***H$_2$-C=O lipoic); 32.5, 30.7, 26.2, 25.5 (overlapped signals, 4 aliphatic carbons of lipoic, ***C***H$_2$-a); 28.1 (***C***H$_3$ of -*t*Bu); 24.8 (***C***H$_2$-b).

MALDI-MS (positive ions): calculated for $C_{37}H_{67}N_5O_8S_2$, 773.44; found *m/z*: 774.41 [M+H$^+$]; 796.39 [M+Na$^+$].

Synthesis of NOTA-LIP

Compound **27b** (18.0 mg, 0.02 mmol) was dissolved in 1 mL of dry CH_2Cl_2 and then 1 mL of a 10 % TFA solution in CH_2Cl_2 was added. The reaction mixture was left under stirring at r. t. and checked by TLC until disappearance of the starting compound. After 15 h, the crude product was concentrated *in vacuo* and then coevaporated three times with dry *n*-isopropanol and successively taken at the oil pump for several hours. Without further purification steps, the final product NOTA-Lip was recovered in a pure form with 95% yields (11.5 mg, 0.02 mmol).

NOTA-LIP: oil. R_f = 0 (CH_2Cl_2/MeOH, 8:2, v/v).

^{1}H NMR (400 MHz, CDCl$_3$): *δ* 3.74-3.36 (overlapped signals, 10H, C***H***-S, -C***H*₂**NH lipoic, C***H***-c, C***H*₂**-d, C***H*₂**-e, C***H*₂**-S); 3.07 (overlapped signals, 12H, -NC***H*₂**C***H*₂**N- of the macrocycle); 2.70-2.63 (overlapped signals, 4H, C***H*₂**-a, -C***H*₂**NH NOTA); 2.33-2.16 (overlapped signals, 12H, C***H*₂**a-CH$_2$-S, -C***H*₂**-C=O lipoic, C***H*₂**-b, C***H*₂**b-CH$_2$-S, 3x C***H*₂** lipoic).

^{13}C NMR (100 MHz, CDCl$_3$): *δ* 174.0 (3x ***C***OOH); 172.7 (overlapped signals, ***C***=O NOTA, **C**=O lipoic); 66.4 (***C***H-c); 59.0 (overlapped signals, ***C***H$_2$-d and ***C***H$_2$-e, ***C***H-S); 55.3, 49.9 (overlapped signals, -N***C***H$_2$***C***H$_2$N- of the macrocycle); 40.7 (overlapped signals, -***C***H$_2$NH lipoic, ***C***H$_2$-S); 33.7 (overlapped signals, -***C***H$_2$NH NOTA, ***C***H$_2$-C=O lipoic); 27.4, 27.0, 26.5 (overlapped signals, 4 aliphatic carbons of lipoic, ***C***H$_2$-a); 24.8 (***C***H$_2$-b).

ESI-MS (positive ions): calculated $C_{25}H_{43}N_5O_8S_2$, 605.26; found *m/z*: 606.67 [M+H$^+$].

- **Synthesis of NOTA-Bio**

Synthesis of N-{2-(4-methoxyphenyldiphenylmethylamino)ethyl-6-[5-(2-oxo-hexahydro-1H-thieno[3,4-d]imidazol-4-yl]pentanamido}hexanamide (25c)

Commercially available biotinyl-6-aminocaproic acid (43.4 mg, 0.12 mmol) was dissolved in 6 mL of dry DMF and then DMAP (29.7 mg, 0.24 mmol) and DCC (75.1 mg, 0.36 mmol) were added. After 1 h compound **24** was added to the reaction mixture in a little stoichiometric excess (43.2 mg, 0.13 mmol). After stirring for 15 h at r. t. TLC analysis indicated the complete transformation of the starting biotinyl-6-aminocaproic acid into a more apolar product. Thus, the reaction mixture was quenched by addition of MeOH and the solvent was removed under reduced pressure. The crude product was purified by chromatography on a silica gel column using CH_2Cl_2/MeOH (95:5, v/v) as eluent, containing 2 % of TEA, giving desired compound **25c** in 83 % yields (69.8 mg, 0.10 mmol).

25c: pale yellow oil. $R_f = 0.4$ (CH_2Cl_2/MeOH, 95:5, v/v).

^{1}H NMR (400 MHz, $CDCl_3$): δ 7.35 (d, J = 7.6 Hz, 4H, 4x ***H***α); 7.25 (d, J = 8.7 Hz, 2H, 2x ***H***α’); 7.19 (t, J = 7.4 Hz, 4H, 4x ***H***β); 7.08 (d, J = 7.1 Hz, 2H, 2x ***H***γ); 6.71 (d, J = 8.7 Hz, 2H, 2x Hβ’); 6.60 (bs, 1H, N***H***C=O); 6.54 (s, N***H***C=ONH); 5.63 (s, 1H, NHC=ON***H***); 4.36 (m, 1H, C***H***-13’’); 4.21 (bt, 1H, C***H***-12’’); 3.68 (s, 3H, -OC***H₃***); 3.36 (m, 1H, C***H***-11’’); 3.23 (q, 2H, C***H₂***-6’’); 2.91 (bt, 2H, -C***H₂***NH biotin); 2.75-2.65 (m, 2H, C***H₂***-14’’); 2.18 (bt, 2H, -C***H₂***NH MMT); 2.13-2.10 (overlapped signals, 4H, C***H₂***-2’’, 7’’); 1.64-1.21 (m, 12H, 6x C***H₂***-3’’, 4’’, 5’’, 8’’, 9’’, 10’’).

^{13}C NMR (100 MHz, $CDCl_3$): δ 173.4 (overlapped signals, NH**C**=O, **C**=O biotin); 163.7 (NH***C***=ONH); 157.7 (***C***-8); 145.9 (2x ***C***-1); 137.8 (***C***-5); 129.5 (2x ***C***-6); 128.2 (4x ***C***-2); 127.6 (4x ***C***-3); 126.0 (2x ***C***-4); 112.9 (2x ***C***-7); 70.0 (quaternary carbon of MMT); 61.6 (***C***H-12’’); 59.9 (***C***H-13’’); 55.4 (***C***H-11’’); 54.9 (-O***C***H₃); 43.3 (-***C***H₂NH biotin); 40.2 (-***C***H₂NH MMT); 39.8 (***C***H₂-14’’); 38.9 (***C***H₂-6’’); 36.1 (***C***H₂-2’’); 35.5 (***C***H₂-7’’); 28.7 (***C***H₂-5’’); 27.7, 26.1, 26.0, 25.4, 25.0 (overlapped signals, 5x ***C***H₂-3’’, 4’’, 6’’, 9’’, 10’’).

MALDI-MS (positive ions): calculated for $C_{38}H_{49}N_5O_4S$, 671.35; found *m/z*: 670.36 [$M+H^+$]; 694.36 [$M+Na^+$]; 400.25 [$M-MMT+H^+$]; 422.24 [$M-MMT+Na^+$]; 438.20 [$M-MMT+K^+$].

Synthesis of N-(2-aminoethyl)-6-{5-(2-oxo-hexahydro-1H-thieno[3,4-d]imidazol-4-yl) pentanamido}hexanamide (26c)

Compound **25c** (85.0 mg, 0.13 mmol) was dissolved in 4 mL of a 2 % TCA solution in CH_2Cl_2. Upon addition of TCA, the reaction mixture showed an intense yellow-orange coloration, typical of the MMT cation. After 1 h, TLC analysis indicated the complete disappearance of the starting material and the appearance of a new, more polar compound. To quench the reaction, MeOH was added until disappearance of the orange colour, followed by TEA until neutralization. The crude product was extracted with CH_2Cl_2/H_2O, recovering the desired compound in the aqueous phases. Then, in order to recover the desired compound in a pure form, another extraction was performed using MeOH/H_2O providing compound **26c** in the organic solvent in 77 % isolated yields (40.1 mg, 0.10 mmol).

26c: pale yellow oil. R_f = 0.3 ($CHCl_3$/MeOH, 7:3, v/v).

^{1}H NMR (400 MHz, MeOD): δ 4.43 (m, 1H, C***H***-13''); 4.33 (bt, 1H, C***H***-14''); 3.29 (bt, *J* = 5.6 and 5.5 Hz, 2H, -C***H₂***NH₂); 3.14 (m, 1H, C***H***-11''); 3.07 (q, 2H, C***H₂***-6''); 2.78 (bt, *J* = 5.7 and 5.5 Hz, 2H, -C***H₂***NH biotin); 2.75-2.55 (m, 2H, C***H₂***-14''); 2.11-2.02 (overlapped signals, 4H, C***H₂***-2'', 7''); 1.53-1.25 (m, 12H, 6x C***H₂***-3'', 4'', 5'', 8'', 9'', 10'').

^{13}C NMR (100 MHz, MeOD): δ 177.4 (**C**=O biotin); 176.0 (NH**C**=O); 166.2 (NH***C***=ONH); 63.4 (***C***H-12''); 61.7 (***C***H-13''); 57.0 (***C***H-11''); 41.1 (-***C***H₂NH₂); 40.9 (-***C***H₂NH biotin); 40.2 (***C***H₂-14''); 38.3 (***C***H₂-6''); 36.8 (***C***H₂-2''); 30.2 (***C***H₂-7''); 29.7 (***C***H₂-5''); 29.5, 27.6, 26.9, 26.3 (overlapped signals, 5x ***C***H₂-3'', 4'', 8'', 9'', 10'').

MALDI-MS (positive ions): calculated for $C_{18}H_{33}N_5O_3S$, 399.23; found *m/z*: 400.25 [M+H$^+$]; 422.23 [M+Na$^+$]; 438.20 [M+K$^+$].

Synthesis of di-*tert*-butyl 2,2'-{7-[2,2-dimethyl-4,8,13,20-tetraoxo-24-(2-oxo-hexahydro-1H-thieno[3,4-d]imidazol-4-yl)-3-oxa-9,12,19-triazatetracosan-5-yl]-1,4,7-triazonane-1,4-diyl}diacetate (27c)

Commercially available NOTA derivative NODA-Ga(*t*Bu)₃ (39.0 mg, 0.07 mmol) was dissolved in 3 mL of dry DMF; then DMAP (17.1 mg, 0.14 mmol) and DCC (43.3 mg, 0.21 mmol) were added to the resulting solution. The reaction mixture was left under stirring and argon flow at r. t. for ca. 1 h. After activation of the carboxylic group of NOTA, compound **26c** was added in slight stoichiometric excess (32.0 mg, 0.08 mmol) dissolved in 5 mL of dry DMF. After 15 h the reaction, monitored *via* TLC, indicated the complete disappearance of both starting products and the appearance of a new product. So the reaction was quenched by addition of MeOH; the solvent was removed under reduced pressure and the crude product was purified by chromatographic column eluting with $CHCl_3$/MeOH (95:5, v/v), affording pure compound **27c** with 71 % isolated yields (46.3 mg, 0.05 mmol).

27c: yellow oil. R_f = 0.6 ($CHCl_3$/MeOH, 8:2, v/v).

^{1}H NMR (400 MHz, MeOD): δ 4.43 (m, 1H, C***H***-13''); 4.33 (bt, 1H, C***H***-12''); 3.92-3.89 (overlapped signals, 7H, -C***H₂***NH NOTA, C***H₂***-d, C***H₂***-e, C***H***-c); 3.54-3.46 (overlapped signals, 15H, -NC***H₂***C***H₂***N- of macrocycle, C***H***-11'', C***H₂***-6''); 2.96-2.76 (overlapped signals, 4H, -

C***H***$_2$NH-biotin, C***H***$_2$-14''); 2.43-1.96 (overlapped signals, 8H, C***H***$_2$-a, C***H***$_2$-b, C***H***$_2$-2'', C***H***$_2$-7''); 1,43 (s, 27H, C***H***$_3$ of -*t*Bu); 1.46-1.27 (m, 12H, 6x C***H***$_2$-3'', 4'', 5'', 8'', 9'', 10'').

^{13}C NMR (100 MHz, MeOD): δ 171.6 (overlapped signals, **C**=O biotin, NH**C**=O, **C**=O NOTA); 171.1 (overlapped signals, 3x ***C***OO*t*Bu); 164.6 (NH***C***=ONH); 81.6, 81.1 (overlapped signals, 3x quaternary carbons of *t*Bu); 63.5 (overlapped signlas, ***C***H-c, ***C***H-12'', ***C***H-13''); 57.0 (***C***H-11''); 55.7 (overlapped signals, ***C***H$_2$-d and ***C***H$_2$-e); 55.6, 49.9, 46.6, 45.7 (overlapped signals, -N***C***H$_2$***C***H$_2$N- of the macrocycle); 41.1 (-***C***H$_2$NH biotin); 40.9 (-***C***H$_2$NH NOTA); 40.2 (***C***H$_2$-14''); 38.3 (***C***H$_2$-6''); 36.8 (***C***H$_2$-2''); 32.4 (***C***H$_2$-a); 32.3 (***C***H$_2$-7''); 31.7 (***C***H$_2$-5''); 30.8, 29.6, 28.0, 27.9 (overlapped signals, 5x ***C***H$_2$-3'', 4'', 8'', 9'', 10''), 28.1 (***C***H$_3$ of -*t*Bu); 25.2 (***C***H$_2$-b).

MALDI-MS (positive ions): calculated for $C_{45}H_{80}N_8O_{10}S$, 924.57; found *m/z*: 925.85 [M+H$^+$].

Synthesis of NOTA-Bio

Compound **27c** (12.1 mg, 0.01 mmol) was dissolved in 2 mL of CH_2Cl_2 dry and then 1 mL of a 10 % TFA solution in CH_2Cl_2 was added. The reaction mixture was left under stirring at r. t. and was checked by TLC until the disappearance of the starting compound. After 15 h, the crude reaction was concentrated *in vacuo* to get rid of the solvent. Subsequently, in order to remove even traces of trifluoroacetic acid, the crude product was coevaporated three times with dry *n*-isopropanol and then taken at the oil pump for several hours. In this way, without further purification steps, NOTA-Bio was recovered with 95% yields (7.20 mg, 9.5 µmol).

NOTA-Bio: oil. $R_f = 0$ (CH_2Cl_2/MeOH, 8:2, v/v).

^{1}H NMR (400 MHz, MeOD): δ 4.43 (m, 1H, C***H***-13''); 4.33 (bt, 1H, C***H***-12''); 3.93-3.76 (overlapped signals, 7H, -C***H***$_2$NH NOTA, C***H***$_2$-d, C***H***$_2$-e, C***H***-c); 3.63-3.46 (overlapped signals, 15H, -NC***H***$_2$C***H***$_2$N- of macrocycle, C***H***-11'', C***H***$_2$-6''); 2.92-2.84 (overlapped signals, 4H, -C***H***$_2$NH biotin, C***H***$_2$-14''); 2.25-1.96 (overlapped signals, 8H, C***H***$_2$-a, C***H***$_2$-b, C***H***$_2$-2'', C***H***$_2$-7''); 1.52-1.21 (m, 12H, 6x C***H***$_2$-3'', 4'', 5'', 8'', 9'', 10'').

^{13}C NMR (100 MHz, MeOD): δ 175.5 (3x ***C***OOH); 172.5 (overlapped signals, **C**=O biotin, NH**C**=O, **C**=O NOTA); 164.6 (NH***C***=ONH); 64.6 (overlapped signals, ***C***H-c, ***C***H-12'', ***C***H-13''); 55.6 (overlapped signals, ***C***H$_2$-d and ***C***H$_2$-e); 57.0 (***C***H-11''); 56.3, 49.9, 46.6, 45.7 (overlapped signals, -N***C***H$_2$***C***H$_2$N- of the macrocycle); 41.1 (-***C***H$_2$NH biotin); 40.9 (-***C***H$_2$NH NOTA); 40.2 (***C***H$_2$-14''); 38.3 (***C***H$_2$-6''); 36.8 (***C***H$_2$-2''); 33.7 (***C***H$_2$-a); 33.0 (***C***H$_2$-7''); 32.5 (***C***H$_2$-5''); 32.1, 29.6, 27.5, 27.0 (overlapped signals, 5x ***C***H$_2$-3'', 4'', 8'', 9'', 10''), 26.5 (***C***H$_2$-b).

MALDI-MS (positive ions): calculated for $C_{33}H_{56}N_8O_{10}S$, 756.38; found *m/z*: 757.65 [M+H$^+$].

Chapter 4

Aptamers as targeting ligands

1. G-quadruplex-based aptamers: introduction

Nucleic acid aptamers are single-stranded DNA or RNA molecules, generally 25 to 60 bases in length, identified from pools of random- sequence oligonucleotides (ONs) by an *in vitro* selection process called SELEX (Systematic Evolution of Ligands by EXponential enrichment),[258] introduced in the early 90s independently by the research groups of Gold and Szostak.[259–261]

Thanks to their unique three-dimensional folding, aptamers can recognize a wide range of molecular targets including proteins, small molecules, ions, whole cells and even entire organisms, such as viruses or bacteria, with affinities, expressed in terms of dissociation constants (K_d), ranging from picomolar (pM) to micromolar (μM).[262–264]

The high affinity and selectivity for the target, as well as the multiplicity of possible target types, make aptamers a valid alternative to antibodies in a wide variety of applications, from therapeutics (as drugs or drug-delivery systems) to diagnostic and sensing devices.[265–272]

Nucleic acid aptamers exhibit significant advantages over antibodies, such as smaller size, lower immunogenicity, remarkable stability in a wide range of pH (≈ 4–9) and temperature; in addition, aptamers allow an easy control of their folding processes, which, even after prolonged denaturation, are typically reversible upon restoring the native conditions. In addition, once selected, oligonucleotide-based aptamers can be easily synthesized. Chemical synthesis allows also easily introducing *ad hoc* tailored chemical modifications that can increase the aptamer stability and bring the production costs well below those of antibodies.[273,274]

1.1. SELEX technology

As mentioned before, aptamer development generally exploits the SELEX methodology which involves an *in vitro* iterative selection procedure consisting of three main steps: (i) binding (capture), where a random ODN library is incubated with the desired target molecule under defined conditions; (ii) partitioning, in which the target-bound ODN aptamers are separated from unbound ones; and (iii) amplification, where the enriched pool of selected aptamers is amplified before being used in the successive round of selection. During these processes, the best aptamers for the selected target are enriched and the initial ODN library complexity is decreased (Figure 46, left side). The starting pool, whose appropriate choice represents a crucial point for the success of the SELEX method, can contain 10^{12}-10^{16} DNA or RNA single strands, each with an internal randomized sequence of usually 30-80 nucleotides and terminal fixed sequences, complementary to pre-defined primers used in the amplification step. Aptamer libraries can be derived from chemical synthesis, genomic DNA,[275] or transcriptomic sources,[276] and can be realized with deoxyribo-, ribo-, or modified nucleotides.[277–280] Modified nucleotides are primarily used to increase the chemical and enzymatic stability of aptamers, but can also contribute to broaden their chemical diversity, improving their binding affinity and specificity for a selected target.

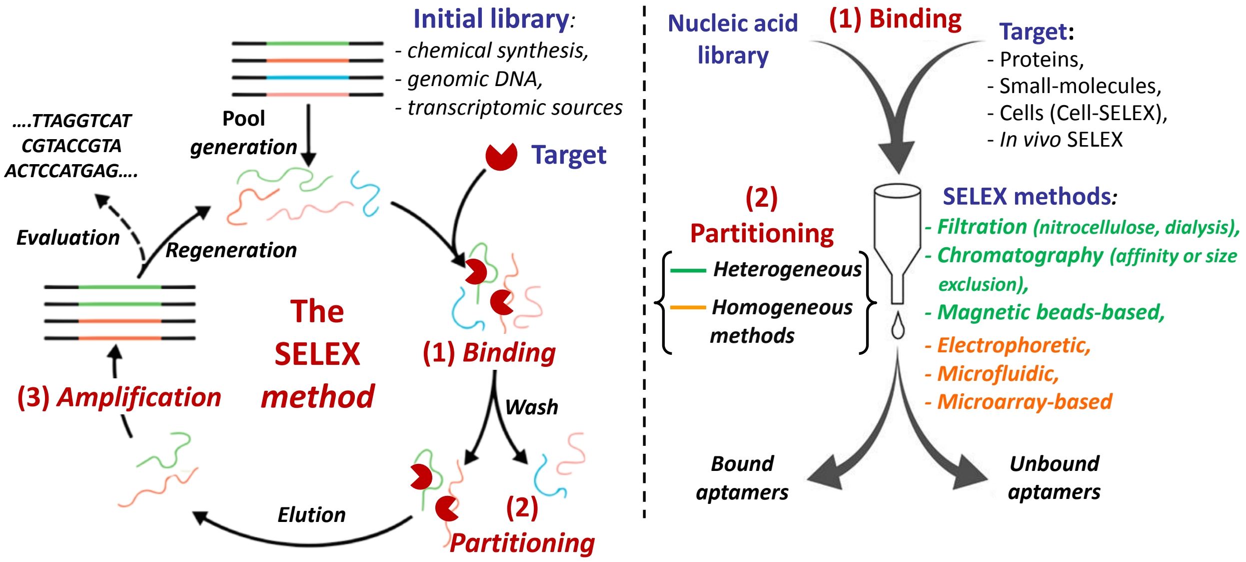

Figure 46. Schematic representation of the SELEX process.

After incubation of the library with the selected target, partition of bound from unbound sequences can be obtained using different strategies (Figure 46, right side), such as filtration, affinity chromatography, or (iii) magnetic beads-based separation.[281] Following partitioning, the target-bound oligonucleotides are eluted from the target and amplified by PCR (DNA SELEX) or reverse transcription PCR (RNA SELEX) to give an enriched pool of selected oligonucleotides, which is used in the successive SELEX round. With increasingly stringent conditions (shorter incubation times, higher temperatures, higher ODN/target ratios) in successive rounds of SELEX, the high-affinity oligonucleotides are enriched. Traditionally, enriched aptamer pools from the SELEX experiments are cloned into a plasmid and a few hundred individual clones, at most, have to be sequenced to identify high affinity aptamers. However, the recent applications of next-generation sequencing (NGS) combined with bioinformatic analysis of the growing aptamer populations allow greatly improving the SELEX procedure.[282] Next steps for obtaining functional aptamers are structure- and sequence- guided molecular engineering that include truncations and/or mutations of the sequence(s) to develop the shortest aptamer(s) with the highest affinity and specificity.[258] Once identified, the putative aptamers can be synthesized and analysed to determine the target affinity and specificity of binding vs. other possible targets.

Despite the remarkable success of aptamers, their commercial application remains relatively undeveloped, probably because of the overwhelming antibody-based market and a certain degree of hesitation to move to new products. To date, Macugen (pegaptanib sodium), selected against the vascular endothelial growth factor (VEGF), is the only existing aptamer-based drug, approved by the US Food and Drug Administration for the treatment of neovascular age-related macular degeneration (AMD), also undergoing clinical trials for the treatment of diabetic macular oedema.[283] Nevertheless, new aptamer-based candidate drugs are undertaking clinical trials,[272,284] and plausibly more aptamers will be approved as drugs in the next future.

1.2. G-quadruplex (G4) motifs in oligonucleotide aptamers

Among the combinatorially selected aptamers endowed with significant bioactivity, many are G-rich oligomers sharing a common structural feature, *i.e.* the ability to fold into stable G-quadruplex (G4) conformations under physiological conditions and recognize very different protein targets.[285,286] This can be easily explained considering the extremely high polymorphism of G4 structures, non-canonical nucleic acid conformations in which the core unit is the guanine tetrad, a cyclic planar arrangement of four guanines linked through Hoogsteen-type hydrogen bonds (Figure 47). Stacking of two or more guanine tetrads generates a G4 motif, which is further stabilized by cations hosted in the central cavity of the G4.[287,288]

The apparently rigid G4 structure is indeed rather plastic and can fit into widely different nucleic acid architectures. Multiple elements participate in conferring G4 structures a high level of adaptability: 1) the intramolecular or intermolecular character of the system; 2) the parallel or antiparallel direction of the guanine-rich tracts in the G4 assembly; 3) the length, sequence and direction of the loops; 4) the *syn* or *anti* guanine orientation around the N-glycosidic bonds; and 5) the number of consecutive G-quartets formed. Furthermore, other individual differentiating elements can be additionally present in the G4-based aptamers, such as bulges,[289] mixed G:A:G:A, G:T:G:T and G:C:G:C tetrads,[290,291] G-vacancies,[292] A-tetrads sandwiched between G-tetrads[293] or A:G4 pentads.[294] An additional level of structural diversity is related to the possibility of raising both DNA and RNA G4-based aptamers.[295,296]

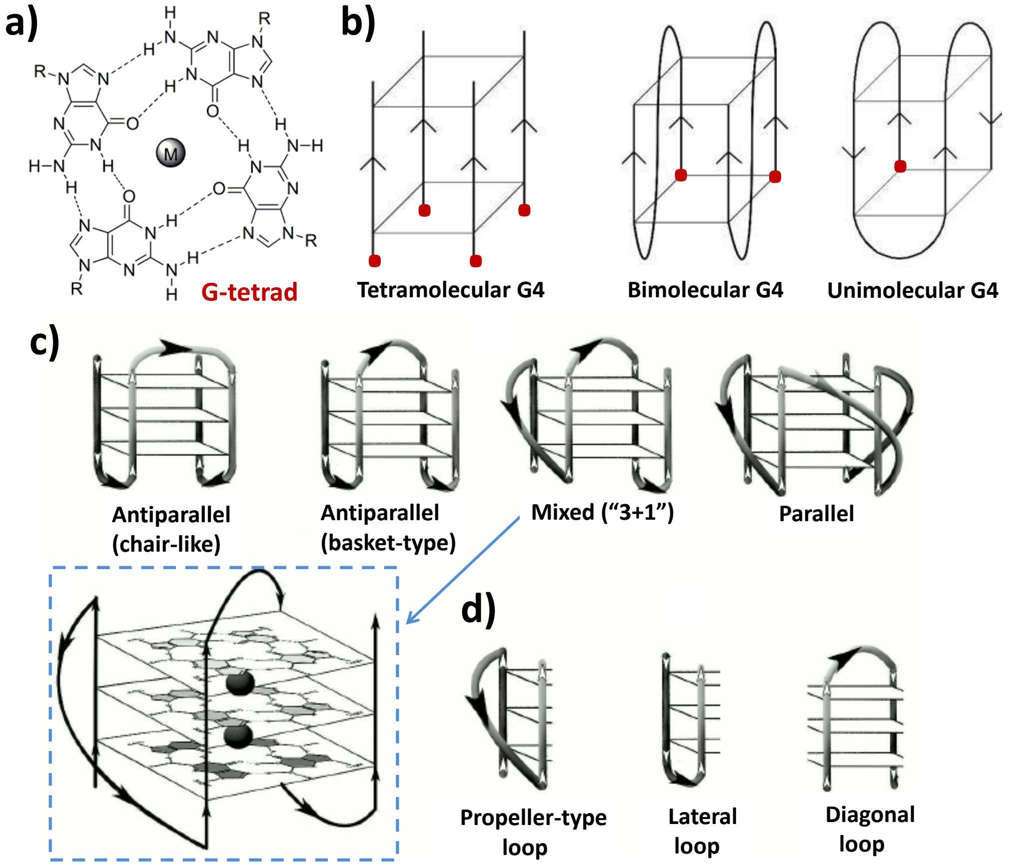

Figure 47. Schematic representations of: a) a G-tetrad stabilized by a metal ion in the central cavity; b) some possible topologies for simple tetramolecular, bimolecular and unimolecular G4s (strand polarities are indicated by arrows); c) examples of unimolecular G4s that differ in strand orientation within the G4 core; and d) types of loops that join G-rich tracts in the G4 structure.

1.3. G4-forming aptamers in therapeutic applications

In the last two decades, aptamers proved to be very attractive as therapeutic agents mainly for their enhanced cellular uptake, non-immunogenicity and lower production costs.[297] Several aptamers against different human pathologies, such as neurodegenerative diseases,[298] age-related macular degeneration,[299] inflammation,[300] thrombosis,[301] diabetes,[285] cancer,[302,303] human immunodeficiency virus (HIV)[304] and coagulation[305] have been discovered and evaluated. Their properties, targets of interest and current clinical evaluation have been recently reviewed in detail.[306]

2. Fluorescent TBA-tagged nanoparticles for an efficient and reversible control of thrombin activity

The 15-mer G-rich oligonucleotide TBA (Thrombin Binding Aptamer or TBA_{15}) is the best characterized aptamer of thrombin, a “trypsin-like” serine protease involved in coagulation processes able to convert soluble fibrinogen into insoluble strands of fibrin.[305,307–311] TBA has been proposed as a valuable alternative to classical thrombin inhibitors used in clinic, such as heparin, warfarin and bivalirudin, showing severe side effects or suffering from narrow therapeutic windows.[312–314] Upon folding into an antiparallel, chair-like G-quadruplex structure, TBA can strongly and selectively recognize the fibrinogen-binding exosite I of human thrombin,[315–318] inhibiting its key function in the coagulation cascade.[319]

Due to its intrinsic instability to nucleases in physiological media, TBA did not progress to advanced clinical trials, being blocked after Phase I studies. To overcome these drawbacks, several TBA analogues have been proposed in the literature, carrying either backbone modifications[320–323] or specific conjugations (with PEG[324] or different kinds of nanoparticles[325–334]), aimed at improving its pharmacokinetic profile and reducing the enzymatic degradation by nucleases.[335–340]

TBA and its variants are important not only for their therapeutic potential, but also for possible applications as biotechnological and bioanalytical tools. Noteworthy is the possibility to label these aptamers with fluorescent probes,[330,334,341–345] which in principle allow monitoring their correct folding and, following their turn-off/turn-on fluorescence responses, the target recognition processes, particularly crucial for sensitive thrombin detection.

Thus, with the aim of optimizing the *in vivo* performance of TBA, a new tris-conjugated TBA (here named tris-mTBA, Figure 48) containing an environment-sensitive fluorescent probe has been prepared, characterized and then incorporated into silica nanoparticles (commercially available as Sicastar®). Tris-mTBA has been designed to carry a dansyl group at the 3’-, and a β-cyclodextrin and a biotin moiety at the 5’-end. The host-guest system dansyl/β-cyclodextrin - based on the well-known inclusion properties of cyclodextrins,[344,346–352] able to capture the dansyl fluorescent group - has been selected to monitor the correct G-quadruplex folding of the aptamer decorating the nanoparticle surface *via* simple fluorescence measurements. In fact, when TBA is unfolded, the dansyl probe, very sensitive to external stimuli,[353–355] is exposed to bulk water and only basal fluorescence is observed. In turn, when TBA is structured into an antiparallel, unimolecular G-quadruplex, the 5’ and 3’ ends of the oligonucleotide strand are in close proximity, favouring the encapsulation of the dansyl group into the hydrophobic cyclodextrin cavity. Under these conditions a marked fluorescence enhancement is observed, as demonstrated in our previous work, investigating as a model system the parent bis-modified TBA, derivatized with a dansyl group at the

3’- and a β-cyclodextrin at the 5’-end.[344] TBA has been here conjugated with an additional tag, inserting a biotin residue to allow its rapid and efficient binding to streptavidin-coated Sicastar® nanoparticles (NPs), exploiting the high affinity and specificity between this ligand and the surface-bound protein.[50,356,357] Notably, the streptavidin-biotin complex is stable in a broad range of pH, ionic strength and temperature,[358,359] and thus ensures a very stable TBA decoration on the nanoparticles.

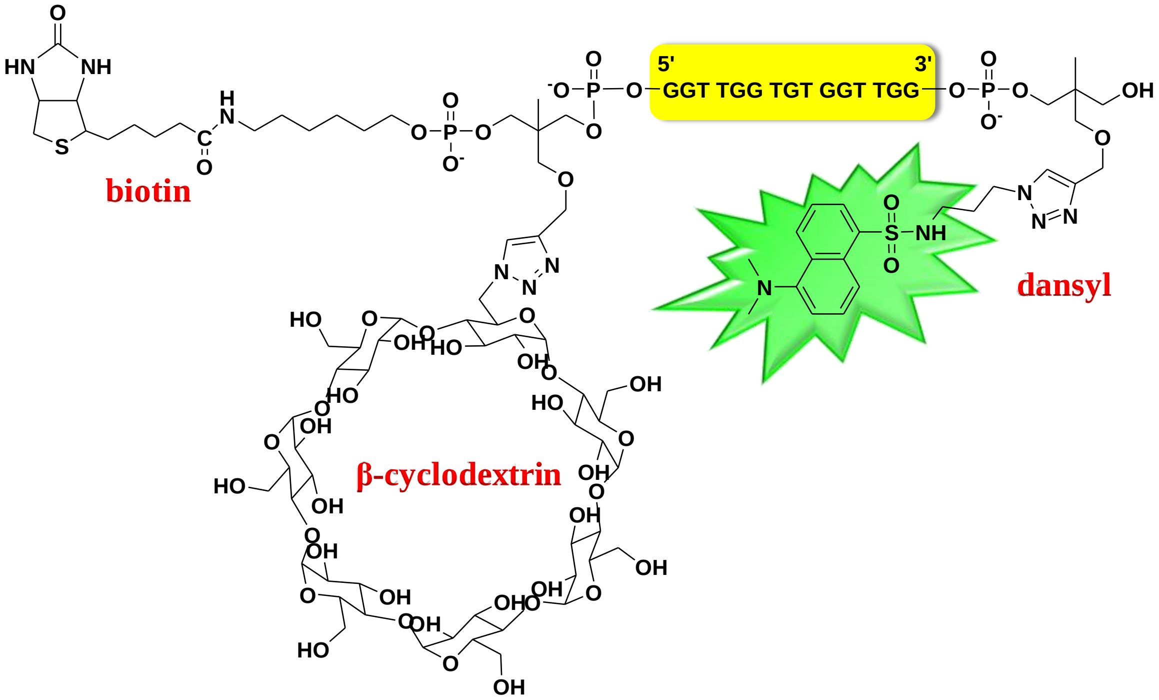

Figure 48. Molecular structure of the tris-mTBA. The TBA oligonucleotide sequence and the dansyl moiety are highlighted in yellow and green, respectively.

Among the commercially available streptavidin-coated NPs, streptavidin-coated Sicastar® NPs with hydrodynamic diameter of 50 nm have been selected. According to the literature, NPs of this size seem to be the best compromise between optimization of the *in vivo* NP biodistribution and preservation of the biotin-streptavidin interactions.

As far as the NP pharmacokinetic profile is concerned, it is generally accepted that very small NPs (hydrodynamic radius < 5 nm) are rapidly excreted from the body through extravasation or renal clearance,[360,361] while NPs in the μm range can easily accumulate in the body, especially in liver, spleen and bone marrow.[362,363] On the contrary, NPs with hydrodynamic radius in the 50-100 nm range, though showing a characteristic biodistribution and cellular uptake behaviour critically depending on the specific cell type,[364,365] in most cases are trapped by mechanical filtration operated by sinusoids in the spleen and then rapidly removed from the bloodstream by the reticuloendothelial system (RES) cells.[366]

Concerning the preservation of the biotin-streptavidin interactions on the silica NP surface, a typical stability trend has been observed as a function of the NP size: on increasing their hydrodynamic radius from 50 to 200 nm, the affinity (in terms of K_d) between biotin and streptavidin is progressively reduced.[367] This effect, probably due to steric constraints or diffusion limitations, negatively affecting the ligand-receptor interactions, leads to conclude that NPs suitable for bioanalytical applications should not exceed the 50-100 nm size.

Then, as for the kind of NP core here used, we specifically selected silica nanoparticles, rather than metal or metal oxide-based platforms, for their low cytotoxicity, high biocompatibility, and, mainly, for not causing fluorescence quenching or general interference with the properties of TBA.[368–375]

The synthesis and purification of this modified aptamer has been realized by dr. Francois Morvan and his group at Institut des Biomolécules Max Mousseron in Montpellier. Then, we have investigated it by means of UV, CD and fluorescence spectroscopy to get information on its conformational behaviour under different solution conditions. Finally, tris-mTBA has been immobilized onto Sicastar® nanoparticles, obtaining the corresponding functionalized Sicastar® system. These nanoparticles have been characterized – in collaboration with the research group of prof. Luigi Paduano at Department of Chemical Sciences of University of Napoli Federico II - using a combined approach including dynamic and static light scattering (DLS and SLS), gel electrophoresis and fluorescence spectroscopy analyses. The inhibitory activity of the TBA-conjugated silica nanoparticles towards human α-thrombin has been evaluated by means of light scattering experiments, following the conversion of fibrinogen into fibrin promoted by the protein, and compared with free tris-mTBA and unmodified TBA. Control experiments with the oligonucleotide sequence complementary to TBA (cTBA), carried out on the tris-mTBA both in free form and conjugated to the silica nanoparticles, allowed verifying that – exploiting the higher thermodynamic stability of a duplex structure *vs*. the corresponding G-quadruplex + single strand system – the anticoagulant activity of these TBA-functionalized NPs can be reversed and blood clotting restored, by simply using cTBA as an antidote.

2.1. Results and discussion

2.1.1. Synthesis of tris-mTBA

Tris-mTBA **35** was prepared in three main steps, as described in Scheme 8. First, dansyl azide derivative **29**[376] was immobilized *via* a Cu(I)-catalyzed azide-alkyne cycloaddition protocol (CuAAC)[377,378] on alkyne-functionalized solid support **28**[379] using the $CuSO_4$/sodium ascorbate catalytic system under microwave irradiation[380] for 1 h at 60 °C. Then, the resulting solid support **30** was used for the solid phase assembly of the TBA oligonucleotide sequence d(GGTTGGTGTGGTTGG) on a DNA synthesizer using standard phosphoramidite chemistry. Once the desired sequence was assembled, two additional couplings were performed: the first one with the DMTr-THME propargyl phosphoramidite **31**,[379] introducing an alkyne moiety in the oligonucleotide, and the second one with the commercially available biotin phosphoramidite **32**.

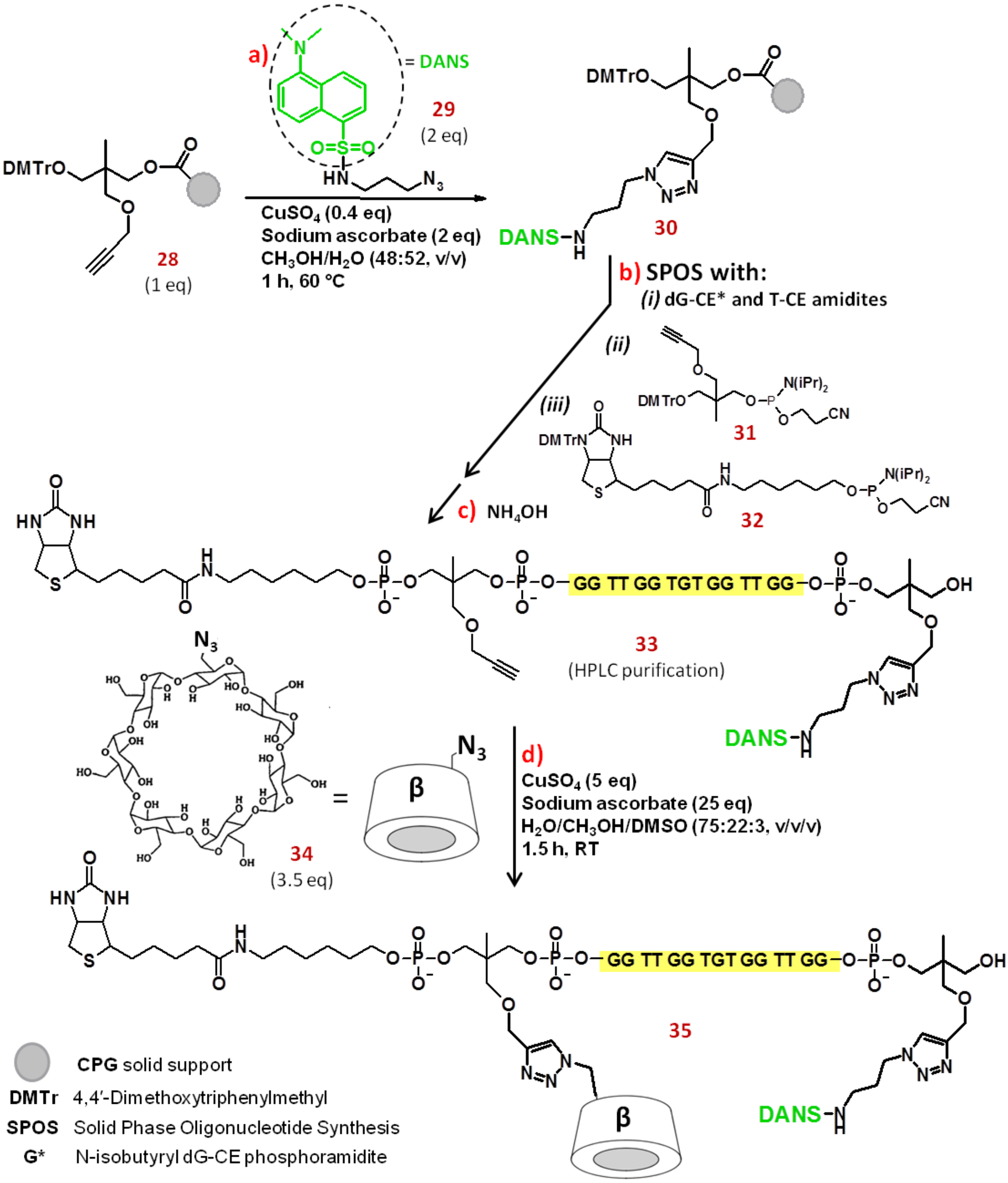

Scheme 8. Synthetic scheme for the preparation of tris-mTBA **35**.

After final DMTr removal, followed by standard ammonia deprotection of the functionalized solid support, the 5’-biotin, 3'-dansyl TBA **33** was released in solution, purified by reverse-phase HPLC and then characterized by MALDI-TOF MS. Finally, β-cyclodextrin, in the form of mono-azide derivative **34**,[381] was coupled in solution with the alkyne-containing oligonucleotide **33** through Cu(I)-promoted cycloaddition for 1.5 h at r.t., yielding the target tris-mTBA **35**. The desired oligomer was purified by gel filtration and characterized by MALDI-TOF MS (Figure 49). Successively, **35** was converted into the corresponding potassium salt by treatment with a 1 M KCl aq. solution and then desalted using size exclusion chromatography.

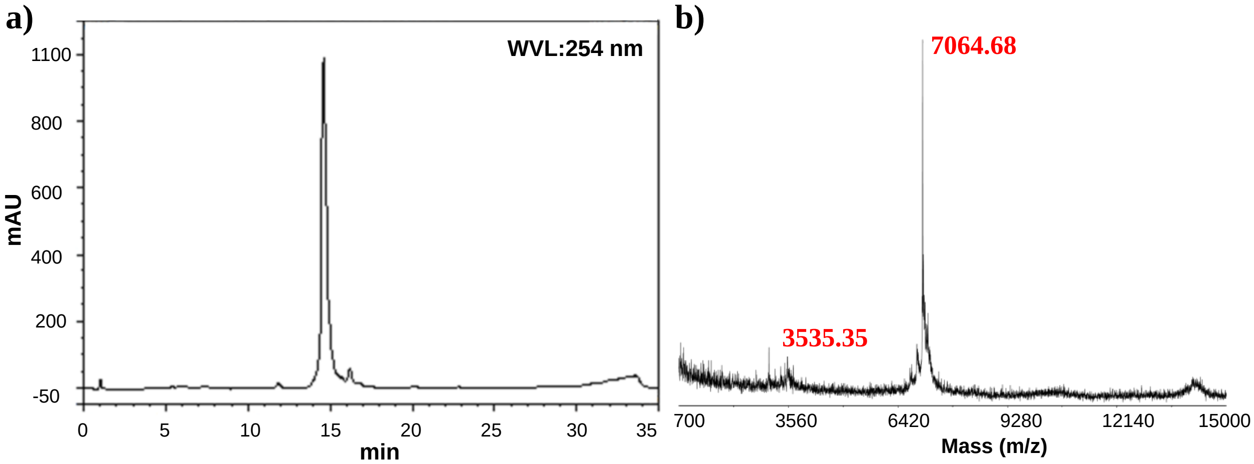

Figure 49. a) HPLC profile and **b**) MALDI-TOF MS spectrum of pure tris-mTBA **35**. Linear gradient: 10 to 30 % B in A for 20 min, **35** t_R: 14.6 min.

2.1.2. Spectroscopic properties of tris-mTBA in solution

The conformational behaviour in solution of tris-mTBA was investigated combining UV, CD and fluorescence data. The spectra collected with the different techniques were obtained from a phosphate buffered solution containing 80 mM K^+ ions (10 mM KH_2PO_4, 70 mM KCl, 0.2 mM EDTA, pH 7.0), in analogy with the previous study performed on the bis-conjugated TBA derivative[344] (here named bis-mTBA), used as a model to evaluate the host-guest system dansyl/β-cyclodextrin on this G-quadruplex forming oligonucleotide.

The CD spectrum of tris-mTBA at 10 °C shows two positive bands with maxima centred at 295 and 246 nm and a negative band with minimum at 266 nm (Figure 50a). These spectral features are consistent with those reported for the unmodified TBA, forming a chair-like antiparallel G-quadruplex structure;[320,382–387] thus confirming that the conjugation with the three sterically hindered reporter groups (*i.e.*, dansyl, β-cyclodextrin and biotin) does not impair the G-quadruplex formation of TBA nor affects the topology of its conformation.

The CD melting profile, monitoring at 295 nm, provided a melting temperature of 39 °C in the selected buffer (Figure 50b). No hysteresis was observed on comparing the heating and cooling profiles, indicating that, under the studied experimental conditions, the system is at equilibrium.

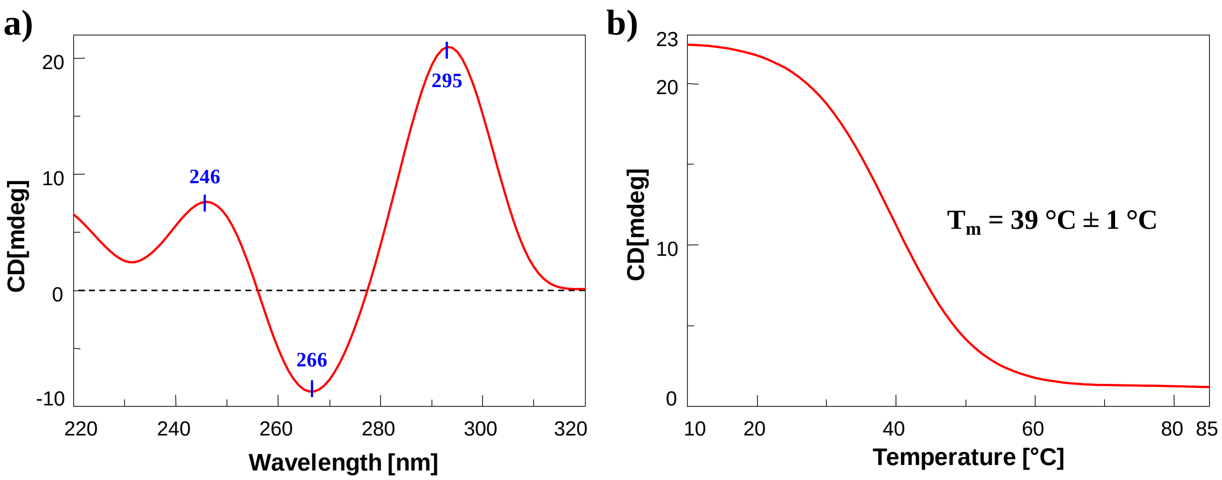

Figure 50. CD spectrum registered at 10 °C (**a**) and CD melting profile recorded at 295 nm (temperature scan rate = 1 °C/min) (**b**) of a 5 μM tris-mTBA solution in 10 mM KH_2PO_4, 70 mM KCl, 0.2 mM EDTA (pH 7.0).

The CD spectrum of tris-mTBA was also recorded in PBS, the buffer solution here used for the successive functionalization of Sicastar® nanoparticles (see below), containing a lower K^+ concentration with respect to the previously used buffer (4.5 *vs.* 80 mM), and a high content of Na^+ ions (157 mM). Also under these conditions, tris-mTBA maintains the same CD profile as in the 80 mM K^+-buffer, with the positive CD band having the maximum at 295 nm (Figure 51) diagnostic of an antiparallel G-quadruplex structure.

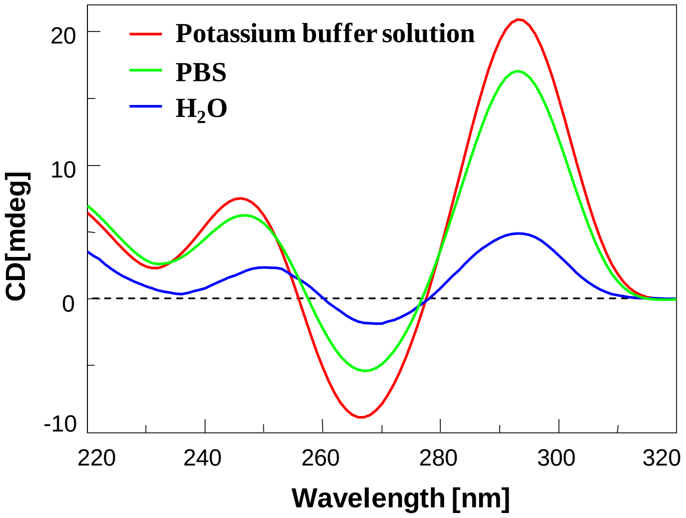

Figure 51. Overlapped CD spectra of tris-mTBA at 5 μM concentration in different solution conditions: 80 mM K^+-buffer solution (red line), PBS (green line), pure water (blu line).

In PBS solution tris-mTBA has a lower structuration degree than in the phosphate buffer containing only K^+ as cation, as expected considering that this species can stabilize G-quadruplex structures better than Na^+.[388–391] The CD spectrum of tris-mTBA in pure water proves that in the absence of stabilizing cations, this aptamer is very poorly structured.

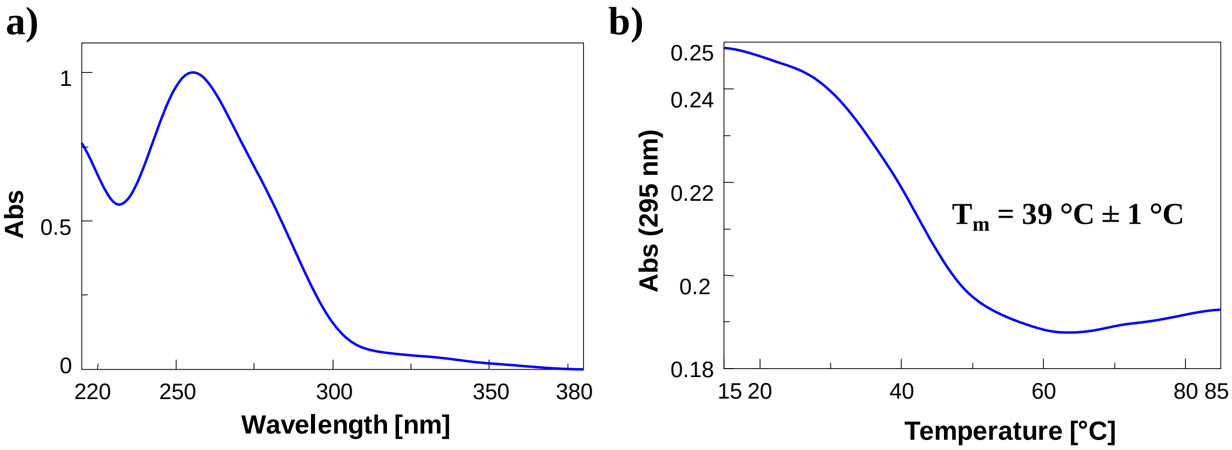

Figure 52. a) UV spectrum and **b**) UV melting profile (15-85 °C, temperature scan rate = 1 °C/min) of tris-mTBA, both recorded in a 10 mM KH_2PO_4, 70 mM KCl, 0.2 mM EDTA (pH 7.0) solution at 5 µM concentration.

Next, the UV spectrum of tris-mTBA, registered at 5 µM concentration in the 10 mM KH_2PO_4, 70 mM KCl, 0.2 mM EDTA (pH 7.0) buffer solution, revealed the characteristic absorption of TBA, with the double-hump band between 230 and 300 nm (Figure 52a). As determined from comparison with the unmodified TBA under the same concentration and solution conditions, the contribution of the dansyl, β-cyclodextrin and biotin moieties can be considered negligible with respect to the oligonucleotide absorbance. From the UV-melting curve recorded at 295 nm,[386,392,393] a T_m of 39 °C was derived (Figure 52b), in perfect accordance with the T_m from the CD melting registered at the same wavelength. Even in this case, no significant hysteresis was observed on comparing the heating and cooling processes (data not shown), indicating a fully reversible process.

The thermal denaturation of tris-mTBA was also analysed by monitoring the changes of the fluorescence emission of the dansyl group, upon excitation at 327 nm, as a function of the temperature on an annealed aptamer solution. On increasing the temperature, a gradual, marked decrease in the fluorescence intensity, as well as an emission maximum shift from 534 to 551 nm, were observed (Figure 53a). These fluorescence features clearly indicate that the dansyl group experiences dramatically different environments upon temperature-induced unfolding. These findings are consistent with the dansyl residue being encapsulated inside the β-cyclodextrin ring in the folded state (low temperature) and pointing outside, exposed to the aqueous solution, in the unfolded state (high temperature), as already observed in the case of bis-mTBA.[344]

The fluorescence-monitored melting curve was obtained reporting the wavelength at the fluorescence emission maximum as a function of the temperature (Figure 53b).[344] The obtained T_m value (40 °C) is, within the experimental error, in good accordance with the results obtained from CD and UV data, indicating that the dansyl group is thrown out from the cyclodextrin cavity in concomitance with the unfolding of the whole G-quadruplex structure. Also in this case, the heating and cooling profiles were essentially superimposable (data not shown).

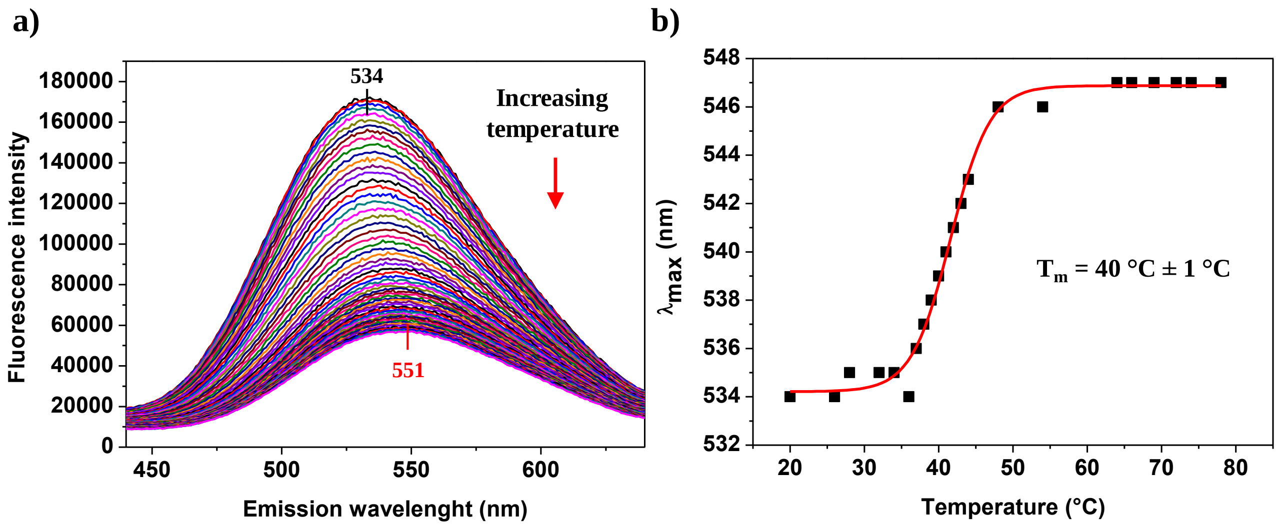

Figure 53. a) Overlapped emission fluorescence spectra (λ_{ex} = 327 nm) of tris-mTBA, recorded at 2 μM concentration in a 10 mM KH_2PO_4, 70 mM KCl, 0.2 mM EDTA (pH 7.0) buffer solution, on increasing the temperature from 20 to 80 °C; **b**) fluorescence melting profile obtained reporting the wavelength at the fluorescence emission maximum as a function of temperature (range 20-80 °C).

In summary, these results show that tris-mTBA qualitatively behaves as bis-mTBA[344] and the unmodified TBA.[320,384,385,387] As expected, the presence of three bulky conjugating groups affects the apparent T_m of tris-mTBA, which is ca. 10 °C lower than that of TBA and of bis-mTBA (39 *vs.* 49 °C), showing a marked loss in thermal stability in the explored conditions. However, these data also confirm that, in a pseudo-physiological solution, tris-mTBA is mainly present as a G4 structure. It can be also speculated that the G4 structuring of tris-mTBA should be further enhanced when conjugated to the NPs, if other interfering surface processes do not intervene. In fact, once the biotin residue of tris-mTBA is captured by the streptavidin coating of the NPs, any competition is prevented between the dansyl and biotin for cyclodextrin recognition (which is however possible in tris-mTBA in solution since the binding constants for their complexes with β-cyclodextrin are in the same order of magnitude (*Ka* ~10^2 M^{-1})[394,395] and could disturb the correct G4 folding).

2.1.3. CD experiments with cTBA sequence

Reversibility of binding between inhibitors and coagulant factors is essential in drug treatments. In fact, in case of clinical complications, such as haemorrhage, physicians need rapidly and safely reversing coagulation inhibition. The 15-mer d(CCAACCACACCAACC), here indicated as cTBA, complementary to the TBA sequence and able to hybridize it forming a duplex structure, can profitably modulate the activity of TBA, reversing its anticoagulation activity.[301,396] Thus TBA and cTBA can be considered a very effective drug/antidote pair for thrombin.[397]

In this frame, the ability of tris-mTBA to form a duplex structure with cTBA was investigated by CD measurements and compared with the unmodified TBA. The CD experiments were carried out using a *tandem cell*, a quartz cuvette composed of two distinct compartments, which allows recording the *sum* and *mix* spectra of two components (*i.e.* the spectrum obtained by maintaining the cTBA and TBA as separate systems, and the one obtained after mixing the two solutions).

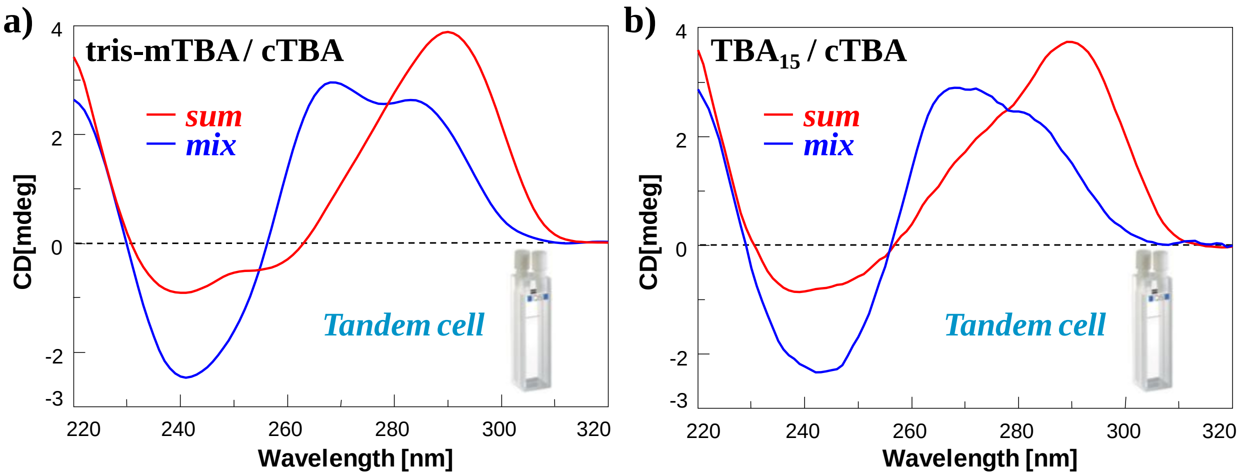

Figure 54. CD spectra registered as *sum* (red lines) and *mix* (blue lines) of tris-mTBA/cTBA (**a**) and unmodified TBA/cTBA (**b**) systems in a *tandem cell*. Each oligonucleotide was analysed at 2.5 μM concentration in PBS solution.

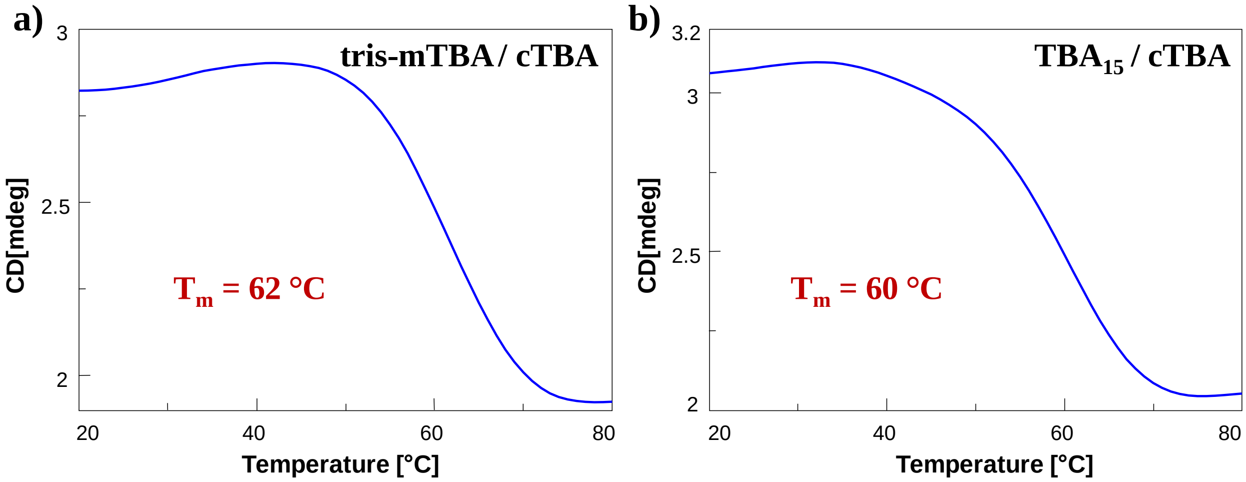

Figure 55. CD melting curves for the *mix* solutions of tris-mTBA/cTBA (**a**) and unmodified TBA/cTBA (**b**), recorded in a *tandem cell* in PBS solution at 268 nm (scan rate = 1 °C/min).

In both cases the *sum* (red lines) and *mix* (blue lines) spectra were not superimposable, denoting the rapid interaction of the two strands (Figure 54). Thus, for tris-mTBA the formation of a duplex structure upon cTBA addition efficiently competes with the G-quadruplex, in analogy with the unmodified TBA behaviour. After mixing the solutions and stabilization of the CD signal, a denaturation curve was recorded at 268 nm for each duplex (Figure 55), showing similar T_m values for the two systems (62 and 60 °C for tris-mTBA/cTBA and TBA/cTBA, respectively). An end-stacking stabilizing effect produced by the dansyl moiety could account for the slightly higher T_m of the duplex structure containing tris-mTBA. The CD melting curves were almost superimposable to the corresponding annealing profiles, not evidencing hysteresis phenomena.

These data clearly indicate that the residues inserted at the ends of tris-mTBA do not perturb its ability to bind its complementary strand, forming a stable duplex under pseudo-physiological conditions, necessary pre-requisite for using tris-mTBA/cTBA as an anticoagulant/antidote couple.

2.1.4. Preparation of the tris-mTBA-functionalized Sicastar® nanoparticles

Once having fully characterized the behaviour of tris-mTBA in solution, this aptamer was conjugated to Sicastar® NPs as schematically represented in Figure 56.

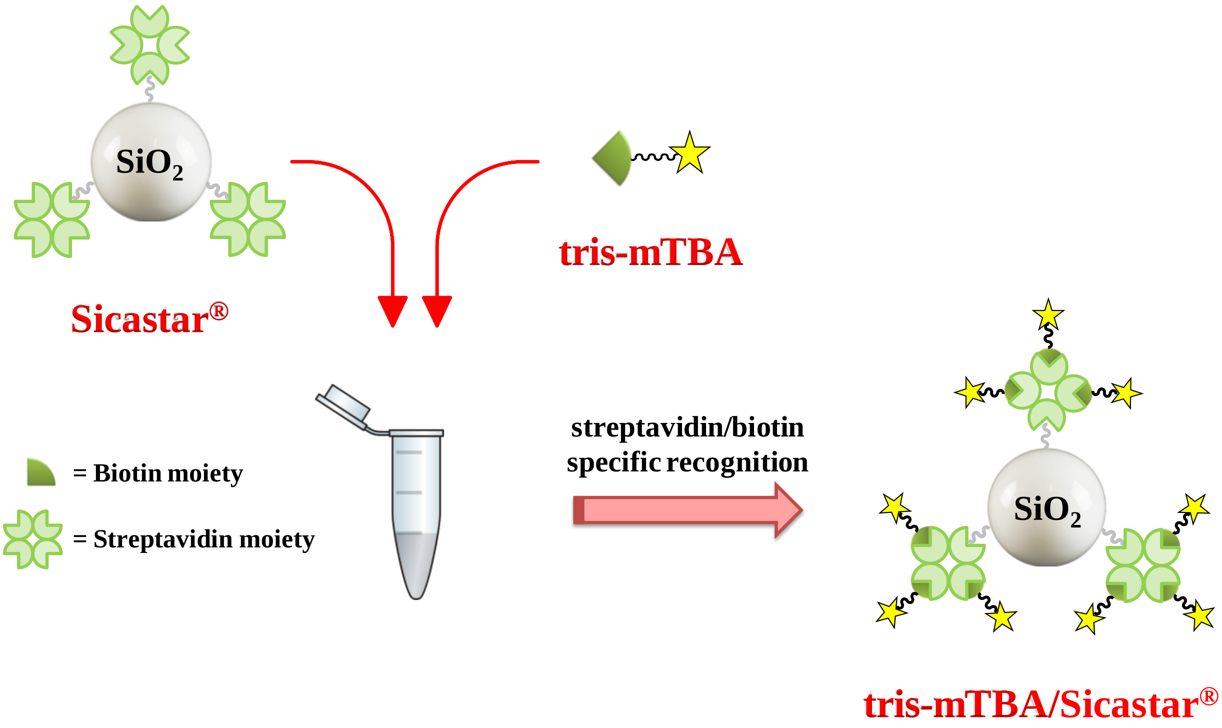

Figure 56. Schematic representation of the Sicastar® functionalization with the tris-mTBA.

The functionalization of the streptavidin-coated silica nanoparticles with tris-mTBA is based on the high affinity of streptavidin/biotin recognition (K_d ~10^{-14} M).[50] Thus, by simply mixing in an eppendorf tube the Sicastar® NPs and tris-mTBA both in PBS buffer (using a biotin/streptavidin 1:1 ratio) under gentle stirring for 1 h, the conjugated tris-mTBA/Sicastar® NPs were obtained. The functionalization protocol was optimized on the basis of DLS results. In fact, specific functionalization conditions were necessary to obtain a single NP population (see below), which was then analysed using different techniques.

2.1.5. Dynamic and Static Light Scattering analysis of functionalized Sicastar® NPs

In order to characterize the tris-mTBA-functionalized Sicastar® NPs, dynamic light scattering analyses were carried out on the nanoparticles before and after the functionalization with the aptamer. The streptavidin-coated Sicastar® NPs – analysed as received from the commercial supplier - showed a well-defined, single population, with hydrodynamic radius of ca. 50 nm, accounting for more than 95% of the scattering intensity, accompanied by a very small population of higher size. Analysis of the tris-mTBA-functionalized NPs samples showed that when the functionalization was performed mixing Sicastar® NPs and tris-mTBA so to have a 1:1 or 1:0.9 streptavidin/biotin ratio, with short incubation times, only a single monodispersed NP population was obtained. On the contrary, DLS curves of the functionalized NPs obtained using high biotin:streptavidin ratios or long incubation times showed, in addition to the main population, also detectable amounts of larger species, likely aggregates (data not shown).

As expected, due to the negligible size of the aptamer with respect to the streptavidin-coated silica NPs, no effect on the overall dimensions of the Sicastar® system was detected after functionalization with tris-mTBA, as determined by DLS.

Static light scattering analysis and Zimm plot elaboration were also exploited to characterize the tris-mTBA/Sicastar® NPs system, providing the molecular weight of the NPs before and after functionalization. Notably, unfunctionalized NPs showed a molecular weight of the same order of magnitude as the tris-mTBA-functionalized Sicastar® NPs (5.4×10^6 *vs.* 5.3×10^6 Da before and after functionalization, respectively). As in the case of the overall size determined by DLS, also in terms of molecular weight the contribution of tris-mTBA, upon conjugation to the Sicastar® NPs, is negligible: indeed, the expected increase in molecular weight after the functionalization falls within the uncertainty of the method, which allows a molecular weight evaluation with an error of ca. ±10%. However, a quite unexpected and remarkable finding is the different slope of the Zimm plots relative to the NPs before and after the functionalization (Figure 57a and 57b). In the former case a positive slope was observed, indicating a good NP system-solvent interaction, while the latter system showed a negative slope, indicating that the interactions among the NPs are favoured over the NPs-solvent ones, and therefore an intrinsic tendency of the tris-mTBA/Sicastar® NPs to self-aggregate should be considered.

Moving from this result, DLS was further employed to check the stability over time of Sicastar® NPs before and after the tris-mTBA functionalization. Remarkably, no detectable change in the

DLS profiles of unfunctionalized Sicastar® NPs in PBS solution was observed over a period of several months. In contrast, in the case of functionalized NPs, DLS analysis showed the appearance of new, even if very small, populations of bigger aggregates starting from ca. 4 weeks from the functionalization procedure, in close agreement with the results of the Zimm plot analysis (Figure 57c). However, despite their inherent tendency to aggregate with time, these data prove that the functionalized tris-mTBA/Sicastar® NPs can be considered stable in pseudo-physiological solutions for ca. one month, a time range well beyond that needed for biomedical applications.

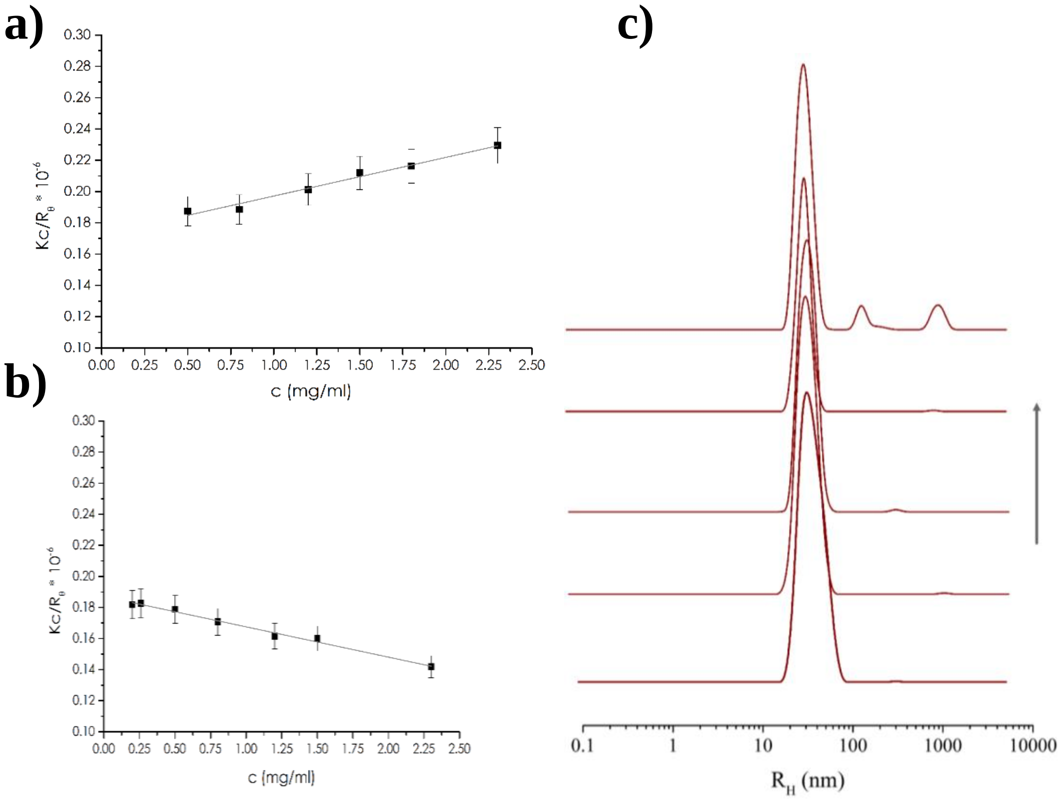

Figure 57. Zimm plot of Sicastar® NPs before (**a**) and after (**b**) the functionalization with tris-mTBA. **c**) Overlapped DLS profiles of the tris-mTBA/Sicastar® NPs in PBS solution, registered at t=0, 1 week, 2 weeks, 3 weeks or 4 weeks after their preparation.

2.1.6. Gel electrophoresis analysis

Gel electrophoresis analysis was used to further characterize the modified aptamer and the Sicastar® NPs in solution. In Figure 58 the photograph of a representative 1 % agarose gel, run under native conditions, is reported. A detectable difference in electrophoretic mobility was observed for the unmodified TBA and tris-mTBA, both previously annealed in PBS, proving that the three bulky, pendant groups here introduced on tris-mTBA somehow affected the migration ability of TBA. Interestingly, upon UV visualization, the tris-mTBA band showed a different colour with respect to the unmodified TBA, probably conferred by the dansyl group (*cfr*. lanes 3 and 4 in Figure 58, respectively). As far as the nanoparticles are concerned, both the unfunctionalized and tris-mTBA-functionalized Sicastar® NPs loaded on the gel (lanes 1 and 2, respectively) showed retarded bands with respect to the free aptamers in solution. They revealed the same mobility under the used conditions, clear evidence that the TBA functionalization of the Sicastar® NPs did not alter their migration on an agarose gel, *i.e.* their overall size and shape, as expected considering the relative weight of the streptavidin-coated NPs and of tris-mTBA and in accordance with the DLS and SLS analyses. Remarkably, the functionalized NPs loaded on the gel (lane 2) did not show detectable bands in correspondence of the free tris-mTBA. Taking into account that gel electrophoresis is a low resolution technique, these results however provide an indication that, within the detection limit of the method, the functionalized NPs do not contain unbound tris-mTBA.

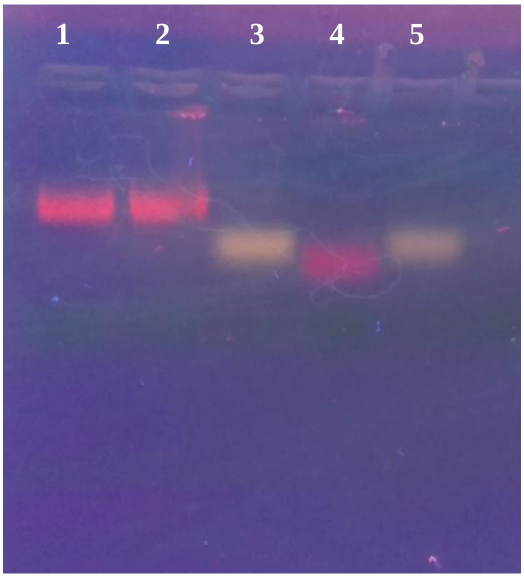

Figure 58. 1% agarose gel electrophoresis under native conditions of the analysed TBA and NP systems; Lane 1: Sicastar® NPs (2.5 mg/mL); Lane 2: tris-mTBA/Sicastar® (2.5 mg/mL); Lane 3: tris-mTBA (3.3 µM); Lane 4: unmodified TBA (3.3 µM); Lane 5: tris-mTBA (2.0 µM).

2.1.7. Fluorescence spectroscopy analysis of free and NP-conjugated tris-mTBA

Fluorescence measurements allowed monitoring the fluorescence emission of the dansyl group. Since this fluorescent probe is extremely sensitive to its environment, the persistence of substantial fluorescence emission, with the same maximum as observed in the G4-structured tris-mTBA solution before the NPs functionalization, can provide evidence of complete encapsulation of dansyl within the cyclodextrin cavity even in the NP-immobilized aptamer. As demonstrated in solution studies, this event is strictly connected with the correct G4-structuring of tris-mTBA and can thus provide information on the effective conformation adopted by the aptamer on the NP surface after the functionalization procedure. In Figure 59 overlapped fluorescence spectra of tris-mTBA and tris-mTBA/Sicastar® in PBS solution at the same aptamer concentration are reported, after subtracting the contributions of the buffer and of Sicastar® NPs alone. These spectra are qualitatively similar, with a fluorescence difference of less than 20%. The perfect coincidence of the fluorescence maxima proved that, after immobilization onto Sicastar®, tris-mTBA maintained its original fluorescence features. It can be thus deduced that the peculiar G4 conformation of tris-mTBA, essential for thrombin recognition, is overall preserved on the functionalized Sicastar® NPs.

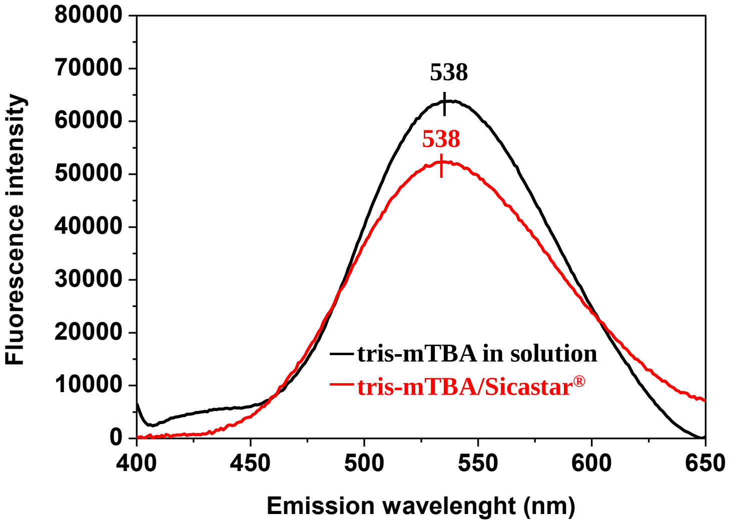

Figure 59. Overlapped fluorescence spectra of tris-mTBA and tris-mTBA/Sicastar® NPs (black and red curves, respectively) in PBS solution, with the emission maximum marked for each spectrum.

2.1.8. Anticoagulant activity

The anticoagulant activity of tris-mTBA and tris-mTBA/Sicastar® NPs was evaluated following the conversion of fibrinogen in fibrin induced by thrombin by means of light scattering experiments, and compared with the activity of free TBAs. A rapid increase of the scattered intensity with time indicated the progression of fibrin formation in samples only containing fibrinogen and thrombin (Figure 60). The addition of the aptamers, TBA or tris-mTBA, caused a marked decrease of the scattered intensity with respect to the untreated samples, evidencing the inhibition of thrombin coagulation activity. The observed anticoagulant effect was significantly influenced by the conjugating groups on TBA. Indeed, tris-mTBA was ca. 10 times more effective than TBA itself under the same experimental conditions, probably as a result of its higher affinity for thrombin imparted by the presence of the pendant groups. Upon treatment with the tris-mTBA/Sicastar® NPs, no increase of the scattered intensity over time was detected, indicating that the coagulation process was completely blocked by the functionalized NPs, proving to be much more efficient as anticoagulant than both the free TBAs.

Finally, we verified if the anticoagulant activity of tris-mTBA could be controlled by addition of the antidote of TBA (*i.e.*, cTBA) even when the aptamer was bound on the NP surface. A 10-fold excess of cTBA was added to the tris-mTBA/Sicastar® NPs and the scattered intensity of the resulting mixture monitored over time. A significant increase of the scattered intensity was detected about 30 minutes after the cTBA addition, indicating that the antidote is effectively able to reverse the tris-mTBA anticoagulant activity even when the aptamer is immobilized on the NP surface (Figure 60).

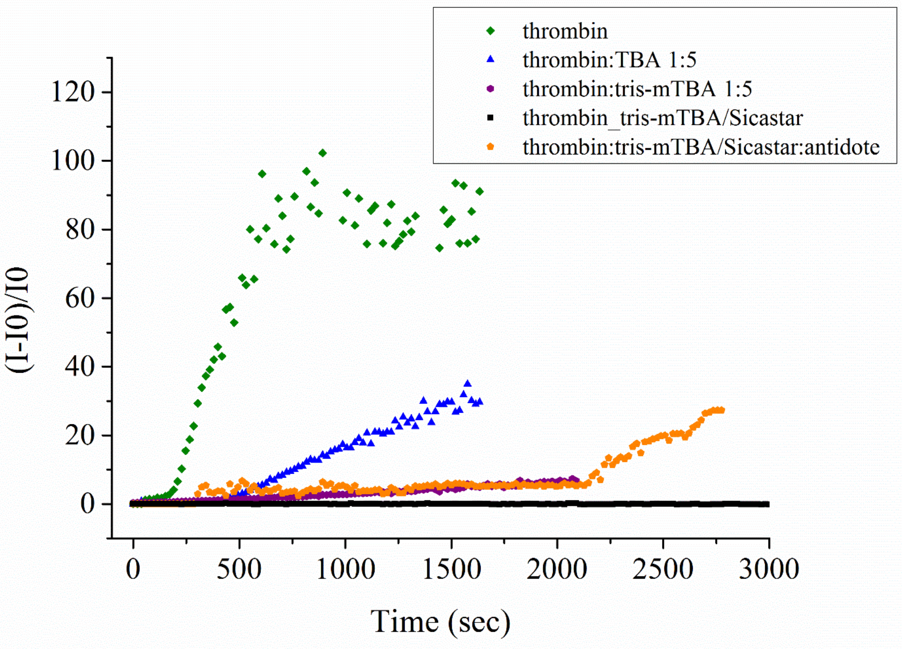

Figure 60. Coagulation curves of fibrinogen in the presence of thrombin and different anticoagulant agents (TBA; tris-mTBA, tris-mTBA/Sicastar$^{®}$ NPs and cTBA).

Control experiments performed in the presence of not functionalized Sicastar® show an almost sudden increase of the light scattered intensity, which does not change further with time, in apparent contrast with the coagulation of fibrinogen. Thus to get a further insight into the process, we also analysed the autocorrelation functions obtained for the different systems at different times. Indeed, the analysis of the normalized autocorrelation function gives us a direct information on the size of the species in the system, a different experimental view of the coagulation process.

As emerges from Figure 61a, in the presence of thrombin, a shift of the curves with respect to pure fibrinogen (fibr t=0) occurs at increasing times because of the formation of fibrin. Remarkably, the autocorrelation curves at the end of the coagulation experiment ($t=t_f$) differ depending on the anticoagulant agent. When no anticoagulant is present, the curve does not reach zero even at very long times, clearly indicating the formation of very big aggregates. In the presence of TBA the strong noise at long times also points towards the formation of big species; while, in the case of tris-mTBA, the position of the curve and the flat region at long times indicate that only soluble, smaller species are present. Finally, in the presence of tris-mTBA/Sicastar$^{®}$ NPs no appreciable shift of the autocorrelation curve is observed with time. It is interesting to note that in the control system containing not functionalized Sicastar®, the initial curve is intermediate between that of the system containing fibrinogen and tris-mTBA/Sicastar® NPs and that of coagulated fibrinogen, suggesting the presence of some aggregated species formed upon interaction between NPs and fibrinogen. However, at the end of the experiment the normalized autocorrelation curve is superimposable with that of coagulated fibrinogen. The conversion of fibrinogen coated NPs into coagulated fibrinogen does not result in a significant change of intensity. So, although monitoring of the light scattered intensity over time is a good method to follow the coagulation of fibrinogen, nonetheless in some cases it fails to reveals what actually happens in the system, and only a concomitant analysis of the autocorrelation function can give a clear picture of the system.

Indeed, the normalized autocorrelation function, compared with that of the other systems containing Sicastar® NPs (Figure 61b), upon addition of the antidote, at the end of the measurements, proved to be superimposable to that of the control experiment with no anticoagulant agent.

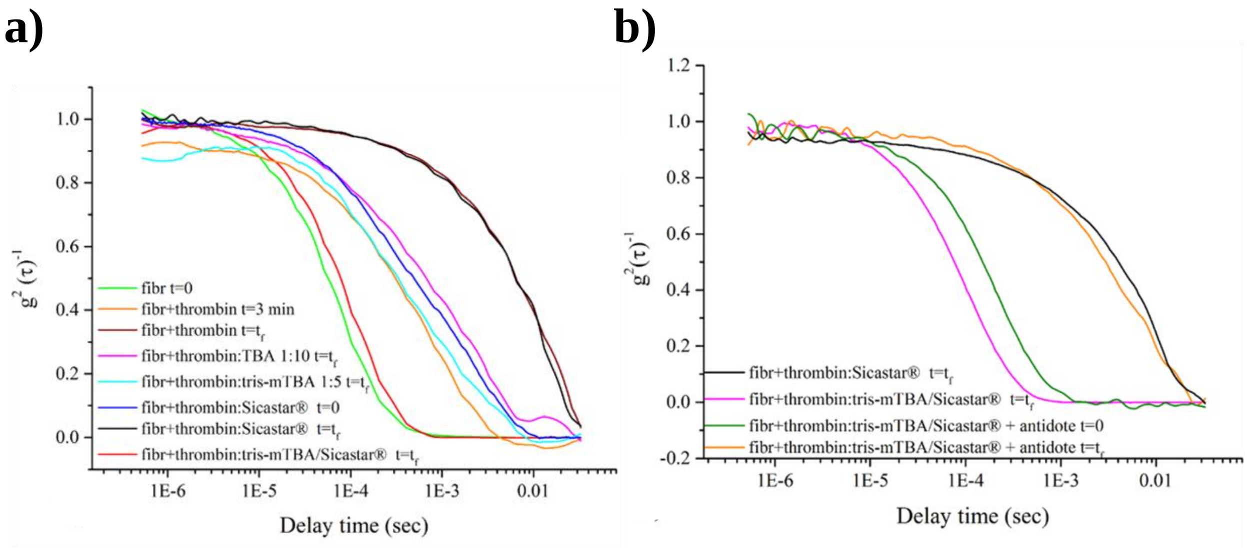

Figure 61. a) Normalized autocorrelation function at different times and in the presence of different anticoagulant agents (TBA; tris-mTBA and tris-mTBA-NPs) and in the presence of not functionalized Sicastar®; **b**) Comparison of the normalized autocorrelation function upon addition of the antidote with respect to systems containing not functionalized and functionalized Sicastar®.

2.2. Experimental section

- **Materials and general methods**

All the reagents and solvents were of the highest commercially available quality and used as received.

The Sicastar® nanoparticles were purchased from Micromod (Germany) and consisted of a suspension of spherical amorphous silica particles with a hydrodynamic radius of 50 nm (10 mg/mL, 7.6×10^{12} particles *per* mg, density: 2.0 g/cm^3) in PBS buffer, stabilized with 0.02%

sodium azide. The particle surface was covered with covalently-bound streptavidin (protein content: 2500 ng/mg, corresponding to ca. 3 molecules of streptavidin per single particle).

UV measurements were obtained on a JASCO V-530 UV/vis spectrophotometer equipped with a Peltier block JASCO ETC-505T, by using 1-cm quartz cells of 0.5 and 3 mL internal volume (Hellma). The spectra were recorded with a response of 1 s, a scanning speed of 100 nm/min and a 2.0 nm bandwidth, and corrected by subtracting the buffer background scan.

CD spectra and CD-monitored melting curves were recorded on a Jasco J-715 spectropolarimeter equipped with a Peltier-type temperature control system (model PTC-348WI), using a quartz cuvette with a path length of 1 cm (3 mL internal volume, Hellma) or a tandem cell (2 × 0.4375 cm, Hellma). CD parameters for spectra recording were: spectral window 220-320 nm, data pitch 1 nm, band width 2 nm, response 4 s, scanning speed 100 nm/min, 3 accumulations. CD melting was performed at 1 °C/min scan rate.

Fluorescence spectra were collected in a 1 cm path length cuvette with a HORIBA Jobin Yvon Inc. FluoroMax®-4 spectrofluorometer equipped with F-3004 Sample Heater/Cooler Peltier.

- **Preparation of oligonucleotide samples**

Purified and lyophilized oligonucleotides tris-mTBA **8**, unmodified TBA and cTBA were dissolved in a known volume of Milli-Q water and their concentrations determined by UV spectroscopy in 1 cm path length cuvette measuring the absorbance at 260 nm (85 °C) using the following molar extinction coefficients: for unmodified TBA and tris-mTBA, ε_{260} = 158478 cm^{-1} M^{-1}; for cTBA, ε_{260} = 154655 cm^{-1} M^{-1}. Then the oligonucleotides from the stock solutions were diluted in the selected buffer and annealed by heating each solution for 5 min at 90 °C and then leaving it to slowly cool to r.t. overnight. Annealed samples were then kept at 4° C until use.

- **Spectroscopic characterization of tris m-TBA**

CD experiments. The CD spectra were collected at 10 °C in the range 220-320 nm. The characterization of tris-mTBA was performed at 5 μM concentration taking a suitable initial aliquot from a 335 μM stock solution in H_2O. For the CD melting experiments, the CD signal at 295 nm was recorded *vs*. the temperature in the range 10-85 °C. The CD experiments carried out with the unmodified TBA or tris-mTBA and the corresponding complementary strand (cTBA) were performed in a tandem cell by placing, in one chamber, the TBA sequence, and in the other the complementary strand, each at 2.5 μM concentration in PBS solution. Two CD spectra were registered for each experiment: the first one was recorded as the sum of the separate components, here named as the *sum* spectrum, and the second one was recorded after mixing the two solutions and stabilization of the signal, here named as *mix* spectrum. After mixing the two solutions, the duplex concentration was reduced by a factor of 2 and the solution path length increased from 0.437

to 0.875 cm. Thermal denaturation-renaturation curves of the resulting duplex were recorded following the CD signal at 268 nm. The error associated with the T_m determination was ± 1 °C.

UV-vis absorption experiments. The UV-vis measurements were registered in the range 220–380 nm using 1 cm path length cuvette. The absorbance *vs.* temperature profiles were recorded by following the absorbance changes at 295 nm on increasing the temperature (heating scan rate 1 °C/min). The tris-mTBA solution used for these experiments was 5 μM in a 10 mM KH_2PO_4, 70 mM KCl, 0.2 mM EDTA (pH 7.0) buffer, prepared diluting the original stock solution of the oligonucleotide in H_2O. The error associated with the T_m determination was ± 1 °C.

Fluorescence Spectroscopy experiments. The fluorescence emission spectra were recorded from 440 to 640 nm, exciting at 327 nm and maintaining the excitation and emission slits at 10 nm. The oligonucleotide concentration was 2 μM in a 10 mM KH_2PO_4, 70 mM KCl, 0.2 mM EDTA (pH 7.0) solution. Fluorescence melting curves were obtained by reporting the wavelength shift of the emission maximum as a function of temperature (from 20 to 80 °C). The error associated with the T_m determination was ± 1 °C.

- **Sicastar® functionalization and characterization**

750 μL of a 0.4 μM solution of tris-mTBA in PBS were first subjected to annealing, heating the sample at 95 °C for 5 min and then leaving it to slowly cool to r.t. The formation of the desired antiparallel G-quadruplex structure of tris-mTBA was confirmed in this buffer solution by CD and fluorescence spectra. Then 250 μL of a Sicastar® NPs suspension in PBS buffer (10 mg/mL) were added to the tris-mTBA reaching a final volume of 1 mL (Sicastar® NPs 2.5 mg/mL; tris-mTBA 0.3 μM) and the reaction mixture was gently stirred at r.t. for 1 h.

Gel electrophoresis. Non denaturing agarose (1% w/v) gel electrophoresis was performed loading unmodified TBA, tris-mTBA, Sicastar® NPs and tris-mTBA/Sicastar® NPs on the gel with 3% of GelRed dye. The samples were then run at 100 V for 30 min at r.t. in Tris-acetate-EDTA (TAE) buffer and visualized under UV light.

Fluorescence analysis. Fluorescence spectra of the tris-mTBA/Sicastar® NP solution were recorded in PBS buffer (0.3 μM oligonucleotide concentration) from 400 to 650 nm exciting at 340 nm and maintaining the excitation and emission slits at 10 nm. Fluorescence spectra of the free tris-mTBA in solution under the same conditions were also registered.

3. G-quadruplex oligonucleotide AS1411 as a cancer cell-targeting agent: introduction

In the last decade, AS1411 has been the subject of a high number of publications.[398] This escalation of interest is largely driven by the use of AS1411 as a ligand for the tumor-selective delivery of therapeutic or imaging agents, especially in fields related to nanotechnology.[398] AS1411 is a 26-mer G-rich DNA oligonucleotide with sequence $^{5'}$GGTGGTGGTGGTTGTGGTGGTGGTGG$^{3'}$. It is well established that AS1411 and longer versions of this sequence, such as GRO29A, form G-quadruplex-containing structures showing cancer-selective antiproliferative activity and efficient cellular internalization.[399–404] No definitive crystal or NMR structure of AS1411 is available, but it is known that this sequence displays a high degree of structural polymorphism in solution,[404] as also already observed for many other biologically relevant G4-forming sequences.[405–408] Trent and coworkers discovered that at least 8 different forms of AS1411 could be detected by size exclusion chromatography (SEC) analysis.[404] Using preparative SEC, they isolated and characterized 5 distinct AS1411 fractions, which contained either monomolecular quadruplexes or a mixture of monomer and dimer quadruplexes.[404] The isolated species were indistinguishable by most biophysical techniques, but had significantly different NMR and circular dichroism (CD) spectra. In the presence of K^+ ions, 4 of the 5 fractions displayed the classical CD features of a parallel G4 (positive peak at 264 nm), whereas one fraction (Fraction 2) had a very unusual CD spectrum with a positive peak at 245 nm and a strong negative ellipticity at 277 nm,[404] which can likely contain a left-handed quadruplex form (Z-G4) of AS1411.[409] Possible G4 structures for AS1411 are illustrated in Figure 62.

The type(s) of quadruplex formed by AS1411 *in vivo* and how the structure of AS1411 relates to its biological activities remains an open question and may be influenced by a number of factors, such as protein binding and localization in the body (*e.g.* in the blood there is ca. 140 mM Na^+/5 mM K^+ compared to ca. 150 mM K^+/10 mM Na^+ inside cells).[398] However, some early studies of a series of G-rich oligonucleotides indicated that G4 formation is necessary, but not sufficient, for antiproliferative effects.[399–401] A few studies have explicitly investigated whether the G4 structure of AS1411 is affected by attaching it to various particles. Based on CD analyses, AS1411 maintains its parallel-type G4 structure when is conjugated to gold nanospheres[410,411] gold nanostars,[412] gold nanoclusters,[413] or quantum dots.[414] Only in one study performed by Odom *et al.*, after immobilization of the sequence onto gold nanostars, an antiparallel G4 CD signature has been observed, probably due to the specific experimental conditions or their use of a modified AS1411 sequence lacking the final 3′-G base.[415]

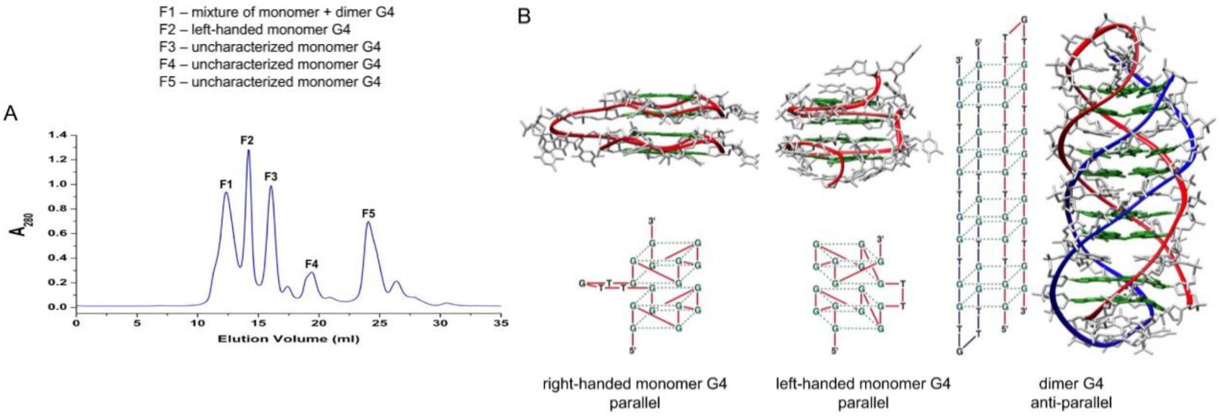

Figure 62. Structures of AS1411. (A) Size exclusion chromatogram showing a number of distinct G4 species formed by AS1411 in a K^+-containing solution. (B) Possible G4 structures of AS1411. For clarity, the single Ts in the loops of the monomer structures are not shown. Picture reproduced from Trent et al.[398]

3.1. Clinical development of AS1411

The clinical development of AS1411 has been reviewed in several articles[398,402,416,417] and in a book.[418] Aptamera, a Louisville-based start-up company, initiated Phase I clinical trials of AS1411 (known at that time as AGRO100) in 17 patients with advanced cancers in 2003 and British biotechnology company Antisoma acquired Aptamera in 2005 following its promising results.[419,420] Antisoma extended the Phase I studies (clinicaltrials.gov identifier: NCT00881244) and performed Phase II trials of AS1411 as monotherapy in patients with renal cell carcinoma who had failed or were unable to tolerate standard treatment (NCT00740441) and in combination with cytarabine in patients with refractory or relapsed acute myeloid leukemia (NCT00512083). In 2011, Antisoma stopped drug development operations after its lead drug candidate (a small molecule named AS1413, which is unrelated to AS1411) failed in pivotal Phase III trials and consequently the ongoing Phase IIb trial of AS1411 (NCT01034410) was terminated.[421] Advanced Cancer Therapeutics have since acquired the rights to AS1411 and the drug has been renamed ACT-GRO-777. To our knowledge, there are no clinical studies of AS1411 being carried out at present.

Based on published articles and meeting reports,[402,419,420,422–425] the clinical results for AS1411 can be thus summarized: (i) AS1411, tested in over 100 patients, is well tolerated with no evidence of severe side effects with continuous infusion dosing of up to 40 mg/kg/day for 7 days, (ii) the overall response rate is low but at least 7 patients - 3 with renal cell carcinoma and 4 with acute myeloid leukemia - had long-lasting clinical responses where their cancers disappeared or shrank substantially, and (iii) steady-state plasma concentrations of AS1411 have been in the range of 1–6 μM or less during clinical trials.

Thus, AS1411 has still some potential for clinical impact due to its excellent safety profile and ability to induce durable responses in some patients with intractable cancers.[398]

However, the suboptimal pharmacology and low potency of this unmodified DNA may limit its future development in unselected cancer patients. Therefore, a valuable alternative approach would be to develop novel formulations of AS1411 with improved pharmacokinetics and higher potency compared to the original, such as the gold nanosphere and nanostar-linked versions.[426–430] Other possibilities include identifying synergistic combinations of AS1411 with existing drugs, developing modified versions of AS1411 with alternative nucleobases or backbones (though this has led to only modest improvements so far),[431–435] or using the targeting properties of AS1411 to deliver drugs or contrast agents selectively to cancer cells.

3.2. Nanoformulations of AS1411 with improved activity

Several examples of nanoformulations of AS1411 have been reported in literature. Bates *et al.* have described stable gold nanospheres (GNS) consisting of 6 nm cores coated with ca. 40 strands of AS1411.[430] *In vivo* experiments, using nude mice with breast cancer xenografts, demonstrated that the conjugation dramatically increased the cellular accumulation, antiproliferative activity, and cytotoxicity of the aptamer, maintaining its selectivity for cancer cells.[430]

On the other hand, also “Apt-AuNS” - consisting of 25-45 nm gold nanostars coated with 110-950 strands of AS1411[412,426–428], developed by Odom *et al.* - proved to be able to accumulate around and inside the nucleus of cancer cells and to reduce the viability of cancer cells when used alone or following laser light irradiation to stimulate the release of AS1411 from the nanostars.[412,415,426–429] Apt-AuNS have shown high antiproliferative effects against a broad range of cancer cell types with no inhibitory effects on non-malignant cells at comparable concentrations,[412,428] even in organs with high uptake levels (*e.g.* liver, spleen).[429] In addition, AS1411-GNS and Apt-AuNS may also be useful as cancer-targeted radiosensitizers in radiation therapy, allowing to improve accumulation and cell uptake in tumor tissues, *i.e.* the main limitations of untargeted gold nanoparticles.[436]

3.3. AS1411 as a targeting agent for cancer-selective drug delivery and imaging

Another attractive feature of AS1411 is the possibility of using this aptamer to direct into malignant cells attached molecules or particles (Figure 63). Some of the earliest examples have involved coating liposomes, quantum dots, or iron oxide nanocrystals with the aptamer for cancer-selective delivery of drugs or imaging agents.[414,437–439]

Very recently a resuming overview of the applications of AS1411-linked nanomaterials as therapeutic and imaging agents has been reported.[398]

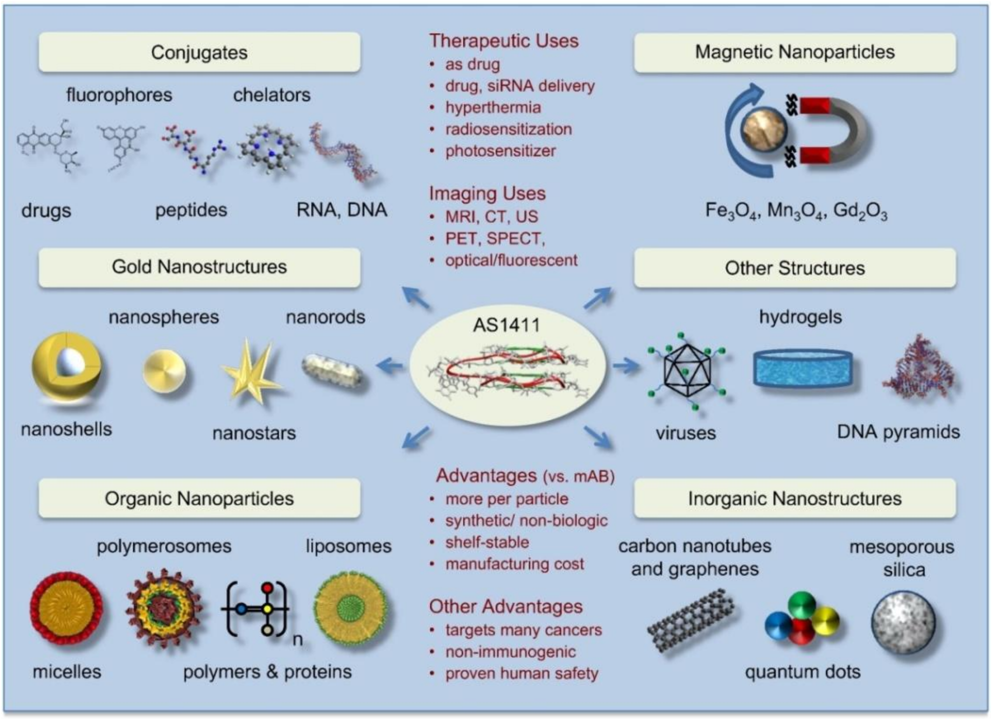

Figure 63. Schematic representation of the uses and advantages of AS1411 as a cancer-targeting agent, showing the variety of structures that AS1411 has been conjugated to for cancer targeting. The bullet points (red text) indicate potential clinical applications for AS1411-conjugated materials and advantages of using AS1411 compared to monoclonal antibodies or alternative targeting agents (*e.g.* other aptamers, small molecules, peptides). Picture reproduced from Trent et al.[398]

Several AS1411-linked conjugates or particles - mainly based on nanoparticles or liposomes - for the delivery of chemotherapeutic agents (as Paclitaxel,[440,441] Docetaxel,[442–444] Doxorubicin,[413,445–452] and Epirubicin)[453] small interfering RNA (siRNA)[454,455] and therapeutic protein[456] have been tested *in vivo* and/or in animal models for therapeutic effects. On the other hand, also AS1411-linked conjugates or particles have been developed and tested *in vivo* and in animal models as imaging agents for PET, SPECT, CT, MRI and fluorescence analysis.[413,432,457–466]

AS1411-linked materials have superior cancer cell uptake and/or tumor accumulation compared to untargeted materials or free drugs, though not all include other important controls such as non-aptamer DNA-linked materials. For small molecule chemotherapy drugs, there is some evidence that delivery *via* AS1411-conjugated particles can circumvent drug-resistance pumps,[451] pass the blood-brain barrier,[442] and reduce toxicity to normal tissues.[448,449,451]

3.4. Role of nucleolin in the mechanism of AS1411

Despite the widespread use of AS1411 and the general acceptance that it functions as a nucleolin aptamer, its precise mechanism of action is still uncertain.

The presence of nucleolin on the cell surface, initially assumed as surprising for a protein considered to be predominantly nucleolar, has been then largely demonstrated.[467–469] In addition to mediating cellular internalization, nucleolin is also implicated in trafficking molecules throughout the cell and mediating their signaling from the plasma membrane. Nucleolin expression is also strongly induced in response to various forms of cellular stress.[470–474] Hovanessian and colleagues have reported that nucleolin is translocated from the cytoplasm to the cell surface *via* an unconventional secretory pathway in response to mitogenic stimuli, and have proposed that binding of ligands to cell surface nucleolin results in clustering that triggers cell entry by an actin- and Ca^{2+}-dependent process.[470,475] Notably, proliferating cancer cells continuously produce nucleolin in comparison with non-malignant cells to constitutively express nucleolin on cell surface.[398,470] In addition, nucleolin is also involved in the biology of several viral pathologies; in fact AS1411 recently proved to have potent antiviral activity against HIV-1, RSV, and dengue in model systems.[476–478]

Although it is well established that AS1411 is selectively internalized in cancer cells *via* nucleolin and here interferes with certain cancer-associated functions of nucleolin resulting in cancer cell death,[402] several different mechanisms have been proposed to explain the antiproliferative activity of AS1411[399,433,479–489] and recently other studies have suggested a new mode of action for the cancer-targeting mechanism of AS1411 (Figure 64).[490,491]

In 2010, Bates *et al*. studied the uptake of a fluorescently labeled AS1411 at therapeutic concentrations in comparison with a control oligonucleotide (CRO) in several cancer cell lines and in non-malignant cells.[490] They observed that the uptake of AS1411 was much higher than that of the CRO control in the cancer cells, probably through an active transport mechanism since the process was temperature-dependent. Surprisingly, the initial uptake of AS1411 (2 h after addition) was slightly higher in the non-malignant cells than in the cancer cells and was independent of nucleolin. They also investigated which of the various forms of endocytosis (*e.g.* clathrin-mediated, caveolin-mediated, or macropinocytosis)[492] contributes to AS1411 internalization, finding as main mechanism the macropinocytosis, which is an actin-driven, ligand-independent mechanism where cells “gulp” the surrounding medium and any macromolecules it contains.[490,491]

On the contrary, evaluating the uptake of AS1411 at later time points (24–72 h after addition), the same group discovered that AS1411 stimulates macropinocytosis in cancer cells but not in non-malignant cells, leading to additional cancer-selective uptake of the aptamer. This AS1411-stimulated form of macropinocytosis was found to be dependent on nucleolin.[490,491] These results are not unprecedented since macropinocytosis has been reported as a major route of internalization for naked DNA, naked RNA, aptamer conjugates, nanoparticles, and many viruses,[493–497] since cancer cells have inherently high levels of macropinocytosis compared to normal cells.[490,498] In the final phase, the nucleolin-mediated trafficking is suppressed and the aptamer is trapped inside cancer cells.[491]

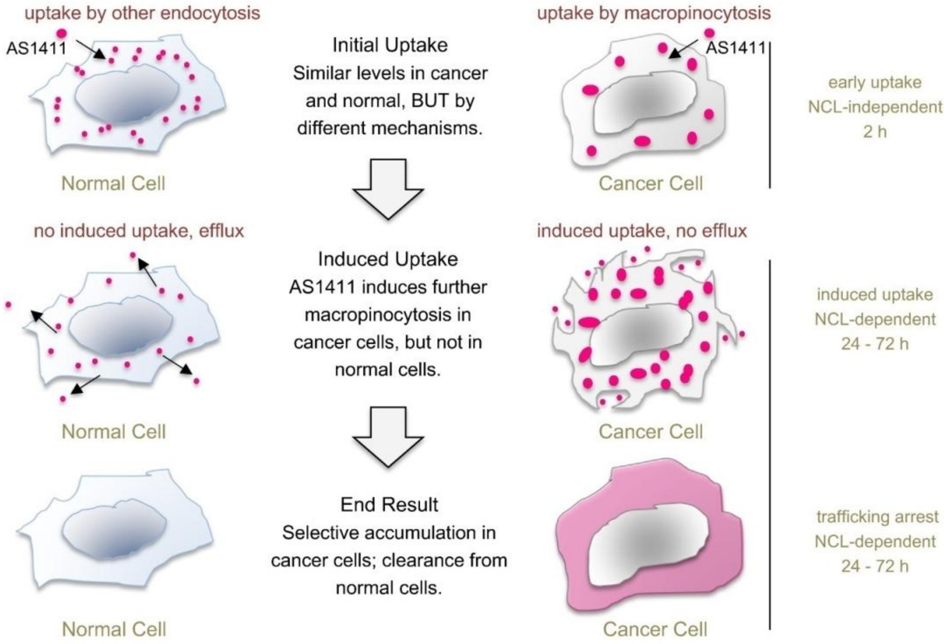

Figure 64. Model for the mechanism of AS1411 selective accumulation in cancer cells. AS1411 is efficiently taken up in cancer and normal cells at early time points, but by different endocytic pathways. Then, AS1411 induces further macropinocytosis and trafficking arrest in cancer cells but not in normal cells. These effects are nucleolin (NCL)-dependent and result in AS1411 being selectively retained in cancer cells compared to normal cells.

To explain why AS1411 and AS1411-conjugates have selective accumulation in cancer cells compared to normal cells, it has been proposed that, after initial uptake by a non-macropinocytosis form of endocytosis, AS1411 is gradually cleared from normal cells - by efflux or exocytosis – or it undergoes lysosomal degradation in normal cells. In other words, the selective accumulation of AS1411 in cancer cells is due to both enhanced uptake and increased retention.[398]

Although there are several evidences to support this model[490,491] some differences emerged in the uptake and trafficking of AS1411-linked particles of malignant *vs.* non-malignant cells,[499,500] with some contradictory findings on the initial nucleolin-dependence and subsequent trafficking.[495,501]

In addition, from Phase II trials an activating mutation in mTOR has been highlighted in patients who had a dramatic response to AS1411.[425] This finding is particularly intriguing because mTOR is regulated by Rac1 and has roles in macropinocytosis and intracellular trafficking;[502–510] however, additional research will be needed to confirm the possible role of mTOR in AS1411 activity. At present, it is unclear how to reconcile the many different proposed mechanisms; most likely, AS1411 can induce multiple biological effects and its internalization and trafficking depends on a large number of variables (such as concentration, time, cell type, and attached cargo).

4. Studies on the conformational behaviour and molecularity of natural and modified AS1411 aptamers

Considering its great potential for the cancer cell-selective recognition, in principle useful also for the delivery of drugs and imaging agents, AS1411 can represent a perfect active targeting ligand in the construction of multifunctional systems for anticancer applications. Although much attention has been paid to AS1411 *in vivo* functions, its structural features, and particularly its bioactive conformation, are still largely unknown. Indeed, some discrepancies on the preferred AS1411 conformation, in some cases described as a parallel[404,410–414] and in others as antiparallel G-quadruplex,[415] have been reported. Furthermore, only few studies have been carried out in order to get detailed information on the structure, molecularity and thermal stability of this aptamer[404]. Recently, Azizi and collegues[511] have investigated the optical properties and thermodynamic stability of AS1411 in the presence of different concentrations of metal ions (K^+ and Pb^{2+}) and in molecular crowding condition, confirming that AS1411 folds into a parallel G4 structure in the presence of both metal ions as well as of PEG.

Therefore, with the aim of exploiting AS1411 as an active targeting agent for multifunctional, theranostic nanoplatforms, we here selected some AS1411 derivatives (Figure 65) presenting at their 5'-end biocompatible lipophilic tails, useful for their subsequent insertion into liposomes or lipid coated-NPs. In detail, we focused on the 5'-stearyl-AS1411, presenting a saturated 18-carbon alkyl chain, and other two derivatives, the 5'-cholesteryl-TEG- and the 5'-cholesteryl-C6-AS1411, both presenting a cholesterol residue linked to the oligonucleotide sequence through a triethylene glycol or a 6-carbon atoms alkyl chain, respectively. In particular, the 5'-stearyl-AS1411 has a lipophilic tail of the same length as 18LPC, recently used as coating of superparamagnetic nanoparticles (SPIONs) with a core/double shell architecture[174] - developed by the research group of prof. Luigi Paduano. Thus, this conjugating agent is in principle able to establish hydrophobic interactions with 18LPC and, more in general, with any lipid residue (*e.g.* liposome-based platforms). On the other hand, the cholesterol residue already proved to be effective to ensure the insertion of specific agents in a liposome structure[136,137] or into phosphocholine-functionalized SPIONs (18LPC/SPIONs).[174]

In this frame, during my PhD thesis, the behavior of these AS1411 derivatives has been investigated also in solution using different techniques, in comparison with the unmodified aptamer. In particular, CD, CD-melting, UV-melting, gel electrophoresis and size exclusion chromatography analysis have been carried out to get information on their conformational behaviour, secondary structure and thermal stability of their preferred conformations. This study was carried out in two different buffered solutions and at different oligonucleotide concentrations; special attention was devoted to the investigation of possible effects due to the nature of the lipophilic tail, or of the specific linker inserted, on the overall structure and conformation of the aptamer.

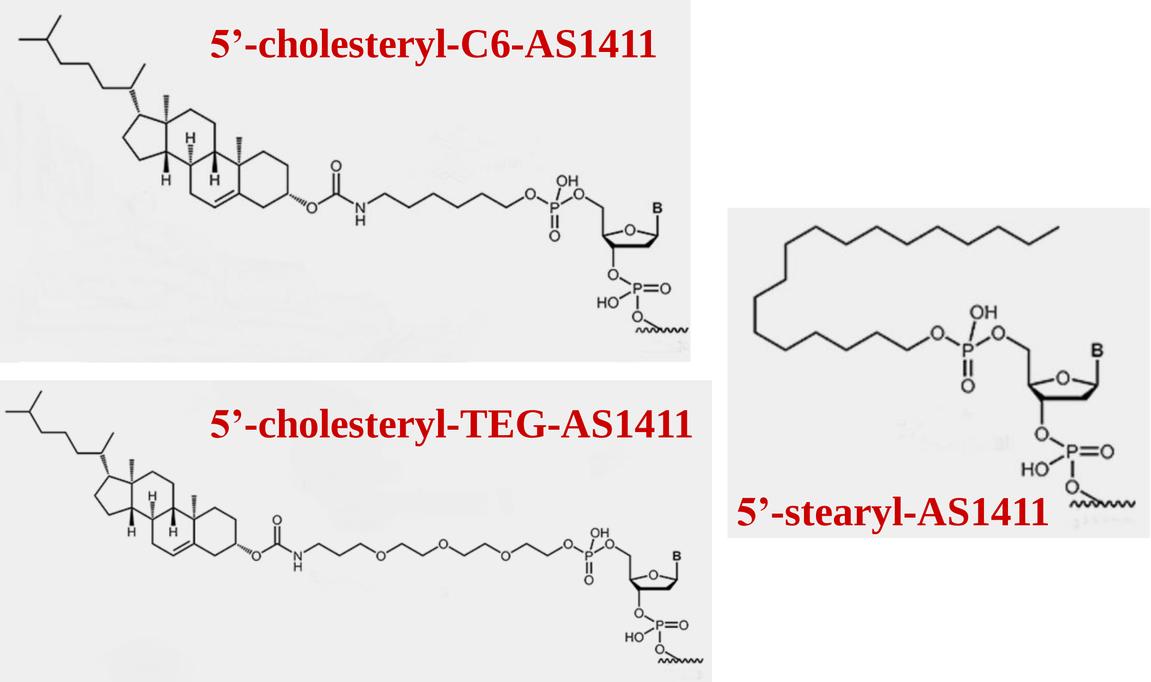

Figure 65. AS1411 derivatives selected as potential active targeting ligands in the construction of liposome or NP-based anticancer multifunctional systems.

4.1. Results and discussion

4.1.1. Spectroscopic properties and solution behaviour of AS1411

The conformational behaviour in solution of AS1411 was investigated combining CD, CD-melting and UV-melting data. The spectra and melting/annealing profiles were recorded in two different phosphate buffered solutions containing a high content of K^+ (10 mM KH_2PO_4, 70 mM KCl, 0.2 mM EDTA, pH 7.0) or of Na^+ ions (PBS: 137 mM NaCl, 2.7 mM KCl, 10 mM Na_2HPO_4, 1.8 mM KH_2PO_4, pH 7.4) in order to evaluate the effect of different saline conditions. In addition, we also tested three different concentrations of each aptamer (10, 5 and 2.5 μM) to investigate possible concentration-dependent effects on its conformation and stability.

The CD spectra at r.t. of AS1411 at the analysed concentrations, either in K^+ or Na^+ buffer solutions, in all cases show a negative band with a minimum at ca. 241 nm, and two positive bands with maxima centred at 263 nm, the highest one, and at ca. 295 nm, the weakest (Figure 66). In PBS solution the aptamer presents a lower degree of structuration than in the phosphate buffer containing only K^+ ions, as expected considering that these cations can better stabilize G4 structures than Na^+, in accordance with literature studies.[388–391] In addition, the weak band at ca. 295 nm is more evident in the spectra recorded in Na^+ buffer.

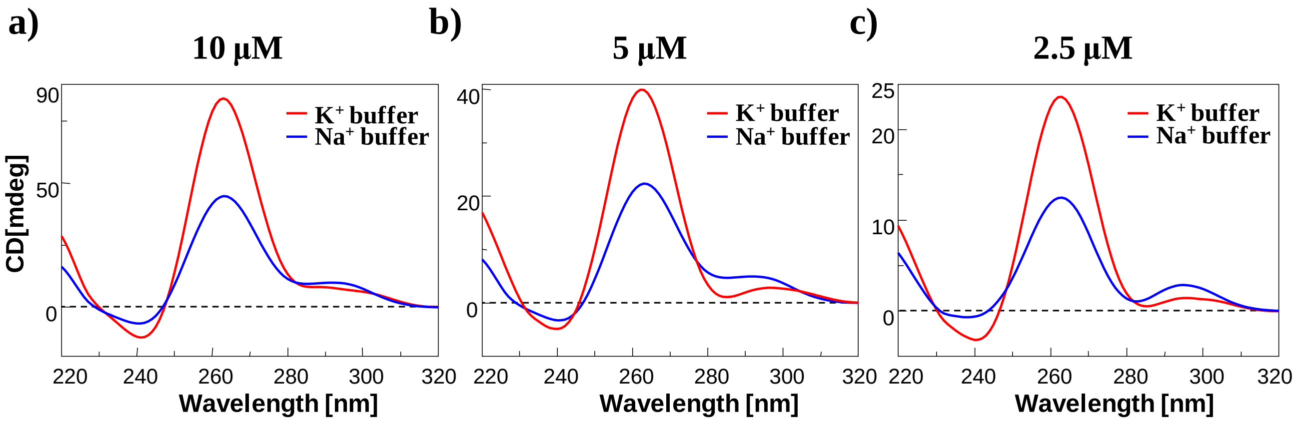

Figure 66. Overlapped CD spectra of AS1411 at 10 µM (**a**), 5 µM (**b**) and 2.5 µM (**c**) in different saline conditions: potassium buffer (red line) and sodium buffer (blue line) solutions.

These spectral features are consistent with a predominant parallel G-quadruplex structure[382–387,512] and in agreement with the CD spectrum of AS1411 reported in previous works,[402,404,434] with only a very low fraction of an antiparallel conformation, as evidenced by the weak band at ca. 295 nm. The CD melting profile, monitored at 263 nm in K^+ buffer, provided a melting temperature of 66 °C at 10 µM (Figure 67) and of 68 °C at 5 and 2.5 µM concentrations (Figure 68a and 68b, respectively), indicating the formation of quite stable species. No significant hysteresis emerged on comparing the heating and cooling curves (Figure 67), thereby indicating that, under the experimental conditions used (scan rate: 1 °C/min), the studied systems are in equilibrium. The comparison between heating and cooling profiles is reported only for the 10 µM conc. sample as a representative example.

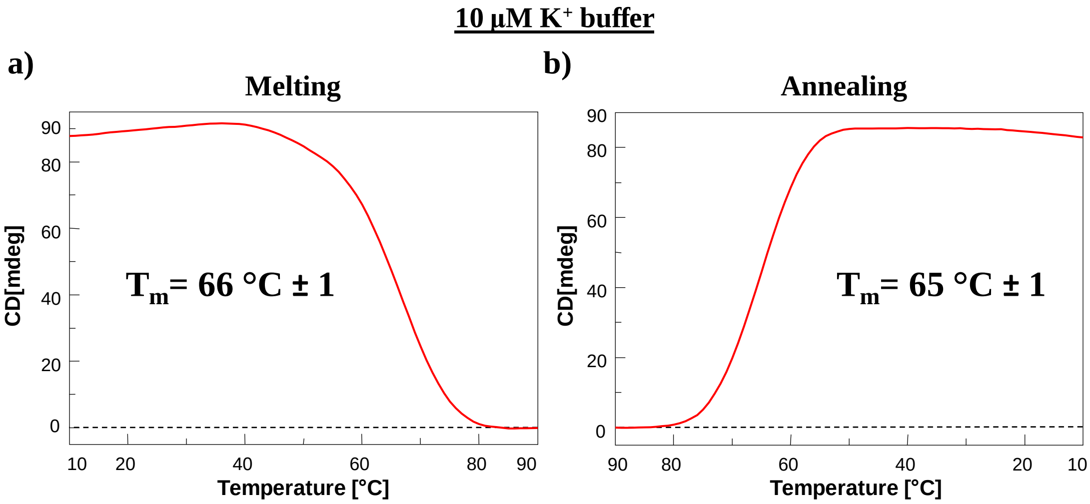

Figure 67. **a**) CD melting and **b**) CD annealing profiles of AS1411 in the selected K^+ buffer solution at 10 µM concentration, recorded at 263 nm (scan rate: 1 °C/min).

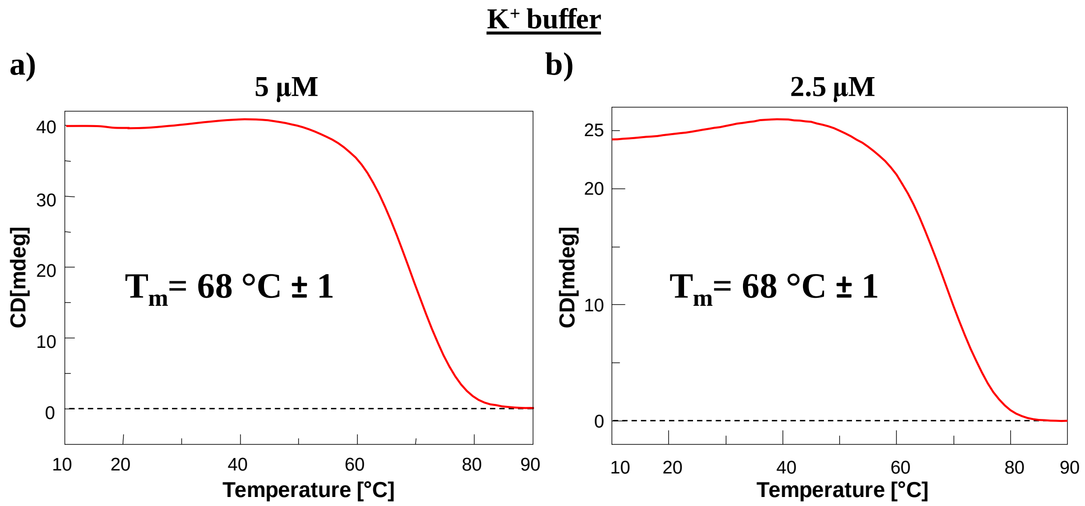

Figure 68. CD melting profiles of AS1411 in the selected K^+ buffer solution at 5 µM (**a**) and 2.5 µM (**b**) concentrations, recorded at 263 nm (scan rate: 1 °C/min).

Lower melting temperatures were observed in the Na^+ buffer solution with respect to the K^+ buffer, monitoring the CD signal at 263 nm on increasing the temperature: melting temperatures of 38 °C at 5 µM concentration (Figure 70a) and of 37 °C at 10 and 2.5 µM concentration (Figure 69a and 70b, respectively) were found. Also for these systems, no significant hysteresis emerged on analysing the heating and cooling profiles; as a representative example, this comparison is reported for the 10 µM concentration sample (Figure 69).

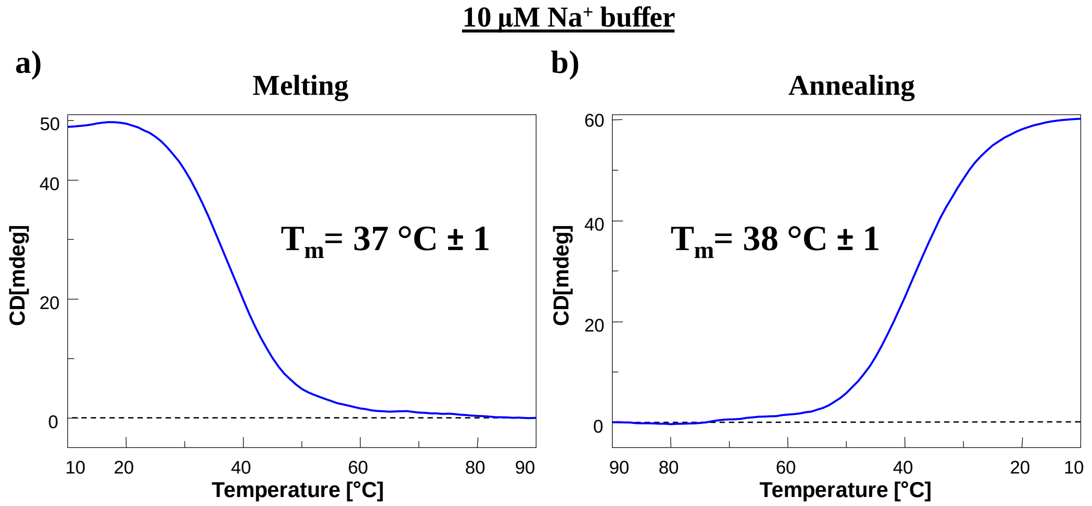

Figure 69. **a**) CD melting and **b**) CD annealing profiles of AS1411 in the selected Na^+ buffer solution at 10 µM concentration, recorded at 263 nm (scan rate: 1 °C/min).

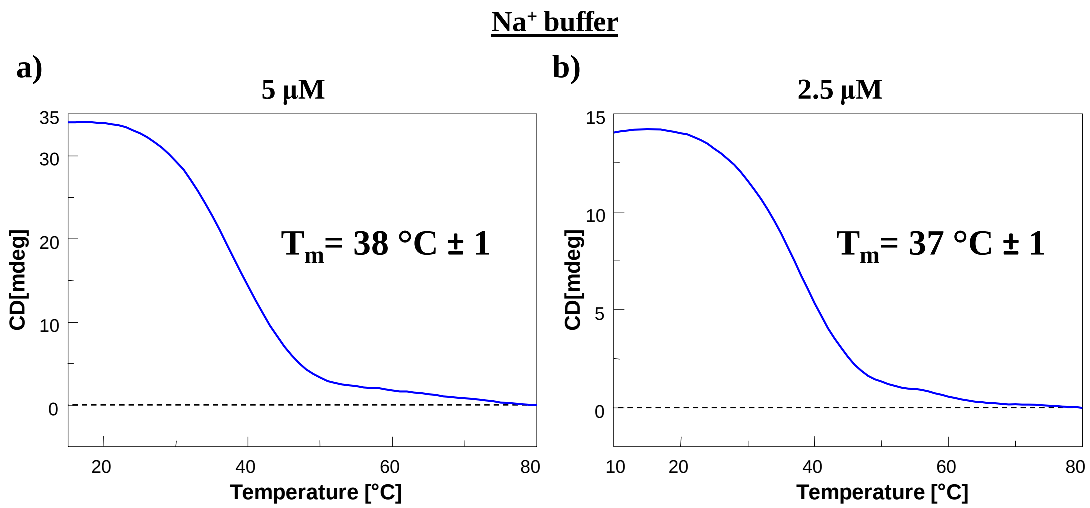

Figure 70. CD melting profiles of AS1411 in the selected Na$^+$ buffer solution at 5 µM (**a**) and 2.5 µM (**b**) concentrations, recorded at 263 nm (scan rate: 1 °C/min).

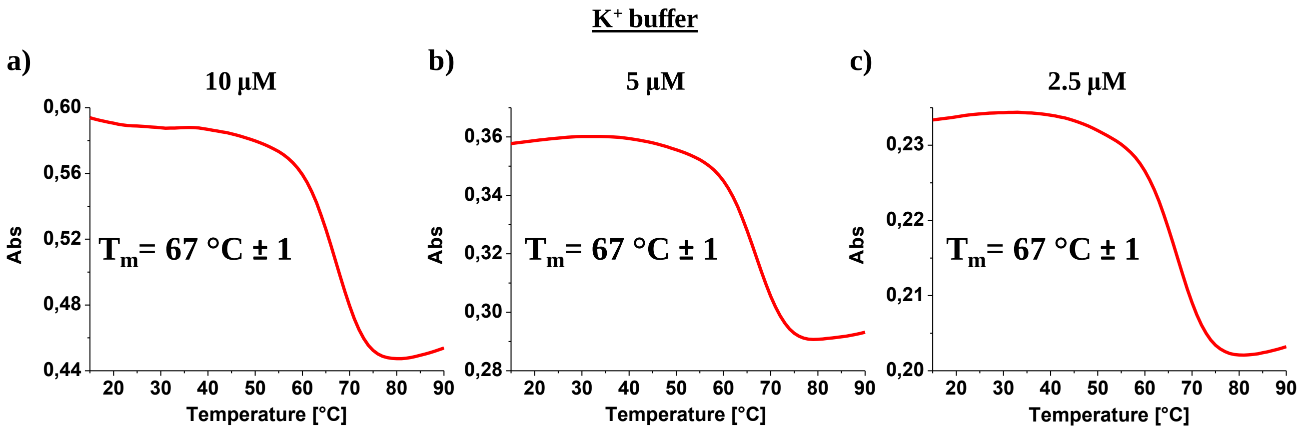

Figure 71. UV-melting profiles of AS1411 in the selected K$^+$ buffer solution at 10 µM (**a**), 5 µM (**b**) and 2.5 µM (**c**) concentrations, recorded at 295 nm (scan rate: 1 °C/min).

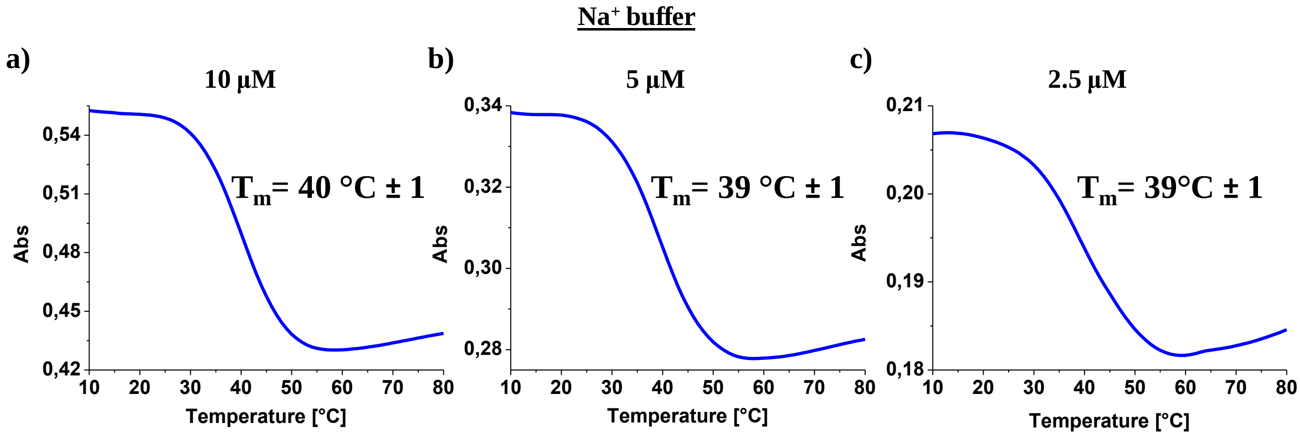

Figure 72. UV-melting profiles of AS1411 in the selected Na$^+$ buffer solution at 10 µM (**a**), 5 µM (**b**) and 2.5 µM (**c**) concentration, recorded at 295 nm (scan rate: 1 °C/min).

In agreement with the CD data, from the UV-melting curve monitored at 295 nm,[386,392,393] a T_m of 67 °C in K$^+$ buffer was obtained at all the tested concentrations, evidence of thermodynamically stable species (Figure 71). In turn, in the Na^+ buffer solution a T_m of 40 °C at 10 μM concentration (Figure 72a) and of 39 °C at 5 and 2.5 μM concentration (Figure 72b and 72c, respectively) was found. Also in this case, the melting process was fully reversible, with no significant hysteresis observed on comparing the heating and cooling processes (data not shown).

In summary, a good agreement between the T_m values determined by UV- and CD-melting experiments (Table 7), within the experimental error, was always found. As expected, AS1411 formed G-quadruplex structures with higher stability in the K^+ buffer solution than in Na^+. Taking into account these experiments, this different thermal stability is mainly dependent on the saline conditions and not on the concentration, proving that AS1411 mainly forms a unimolecular G-quadruplex, at least at the analysed concentrations.

	K^+ buffer		**Na^+ buffer**	
AS1411 conc.	**CD T_m (°C) ± 1**	**UV T_m (°C) ± 1**	**CD T_m (°C) ± 1**	**UV T_m (°C) ± 1**
10 μM	**66**	**67**	**37**	**40**
5 μM	**68**	**67**	**38**	**39**
2.5 μM	**68**	**67**	**37**	**39**

Table 7. Melting temperature values obtained by UV- and CD-melting experiments for AS1411.

4.1.2. Spectroscopic properties and solution behaviour of lipophilic AS1411 derivatives

All the here examined AS1411 derivatives have been analysed using the same kind of spectroscopic characterization performed to investigate if the presence of a lipophilic tail can influence the preferential conformations of AS1411 in solution. Thus, UV and CD experiments were performed at three different concentrations and in two different phosphate buffers.

5'-stearyl-AS1411

The CD spectrum at r.t. of 5'-stearyl-AS1411 shows a positive ellipticity maximum at 263 nm and a negative ellipticity minimum at ca. 241 nm (Figure 73), both in K^+ and Na^+ buffer solutions, characteristic of a prevalent parallel G-quadruplex conformation, as in the case of the unmodified aptamer. The weak positive band at 295 nm present in the CD spectra of AS1411 was not evident in this case at 10 μM concentration both in K^+ and Na^+ buffer, and in turn appeared as a broad double-dump band in K^+ buffer and as a broad shoulder in Na^+ buffer (both at 5 and 2.5 μM). Again the K^+ ions show higher structuring effect on G-quadruplex formation.

The CD melting profile, monitored at 263 nm, provided a melting temperature of 59 °C in K^+ buffer solution at all the tested concentrations (Figures 74 and 75). No significant hysteresis was observed between the melting and cooling profiles - reported only at 10 μM concentration as representative example - suggesting a reversible process at the scan rate used (1 °C/min).

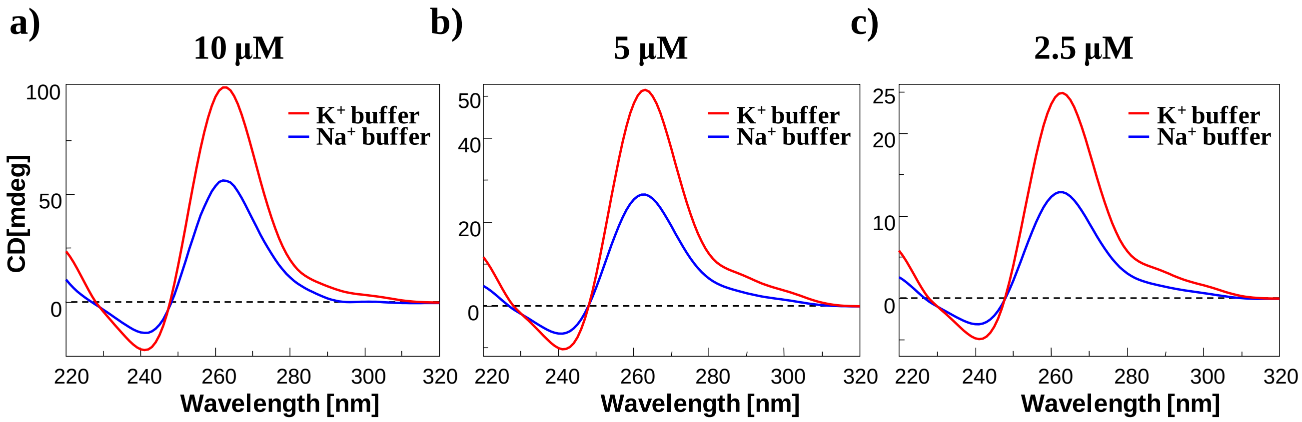

Figure 73. Overlapped CD spectra of 5’-stearyl-AS1411 at 10 µM (**a**), 5 µM (**b**) and 2.5 µM (**c**) in different saline conditions: potassium buffer (red line) and sodium buffer (blue line) solutions.

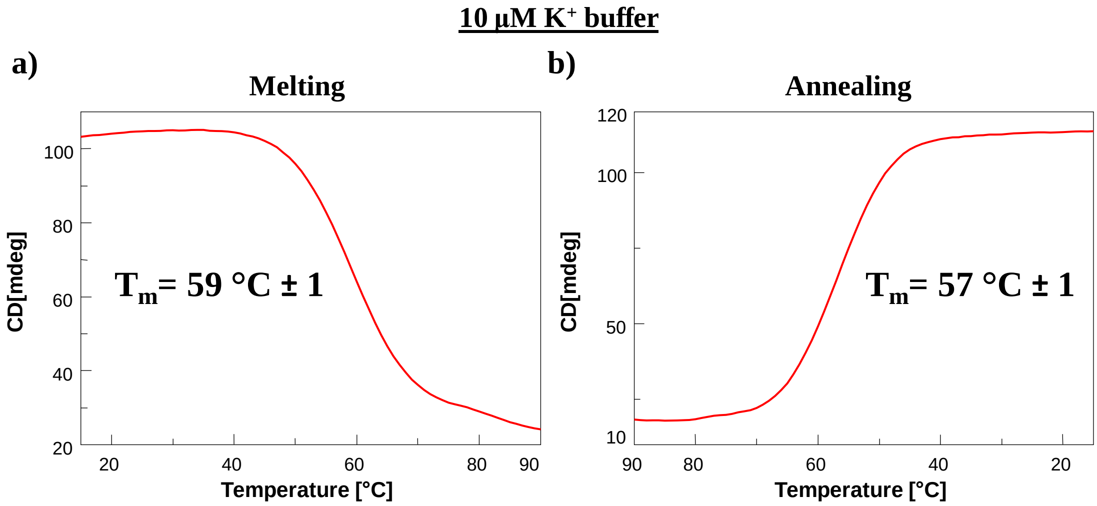

Figure 74. **a**) CD melting and **b**) CD annealing profiles of 5’-stearyl-AS1411 in the selected K$^+$ buffer solution at 10 µM concentration, recorded at 263 nm (scan rate: 1 °C/min).

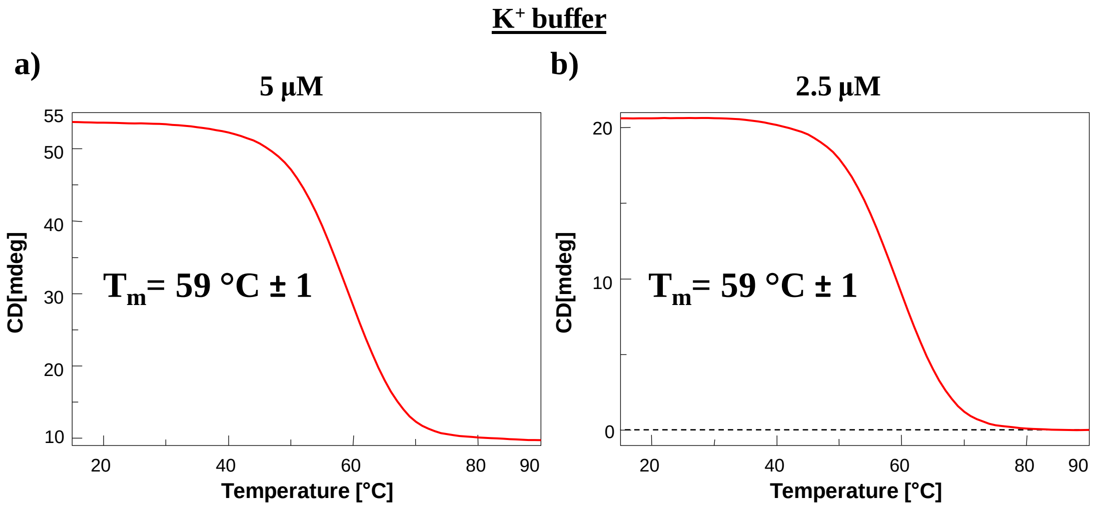

Figure 75. CD melting profiles of 5’-stearyl-AS1411 in the selected K$^+$ buffer solution at 5 µM (**a**) and 2.5 µM (**b**) concentrations, recorded at 263 nm (scan rate: 1 °C/min).

CD melting profiles, monitored at 263 nm, in Na^+ buffer solution, evidenced lower T_m values, of 40 and 39 °C, respectively at 5 and 2.5 µM concentrations (Figures 76a and 76c) with small hysteresis effects only in the case of the 5 µM conc. sample: at this concentration the annealing profile provided a T_m of 37 °C (Figure 76b).

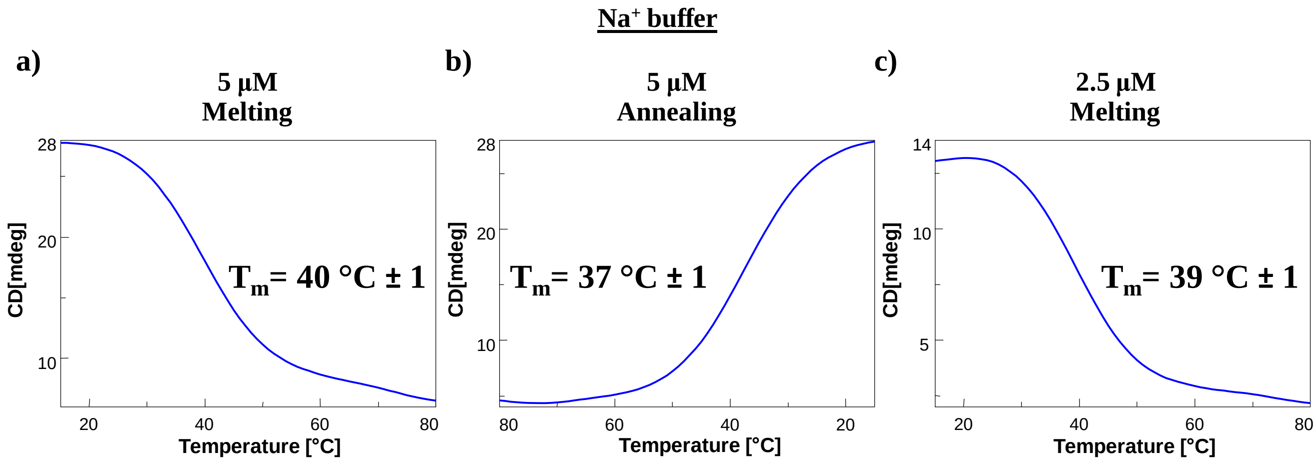

Figure 76. CD melting (**a**,**c**) and CD annealing profiles (**b**) of 5’-stearyl-AS1411 in the selected Na^+ buffer solution at 5 µM (**a, b**) and 2.5 µM (**c**) conc., recorded at 263 nm (scan rate: 1 °C/min).

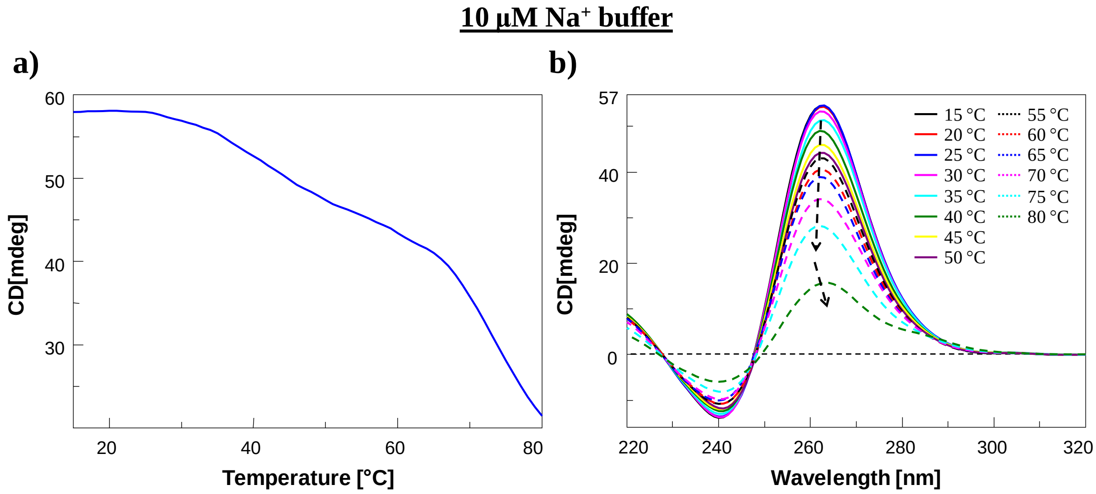

Figure 77. **a**) CD melting profile and **b**) spectra recorded every 5 °C of 5’-stearyl-AS1411 in the selected Na^+ buffer solution at 10 µM concentration, recorded at 263 nm (scan rate: 1 °C/min).

Notably, at 10 µM concentration in Na^+ buffer a peculiar behaviour was found: the melting profile did not show the typical sigmoidal shape, but a curve with multiple transitions, with a not complete denaturation of the structures in solution at 80 °C (Figure 77). From the analysis of the CD spectra at increasing temperatures the appearance of a new, weak band at 285 nm visible starting from 75 °C was evidenced (light blue and green dashed lines in Figure 77b). In addition, on increasing the temperature, a shift in the maximum of the positive band was also observed. Thus, starting from 30

°C the positive maximum shifts at 262 nm and then returns at 263 nm at 80 °C. Probably, multiple events occur during the thermal denaturation process (*e.g.* unfolding/refolding of different G4 species), overlapping with the dissociation of the prevailing G4 structure.

The UV-melting profiles, monitored at 295 nm, provided at all tested concentrations a melting temperature of 59 °C and 40 °C in K^+ and Na^+ buffer solutions, respectively (Figures 78 and 79). Also in this case, the melting process was fully reversible, with no significant hysteresis observed on comparing the heating and cooling processes (data not shown).

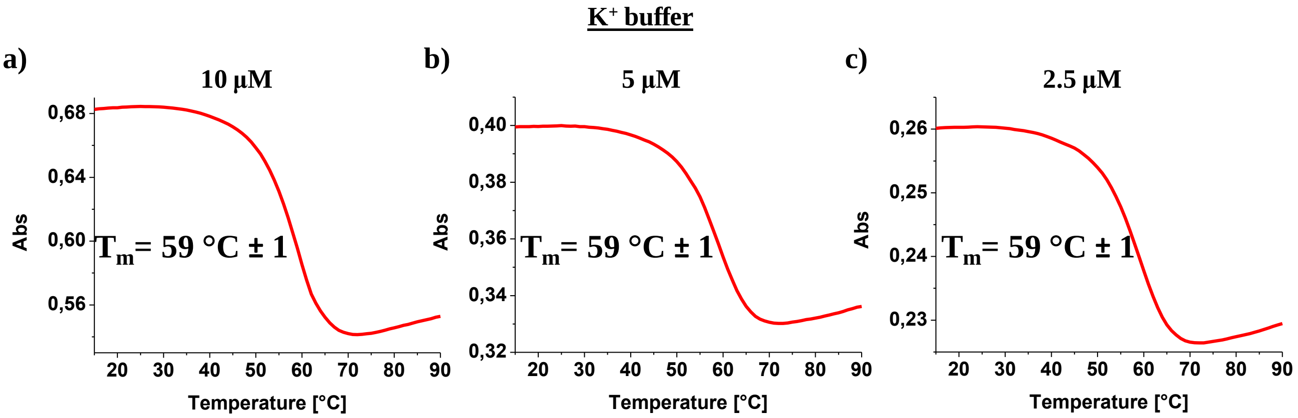

Figure 78. UV-melting profiles of 5’-stearyl-AS1411 in the selected K^+ buffer solution at 10 µM (**a**), 5 µM (**b**) and 2.5 µM (**c**) concentration, recorded at 295 nm (scan rate: 1 °C/min).

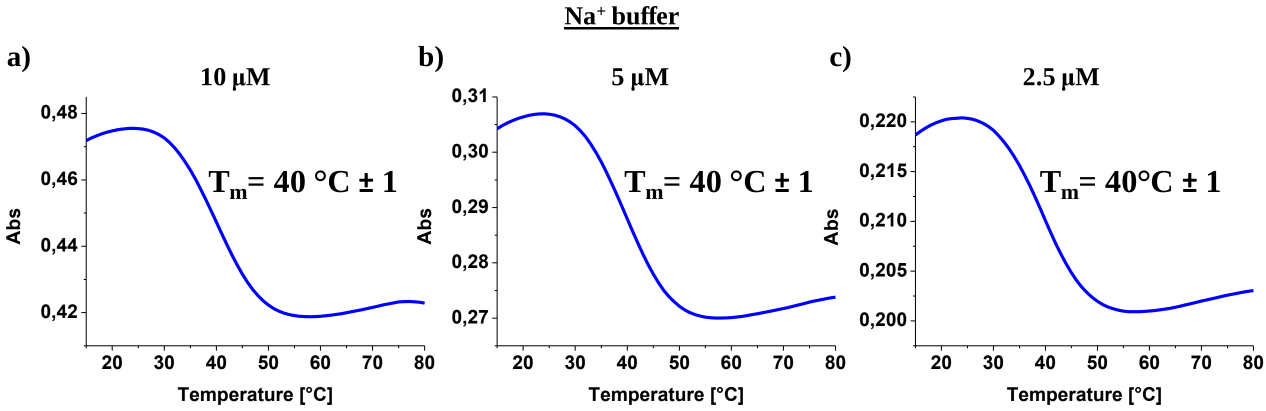

Figure 79. UV-melting profiles of 5’-stearyl-AS1411 in the selected Na^+ buffer solution at 10 µM (**a**), 5 µM (**b**) and 2.5 µM (**c**) concentration, recorded at 295 nm (scan rate: 1 °C/min).

In summary, a good agreement of T_m values determined by UV- and CD-melting experiments was found (Table 8) for all the conditions except for the 10 µM concentration in Na^+ buffer solution. Furthermore, the T_m values obtained in Na^+ buffer solution for this modified aptamer are very similar to those obtained for AS1411, while in K^+ buffer solution the 5’-stearyl derivative showed a lower thermal stability than AS1411, still remaining very high.

	CD T_m (°C) ± 1		UV T_m (°C) ± 1	
	AS1411	**5’-stearyl-AS1411**	**AS1411**	**5’-stearyl-AS1411**
		K^+ buffer		
10 µM	66	59	67	59
5 µM	68	59	67	59
2.5 µM	68	59	67	59
		Na^+ buffer		
10 µM	37	n.d.	40	40
5 µM	38	40	39	40
2.5 µM	37	39	39	40

Table 8. Melting temperature values obtained by UV- and CD-melting experiments for 5’-stearyl-AS1411 (n.d. = not determined).

5’-cholesteryl-TEG-AS1411

As in the case of AS1411 and of 5’-stearyl-AS1411, the CD spectra of 5’-chol-TEG-AS1411 suggest the formation of a parallel G4 structure showing a predominant positive band at 263 nm and a negative peak at ca. 241 nm (Figure 80), both in K^+ and Na^+ buffer solutions. A lower degree of structuration was observed in the Na^+-containing solution and in all cases, analogously to 5’-stearyl-AS1411, no positive band was present at ca. 295 nm.

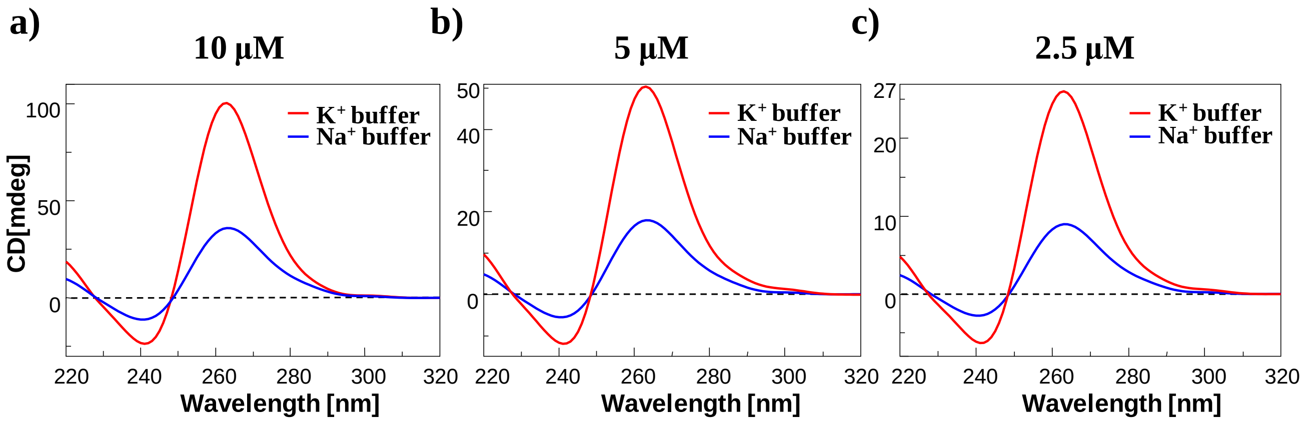

Figure 80. Overlapped CD spectra of 5’-chol-TEG-AS1411 at 10 µM (**a**), 5 µM (**b**) and 2.5 µM (**c**) in different saline conditions: potassium buffer (red line) and sodium buffer (blue line) solutions.

In K^+ buffer solution, CD-melting curves at 263 nm provided similar T_m values at 5 and 2.5 µM concentrations (Figure 81b and 81c, respectively) indicating conversely a lower stability for the system at 10 µM concentration (Figure 81a). In any case, the melting process was fully reversible, with no significant hysteresis observed (data not shown).

Remarkably, in Na^+ buffer solution at 5 and 2.5 µM concentrations a similar behaviour to 5’-stearyl-AS1411 (at 10 µM concentration, Figure 77) was found. Also in this case at 80 °C the structures in solution were not completely denatured. In addition, on increasing the temperature there was a shift in the maximum of the positive band. In this case, starting from 45 °C the positive maximum shifted from 263 nm to 262 nm and remained at this value until 80 °C (Figure 82). This event can be attributed to possible G4 rearrangements and will require a deeper investigation, combining also other techniques for their genuine elucidation.

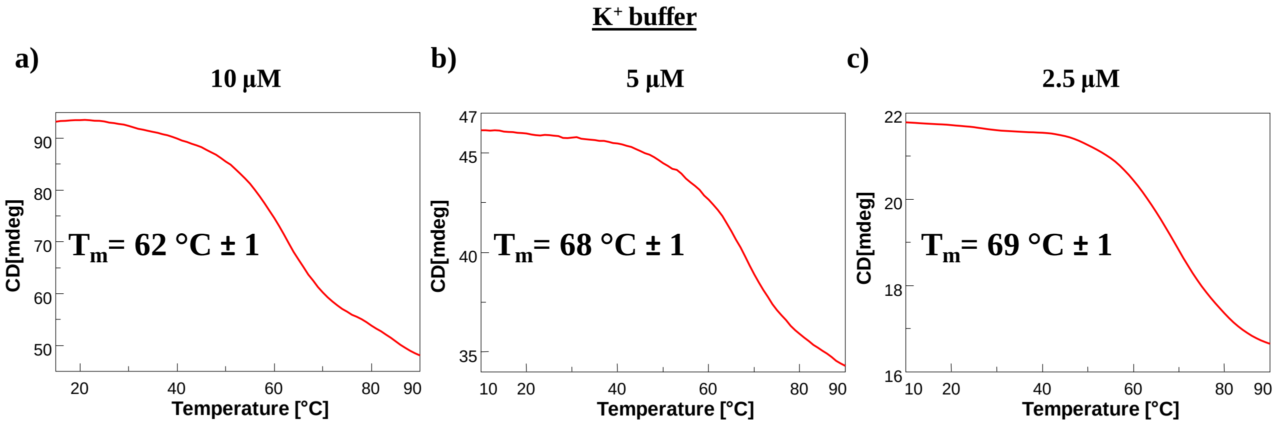

Figure 81. CD melting profiles of 5’-chol-TEG-AS1411 in the selected K^+ buffer solution at 10 µM (**a**), 5 µM (**b**) and 2.5 µM (**c**) concentrations, recorded at 263 nm (scan rate: 1 °C/min).

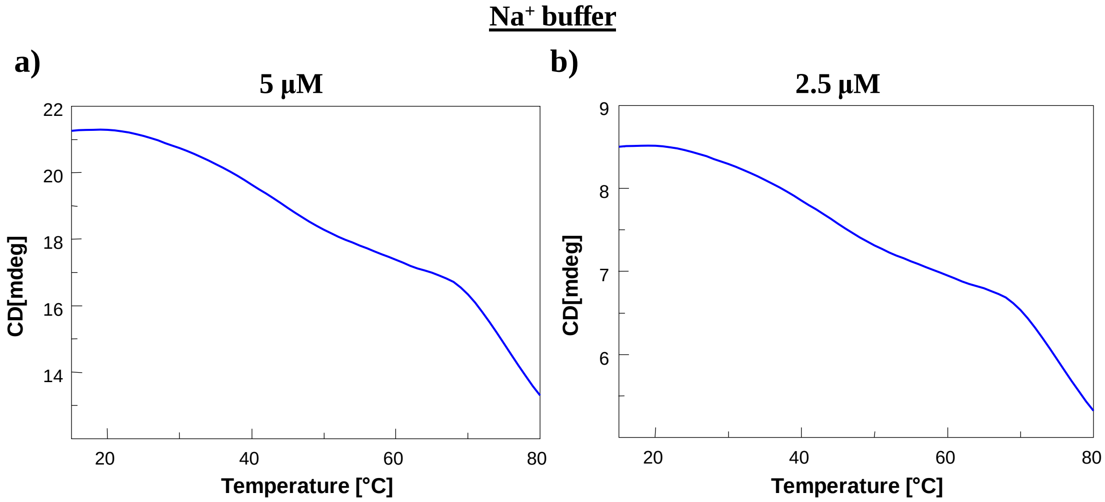

Figure 82. CD melting profiles of 5’-chol-TEG-AS1411 in the selected Na^+ buffer solution at 5 µM (**a**) and 2.5 µM (**b**) concentrations, recorded at 263 nm (scan rate: 1 °C/min).

Next, in the case of melting profile obtained at 10 µM concentration in Na^+ buffer solution, another different behaviour was observed (Figure 83). Initially, the CD signal decreased up to 40 °C, with the positive maximum stable at 263 nm. From 45 °C on, the CD signal intensity began increasing and at 50 ° C a shift of the maximum to 262 nm was also observed. At 65 °C the maximum positive moved back to 263 nm and from 75 °C on a decrease in the CD signal intensity was observed again. The overall result of these events is shown in Figure 83, resulting in an apparent melting temperature of 57 °C. A similar melting profile was already observed in a Na^+ buffer solution for the anomalous “Fraction 2” isolated from AS1411 by Trent *et al.* More in general, melting profiles of fractions recovered from AS1411, recorded in Na$^+$ buffer solution, showed a peculiar behaviour, not indicative of a simple two-state melting process.[404]

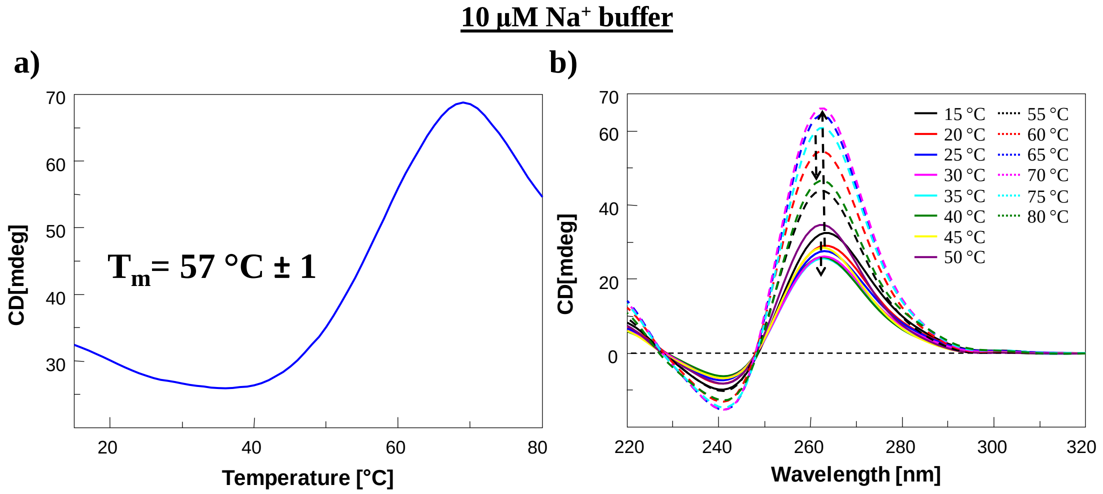
10 μM Na$^+$ buffer

Figure 83. a) CD melting profile and **b**) spectra recorded every 5 °C of 5’-chol-TEG-AS1411 in the selected Na$^+$ buffer solution at 10 μM concentration, recorded at 263 nm (scan rate: 1 °C/min).

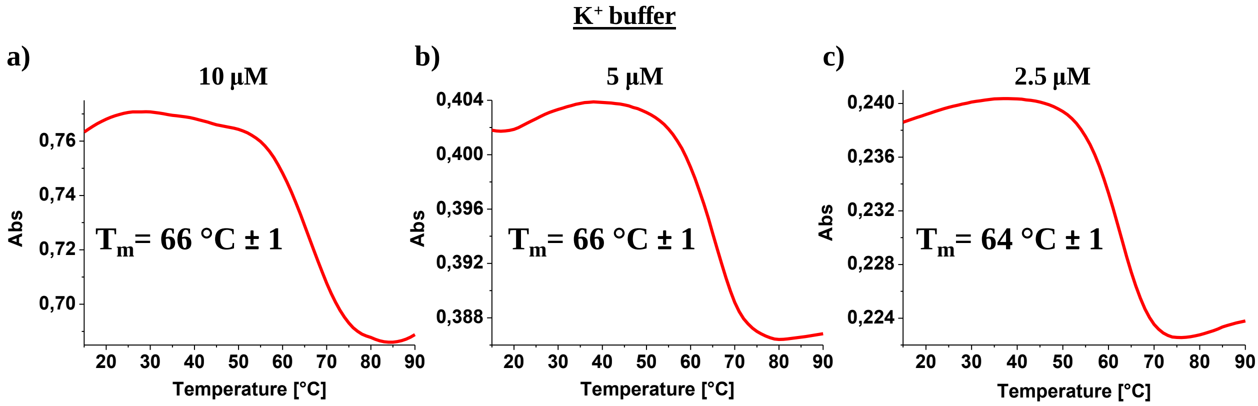
K$^+$ buffer

Figure 84. UV-melting profiles of 5’-chol-TEG-AS1411 in the selected K$^+$ buffer solution at 10 μM (**a**), 5 μM (**b**) and 2.5 μM (**c**) concentration, recorded at 295 nm (scan rate: 1 °C/min).

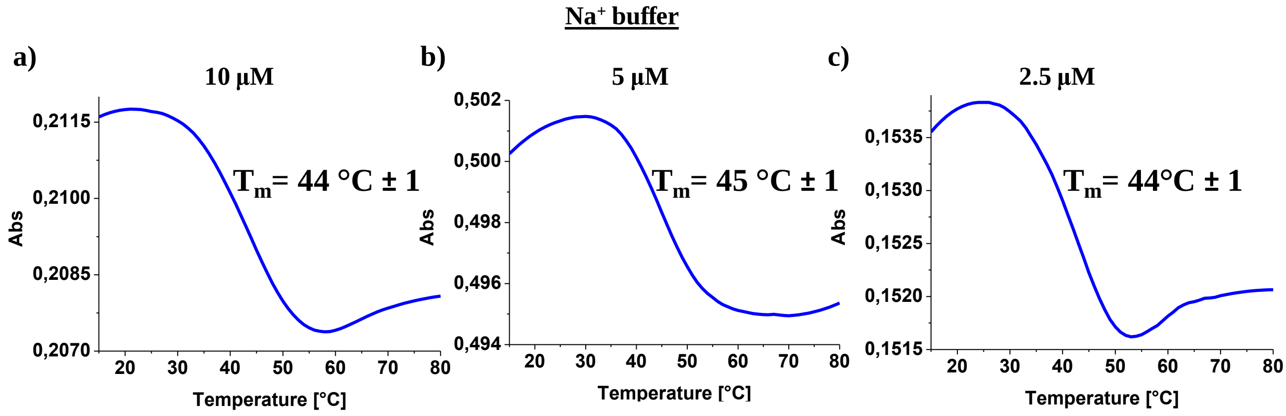
Na$^+$ buffer

Figure 85. UV-melting profiles of 5’-chol-TEG-AS1411 in the selected Na$^+$ buffer solution at 10 μM (**a**), 5 μM (**b**) and 2.5 μM (**c**) concentration, recorded at 295 nm (scan rate: 1 °C/min).

In K^+ buffer solution, the UV-melting curves at 295 nm provided a T_m value of 66 °C at 10 and 5 µM concentrations (Figure 84a and 84b, respectively) and of 64 °C at 2.5 µM concentration (Figure 84c) with no detectable difference between the melting and annealing profiles (data not shown).

In the Na^+ buffer solution the T_m values obtained were very similar, even if in this case a little hysteresis (ca 4 °C) emerged on comparing the melting and annealing profiles (data not shown).

	CD T_m (°C) ± 1		**UV T_m (°C) ± 1**	
	AS1411	**5'-chol-TEG-AS1411**	**AS1411**	**5'-chol-TEG-AS1411**
		K^+ buffer		
10 µM	**66**	**62**	**67**	**66**
5 µM	**68**	**68**	**67**	**66**
2.5 µM	**68**	**69**	**67**	**64**
		Na^+ buffer		
10 µM	**37**	**57**	**40**	**44**
5 µM	**38**	**n.d.**	**39**	**45**
2.5 µM	**37**	**n.d.**	**39**	**44**

Table 9. Melting temperature values obtained by UV- and CD-melting experiments for 5'-chol-TEG-AS1411 (n.d. = not determined).

In summary, the T_m values determined by UV- and CD- melting experiments in K^+ buffer solution (Table 9) are in good agreement among them and with those obtained for AS1411, except for the 10 µM concentration, in which a lower stability was observed. From the UV data in Na^+ buffer solution, 5'-chol-TEG-AS1411 proved to give a slightly more stable superstructure than unmodified AS1411. Remarkably, CD results indicated a peculiar behaviour associated also to folding/unfolding processes of other G4 structures or of higher order structures.

5'-cholesteryl-C6-AS1411

Similarly to previous AS1411 derivatives, 5'-chol-C6-AS1411 folds into a parallel G4 structure which exhibits a strong positive band at 263 nm and a negative band at 241 nm (Figure 86), both in K^+ and Na^+ buffer solutions, with a lower degree of structuration in Na^+ ions solution.

In K^+ buffer solution, CD melting curves at 263 nm provided T_m values of 64, 68 and 70 °C at 10, 5 and 2.5 µM concentrations, respectively (Figure 87), indicating a lower stability at higher concentrations, similarly to what observed in the same conditions for 5'-chol-TEG-AS1411. In all cases, the melting process was fully reversible, with no significant hysteresis observed between the heating and cooling processes (data not shown).

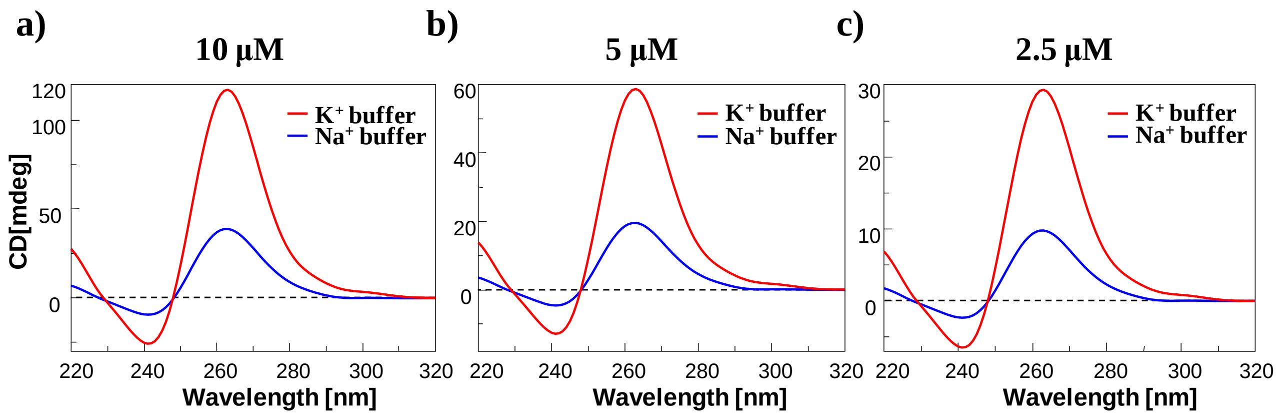

Figure 86. Overlapped CD spectra of 5’-chol-C6-AS1411 at 10 µM (**a**), 5 µM (**b**) and 2.5 µM (**c**) in different saline conditions: potassium buffer (red line) and sodium buffer (blue line) solutions.

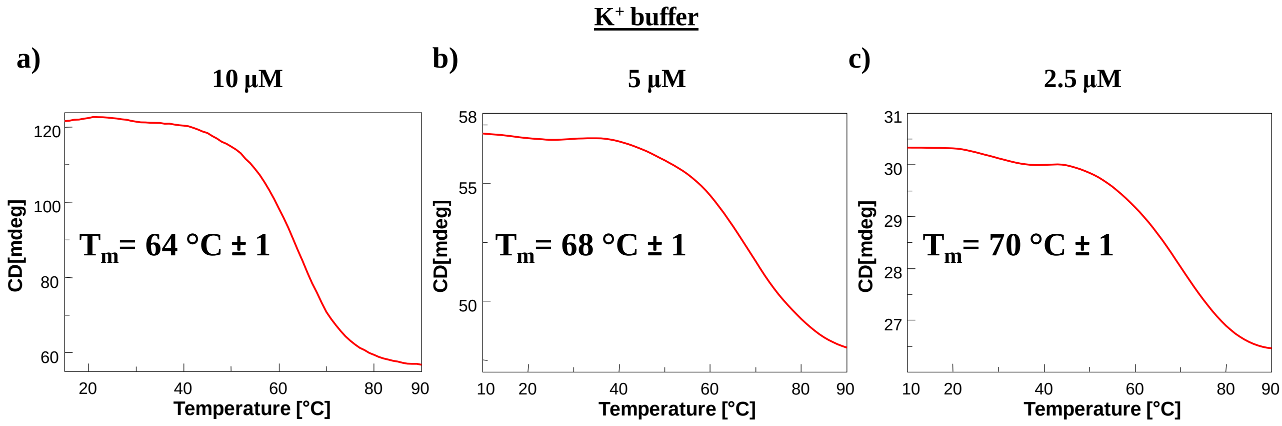

Figure 87. CD melting profiles of 5’-chol-C6-AS1411 in the selected K^+ buffer solution at 10 µM (**a**), 5 µM (**b**) and 2.5 µM (**c**) concentration, recorded at 263 nm (scan rate: 1 °C/min).

Instead, in the case of Na^+ buffer solution, the melting profile showed at all tested concentrations a shift of the positive maximum on increasing the temperature (Figure 88), resulting in an atypical melting curve, as already observed for both 5’-stearyl-AS1411 and for 5’-chol-TEG-AS1411.

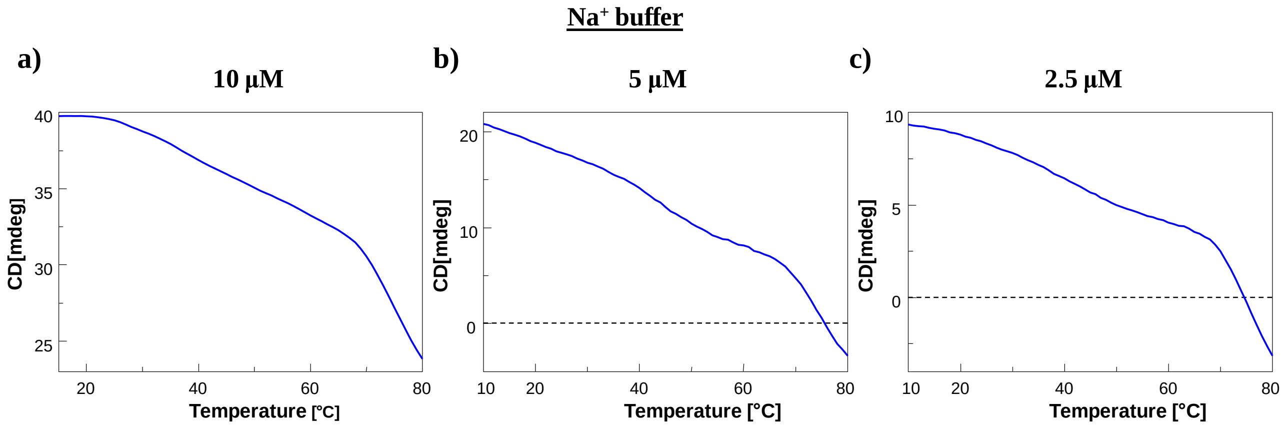

Figure 88. CD melting profiles of 5’-chol-C6-AS1411 in the selected Na^+ buffer solution at 10 µM (**a**), 5 µM (**b**) and 2.5 µM (**c**) concentration, recorded at 263 nm (scan rate: 1 °C/min).

In K^+ buffer solution, UV-melting curves at 295 nm provided a T_m value of 67 °C at 5 and 2.5 µM concentrations (Figures 89b and 89c, respectively) and of 65 °C at 10 µM concentration (Figure 89a). In turn, in the Na^+ buffer solution the T_m values were 44 °C at 10 and 2.5 µM concentrations (Figures 90a and 90c, respectively) and of 43 °C at 5 µM concentration (Figure 90b). However, in both saline conditions, no hysteresis phenomena emerged comparing melting and annealing profiles (data not shown).

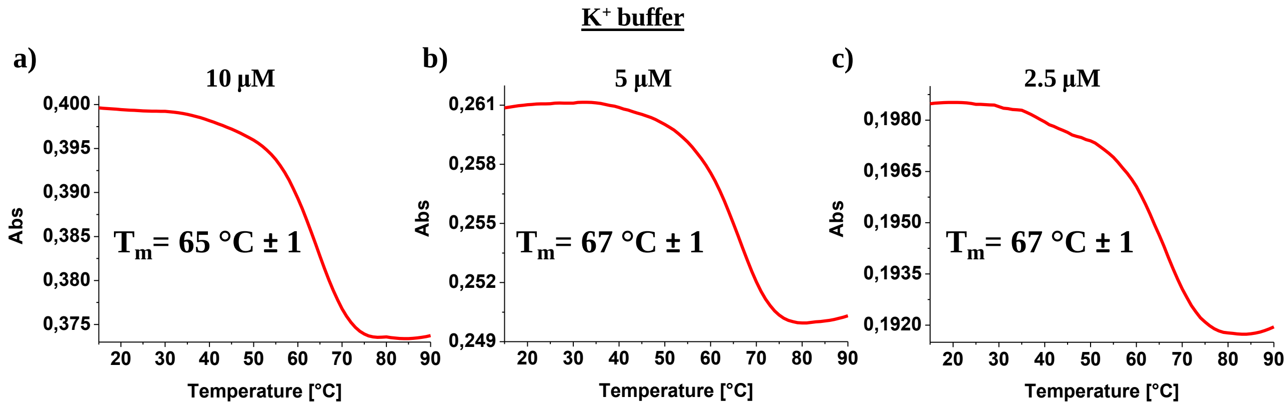

Figure 89. UV-melting profiles of 5'-chol-C6-AS1411 in the selected K^+ buffer solution at 10 µM (**a**), 5 µM (**b**) and 2.5 µM (**c**) concentration, recorded at 295 nm (scan rate: 1 °C/min).

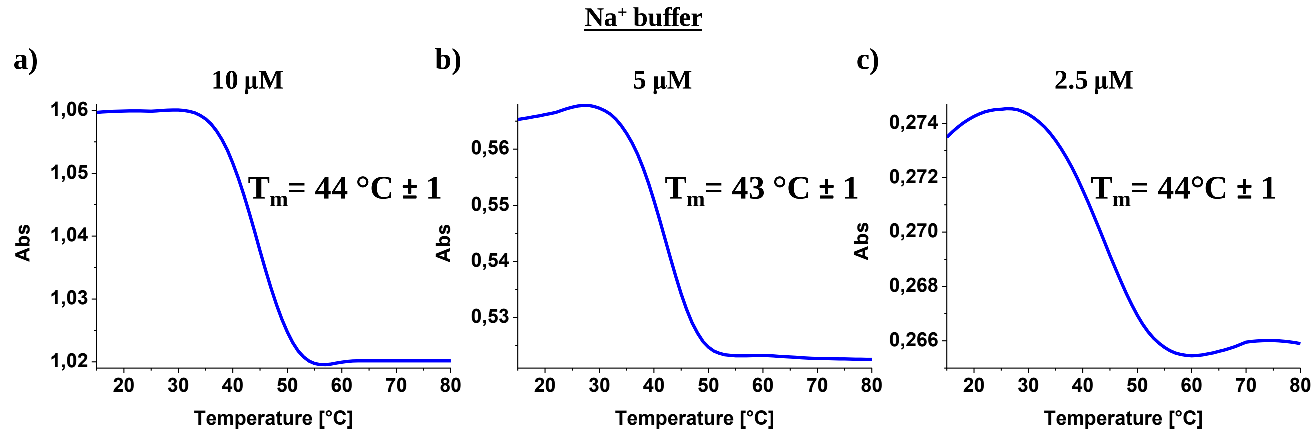

Figure 90. UV-melting profiles of 5'-chol-C6-AS1411 in the selected Na^+ buffer solution at 10 µM (**a**), 5 µM (**b**) and 2.5 µM (**c**) concentration, recorded at 295 nm (scan rate: 1 °C/min).

In summary, T_m values determined by UV- and CD- melting experiments in K^+ buffer solution (Table 10) are in good agreement among them and with those obtained for AS1411, except for the 10 µM concentration samples, in which the CD melting profile of 5'-chol-C6-AS1411 showed a G4v structure with lower stability. UV data in Na^+ buffer solution indicated for 5'-chol-TEG-AS1411 formation of G4 structures with slightly higher stability; while CD results indicated a peculiar behaviour not directly associated only to folding/unfolding processes of a single G4 structure.

Taken together these results certainly indicated a higher degree of polymorphism of the AS1411 derivatives in comparison with unmodified AS1411. To better elucidate what happens to G4 structure on increasing the temperature, the combination with other techniques such as gel electrophoresis, size exclusion chromatography and dynamic light scattering (DLS) analyses are needed.

	CD T_m (°C) ± 1		UV T_m (°C) ± 1	
	AS1411	5’-chol-C6-AS1411	AS1411	5’-chol-C6-AS1411
		K^+ buffer		
10 µM	66	64	67	65
5 µM	68	68	67	67
2.5 µM	68	70	67	67
		Na^+ buffer		
10 µM	37	n.d.	40	44
5 µM	38	n.d.	39	43
2.5 µM	37	n.d.	39	44

Table 10. Melting temperature values obtained by UV- and CD-melting experiments for 5’-chol-C6-AS1411 (n.d. = not determined).

4.1.3. Gel electrophoresis analysis

Gel electrophoresis analysis was used to further characterize AS1411 and its derivatives. Also in this case, we tested three different concentrations of the oligonucleotides (5, 10 and 50 µM) in K^+ and Na^+ phosphate buffered solutions, using tel_{26} aptamer as reference oligonucleotide, known to adopt a unimolecolar G4 structure.[513,514]

In Figure 91-93 the photographs of 7 % polyacrylamide gels, run under native conditions, are reported.

In comparison with $tel_{26,}$ which migrates on a polyacrylamide gel as a single band, AS1411 in the same conditions migrates as a double band (at 10 µM concentration, lines 3 and 7) and as poorly resolved three bands (at 50 µM concentration, lines 4 and 8), both in K^+ and Na^+ phosphate buffered solutions (Figure 91a). These bands showed however almost the same apparent mobility of tel_{26} confirming a similar charge and overall size distribution.

Instead, in the case of 5’-stearyl-AS1411 (Figure 91b), a detectable difference in electrophoretic mobility was observed: the photograph of the gel shows a band with a similar but not identical electrophoretic mobility as tel_{26} (at lower concentrations) and a retarded band, which can be a multimeric species or an aggregate form of the aptamer. This retarded band is not clearly visible at 10 µM concentration (lines 3 and 7) and becomes clearly visible at 50 µM concentration (lines 4 and 8).

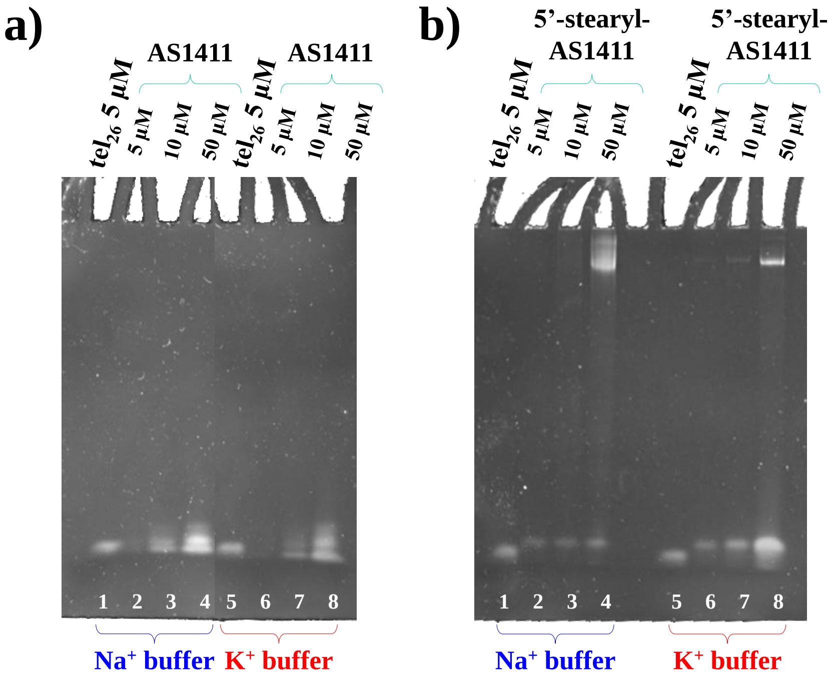

Figure 91. 7% polyacrylamide gel electrophoresis under native conditions of the analysed AS1411 (**a**) and 5'-stearyl-AS1411 (**b**) run at 100 V at r.t. for 1 h 15 min. (**a**) Lane 1: tel$_{26}$ (5 µM); Lane 2: AS1411 (5 µM); Lane 3: AS1411 (10 µM); Lane 4: AS1411 (50 µM), in Na$^+$ buffer solution; Lane 5: tel$_{26}$ (5 µM); Lane 6: AS1411 (5 µM); Lane 7: AS1411 (10 µM); Lane 8: AS1411 (50 µM), in K$^+$ buffer solution; (**b**) Lane 1: tel$_{26}$ (5 µM); Lane 2: 5'-stearyl-AS1411 (5 µM); Lane 3: 5'-stearyl-AS1411 (10 µM); Lane 4: 5'-stearyl-AS1411 (50 µM), in Na$^+$ buffer solution; Lane 5: tel$_{26}$ (5 µM); Lane 6: 5'-stearyl-AS1411 (5 µM); Lane 7: 5'-stearyl-AS1411 (10 µM); Lane 8: 5'-stearyl-AS1411 (50 µM), in K$^+$ buffer solution.

In the case of 5'-chol-TEG-AS1411 the band with the same electrophoretic mobility of tel$_{26}$ is observable only in K+ buffer solution together with more retarded bands, not well distinguishable, on the top of the gel (Figure 92, left side). In presence of Na$^+$ ions, only the retarded bands are clearly visible. In order to better investigate these retarded bands, the gel was run also for 2 h and 30 min and 3 h and 15 min. respectively (Figure 92, right side). Also in these conditions, the bands migrate poorly, indicating the formation of bigger species which are also more numerous in the presence of K$^+$ ions.

Concerning 5'-chol-C6-AS1411, the gel showed at all the conditions tested (different concentrations and saline solutions) both the presence of a band with the same mobility as tel$_{26}$ and more retarded bands (Figure 93, left side). Also in this case, the gel was run for 2 h and 30 min and 3 h and 15 min (Figure 93, right side), in an attempt to separate the retarded bands.

Taking into account that gel electrophoresis is a low resolution technique, however these results provide a good indication that all AS1411 oligonucleotides form more species in solution. Probably the bands with the same mobility of tel$_{26}$ are monomolecular forms, but the retarded species should be bigger or agglomerate forms. These data also confirm some not canonical CD melting profiles clearly showing the presence, particularly at high concentrations, of higher order G4 structures.

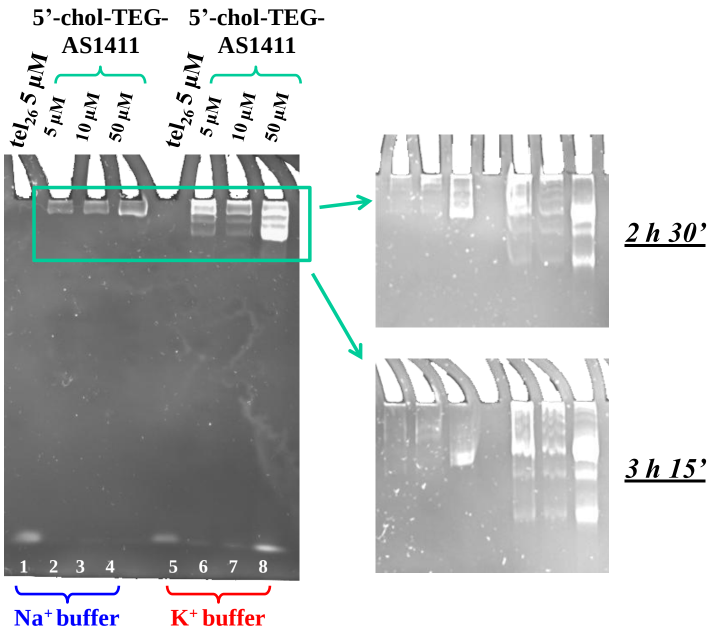

Figure 92. 7% polyacrylamide gel electrophoresis under native conditions of the 5’-chol-TEG-AS1411 run at 100 V at r.t. for 1 h 15 min. Lane 1: tel$_{26}$ (5 µM); Lane 2: 5’-chol-TEG-AS1411 (5 µM); Lane 3: 5’-chol-TEG-AS1411 (10 µM); Lane 4: 5’-chol-TEG-AS1411 (50 µM), in Na$^+$ buffer solution; Lane 5: tel$_{26}$ (5 µM); Lane 6: 5’-chol-TEG-AS1411 (5 µM); Lane 7: 5’-chol-TEG-AS1411 (10 µM); Lane 8: 5’-chol-TEG-AS1411 (50 µM), in K$^+$ buffer solution; On the right side the magnification of the gel run at 100 V at r.t. for 2 h 30 min (top) and 3 h 15 min (bottom) are shown.

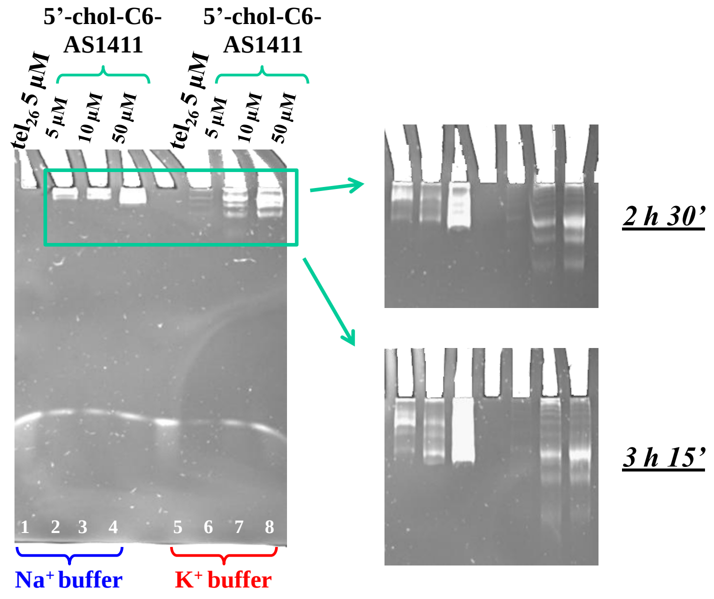

Figure 93. 7% polyacrylamide gel electrophoresis under native conditions of 5’-chol-C6-AS1411 run at 100 V at r.t. for 1 h 15 min. Lane 1: tel$_{26}$ (5 µM); Lane 2: 5’-chol-C6-AS1411 (5 µM); Lane 3: 5’-chol-C6-AS1411 (10 µM); Lane 4: 5’-chol-C6-AS1411 (50 µM), in Na$^+$ buffer solution; Lane 5: tel$_{26}$ (5 µM); Lane 6: 5’-chol-C6-AS1411 (5 µM); Lane 7: 5’-chol-C6-AS1411 (10 µM); Lane 8: 5’-chol-C6-AS1411 (50 µM), in K$^+$ buffer solution; On the right side the magnification of the gel run at 100 V at r.t. for 2 h 30 min (top) and 3 h 15 min (bottom) are shown.

4.1.4. Size exclusion chromatography analyses

In order to further characterize AS1411 oligonucleotides and better investigate the number of species formed in solution, the samples were also analysed *via* size exclusion chromatography. Also in this case, we tested three different concentrations of the oligonucleotides (5, 10 and 50 μM) in K^+ and Na^+ phosphate buffered solutions, using tel_{26} as the reference oligonucleotide.

For the 26-mer d($^{5'}$TTAGGG)$_4$TT$^{3'}$ taken from the human telomere, typically indicated as tel_{26}, it is well known that the exact folded structure adopted in solution critically depends on the cation composition of the solution. Indeed, in the presence of sodium, one main species consisting in an antiparallel “basket” structure is observed; instead, in potassium solution, two types of antiparallel “hybrid” structures are known.[513,514]

In Figure 94 the chromatogram of the slowly annealed tel_{26} is shown: in the presence of Na^+ ions (Figure 94a), only one peak (t_R = 6.18) is present, while in the case of K^+ ions (Figure 94b), besides the main peak (t_R = 6.62), also another species (corresponding to 12.6 % in area) is detectable. These results are in accordance with the possible structures that tel_{26} can form in solution.

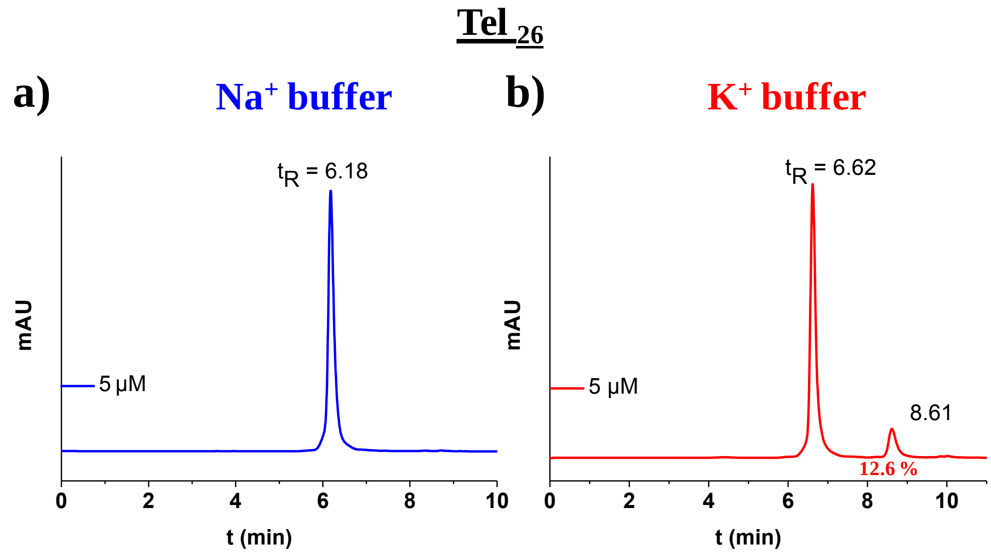

Figure 94. Size exclusion chromatography of tel_{26} in K^+ (**a**) and Na^+ (**b**) buffer solution at 5 μM concentration.

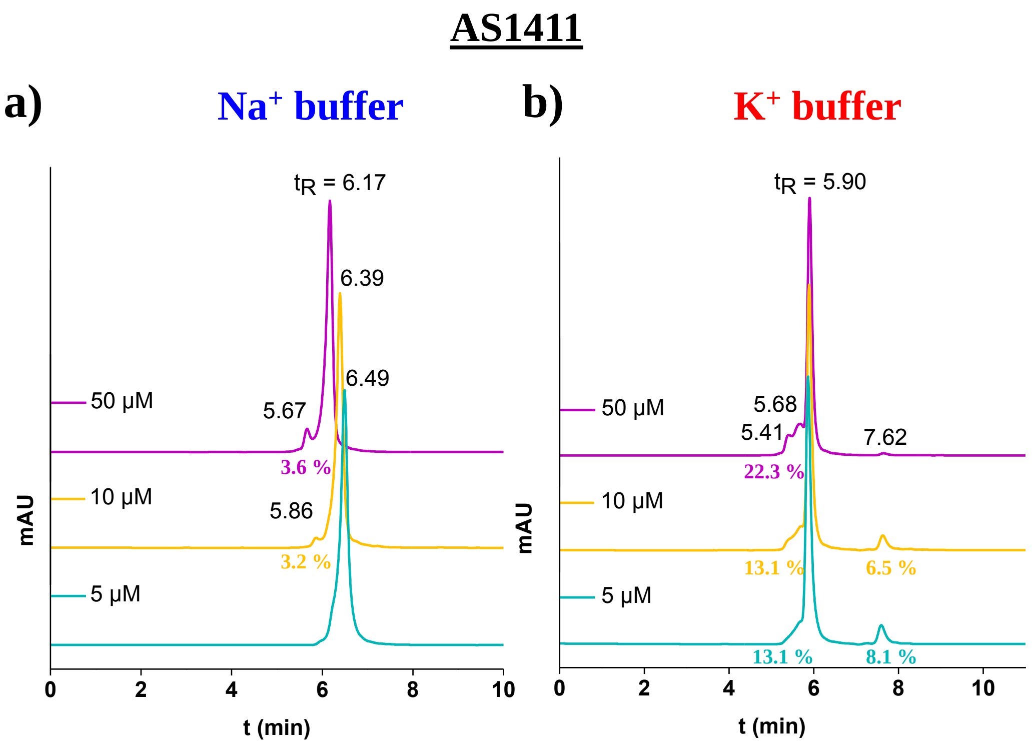

Figure 95. Size exclusion chromatography of AS1411 in K^+ (**a**) and Na^+ (**b**) buffer solution at 5, 10 and 50 µM concentration (green, yellow and purple lines, respectively).

In the case of AS1411, a similar trend was found (Figure 95). In the presence of Na^+ ions (Figure 95a), only one peak was observed, even if the retention times are slightly different at the tested concentrations (t_R = 6.49, 6.39, 6.17 at 5, 10 and 50 µM, respectively). However, upon increasing the concentration, another peak with shorter elution times appeared, accounting for an area of 3.2 and 3.6 % at 10 and 50 µM, respectively.

In K^+ buffer (Figure 95b), a main peak with t_R = 5.90 min was present at all the concentrations tested. Similarly to tel_{26}, also another peak was observed with longer elution times (t_R = 7.62), whose area gradually decreased on increasing the concentration (from 8.1 to 6.5 %, going from 5 to 10 µM) until it completely disappeared at higher concentrations. At the same time, a little shoulder under the main peak was detectable (t_R = 5.68), which had an almost constant percentage area at 5 and 10 µM concentrations (13.1 % in area), but increased at 50 µM up to 22.3 %.

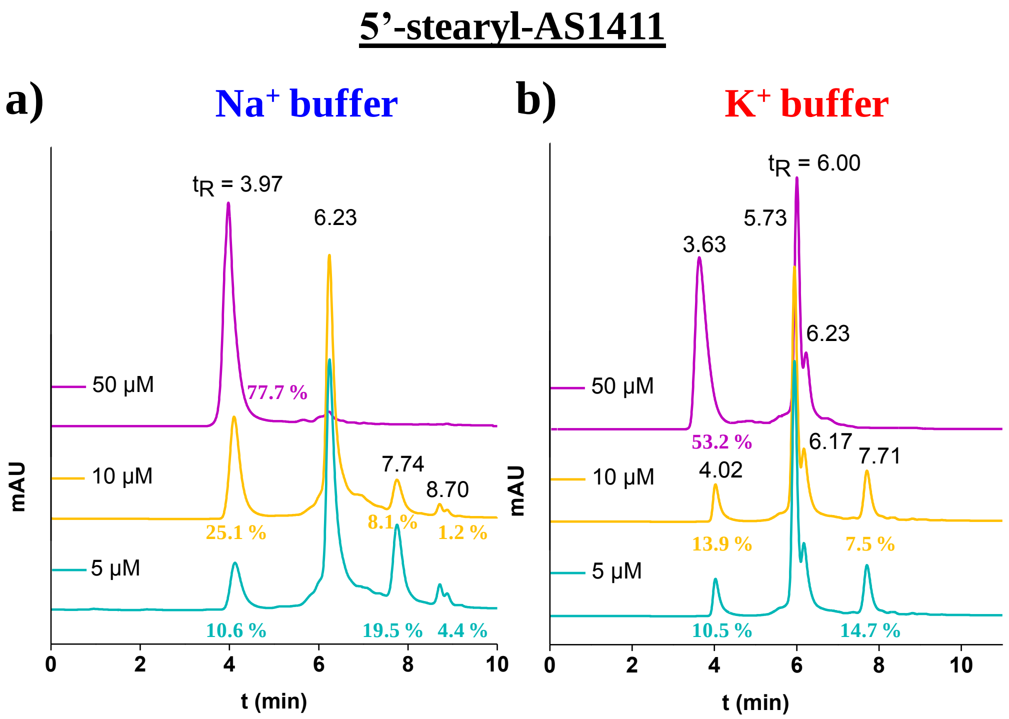

Figure 96. Size exclusion chromatography of 5'-stearyl-AS1411 in K^+ (**a**) and Na^+ (**b**) buffer solution at 5, 10 and 50 µM concentration (green, yellow and purple lines, respectively).

For 5'-stearyl-AS1411, several peaks were present already at low concentrations, both in Na^+ and K^+ buffer. In Na^+ buffer (Figure 96a), the chromatogram at 5 µM showed a predominant peak (t_R = 6.23) and other three peaks representing 10.6, 19.5 and 4.4 % (at t_R = 3.97, 7.74 and 8.70, respectively). At 10 µM concentration, the peaks with t_R = 7.74 and 8.70 decreased in intensity (8.1 and 1.2 %, respectively) until disappearance at higher concentration. Instead, the peak with t_R = 3.97 became more evident (25.1 % at 10 µM), finally being the predominant one at 50 µM concentration (77.7 %). Species with so short elution times should be very large aggregates, in accordance with the retarded bands observed on polyacrylamide gels. In the chromatogram recorded using the K^+ buffer solution as mobile phase (Figure 96b), three peaks are visible at lower concentrations with retention times of 4.02, 6.00 and 7.71. Indeed, the prevalent peak was accompanied by another species with t_R of 6.17 min. On increasing the concentrations, a similar behaviour was found: the peak at t_R 7.71 min decreased from 14.7 to 7.5 %, finally disappearing at 50 µM, while the peak at ca 4 increased from 10.5 to 13.9 %, becoming almost the predominant one at 50 µM concentration (53.2 % in area).

Thus, in the case of AS1411 and 5'-stearyl-AS1411, the main peak was always observed at retention times of about 6 min and its intensity – upon increasing the concentration - decreased in favour of other species with shorter elution times and thus associated with good approximation to aggregates with large dimensions.

In the case of 5’-chol-TEG-AS1411, already at low concentrations, the predominant peak in intensity had a retention time of ca. 4 min in both saline conditions tested (Figure 97). The chromatogram in Na^+ buffer (Figure 97a) indicated the presence of two peaks at 5 µM concentration: one predominant (t_R = 3.96) and a weaker one (t_R = 6.14), which further decreased on increasing the concentration (from 24.8 to 15.8 and 5.1 % at 5, 10 and 50 µM concentration, respectively). In the case of K^+ buffer, in addition to the dominant peak (t_R = 4.53) also other two peaks at 5 µM concentration (t_R = 6.77 and 8.77) were observed, representing the 5.5 and 13.7 % in area, respectively (Figure 97b). At higher concentrations, the peak with t_R = 6.77 kept an almost constant intensity, while the other one (t_R = 8.77) decreased to 9.9 and 2.5 % at 10 and 50 µM concentration, respectively. At the same time, starting from 10 µM concentration a shoulder under the main peak (18.1 %) and another visible peak (with t_R = 7.55 and 4.2 % in area) appeared in the chromatogram, both maintaining an almost constant intensity also at 50 µM concentration.

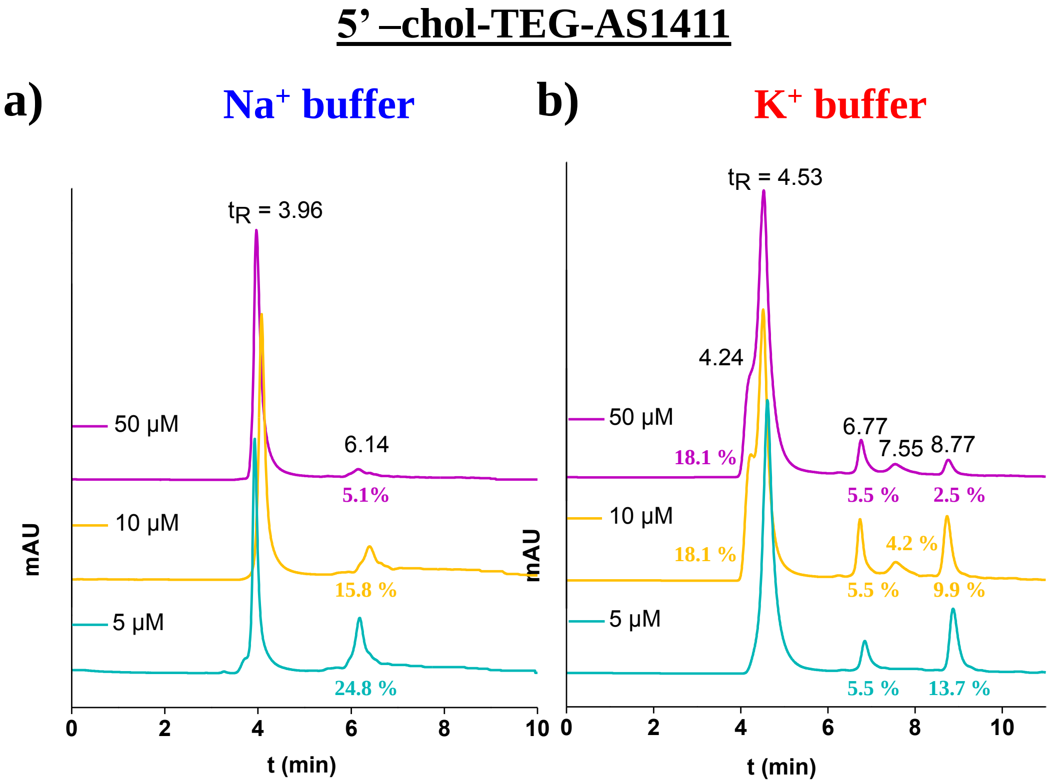

Figure 97. Size exclusion chromatography of 5’-chol-TEG-AS1411 in K^+ (**a**) and Na^+ (**b**) buffer solution at 5, 10 and 50 µM concentration (green, yellow and purple lines, respectively).

Also for 5’-chol-C6-AS1411, already at low concentrations and in both saline conditions tested, the peak corresponding at ca. 4 min retention time was clearly visible (Figure 98).

In the case of Na^+ buffer (Figure 98a), also a weaker peak (t_R = 6.13) was detected, with an almost constant area at the lowest concentrations (8.4 %), then decreasing at 50 µM concentration (5.9 %).

In K^+ buffer (Figure 98b), at 5 µM concentration three peaks with retention times of 4.45, 6.65 and 8.67 min were detected. While the peak with t_R = 4.45 min increased in intensity at higher concentrations (from 35.2 to 92.3 and 94.1 %, on going from 5 μM to 50 concentration), becoming the dominant one at 50 μM concentration, the other two peaks decreased in intensity on increasing the concentration. The major effect was clearly evident for the peak with t_R = 8.67, going from 56.0 % at 5 μM concentration to 3.9 % at 10 μM and finally to 2.0 % at 50 μM. Instead, the peak with t_R = 6.65 represented the 8.9 % at 5 μM, then decreased to 3.9 % at 10 μM and remained constant at 50 μM.

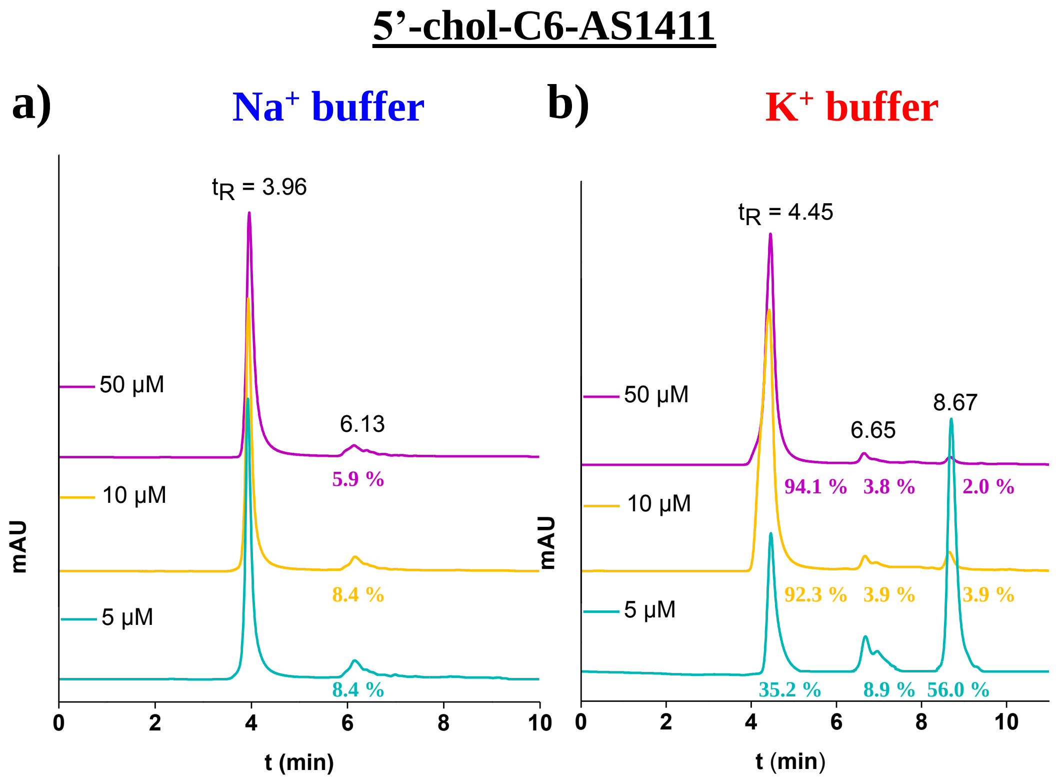

Figure 98. Size exclusion chromatography of 5'-chol-C6-AS1411 in K^+ (**a**) and Na^+ (**b**) buffer solution at 5, 10 and 50 μM concentration (green, yellow and purple lines, respectively).

Summarizing, size exclusion chromatograms showed the presence of more than one species, above all in the case of AS1411 lipophilic derivatives, confirming the high polymorphism of this oligonucleotide. These species could be different conformations with the same molecularity or can represent different molecular structures (*e.g.* monomolecular and bimolecular/tetramolecular structures). The presence of higher order species is validated both from gel electrophoresis (retarded bands observed in native PAGE) and SEC analyses data (peaks with short retention times, *i.e.* totally excluded from the column).

Remarkably, these different species are essentially parallel G4 structures which show a very similar thermal behaviour; nice sigmoids were obtained in all the CD melting experiments, with comparable T_m values.

4.2. Experimental section

- **Materials and general methods**

All the reagents and solvents were of the highest commercially available quality and were used as received. AS1411 ($^{5'}$GGTGGTGGTGGTTGTGGTGGTGGTGG$^{3'}$), 5’-stearyl-AS1411, 5’-cholesteryl-TEG-AS1411 and 5’- cholesteryl-C6-AS1411 oligonucleotides were purchased from Biomers. Ethidium bromide and 5X Green GoTaq Flexi Buffer were purchased from Sigma Aldrich and Fisher Scientific, respectively.

- **Preparation of oligonucleotide samples**

Lyophilized oligonucleotides were dissolved in a known volume of Milli-Q water and their concentrations were determined by UV spectroscopy - on a JASCO V-550 spectrophotometer equipped with a Peltier Thermostat JASCO ETC-505T - in 1 cm path length cuvette measuring the absorbance at 260 nm (85 °C) using the molar extinction coefficient of 281700 cm^{-1} M^{-1}. The spectra were recorded in the range 220–380 nm with a medium response, a scanning speed of 100 nm/min and a 2.0 nm bandwidth, and corrected by subtraction of the background scan with a buffer. Then the oligonucleotides from the stock solutions (574, 459, 425 and 234 µM for AS1411, 5’-stearyl-AS1411, 5’-chol-TEG-AS1411 and 5’-chol-C6-AS1411, respectively) were diluted in the selected buffer and annealed by heating each solution for 5 min at 90 °C and then leaving it to slowly cool to room temperature overnight. Annealed samples were then kept at 4° C until use.

- **Spectroscopic characterization of AS1411 oligonucleotides**

CD experiments. CD spectra and CD-monitored melting curves were recorded on a Jasco J-715 spectropolarimeter equipped with a Peltier-type temperature control system (model PTC-348WI), using a quartz cuvette with a path length of 1 cm (3 mL internal volume, Hellma). CD parameters for spectra recording were the following: spectral window 220-320 nm, data pitch 1 nm, band width 2 nm, response 4 sec, scanning speed 100 nm/min, 3 accumulations. The characterization of oligonucleotides sequences was performed at 2.5, 5 and 10 µM concentrations in K^+ (10 mM KH_2PO_4, 70 mM KCl, 0.2 mM EDTA, pH 7.0) and Na^+ (PBS: 137 mM NaCl, 2.7 mM KCl, 10 mM Na_2HPO_4, 1.8 mM KH_2PO_4, pH 7.4) phosphate buffer solutions, taking a suitable initial aliquot from the stock solution in H_2O. Thermal denaturation-renaturation curves were recorded following the CD signal at 263 nm *vs*. the temperature (scan rate of 1 °C/min) in a range of temperature slightly different depending on saline conditions (generally 15-90 °C for K^+ buffer solution and 15-80 °C for Na^+ buffer solution). Each experiment was performed in duplicate. T_m was estimated from the first derivative of the melting/annealing and the error associated with the T_m values determination was ± 1 °C.

UV-vis absorption experiments. UV-melting curves were obtained on a Cary 5000 UV-Vis-NIR spectrophotometer equipped with a temperature controller system, using 1 cm path length cuvette (1 mL internal volume, Hellma). The absorbance *vs.* temperature profiles were recorded by following the absorbance changes at 295 nm wavelength on increasing the temperature (heating scan rate 1 °C/min). The characterization of the oligonucleotides sequences was performed at 2.5, 5 and 10 μM concentrations in K^+ (10 mM KH_2PO_4, 70 mM KCl, 0.2 mM EDTA, pH 7.0) and Na^+ (PBS: 137 mM NaCl, 2.7 mM KCl, 10 mM Na_2HPO_4, 1.8 mM KH_2PO_4, pH 7.4) phosphate buffer solutions, taking a suitable initial aliquot from the stock solution in H_2O. Each experiment was performed in duplicate. T_m values were calculated as the maxima of the plots of the first derivative of the melting curve (associated error: ± 1 °C).

Gel electrophoresis. Slowly annealed samples of AS1411, 5’-stearyl-AS1411, 5’-chol-TEG-AS1411 and 5’-chol-C6-AS1411 in 40 % of dye (5X Green GoTaq Flexi Buffer) were loaded on 7% acrylamide gels in TBE (Tris-Borate-EDTA, 0.5X) buffer at the different concentrations (5, 10 and 50 μM) and saline conditions analysed (in K^+ and Na^+ phosphate buffer solutions).

The samples were then run at 100 V at room temperature for 75 min, stained with ethidium bromide and finally visualized with a UV transilluminator (BioRad ChemiDoc XRS).

In the case of 5’-chol-TEG-AS1411 and 5’-chol-C6-AS1411, additional runs of 2 h 30 min and 3 h 15 min were performed to better investigate the retarded bands.

Size exclusion chromatography. SEC analyses were performed using an Agilent HPLC system, equipped with a UV/vis detector and a Yarra 3 µm column (300 x 4.60 mm; flow rate 0.5 mL min^{-1}, Phenomenex). Elution was monitored at $\lambda = 254$ nm. The mobile phases used consisted of K^+ (10 mM KH_2PO_4, 70 mM KCl, 0.2 mM EDTA, pH 6.7) and Na^+ (PBS: 137 mM NaCl, 2.7 mM KCl, 10 mM Na_2HPO_4, 1.8 mM KH_2PO_4, pH 7.0) phosphate buffer solutions. All the oligonucleotides tested were injected from stock solutions of the samples annealed at 5, 10 and 50 µM concentrations.

Chapter 5

Multifunctional systems

1. DOTAP-based liposomes loaded with TUGluRu and NOTA-OL

In the construction of multifunctional systems for both therapy and diagnosis of cancer pathology, the use of liposomes is a well established and efficient drug delivery strategy.[29,515,516] This kind of platform allows the incorporation of several functional units on the same scaffold and the protection of the active principle until it reaches the target site, reducing possible toxic side effects.

For this reason, TUGluRu and NOTA-OL (previously described in Chapter 2.3 and 3.2, respectively) have been co-aggregated with the cationic lipid 1,2-dioleyl-3-trimethylammoniumpropane chloride (DOTAP) in order to obtain stable formulations. In the case of NOTA-OL the formulation has the only aim to carry the diagnostic agent at a known, specific concentration, while in the case of TUGluRu, the formulation is aimed at ensuring high stability in aqueous environment even at high Ru-complex content. This nanovector, including both the drug and the imaging agent, represents a good model for the realization of theranostic nanoparticles.

DOTAP liposomes were suitably prepared, mixing the active ingredients and the phospholipid carrier at selected molar ratios, by using the lipid film method and were then resuspended in water. The microstructural characterization of the obtained aggregates was realized using dynamic light scattering (DLS) to estimate aggregate dimensions. Then, in vitro bioactivity profile of the Ru-loaded nanoparticles was investigated on cancer and normal human cell lines, in order to assess the efficacy of TUGluRu co-aggregated with DOTAP, and of its formulation with the imaging agent NOTA-OL. The ruthenium-free DOTAP/NOTA-OL system was also tested to evaluate the biocompatibility of the formulation.

Small angle neutron scattering (SANS) analysis – for a deeper structural characterization of the aggregates - as well as labelling with Ga^{68} radioisotope and evaluation of their efficiency as diagnostic agent in animal models are currently in progress at the University Federico II of Naples, Department of Chemical Sciences by the research group of prof. Luigi Paduano, and at CNR, Institute of Clinical Physiology, Pisa, by dr. Luca Menichetti, respectively.

1.1. Results and dusussion

1.1.1. DOTAP-based liposomes preparation

The samples were prepared by mixing appropriate amounts of DOTAP and TUGluRu and/or NOTA-OL dissolved in chloroform in order to have the prefixed molar ratio. Subsequently, an appropriate amount of this solution was transferred in round-bottom glass tubes. A thin film was obtained through evaporation of the solvent with dry nitrogen and keeping the samples under vacuum for at least 24 h. The samples were then hydrated in water, vortexed and sonicated. The final sample prepared were: DOTAP/TUGluRu (70:30), DOTAP/NOTA-OL (95:5) and DOTAP/TUGluRu/NOTA-OL (65:30:5).

1.1.2. Characterization of DOTAP-based nanoaggregates

Structural characterization of the mixed DOTAP nanoaggregates was carried out through dynamic light scattering (DLS) analyses in water.

In Figure 99, an example of the hydrodynamic radius distribution functions at 90° for the different mixed aggregates formed is reported. For all the investigated systems, a single and monodisperse aggregate population was detected. The hydrodynamic radii for all the systems analysed are located in the range 110−130 nm, which is the typical range of large vesicles.

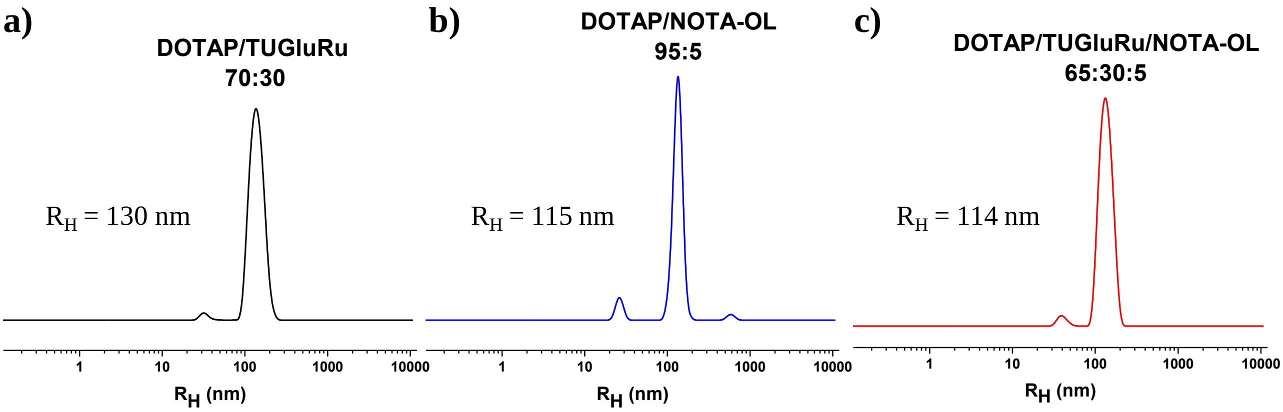

Figure 99. Hydrodynamic radius distribution functions obtained through DLS measurements for DOTAP/TUGluRu 70:30 (**a**), DOTAP/NOTA-OL 95:5 (**b**) and DOTAP/TUGluRu/NOTA-OL 65:30:5 (**c**).

1.1.3. Cell viability

In Figure 100 the cell viability assay data, evaluated by MTT assay procedure, are reported; these were performed on a panel of cancer and normal cell lines, treated for 48 h with a range of concentration (10→250 µM) of the DOTAP/TUGluRu, DOTAP/NOTA-OL, and DOTAP/TUGluRu/NOTA-OL systems. Generally, the dose-response curves showed a quite linear decrease of cell viability with increasing the drug doses. In line with previous results on the other ruthenium-based nanovectors,[137,153] DOTAP/TUGluRu showed selective antiproliferative activity for the cancer cells, with the breast cancer cells found to be the most sensitive ones. However, also the effect on cervix carcinoma and glioma cells was remarkable. The inclusion of NOTA-OL rendered the Ru-free formulation (DOTAP/NOTA-OL) slightly cytotoxic, probably due to its chelating activity; anyhow, such toxicity was negligible, since the cell viability was in all cases higher than 50 % even at 250 µM. Interestingly, this toxic effect was synergic with the ruthenium complex DOTAP/TUGluRu, showing an increased efficacy, still selective against the cancer cells.

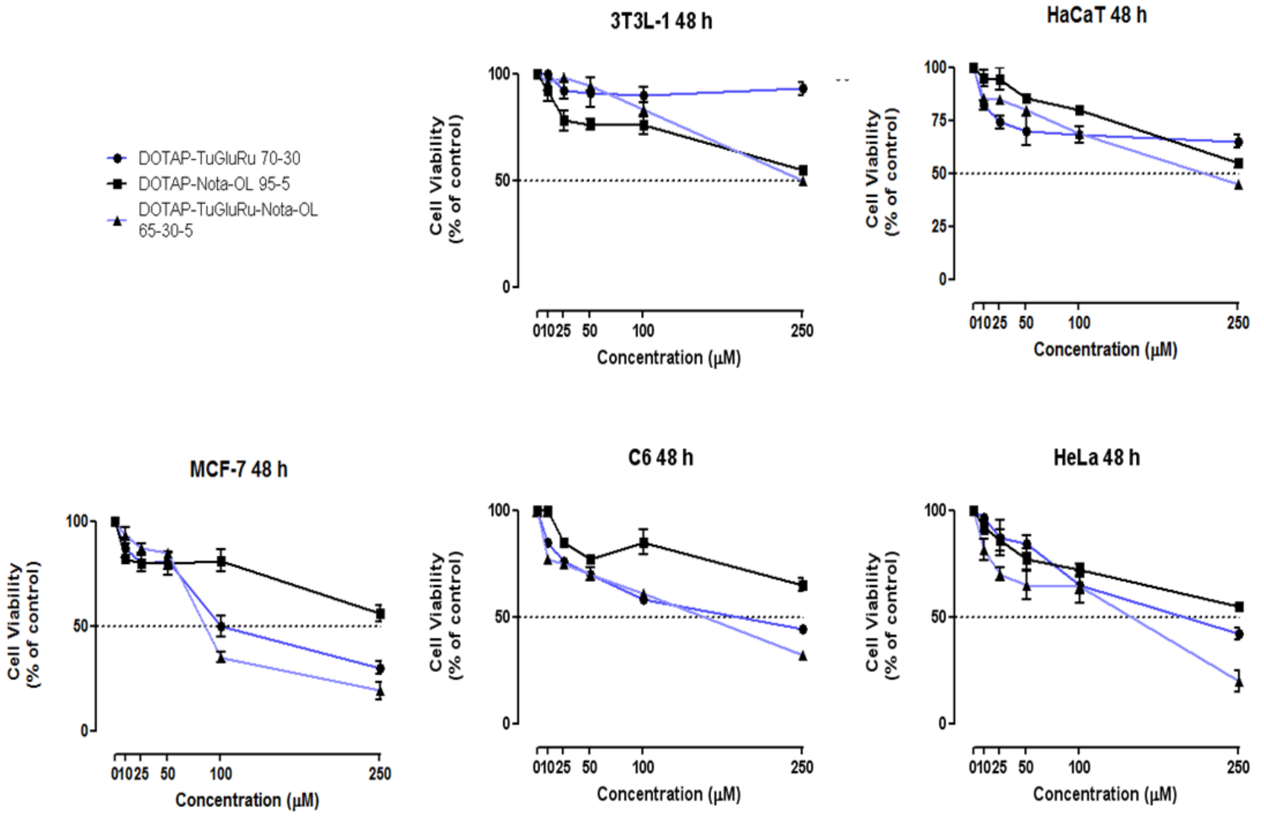

Figure 100. Cell viability curves resulting by MTT assay on 3T3L-1 (murine fibroblasts), HaCaT (human keratinocytes), MCF-7 (breast adenocarcinoma), C6 (glioma), HeLa (human cervical) cell lines incubated for 48 h with DOTAP/TUGluRu, DOTAP/NOTA-OL, DOTAP/TUGluRu/NOTA-OL systems.

1.1.4. IC$_{50}$ evaluation

From the analysis of dose-response curves, the IC$_{50}$ values were calculated, in order to better compare the efficacy of the tested nanovectors (Table 11). In bold, the IC$_{50}$ values relative to the effective concentration of ruthenium (30% of total liposome) were reported. This "normalization" makes possible the comparison with the bioactivity of the previously studied nucleolipidic Ru(III)-based liposomes.[137,153] Through the analysis of these values, it is also possible to highlight the synergic effect of NOTA-OL on the DOTAP/TUGluRu efficacy, producing a reduction of IC$_{50}$ values of about 25 % for MCF-7 and C6, and 50 % for HeLa cells.

	Cancer cells			*Normal cells*	
IC$_{50}$ (μM)	**MCF-7**	**HeLa**	**C6**	**3T3L-1**	**HaCaT**
DOTAP-TuGluRu 70:30	116.7 ± 4.4	186 ± 2.3	164.8 ± 2.5	> 250	> 250
Ru conc.	**35**	**55.8**	**49.4**	**>75**	**>75**
DOTAP-NOTA-OL 95:5	> 250	> 250	> 250	> 250	> 250
DOTAP-TuGluRu – NOTA-OL 65:30:5	88.4 ± 8.9	95.26 ± 8.2	123.7 ± 5.0	> 250	226.6 ± 4.4
Ru conc.	**26.5**	**28.6**	**37.1**	**>75**	**68.0**

Table 11. IC$_{50}$ values reported as mean values ± SEM. In bold, the IC$_{50}$ values referred to the effective ruthenium concentration (30% of total liposome).

2. LipThyRu and AS1411-decorated niosomes as potential anticancer drugs

Niosomes, or non-ionic surfactant vesicles, have gained increasing scientific attention as drug delivery systems with respect to conventional liposomes, due to the use of surfactants in their formulation, which are cheaper and more stable alternatives than phospholipids.[516,517] Niosomes are prepared by mixing non-ionic surfactants, such as alkyl ether, alkyl esters or alkyl amides, fatty acids and amino acid derivatives, with or without other lipids and then subsequently hydrating the mixture.[518–520]The formation of these vesicle-like structures depends on the hydrophilic–lipophilic balance (HLB) of the surfactant, the chemical structure of the components, their geometry and the ratio between the lipid and the surfactant used.[518,521]

The size range of niosomes includes nano and submicron sizes, and the vesicle structure can be unilamellar or multilamellar.[522] Owing to the vesicle structure, niosomes are able to entrap both hydrophilic and hydrophobic drugs, as liposomes do. Interestingly, surfactants can be easily chemically modified, allowing high versatility of vesicular structures. Niosomes are typically very stable, at least in the time range of few months, depending on their components and the presence of additive agents.[523,524] Moreover, the high chemical stability of surfactants, compared with phospholipids, makes niosome purification, handling and storage much easier.[525] Niosome formulations have shown good *in vitro* and *in vivo* efficacy in delivering both pharmaceuticals and biopharmaceuticals.[519,526–528] For example, promising transfection efficiencies have been achieved with niosomes loaded with plasmid DNA after subretinal, intravitreal and brain injections in rats.[529]

With the aim of exploring different, multifunctional nanoplatforms to obtain novel, efficient anticancer drugs, part of this PhD work has been devoted to study niosome formulations - based on the cationic lipid 2,3-di(tetradecyloxy)propan-1-aminium chloride (Figure 101) and polysorbate 80 as surfactant[530] – as suitable carrier system for the nucleolipidic Ru(III)-complex LipThyRu and the oligonucleotide AS1411 (discussed in chapters 2.2 and 4.4, respectively).

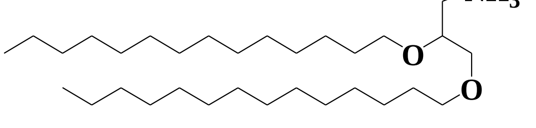

Figure 101. Chemical structure of the cationic lipid 2,3-di(tetradecyloxy)propan-1-aminium chloride used in niosome preparation.

This aminolipid is a bitailed lipid with two saturated alkyl chains and is positively charged as the lipid DOTAP, previously proved to efficiently stabilize and deliver in cell nucleolipidic Ru(III)-complexes.[137,153] LipThyRu has been here selected as the anticancer drug and the nucleolin-selective aptamer AS1411 as the active targeting agent; these systems have been mixed to expectedly operate in synergy against cancer cells. The resulting formulations were optimized and fully characterized using gel electrophoresis, zeta potential and DLS analysis. Finally, the best formulations were tested as antiproliferative agents in preliminary *in vitro* biological evaluations on HeLa cancer cells. This study was carried out in the laboratories of the Spanish National Research Council (CSIC) of Barcelona (Spain) under the supervision of prof. Ramon Eritja Casadellà, where I spent three months of my PhD program.

2.1. Results and Discussion

2.1.1. Oligonucleotide binding ability measurements

As a preliminary experiment, a gel electrophoretic assay under native conditions of different AS1411-loaded niosomes was carried out in order to determine at which oligomer/lipid ratio the oligonucleotides are fully complexed with the niosomes. As shown in Figure 102, free AS1411 and AS1411-loaded niosomes migrated as separate bands in a native polyacrylamide gel electrophoresis. When the oligonucleotide was incorporated within the cationic vesicles, the resulting complexes were retarded on the gel because of their size change. Free AS1411 oligonucleotide was observed in the formulations containing oligonucleotides/lipid ratios from 0 to 1:5. Full incorporation of AS1411 in niosome vesicles was observed starting from 1:8 oligonucleotide/lipid molar ratio.

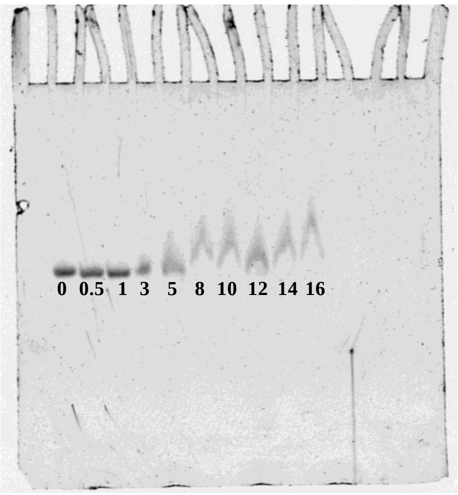

Figure 102. AS1411-loaded niosomes characterization by electrophoretic mobility shift assays. The numbers specify the oligonucleotide/lipid molar ratio, being 1 the amount of oligonucleotide.

2.1.2. Zeta potential measurements

AS1411-functionalized niosomes were first of all characterized in terms of Zeta potential to determine their surface charge. In particular, several formulations have been prepared mixing the niosome vesicles (28.9 mM stock solution in HEPES) in different ratios - ranging from 1:2 to 1:16 -

with fixed amounts of AS1411 oligonucleotide (0.5 µM). Their Zeta potential values have been then measured so to determine the optimal oligonucleotide/lipid molar ratio for the desired complexes.

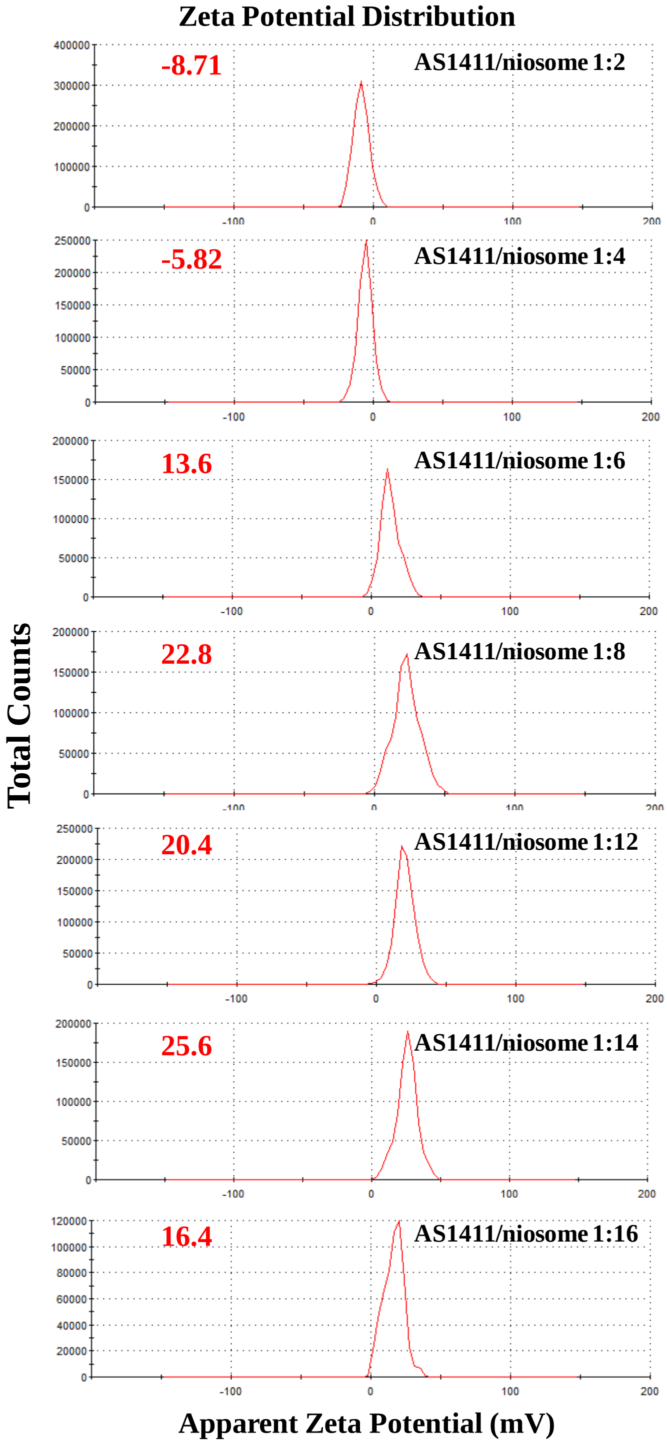

Figure 103. Zeta potential distributions of AS1411/niosome mixtures at the indicated molar ratios.

As depicted in Figures 103 and 104, the Zeta potential results displayed negative values for AS1411-loaded niosomes at the lowest AS1411/niosome ratios investigated (ca. -9 mV for the 1:2 mixture) due to the prevalence of the negative charges of the 26-mer oligonucleotide. Clearly, as the concentration of cationic vesicles increased, the resulting Zeta potential values also increased, finally obtaining positive values constantly in the range +13 - +26 mV, indicating an essentially stable electrostatic level.

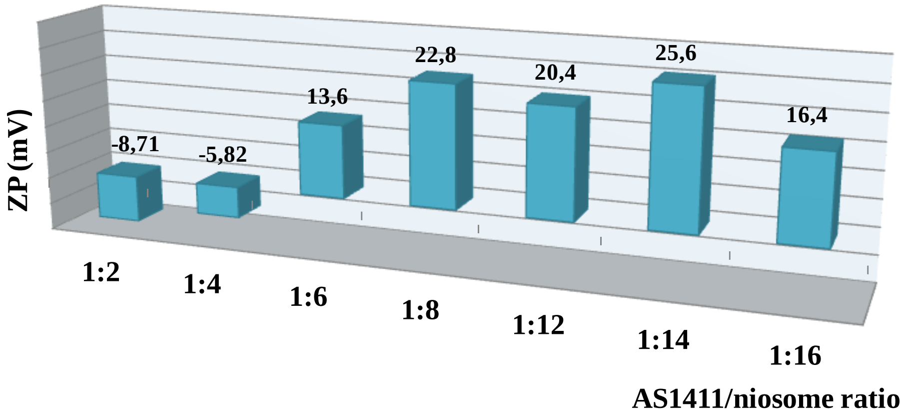

Figure 104. Zeta potential values of AS1411-loaded niosomes at several molar ratios.

2.1.3. Particle size measurements

DLS measurements have been used by Eritja *et al.*[531] to demonstrate that niosome formulations - stored at 4 °C for one month - show an average hydrodynamic radius essentially constant for one month, thus basically proving their full stability under the studied solution conditions.

DLS analysis was here used to determine the average size of niosomes and AS1411-loaded niosome formulations at 1:6 and 1:12 molar ratios (Table 12).

Notably, the average particle size of AS1411/niosome at 1:12 ratio and niosome alone at the same concentration were almost identical (ca. 60 nm in radius). Upon insertion of AS1411 within the niosomes, the system showed a sharper distribution and a lower polydispersity index, indicating the formation of a unique population of stable particles. On the contrary, the AS1411/niosome formulation at 1:6 ratio had a bigger radius and a higher polydispersity. For this reason, the AS1411/niosome formulation with ratio 1:12 was selected for the successive biological evaluations.

	Radius (nm)	**Polydispersity index**
AS1411/niosome 1:6	130.3 ± 3.55	0.46
AS1411/niosome 1:12	62.8 ± 0.67	0.27
niosome	64.5 ± 6.5	0.57

Table 12. Size measurements of niosome and AS1411/niosome at charge ratios of 1:6 and 1:12. The results are means ± S.D. for three independent experiments.

2.1.4. Cell culture

Cell viability and cytotoxicity studies were carried out incubating HeLa cells with AS1411, LipThyRu, niosome_LipThyRu and AS1411/niosome_LipThyRu formulations at oligo/vesicles charge ratios of 1:12 and at 6 µM niosome concentration (corresponding to 500 nM of AS1411 and 250 nM of LipThyRu). The incubation was realized in the presence of DMEM, supplemented with serum (10%) and two antibiotics, using a tetrazolium-based (MTT) colorimetric assay.

In a previous work[531] no significant toxicity was observed in HeLa cells treated with niosomes alone, obtaining viabilities around 90%.

As depicted in Figure 105, no significant toxicity was observed in the cells treated with AS1411 or LipThyRu alone, compared with control samples. A limited decrease in cell viability was observed for the complex niosome_LipThyRu, but a relevant antiproliferative effect was observed for the formulation presenting both the AS1411 oligonucleotide and the Ru(III)-complex, thus nicely indicating that these anticancer agents act in a synergic manner.

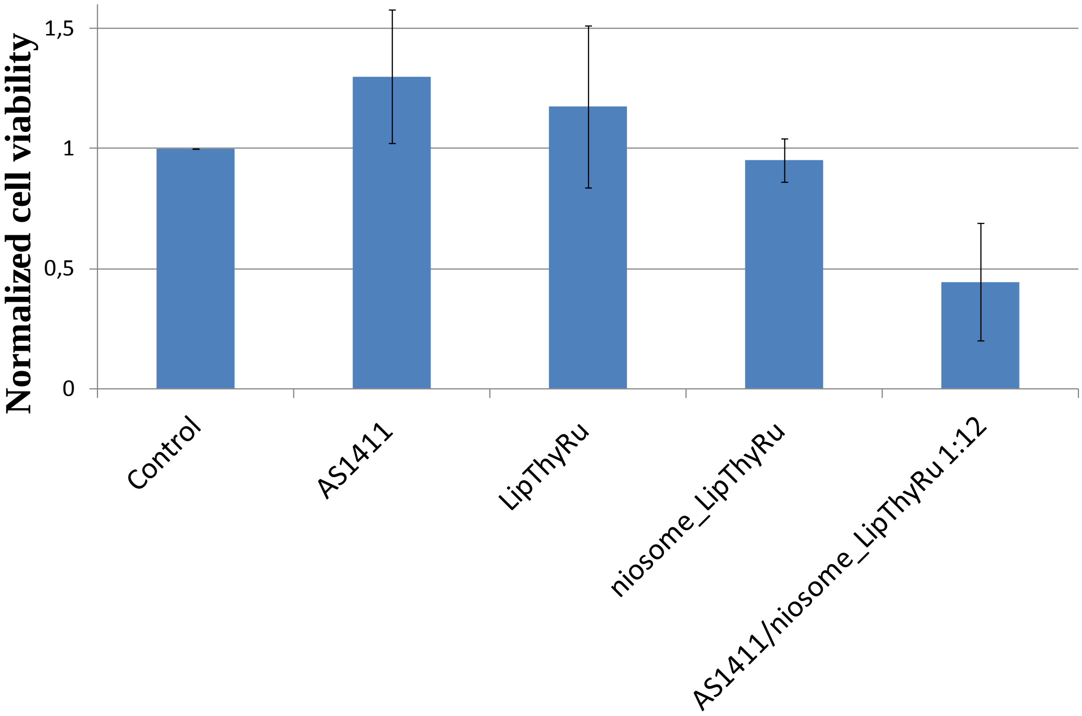

Figure 105. Normalized cell viability of AS1411 (500 nM), LipThyRu (250 nM), niosome_LipThyRu and AS1411/niosome_LipThyRu formulations (at oligo/vesicles 1:12 ratio and 6 µM niosome concentrations). The here reported results are mean values ± S.D. for three independent experiments.

This study requires a deeper characterization and biological evaluation, but preliminary *in vitro* bioscreens results are very promising demonstrating the sinergic effect between the AS1411 oligonucleotide and the LipThyRu Ru-complex, therefore prompting us to continue into this research.

2.2. Experimental section

- **Materials and general methods**

All the reagents and solvents were of the highest commercially available quality and were used as received. Polysorbate-80 (Tween-80), 3-(4,5-dimethylthiazol-2-yl)-2,5-diphenyltetrazolium bromide (MTT reagent) and the AS1411 oligonucleotide (5′-GGTGGTGGTGGTTGTGGTGGTGGTGG-3’) were purchased from Sigma-Aldrich. The cationic lipid 2,3-di(tetradecyloxy)propan-1-aminium chloride was purchased from Sapala Organics Privated Ltd (Telengana St., India). PBS buffer and Dulbecco’s Modified Eagle’s Medium (DMEM), which was supplemented with a 10% heat-inactive fetal serum bovine (FBS), were purchased from Gibco.

- **Preparation of synthetic niosome vesicles**

Niosome vesicles were prepared using a film-hydration method dissolving in 1 mL of chloroform equimolecular amounts of the synthetic cationic lipid [2,3-di(tetradecyloxy)propan-1-aminium chloride] and the non-ionic surfactant polysorbate 80. Then the solvent was evaporated and the resulting crude was kept under vacuum at r.t. overnight. The dried lipid film was hydrated with 1 mL of the selected buffer, heated at 60 °C for 20 min and filtered through a 0.2 μm membrane filter. The dispersion was vortexed and sonicated for 3 min before use. In order to obtain niosome_LipThyRu and AS1411/niosome_LipThyRu, the encapsulation of LipThyRu within the niosomes was carried out mixing 1 mg of the Ru(III) compound (0.78 nmol) with the aminolipid and the surfactant following the previously described procedure and heating the lipid film from 40 to 45 ^{o}C for 40 minutes.

AS1411/niosome and AS1411/niosome_LipThyRu were then obtained by adding the required amount of cationic lipid dispersion to aliquots containing fixed amounts of ODN. The resulting mixtures were vortexed and sonicated for 2 min and finally incubated at 37 °C for 30 min.

- **Electrophoretic mobility shift assay**

AS1411 oligonucleotide (0.5 μM) was mixed with increasing amounts of the niosome (taken from a 28.9 mM stock concentration in HEPES, pH 7.4) providing the system AS1411/niosome ranging from 0 to 1:16 molar ratios (total volume of 25 µL). The resulting samples were incubated at 37 °C for 30 min. These formulations were then analysed using gel electrophoresis carried out on a 20% polyacrylamide gel at 150 V for 5 h at 25 ºC in 1XTBE buffer. Pictures of the obtained gel were taken using Fujifilm LAS-1000 Intelligent Dark Box II using IRLAS-1000 Lite v1.2.

- **Zeta potential**

Zeta potential measurements were obtained by laser doppler velocimetry on a Zetasizer Nano ZS (Malvern Instruments) using AS1411 (from a 0.5 μM stock solution) at a final volume of 50 µL and evaluating different AS1411/niosome molar ratios ranging from 1:2 to 1:16 (using a 28.9 mM niosome stock solution in 20 mM HEPES, pH 7.4). All the measurements were performed at 25 °C using water as solvent (total volume of 1.0 mL). Data are shown as the average value of three independent determinations.

- **Size measurement**

The particle size of niosome vesicles and niosome formulations were determined using a dynamic light scattering instrument (LS Instruments, 3D cross correlation multiple-scattering) equipped with a He–Ne laser (632.8 nm) with variable intensity. The samples were prepared using AS1411 at 1.0 μM concentration in a final volume of 200 μL and the AS1411/niosome system evaluated at 1:6 and 1:12 molar ratios, respectively (using a 28.9 mM niosome stock solution in 20 mM HEPES, pH 7.4). All the niosome formulations were previously sonicated and the measurements taken at a scattering angle of 90° in triplicates, without diluting the samples at a constant temperature of 25 °C. The particle radius was calculated by fitting of the first cumulant parameter.

- **Cell culture**

HeLa cells were cultured at 37 °C, under a 5% CO_2 atmosphere in DMEM partially supplemented with 10% fetal bovine serum with two antibiotics. Cells were regularly passaged in order to maintain exponential growth. 24 h before the experiments, the cells were trypsinized and diluted 1:5 with a fresh medium and 1000 cells were transferred to a 96-well plate (100 μL per well).

- **Analysis of cell viability by the MTT colorimetric assay**

HeLa cells viability in the presence of all niosome formulations was tested at 6 μM concentration (from a 63.3 mM niosome_LipThyRu stock solutions in PBS, respectively) using the MTT colorimetric assay. For each assay, the cells were seeded at 1000 cell/well on a 96-well plate in 100 μL of DMEM and cultured for 24 h. Then the cells were incubated with the different niosome concentrations, after 6 h, the culture medium was discarded, the wells were washed twice with PBS and additional (100 μL) DMEM was added after washing and cultured for 72 h.

After 72 h, MTT was added at a final concentration of 0.5 mg/mL and the resulting system was incubated for 2 h at 37 °C. Finally, the medium was removed and DMSO (100 μL) was added to dissolve formazan crystals (15 min under stirring at room temperature) and finally the absorbance of the solution at $\lambda = 570$ nm was measured using a Glomax spectrophotometer. The experiments were carried out in triplicate.

Chapter 6

1. General conclusions

This work is centred on the preparation of multicomponent systems presenting both therapeutic and diagnostic agents as well as active targeting ligands. Specifically it has been focused on the evaluation of:

1) novel Ru(III)-based complexes with enhanced antiproliferative activity: in this context, the preparation of new ruthenium compounds involving nucleoside- (in the case of LipThyRu) and amino acids-lipid (in the case of TUGluRu and TOTyroRu) as central scaffolds has been described. These derivatives have been designed as prodrugs of a simple Ru(III)-complex named Aziru, showing higher half-lives in comparison with AziRu;

2) NOTA derivatives as imaging agents: in this frame, three novel lipid analogs of the macrocycle NOTA - a well known ^{68}Ga chelator used in PET imaging – presenting lipophilic moieties such as oleyl (NOTA-OL), lipoyl (NOTA-Lip) or biotin (NOTA-Bio), have been synthesized and fully characterized;

3) DNA aptamers, exploring in particular the TBA, selectively targeting thrombin involved in fibrin formation, and the nucleolin-targeting AS1411 aptamer.

TBA has been conjugated with a dansyl at the 3'-end a β-cyclodextrin at the 5'-end plus a biotin, obtaining a tris-modified TBA (tris-mTBA). The couple dansyl/cyclodextrin allows to monitor the folding/unfolding of the aptamer by different spectroscopic techniques, while biotin allows to immobilize this aptamer on streptavidin-coated silica nanoparticles. It has been demonstrated that functionalized nanoparticles with tris-mTBA inhibit the human thrombin activity about 10 times more efficiently than the unmodified TBA. In addition the activity of tris-mTBA can be stopped by addition of the complementary sequence, forming a duplex with the tris-mTBA. Hence it is possible to restore the thrombin ability to convert fibrinogen into fibrin with a tunable control of the coagulation process.

Concerning AS1411, three lipophilic derivatives of this G-quadruplex forming aptamer with cholesteryl or stearyl appendages at the 5’-end have been selected and studied in solution by UV, CD, gel electrophoresis and size exclusion chromatography techniques. The influence of the nature of the cation (Na^+ or K^+) and of concentration on the conformational behaviour and thermal stability of the corresponding G-quadruplex structures has been also evaluated. This study has demonstrated that not only the unmodified AS1411 aptamer but also its 5’-lipophilic conjugates show a high polymorphism forming high order G-quadruplex structures or large aggregates in solution, especially at high concentrations.

In conclusion, my PhD work has put the bases for the preparation of multifunctional nanoparticles for theranostic applications. In particular, with this work suitable targeting, imaging and therapeutic agents have been modified with different derivatizations and thus rendered available for the functionalization of different types of nanoparticle-based systems.

To date, three multifunctional systems have been prepared and tested *in vitro* with very promising results: tris-mTBA-Sicastar® nanoparticles, DOTAP-based liposomes loaded with TUGluRu and NOTA-OL, and niosome-based formulations incorporating LipThyRu and AS1411 oligonuleotide. Further studies are in progress to obtain and characterize multifunctional nanoparticles based on SPIONs, incorporating the here prepared targeting (AS1411 derivatives), anticancer (amphiphilic Ru complexes) and imaging (NOTA derivatives) agents.

2. List of Publications

- Musumeci, D.; **Riccardi, C.**; Montesarchio, D.
  G-Quadruplex forming oligonucleotides as anti-HIV agents.
  Molecules **2015**, *20*, 17511–17532.
- Musumeci, D.; Platella, C.; **Riccardi, C.**; Merlino, A.; Marzo, T.; Massai, L.; Messori, L.; Montesarchio, D.
  A first-in-class and a fished out anticancer platinum compound: cis-[$PtCl_2(NH_3)_2$] and cis-[$PtI_2(NH_3)_2$] compared for their reactivity towards DNA model systems.
  Dalton Trans. **2016**, *45*, 8587–8600.
- Musumeci, D.; Roviello, G. N.; Rigione, G.; Capasso, D.; Di Gaetano, S.; **Riccardi, C.**; Roviello, V.; Montesarchio, D.
  Benzodifuran derivatives as potential antiproliferative agents: possible correlation between their bioactivity and aggregation properties.
  ChemPlusChem **2017**, *82*, 251–260.
- **Riccardi, C.**; Musumeci, D.; Irace, C.; Paduano, L.; Montesarchio, D.
  Ru(III) complexes for anticancer therapy: the importance of being nucleolipidic.
  Eur. J. Org. Chem. **2017**, 1100–1119.
- Platella, C.; **Riccardi, C.**; Montesarchio, D.; Roviello, G. N.; Musumeci, D.
  G-Quadruplex-based aptamers against protein targets in therapy and diagnostics. *Biochim. Biophys. Acta - Gen. Subj.* **2017**,
  http://dx.doi.org/10.1016/j.bbagen.2016.11.027.
- Irace, C.; Misso, G.; Capuozzo, A.; Piccolo, M.; **Riccardi, C.**; Luchini, A.; Caraglia, M.; Paduano, L.; Montesarchio, D.; Santamaria, R.
  Antiproliferative effects of ruthenium-based nucleolipidic nanoaggregates in human models of breast cancer in vitro.
  Sci. Rep., **2017**, *7*, 45236.
- **Riccardi, C.**; Russo Krauss, I.; Musumeci, D.; Morvan, F.; Meyer, A.; Vasseur, J.-J.; Paduano, L.; Montesarchio D.
  Fluorescent thrombin binding aptamer-tagged nanoparticles for an efficient and reversible control of thrombin activity. *Manuscript under review.*

3. Abbreviations

18LPC	1-octadecyl-2-hydroxy-sn-glycero-3-phosphocholine
3T3L-1	murine fibroblasts
A549	human lung adenocarcinoma cell line
AcOEt	ethyl acetate
AMD	neovascular age-related macular degeneration
Bn	benzyl
C6	tumor rat glioma cells
Calu-6	human lung adenocarcinoma cell line
CD	circular dichroism spectroscopy
cDDP	cisplatin
CE	2-cyanoethyl
COSY	correlation spectroscopy
CRO	control oligonucleotides
CT	computed tomography
DCC	*N*,*N*-dicyclohexylcarbodiimide
DEAD	diethyl azodicarboxylate
DHB	2,5-dihydroxybenzoic acid
DIPEA	*N*,*N*-diisopropylethylamine
DLS	dynamic light scattering
DMAP	4-(*N*,*N*-dimethylamino)pyridine
DMEM	Dulbecco’s Modified Eagle’s Medium
DMF	*N*,*N*-dimethylformamide
DMSO	dimethyl sulfoxide
DMT	4,4-dimethoxytriphenylmethyl
DOTA	1,4,7,10-tetraazacyclododecane-1,4,7,10-tetraacetic acid
DOTAP	1,2-dioleoyl-3-trimethylammoniumpropane
ec	end-capped
EDTA	ethylenediaminetetraacetic acid
ESI	electrospray ionization
EtOH	ethanol
FBS	fetal serum bovine
FDG	fluorodeoxyglucose
Fmoc	9-fluorenylmethoxycarbonyl
FTIR-ATR	fourier transformed infrared spectroscopy from attenuated total reflectance
G4	G-quadruplex
GRO	guanine-rich oligonucleotide
HaCaT	non cancer human keratinocytes

HATU	1-[bis(dimethylamino)methylene]-1*H*-1,2,3-triazolo[4,5-*b*]pyridinium 3-oxid hexafluorophosphate
HEG	hexaethylene glycol
HeLa	human cervical cancer cells
HEPES	2-[4-(2-hydroxyethyl)piperazin-1-yl]ethanesulfonic acid
HEWL	hen egg white lysozyme
HIV	human immunodeficiency virus
HPLC	high performance liquid chromatography
HSQC	heteronuclear single quantum correlation
hTf	human serum transferrin
IC_{50}	half-maximal inhibitory concentration
ID	internal diameter
Im	imidazole
Ind	indazole
L6	rat muscle cells
LC	liquid chromatography
LMCT	ligand-to-metal charge transfer transition
m.p.	melting point
MALDI	matrix-assisted laser desorption ionization
MCF-7	human breast adenocarcinoma cell line
MeOH	methanol
MMT	4-monomethoxytrityl
MMT-Cl	4-methoxytriphenylmethyl chloride
MRI	magnetic resonance imaging
MS	mass spectrometry
mTOR	mammalian target of rapamycin
MTT	3-(4,5-dimethylthiazol-2-yl)-2,5-diphenyltetrazolium bromide
NGS	next-generation sequencing
NMR	nuclear magnetic resonance
NOTA	1,4,7-triazacyclononane-1,4,7-triacetic acid
NPs	nanoparticles
ODN	oligonucleotide
PAGE	polyacrylamide gel electrophoresis
PBS	phosphate-buffered saline
PCR	polymerase chain reaction
PEG	polyethylene glycol
PET	positron emission tomography
Ph	phenyl

POPC	1-palmitoyl-2-oleoyl-*sn*-glycero-3-phosphocholine
ppm	parts per million
Py	pyridine
Rac1	Ras-related C3 botulinum toxin substrate 1
RES	reticulo-endothelial system
R_f	retention factor
RNase A	bovine pancreatic ribonuclease
RSV	respiratory syncytial virus
SANS	small angle neutron scattering
SEC	size exclusion chromatography
SELEX	systematic evolution of ligands by exponential enrichment
siRNA	small interfering RNA
SPECT	single photon emission computed tomography
SPIONs	superparamagnetic iron oxide nanoparicles
T2	transversal proton relaxation time
TAE	Tris-acetate-EDTA
TBA	thrombin binding aptamer
***t*Bu**	*tert*-butyl
TCA	trichloroacetic acid
TEA	triethylamine
TEAA	triethylammonium acetate
TEG-OMe	triethylene glycol monomethyl ether
TFA	trifluoroacetic acid
THF	tetrahydrofuran
THME	1,1,1-tris(hydroxymethyl)ethane
Thy	thymidine
TLC	thin layer chromatography
T_m	melting temperature
TOF	time of flight
t_R	retention time
US	ultrasound
UV	ultraviolet spectroscopy
VEGF	vascular endothelial growth factor
WiDr	human epithelial colorectal adenocarcinoma cell line

4. References

[1] I. Velikyan, *Theranostics* **2012**, *2*, 424–426.

[2] G. Bao, S. Mitragotri, S. Tong, *Annu. Rev. Biomed. Eng.* **2013**, *15*, 253–282.

[3] M. Kalia, *Metabolism.* **2013**, *62*, S11–S14.

[4] J. H. Ryu, S. Lee, S. Son, S. H. Kim, J. F. Leary, K. Choi, I. C. Kwon, *J. Control. Release* **2014**, *190*, 477–484.

[5] J. T. Cole, N. B. Holland, *Drug Deliv. Transl. Res.* **2015**, *5*, 295–309.

[6] L. S. Wang, M. C. Chuang, J. A. Ho, *Int. J. Nanomedicine* **2012**, *7*, 4679–95.

[7] S. S. Kelkar, T. M. Reineke, *Bioconjugate Chem.* **2011**, *22*, 1879–1903.

[8] R. P. Baum, H. R. Kulkarni, *Theranostics* **2012**, *2*, 437–447.

[9] D. Y. Lee, K. C. P. Li, *Am. J. Roentgenol.* **2011**, *197*, 318–324.

[10] H. Koo, M. S. Huh, I.-C. Sun, S. H. Yuk, K. Choi, K. Kim, I. C. Know, *Acc. Chem. Res.* **2011**, *44*, 1018–1028.

[11] X. Ma, Y. Zhao, X. J. Liang, *Acc. Chem. Res.* **2011**, *44*, 1114–1122.

[12] K. Y. Choi, G. Liu, S. Lee, X. Chen, *Nanoscale* **2012**, *4*, 330–342.

[13] J. H. Ryu, H. Koo, I. C. Sun, S. H. Yuk, K. Choi, K. Kim, I. C. Kwon, *Adv. Drug Deliv. Rev.* **2012**, *64*, 1447–1458.

[14] H. T. Kim, S. Lee, X. Chen, *Expert Rev. Mol. Diagn.* **2013**, *13*, 257–269.

[15] K. Öberg, *Theranostics* **2012**, *2*, 448–458.

[16] B. Sumer, J. Gao, *Nanomedicine* **2008**, *3*, 137–140.

[17] T. Lammers, S. Aime, W. E. Hennink, G. Storm, F. Kiessling, *Acc. Chem. Res.* **2011**, *44*, 1029–1038.

[18] J. Choi, N. S. Wang, in *Biomed. Eng. - From Theory to Appl.*, Prof. Reza Fazel (Ed.), **2011**, pp. 299 – 314.

[19] M. V. Yezhelyev, X. Gao, Y. Xing, A. Al-Hajj, S. Nie, R. M. O'Regan, *Lancet Oncol.* **2006**, *7*, 657–667.

[20] X. Wang, L. Yang, Z. Chen, D. M. Shin, *A Cancer J. Clin.* **2008**, *58*, 97–110.

[21] N. Sanvicens, M. P. Marco, *Trends Biotechnol.* **2008**, *26*, 425–433.

[22] A. H. Faraji, P. Wipf, *Bioorg. Med. Chem.* **2009**, *17*, 2950–2962.

[23] S. M. Janib, A. S. Moses, J. A. MacKay, *Adv. Drug Deliv. Rev.* **2010**, *62*, 1052–1063.

[24] A. Shapira, Y. D. Livney, H. J. Broxterman, Y. G. Assaraf, *Drug Resist. Updat.* **2011**, *14*, 150–163.

[25] K. H. Bae, H. J. Chung, T. G. Park, *Mol. Cells* **2011**, *31*, 295–302.

[26] M. K. Yu, J. Park, S. Jon, *Theranostics* **2012**, *2*, 3–44.

[27] R. Paliwal, R. J. Babu, S. Palakurthi, *AAPS PharmSciTech* **2014**, *15*, 1527–1534.

[28] A. Radomska, J. Leszczyszyn, M. W. Radomski, *Adv. Clin. Exp. Med.* **2016**, *25*, 151–162.

[29] H. Xing, K. Hwang, Y. Lu, *Theranostics* **2016**, *6*, 1336–1352.

[30] B. Y. S. Kim, J. T. Rutka, W. C. W. Chan, *N. Engl. J. Med.* **2010**, *363*, 2434–2443.

[31] J. D. Heidel, M. E. Davis, *Pharm. Res.* **2011**, *28*, 187–199.

[32] H. C. Huang, S. Barua, G. Sharma, S. K. Dey, K. Rege, *J. Control. Release* **2011**, *155*, 344–357.

[33] H. Maeda, *Adv. Enzyme Regul.* **2001**, *41*, 189–207.

[34] F. Alexis, E. Pridgen, L. K. Molnar, O. C. Farokhzad, *Mol. Pharm.* **2008**, *5*, 505–515.

[35] M. Longmire, P. L. Choyke, H. Kobayashi, *Nanomedicine* **2008**, *3*, 703–717.

[36] S. D. Li, L. Huang, *Mol. Pharm.* **2008**, *5*, 496–504.

[37] V. Mailänder, K. Landfester, *Biomacromolecules* **2009**, *10*, 2379–2400.

[38] B. S. Zolnik, Á. ́ González-Fernández, N. Sadrieh, M. A. Dobrovolskaia, *Endocrinology* **2010**, *151*, 458–465.

[39] K. Shao, S. Singha, X. Clemente-Casares, S. Tsai, Y. Yang, P. Santamaria, *ACS Nano* **2015**, *9*, 16–30.

[40] M. E. Davis, Z. G. Chen, D. M. Shin, *Nat. Rev. Drug Discov.* **2008**, *7*, 771–782.

[41] M. Wang, M. Thanou, *Pharmacol. Res.* **2010**, *62*, 90–99.

[42] J. M. Rademaker-Lakhai, D. Van Den Bongard, D. Pluim, J. H. Beijnen, J. H. M. Schellens, *Clin. Cancer Res.* **2004**, *10*, 3717–3727.

[43] C. G. Hartinger, M. A. Jakupec, S. Zorbas-Seifried, M. Groessl, A. Egger, W. Berger, H. Zorbas, P. J. Dyson, B. K. Keppler, *Chem. Biodivers.* **2008**, *5*, 2140–2155.

[44] F. Lentz, A. Drescher, A. Lindauer, M. Henke, R. A. Hilger, C. G. Hartinger, M. E. Scheulen, C. Dittrich, B. K. Keppler, U. Jaehde, *Anticancer Drugs* **2009**, *20*, 97–103.

[45] S. Leijen, S. A. Burgers, P. Baas, D. Pluim, M. Tibben, E. Van Werkhoven, E. Alessio, G. Sava, J. H. Beijnen, J. H. M. Schellens, *Invest. New Drugs* **2015**, *33*, 201–214.

[46] H. Ding, F. Wu, *Theranostics* **2012**, *2*, 1040–1053.

[47] R. Chakravarty, H. Hong, W. Cai, *Mol. Pharm.* **2014**, *11*, 3777–3797.

[48] H. Grönbeck, A. Curioni, W. Andreoni, *J. Am. Chem. Soc.* **2000**, *122*, 3839–3842.

[49] A. H. Pakiari, Z. Jamshidi, *J. Phys. Chem. A* **2010**, *114*, 9212–9221.

[50] N. M. Green, *Methods Enzymol.* **1990**, *184*, 51–67.

[51] C. Blanpain, *Nat. Cell Biol.* **2013**, *15*, 126–134.

[52] S. Rafique, M. Idrees, A. Nasim, H. Akbar, A. Athar, *Biotechnol. Mol. Biol. Rev.* **2010**, *5*, 38–45.

[53] I. Ott, R. Gust, *Arch. Pharm.* **2007**, *340*, 117–126.

[54] G. Gasser, I. Ott, N. Metzler-Nolte, *J. Med. Chem.* **2011**, *54*, 3–25.

[55] B. Rosenberg, L. Vancamp, T. Krigas, *Nature* **1965**, *205*, 698–699.

[56] E. Renshaw, A. J. Thomson, *J. Bacteriol.* **1967**, *94*, 1915–1918.

[57] B. Rosenberg, L. Van Camp, E. B. Grimley, A. J. Thomson, *J. Biol. Chem.* **1967**, *242*, 1347–1352.

[58] B. Rosenberg, E. Renshaw, L. Vancamp, J. Hartwick, J. Drobnik, *J. Bacteriol.* **1967**, *93*, 716–721.

[59] B. Rosenberg, L. van Camp, J. E. Trosko, V. H. Mansour, *Nature* **1969**, *222*, 385–386.

[60] G. Sava, S. Pacor, F. Bregant, V. Ceschia, G. Mestroni, *Anticancer Drugs* **1990**, *1*, 99–108.

[61] M. J. Clarke, F. Zhu, D. R. Frasca, *Chem. Rev.* **1999**, *99*, 2511–2533.

[62] G. Sava, A. Bergamo, *Int. J. Oncol.* **2000**, *17*, 353–365.

[63] M. J. Clarke, *Coord. Chem. Rev.* **2002**, *232*, 69–93.

[64] M. J. Clarke, *Coord. Chem. Rev.* **2003**, *236*, 209–233.

[65] M. Galanski, V. B. Arion, M. A. Jakupec, B. K. Keppler, *Curr. Pharm. Des.* **2003**, *9*, 2078–2089.

[66] E. Alessio, G. Mestroni, A. Bergamo, G. Sava, *Curr. Top. Med. Chem.* **2004**, *4*, 1525–1535.

[67] I. Kostova, *Curr. Med. Chem.* **2006**, *13*, 1085–1107.

[68] A. Levina, A. Mitra, P. A. Lay, *Metallomics* **2009**, *1*, 458–470.

[69] A. Bergamo, G. Sava, *Dalton Trans.* **2011**, *40*, 7817–7823.

[70] G. Sava, A. Bergamo, P. J. Dyson, *Dalton Trans.* **2011**, *40*, 9069–9075.

[71] A. Bergamo, C. Gaiddon, J. H. Schellens, J. H. Beijnen, G. Sava, *J. Inorg. Biochem.* **2012**, *106*, 90–99.

[72] S. Komeda, A. Casini, *Curr. Top. Med. Chem.* **2012**, *12*, 219–235.

[73] C. Riccardi, D. Musumeci, C. Irace, L. Paduano, D. Montesarchio, *Eur. J. Org. Chem.* **2017**, 1100–1119.

[74] W. J. Zeller, S. Frühauf, G. Chen, B. K. Keppler, E. Frei, M. Kaufmann, *Eur. J. Cancer* **1991**, *27*, 62–67.

[75] M. Coluccia, G. Sava, F. Loseto, A. Nassi, A. Boccarelli, D. Giordano, E. Alessio, G. Mestroni, *Eur. J. Cancer* **1993**, *29*, 1873–1879.

[76] E. Alessio, G. Mestroni, A. Bergamo, G. Sava, in *Met. Ions Biol. Syst.* (Eds.: A. Sigel, H. Sigel), Marcel Dekker, New York, **2004**, pp. 323–351.

[77] V. Brabec, O. Novàkovà, *Drug Resist. Updat.* **2006**, *9*, 111–122.

[78] B. K. Keppler, W. Rupp, U. M. Juhl, H. Endres, R. Niebl, W. Balzer, *Inorg. Chem.* **1987**, *26*, 4366–4370.

[79] E. D. Kreuser, B. K. Keppler, W. E. Berdel, A. Piest, E. Thiel, *Semin. Oncol.* **1992**, *19*, 73–81.

[80] V. Singh, G. K. Azad, P. Mandal, M. A. Reddy, R. S. Tomar, *FEBS Lett.* **2014**, *588*, 1044–1052.

[81] G. Mestroni, E. Alessio, G. Sava, S. Pacor, M. Coluccia, A. Boccarelli, *Met. Based Drugs* **1994**, *1*, 41–63.

[82] G. Sava, I. Capozzi, K. Clerici, G. Gagliardi, E. Alessio, G. Mestroni, *Clin. Exp. Metastasis* **1998**, *16*, 371–379.

[83] M. Brindell, D. Piotrowska, A. A. Shoukry, G. Stochel, R. Eldik, *J. Biol. Inorg. Chem.* **2007**, *12*, 809–818.

[84] M. Brindell, I. Stawoska, J. Supel, A. Skoczowski, G. Stochel, R. Van Eldik, *J. Biol. Inorg. Chem.* **2008**, *13*, 909–918.

[85] C. Bartel, A. E. Egger, M. A. Jakupec, P. Heffeter, M. Galanski, W. Berger, B. K. Keppler, *J. Biol. Inorg. Chem.* **2011**, *16*, 1205–1215.

[86] C. G. Hartinger, S. Zorbas-Seifried, M. A. Jakupec, B. Kynast, H. Zorbas, B. K. Keppler, *J. Inorg. Biochem.* **2006**, *100*, 891–904.

[87] E. Alessio, *Eur. J. Inorg. Chem.* **2016**, *55*, DOI 10.1002/ejic.201600986.

[88] D. Frasca, J. Ciampa, J. Emerson, R. S. Umans, M. J. Clarke, *Met. Based Drugs* **1996**, *3*, 197–209.

[89] M. Pongratz, P. Schluga, M. A. Jakupec, V. B. Arion, C. G. Hartinger, G. Allmaier, B. K. Keppler, *J. Anal. At. Spectrom.* **2004**, *19*, 46–51.

[90] O. Mazuryk, K. Kurpiewska, K. Lewinski, G. Stochel, M. Brindell, *J. Inorg. Biochem.* **2012**, *116*, 11–18.

[91] A. Bergamo, M. Cocchietto, I. Capozzi, G. Mestroni, E. Alessio, G. Sava, *Anticancer Drugs* **1996**, *7*, 697–702.

[92] G. Sava, K. Cleriri, I. Capozzi, M. Cocchietto, R. Gagliardi, E. Alessio, G. Mestroni, A. Perbellini, *Anticancer drugs* **1999**, *10*, 129–138.

[93] S. Zorzet, A. Bergamo, M. Cocchietto, A. Sorc, B. Gava, E. Alessio, E. Iengo, G. Sava, *J. Pharmacol. Exp. Ther.* **2000**, *295*, 927–933.

[94] S. Zorzet, A. Sorc, C. Casarsa, M. Cocchietto, G. Sava, *Met. Based Drugs* **2001**, *8*, 1–7.

[95] G. Pintus, B. Tadolini, A. M. Posadino, B. Sanna, M. Debidda, F. Bennardini, G. Sava, C. Ventura, *Eur. J. Biochem.* **2002**, *269*, 5861–5870.

[96] A. Bergamo, B. Gava, E. Alessio, G. Mestroni, B. Serli, M. Cocchietto, S. Zorzet, G. Sava, *Int. J. Oncol.* **2002**, *21*, 1331–1338.

[97] G. Sava, S. Zorzet, C. Turrin, F. Vita, M. Soranzo, G. Zabucchi, M. Cocchietto, A. Bergamo, S. Digiovine, G. Pezzoni, et al., *Clin. Cancer Res.* **2003**, *9*, 1898–1905.

[98] S. Pacor, S. Zorzet, M. Cocchietto, M. Bacac, M. Vadori, C. Turrin, B. Gava, A. Castellarin, G. Sava, *J. Pharmacol. Exp. Ther.* **2004**, *310*, 737–744.

[99] M. Bacac, M. Vadori, G. Sava, S. Pacor, *Cancer Immunol. Immunother.* **2004**, *53*, 1101–1110.

[100] M. Bacac, A. C. G. Hotze, K. Van Der Schilden, J. G. Haasnoot, S. Pacor, E. Alessio, G. Sava, J. Reedijk, *J. Inorg. Biochem.* **2004**, *98*, 402–412.

[101] B. Gava, S. Zorzet, P. Spessotto, M. Cocchietto, G. Sava, *J. Pharmacol. Exp. Ther.* **2006**, *317*, 284–291.

[102] A. Bergamo, G. Sava, *Dalton Trans.* **2007**, *36*, 1267–1272.

[103] M. Groessl, E. Reisner, C. G. Hartinger, R. Eichinger, O. Semenova, A. R. Timerbaev, M. A. Jakupec, V. B. Arion, B. K. Keppler, *J. Med. Chem.* **2007**, *50*, 2185–2193.

[104] J. Chen, L. Chen, S. Liao, K. Zheng, L. Ji, *J. Phys. Chem. B* **2007**, *111*, 7862–7869.

[105] N. Besker, C. Coletti, A. Marrone, N. Re, *J. Phys. Chem. B* **2008**, *112*, 3871–3875.

[106] E. Alessio, G. Balducci, A. Lutman, G. Mestroni, M. Calligaris, W. M. Attia, *Inorg. Chim. Acta* **1993**, *203*, 205–217.

[107] B. M. Blunden, M. H. Stenzel, *J. Chem. Technol. Biotechnol.* **2015**, *90*, 1177–1195.

[108] M. Bouma, B. Nuijen, M. T. Jansen, G. Sava, A. Flaibani, A. Bult, J. H. Beijnen, *Int. J. Pharmacol.* **2002**, *248*, 239–246.

[109] I. Bratsos, S. Jedner, T. Gianferrara, E. Alessio, *Chim. Int. J. Chem.* **2007**, *61*, 692–697.

[110] A. V. Vargiu, A. Robertazzi, A. Magistrato, P. Ruggerone, P. Carloni, *J. Phys. Chem. B* **2008**, *112*, 4401–4409.

[111] A. Vacca, M. Bruno, A. Boccarelli, M. Coluccia, D. Ribatti, A. Bergamo, S. Garbisa, L. Sartor, G. Sava, *Br. J. Cancer* **2002**, *86*, 993–998.

[112] L. Messori, P. Orioli, D. Vullo, E. Alessio, E. Iengo, *Eur. J. Biochem.* **2000**, *267*, 1206–1213.

[113] A. Bergamo, R. Gagliardi, V. Scarcia, A. Furlani, E. Alessio, G. Mestroni, G. Sava, *J. Pharmacol. Exp. Ther.* **1999**, *289*, 559–564.

[114] M. R. Berger, F. T. Garzon, B. K. Keppler, D. Schmahl, *Anticancer Res.* **1989**, *9*, 761–765.

[115] A. Galeano, M. R. Berger, B. K. Keppler, *Arzneimittelforschung.* **1992**, *42*, 821–824.

[116] M. H. Seelig, M. R. Berger, B. K. Keppler, *J. Cancer Res. Clin. Oncol.* **1992**, *118*, 195–200.

[117] P. Schluga, C. G. Hartinger, A. Egger, E. Reisner, M. Galanski, M. A. Jakupec, B. K. Keppler, *Dalton Trans.* **2006**, *14*, 1796–1802.

[118] E. Reisner, V. B. Arion, B. K. Keppler, A. J. L. Pombeiro, *Inorg. Chim. Acta* **2008**, *361*, 1569–1583.

[119] C. G. Hartinger, B. K. Keppler, *Electrophoresis* **2007**, *28*, 3436–3446.

[120] S. Kapitza, M. Pongratz, M. A. Jakupec, P. Heffeter, W. Berger, L. Lackinger, B. K. Keppler, B. Marian, *J. Cancer Res. Clin. Oncol.* **2005**, *131*, 101–110.

[121] E. S. Antonarakis, A. Emadi, *Cancer Chemother. Pharmacol.* **2010**, *66*, 1–9.

[122] P. Heffeter, K. Böck, B. Atil, M. A. Reza Hoda, W. Körner, C. Bartel, U. Jungwirth, B. K. Keppler, M. Micksche, W. Berger, et al., *J. Biol. Inorg. Chem.* **2010**, *15*, 737–748.

[123] J. B. Aitken, S. Antony, C. M. Weekley, B. Lai, L. Spiccia, H. H. Harris, *Metallomics* **2012**, *4*, 1051.

[124] A. M. Pizarro, A. Habtemariam, P. J. Sadler, in *Med. Organomet. Chem.* (Eds.: G. Jaouen, N. Metzler-Nolte), Springer-Verlag, Heidelberg (Germany), **2010**, pp. 21–56.

[125] O. Dömötör, C. G. Hartinger, A. K. Bytzek, T. Kiss, B. K. Keppler, E. A. Enyedy, *J. Biol. Inorg. Chem.* **2013**, *18*, 9–17.

[126] A. Bijelic, S. Theiner, B. K. Keppler, A. Rompel, *J. Med. Chem.* **2016**, *59*, 5894–5903.

[127] L. Messori, F. Kratz, E. Alessio, *Met. Based Drugs* **1996**, *3*, 1–9.

[128] A. M. Pizarro, P. J. Sadler, *Biochimie* **2009**, *91*, 1198–1211.

[129] H. Sun, H. Li, P. J. Sadler, *Chem. Rev.* **1999**, *99*, 2817–2842.

[130] M. Groessl, M. Terenghi, A. Casini, L. Elviri, R. Lobinski, P. J. Dyson, *J. Anal . At. Spectrom.* **2010**, *25*, 305–313.

[131] W. Guo, W. Zheng, Q. Luo, X. Li, Y. Zhao, S. Xiong, F. Wang, *Inorg. Chem.* **2013**, *52*, 5328–5338.

[132] K. Spiewak, M. Brindell, *J. Biol. Inorg. Chem.* **2015**, *20*, 695–703.

[133] W. E. Winter, L. A. L. Bazydlo, N. S. Harris, *Lab. Med.* **2014**, *45*, 92–102.

[134] M. I. Webb, R. A. Chard, Y. M. Al-Jobory, M. R. Jones, E. W. Y. Wong, C. J. Walsby, *Inorg. Chem.* **2012**, *51*, 954–966.

[135] G. Mangiapia, G. D'Errico, L. Simeone, C. Irace, A. Radulescu, A. Di Pascale, A. Colonna, D. Montesarchio, L. Paduano, *Biomaterials* **2012**, *33*, 3770–3782.

[136] L. Simeone, G. Mangiapia, G. Vitiello, C. Irace, A. Colonna, O. Ortona, D. Montesarchio, L. Paduano, *Bioconjugate Chem.* **2012**, *23*, 758–770.

[137] G. Vitiello, A. Luchini, G. D'Errico, R. Santamaria, A. Capuozzo, C. Irace, D. Montesarchio, L. Paduano, *J. Mater. Chem. B* **2015**, *3*, 3011–3023.

[138] M. I. Webb, B. Wu, T. Jang, R. A. Chard, E. W. Y. Wong, M. Q. Wong, D. T. T. Yapp, C. J. Walsby, *Chem. Eur. J.* **2013**, *19*, 17031–17042.

[139] S. W. Chang, A. R. Lewis, K. E. Prosser, J. R. Thompson, M. Gladkikh, M. B. Bally, J. J. Warren, C. J. Walsby, *Inorg. Chem.* **2016**, *55*, 4850–4863.

[140] C. Mu, S. W. Chang, K. E. Prosser, A. W. Y. Leung, S. Santacruz, T. Jang, J. R. Thompson, D. T. T. Yapp, J. J. Warren, M. B. Bally, et al., *Inorg. Chem.* **2016**, *55*, 177–190.

[141] C. Tan, S. Wu, S. Lai, M. Wang, Y. Chen, L. Zhou, Y. Zhu, W. Lian, W. Peng, L. Ji, et al., *Dalton Trans.* **2011**, *40*, 8611–8621.

[142] A. Vergara, I. Russo Krauss, D. Montesarchio, L. Paduano, A. Merlino, *Inorg. Chem.* **2013**, *52*, 10714–10716.

[143] A. Vergara, G. D'Errico, D. Montesarchio, L. Paduano, A. Merlino, *Inorg. Chem.* **2013**, *52*, 4157–4159.

[144] L. Messori, A. Merlino, *Dalton Trans.* **2014**, *43*, 6128–6131.

[145] M. I. Webb, C. J. Walsby, *Dalton Trans.* **2011**, *40*, 1322–1331.

[146] L. Kelland, *Nat. Rev. Cancer* **2007**, *7*, 573–584.

[147] D. Musumeci, L. Rozza, A. Merlino, L. Paduano, T. Marzo, L. Massai, L. Messori, D. Montesarchio, *Dalton Trans.* **2015**, *44*, 13914–13925.

[148] G. Sava, A. Bergamo, S. Zorzet, B. Gava, C. Casarsa, M. Cocchietto, A. Furlani, V. Scarcia, B. Serli, E. Iengo, et al., *Eur. J. Cancer* **2002**, *38*, 427–435.

[149] M. Galanski, B. K. Keppler, *Anticancer. Agents Med. Chem.* **2007**, *7*, 55–73.

[150] M. Vaccaro, R. Del Litto, G. Mangiapia, A. M. Carnerup, G. D'Errico, F. Ruffo, L. Paduano, *Chem. Commun.* **2009**, 1404–6.

[151] L. Simeone, G. Mangiapia, C. Irace, A. Di Pascale, A. Colonna, O. Ortona, L. De Napoli, D. Montesarchio, L. Paduano, *Mol. Biosyst.* **2011**, *7*, 3075–3086.

[152] L. Simeone, C. Irace, A. Di Pascale, D. Ciccarelli, G. D'Errico, D. Montesarchio, *Eur. J. Med. Chem.* **2012**, *57*, 429–440.

[153] G. Mangiapia, G. Vitiello, C. Irace, R. Santamaria, A. Colonna, R. Angelico, A. Radulescu, G. D'Errico, D. Montesarchio, L. Paduano, *Biomacromolecules* **2013**, *14*, 2549–2560.

[154] D. Montesarchio, G. Mangiapia, G. Vitiello, D. Musumeci, C. Irace, R. Santamaria, G. D'Errico, L. Paduano, *Dalton Trans.* **2013**, *42*, 16697–16708.

[155] G. Mangiapia, M. Vaccaro, G. D'Errico, H. Frielinghaus, A. Radulescu, V. Pipich, A. M. Carnerup, L. Paduano, *Soft Matter* **2011**, *7*, 10577–10580.

[156] M. Vaccaro, A. Accardo, D. Tesauro, G. Mangiapia, D. Löf, K. Schillén, O. Söderman, G. Morelli, L. Paduano, *Langmuir* **2006**, *22*, 6635–6643.

[157] G. Mangiapia, A. Accardo, F. Lo Celso, D. Tesauro, G. Morelli, A. Radulescu, L. Paduano, *J. Phys.*

Chem. B **2004**, *108*, 17611–17617.
[158] H. Rosemeyer, *Chem. Biodivers.* **2005**, *2*, 977–1063.
[159] D. Berti, F. B. Bombelli, M. Fortini, P. Baglioni, *J. Phys. Chem. B* **2007**, *111*, 11734–11744.
[160] P. Barthélemy, *Comptes Rendus Chim.* **2009**, *12*, 171–179.
[161] V. Allain, C. Bourgaux, P. Couvreur, *Nucleic Acids Res.* **2012**, *40*, 1891–1903.
[162] S. Stolnik, L. Illum, S. S. Davis, *Adv. Drug Deliv. Rev.* **1995**, *16*, 195–214.
[163] N. Nishiyama, K. Kataoka, *Pharmacol. Ther.* **2006**, *112*, 630–648.
[164] M. H. Stenzel, *Chem. Commun.* **2008**, *44*, 3486–3503.
[165] A. Rösler, G. W. M. Vandermeulen, H. A. Klok, *Adv. Drug Deliv. Rev.* **2011**, *53*, 95–108.
[166] L. R. Arriaga, I. López-Montero, F. Monroy, G. Orts-Gil, B. Farago, T. Hellweg, *Biophys. J.* **2009**, *96*, 3629–3637.
[167] N. Larson, H. Ghandehari, *Chem. Mater.* **2012**, *24*, 840–853.
[168] H. Kobayashi, B. Turkbey, R. Watanabe, P. L. Choyke, *Bioconjugate Chem.* **2014**, *25*, 2093–2100.
[169] S. Di-Wen, G. Z. Pan, L. Hao, J. Zhang, Q. Z. Xue, P. Wang, Q. Z. Yuan, *Int. J. Pharm.* **2016**, *500*, 54–61.
[170] R. Satchi-Fainaro, R. Duncan, C. M. Barnes, *Adv. Polym. Sci.* **2006**, *193*, 1–65.
[171] O. Bomati-Miguel, N. Miguel-Sancho, I. Abasolo, A. P. Candiota, A. G. Roca, M. Acosta, S. Schwartz, C. Arus, C. Marquina, G. Martinez, et al., *J. Nanoparticle Res.* **2014**, *16*, 1–13.
[172] F. Dai, M. Du, Y. Liu, G. Liu, Q. Liu, X. Zhang, *J. Mater. Chem. B* **2014**, *2*, 2240–2247.
[173] A. Luchini, G. Vitiello, F. Rossi, O. Ruiz De Ballesteros, A. Radulescu, G. D’Errico, D. Montesarchio, C. de Julián Fernández, L. Paduano, *Phys. Chem. Chem. Phys.* **2015**, *17*, 6087–6097.
[174] A. Luchini, C. Irace, R. Santamaria, D. Montesarchio, R. K. Heenan, N. Szekely, A. Flori, L. Menichetti, L. Paduano, *Nanoscale* **2016**, *8*, 10078–10086.
[175] B. Neises, W. Steglich, *Angew. Chem. - Int. Ed. Eng.* **1978**, *17*, 522–524.
[176] A. Hassner, V. Alexanian, *Tetrahedron Lett.* **1978**, *19*, 4475–4478.
[177] E. Alessio, G. Balducci, M. Calligaris, G. Costa, W. M. Attia, G. Mestroni, *Inorg. Chem.* **1991**, *30*, 609–618.
[178] A. H. Velders, A. Bergamo, E. Alessio, E. Zangrando, J. G. Haasnoot, C. Casarsa, M. Cocchietto, S. Zorzet, G. Sava, *J. Med. Chem.* **2004**, *47*, 1110–1121.
[179] C. E. Hoyle, C. N. Bowman, *Angew. Chem. - Int. Ed. Eng.* **2010**, *49*, 1540–1573.
[180] L. Carpino, *J. Am. Chem. Soc.* **1993**, *115*, 4397–4398.
[181] V. P. Fitzjarrald, R. Pongdee, *Tetrahedron Lett.* **2007**, *48*, 3553–3557.
[182] O. Mitsunobu, M. Yamada, *Bull. Chem. Soc. Jpn.* **1967**, *40*, 2380–2382.
[183] M. Kirihara, Y. Asai, S. Ogawa, T. Noguchi, A. Hatano, Y. Hirai, *J. Synth. Org. Chem.* **2007**, *21*, 3286–3289.
[184] A. Hatefi, T. Minko, *Drug Deliv. Transl. Res.* **2012**, *2*, 1–2.
[185] Y. Zhang, H. F. Chan, K. W. Leong, *Adv. Drug Deliv. Rev.* **2013**, *65*, 104–120.
[186] H. R. Herschman, *Science.* **2003**, *302*, 605–608.
[187] R. Weissleder, M. J. Pittet, *Nature* **2008**, *452*, 580–589.
[188] C. R. Berry, P. Garg, *Semin. Nucl. Med.* **2014**, *44*, 66–75.
[189] L. J. Higgins, M. G. Pomper, *Semin. Oncol.* **2011**, *38*, 3–15.
[190] D. A. Mankoff, *J. Nucl. Med.* **2007**, *48*, 18N–21N.
[191] J. Paeng, D. Lee, *Open Nucl. Med. J.* **2010**, *2*, 145–152.
[192] M. Rudin, R. Weissleder, *Nat. Rev. Drug Discov.* **2003**, *2*, 123–131.
[193] W. B. Cai, X. Y. Chen, *J. Nucl. Med.* **2008**, *49*, 113S–128S.
[194] H. Hong, Y. Zhang, J. Sun, W. Cai, *Nano Today* **2009**, *4*, 399–413.
[195] M. Ryvolova, J. Chomoucka, J. Drbohlavova, P. Kopel, P. Babula, D. Hynek, V. Adam, T. Eckschlager, J. Hubalek, M. Stiborova, et al., *Sensors* **2012**, *12*, 14792–14820.
[196] T. F. Massoud, T. F. Massoud, S. S. Gambhir, S. S. Gambhir, *Genes Dev.* **2003**, *17*, 545–580.
[197] S. M. Ametamey, M. Honer, P. A. Schubiger, *Chem. Rev.* **2008**, *108*, 1501–1516.
[198] L. E. Jennings, N. J. Long, *Chem. Commun.* **2009**, 3511–3524.
[199] F. Kiessling, S. Fokong, J. Bzyl, W. Lederle, M. Palmowski, T. Lammers, *Adv. Drug Deliv. Rev.* **2014**, *72*, 15–27.
[200] B. C. Visser, B. M. Yeh, A. Qayyum, L. W. Way, C. E. McCulloch, F. V. Coakley, *Am. J. Roentgenol.* **2007**, *189*, 648–656.
[201] F. Rösch, R. P. Baum, *Dalton Trans.* **2011**, *40*, 6104–6111.

[202] R. P. Baum, H. R. Kulkarni, C. Carreras, *Semin. Nucl. Med.* **2012**, *42*, 190–207.
[203] S. S. Gambhir, *Nat. Rev. Cancer* **2002**, *2*, 683–693.
[204] R. J. Hicks, M. S. Hofman, *Nat. Rev. Clin. Oncol.* **2012**, *9*, 712–720.
[205] I. Velikyan, *Theranostics* **2014**, *4*, 47–80.
[206] J. Sörensen, *Theranostics* **2012**, *2*, 427–436.
[207] A. A. M. van der Veldt, E. F. Smit, A. A. Lammertsma, *Front. Oncol.* **2013**, *3*, 208–214.
[208] P. Sharma, H. Singh, S. Basu, R. Kumar, *South Asian J. cancer* **2013**, *2*, 171–177.
[209] B. S. Jang, *Toxicol. Res.* **2013**, *29*, 1–6.
[210] L. Cunha, K. Szigeti, D. Mathé, L. F. Metello, *Drug Discov. Today* **2014**, *19*, 936–948.
[211] S. L. Rice, C. A. Roney, P. Daumar, J. S. Lewis, *Semin. Nucl. Med.* **2011**, *41*, 265–282.
[212] R. L. Wahl, J. M. Herman, E. Ford, *Semin. Radiat. Oncol.* **2011**, *21*, 88–100.
[213] I. Velikyan, *Med. Chem.* **2011**, *7*, 345–379.
[214] I. Velikyan, *Molecules* **2015**, *20*, 12913–12943.
[215] S. M. Moerlein, M. J. Welch, *Int. J. Nucl. Med. Biol.* **1981**, *8*, 277–287.
[216] J. Shukla, B. Mittal, *J. Postgrad. Med. Educ. Res.* **2013**, *47*, 74–76.
[217] R. M. Lambrecht, S. Munawwar, *Radiochim. Acta* **1988**, *43*, 171–179.
[218] M. Fani, J. P. André, H. R. Maecke, *Contrast Media Mol. Imaging* **2008**, *3*, 67–77.
[219] W. A. P. Breeman, A. M. Verbruggen, *Eur. J. Nucl. Med. Mol. Imaging* **2007**, *34*, 978–981.
[220] I. Velikyan, A. Sundin, B. Eriksson, H. Lundqvist, J. Sörensen, M. Bergström, B. Långström, *Nucl. Med. Biol.* **2010**, *37*, 265–275.
[221] H. S. Chong, K. Garmestani, D. Ma, D. E. Milenic, T. Overstreet, M. W. Brechbiel, *J. Med. Chem.* **2002**, *45*, 3458–3464.
[222] P. J. Riss, C. Kroll, V. Nagel, F. Rösch, *Bioorg. Med. Chem.* **2008**, *18*, 5364–5367.
[223] I. Velikyan, H. Maecke, B. Langstrom, *Bioconjugate Chem.* **2008**, *19*, 569–573.
[224] J. M. Jeong, M. K. Hong, Y. S. Chang, Y. S. Lee, Y. J. Kim, G. J. Cheon, D. S. Lee, J. K. Chung, M. C. Lee, *J. Nucl. Med.* **2008**, *49*, 830–836.
[225] E. T. Clarke, A. E. Martell, *Inorg. Chim. Acta* **1991**, *190*, 37–46.
[226] E. T. Clarke, A. E. Martell, *Inorg. Chim. Acta* **1991**, *181*, 273–280.
[227] L. Hoigebazar, J. M. Jeong, S. Y. Choi, J. Y. Choi, D. Shetty, Y. S. Lee, D. S. Lee, J. K. Chung, M. C. Lee, Y. K. Chung, *J. Med. Chem.* **2010**, *53*, 6378–6385.
[228] D. Shetty, J. M. Jeong, C. H. Ju, Y. J. Kim, J. Y. Lee, Y. S. Lee, D. S. Lee, J. K. Chung, M. C. Lee, *Bioorg. Med. Chem.* **2010**, *18*, 7338–7347.
[229] D. Shetty, Y. S. Lee, J. M. Jeong, *Nucl. Med. Mol. Imaging.* **2010**, *44*, 233–240.
[230] J. P. L. Cox, A. S. Craig, I. M. Helps, K. J. Jankowski, D. Parker, M. A. W. Eaton, A. T. Millican, K. Millar, N. R. A. Beeley, B. A. Boyce, *J. Chem. Soc.* **1990**, *98*, 2567–2576.
[231] M. Studer, C. F. Meares, *Bioconjugate Chem.* **1992**, *3*, 337–341.
[232] M. W. Brechbiel, T. J. McMurry, O. A. Gansow, *Tetrahedron Lett.* **1993**, *34*, 3691–3694.
[233] J. Cheon, J. H. Lee, *Acc. Chem. Res.* **2008**, *41*, 1630–1640.
[234] D. W. Hwang, H. Y. Ko, S. K. Kim, D. Kim, D. S. Lee, S. Kim, *Chem. Eur. J.* **2009**, *15*, 9387–9393.
[235] B. R. Jarrett, D. L. Kukis, A. Y. Louie, *Bioconjugate Chem.* **2008**, *19*, 1496–1504.
[236] A. Louie, *Chem. Rev.* **2010**, *110*, 3146–3195.
[237] H. P. Schlemmer, B. Pichler, K. Wienhard, M. Schmand, C. Nahmias, D. Townsend, W.-D. Heiss, C. Claussen, *J. Nucl. Med.* **2007**, *48*, 45.
[238] U. A. Gunasekera, Q. A. Pankhurst, M. Douek, *Target. Oncol.* **2009**, *4*, 169–181.
[239] O. Veiseh, C. Sun, J. Gunn, N. Kohler, P. Gabikian, D. Lee, N. Bhattarai, R. Ellenbogen, R. Sze, A. Hallahan, et al., *Nano Lett.* **2005**, *5*, 1003–1008.
[240] S. M. Kim, M. K. Chae, M. S. Yim, I. H. Jeong, J. Cho, C. Lee, E. K. Ryu, *Biomaterials* **2013**, *34*, 8114–8121.
[241] R. Madru, T. A. Tran, J. Axelsson, C. Ingvar, A. Bibic, F. Ståhlberg, L. Knutsson, S.-E. Strand, *Am. J. Nucl. Med. Mol. Imaging* **2014**, *4*, 60–69.
[242] J. Frigell, I. García, V. Gomez-Vallejo, J. Llop, S. Penadés, *J. Am. Chem. Soc.* **2014**, *136*, 449–457.
[243] W. J. M. Mulder, G. J. Strijkers, G. A. F. Van Tilborg, D. P. Cormode, Z. A. Fayad, K. Nicolay, *Acc. Chem. Res.* **2009**, *42*, 904–914.
[244] J. D. Glickson, S. Lund-Katz, R. Zhou, H. Choi, I. W. Chen, H. Li, I. Corbin, A. V. Popov, W. Cao, L. Song, et al., *Adv. Exp. Med. Biol.* **2009**, *645*, 227–239.
[245] E. A. Neuwelt, C. G. Várallyay, S. Manninger, D. Solymosi, M. Haluska, M. A. Hunt, G. Nesbit, A.

Stevens, M. Jerosch-Herold, P. M. Jacobs, et al., *Neurosurgery* **2007**, *60*, 601–611.

[246] V. Clavijo-Jordan, V. D. Kodibagkar, S. C. Beeman, B. D. Hann, K. M. Bennett, *Wiley Interdiscip. Rev. Nanomedicine Nanobiotechnology* **2012**, *4*, 345–365.

[247] E. Locatelli, L. Gil, L. L. Israel, L. Passoni, M. Naddaka, A. Pucci, T. Reese, V. Gomez-Vallejo, P. Milani, M. Matteoli, et al., *Int. J. Nanomedicine* **2012**, *7*, 6021–6033.

[248] G. Ting, C. H. Chang, H. E. Wang, *Anticancer Res.* **2009**, *29*, 4107–4118.

[249] M. Hamoudeh, M. A. Kamleh, R. Diab, H. Fessi, *Adv. Drug Deliv. Rev.* **2008**, *60*, 1329–1346.

[250] M. Shokeen, N. M. Fetting, R. Rossin, *Q J Nucl Med Mol Imaging* **2008**, *52*, 267–277.

[251] G. Loudos, G. C. Kagadis, D. Psimadas, *Eur. J. Radiol.* **2011**, *78*, 287–295.

[252] Y. Liu, M. J. Welch, *Bioconjugate Chem.* **2012**, *23*, 671–682.

[253] M. S. Judenhofer, H. F. Wehrl, D. F. Newport, C. Catana, S. B. Siegel, M. Becker, A. Thielscher, M. Kneilling, M. P. Lichy, M. Eichner, et al., *Nat. Med.* **2008**, *14*, 459–465.

[254] J. Choi, J. C. Park, H. Nah, S. Woo, J. Oh, K. M. Kim, G. J. Cheon, Y. Chang, J. Yoo, J. Cheon, *Angew. Chem. - Int. Ed. Eng.* **2008**, *47*, 6259–6262.

[255] H. S. Chong, X. Sun, Y. Chen, I. Sin, C. S. Kang, M. R. Lewis, D. Liu, V. C. Ruthengael, Y. Zhong, N. Wu, et al., *Bioorg. Med. Chem.* **2015**, *23*, 1169–1178.

[256] O. Schober, K. Rahbar, B. Riemann, *Eur. J. Nucl. Med. Mol. Imaging* **2009**, *36*, 302–314.

[257] Y. Cohen, S. Y. Shoushan, *Curr. Opin. Biotechnol.* **2013**, *24*, 672–681.

[258] R. Stoltenburg, C. Reinemann, B. Strehlitz, *Biomol. Eng.* **2007**, *24*, 381–403.

[259] C. Tuerk, L. Gold, *Science.* **1990**, *249*, 505–510.

[260] A. D. Ellington, J. W. Szostak, *Nature* **1990**, *346*, 818–822.

[261] A. Ellington, J. Szostak, *Nature* **1992**, *355*, 850–852.

[262] J. Banerjee, M. Nilsen-Hamilton, *J. Mol. Med.* **2013**, *91*, 1333–1342.

[263] L. Hernandez, I. Machado, T. Schafer, F. Hernandez, *Curr. Top. Med. Chem.* **2015**, *15*, 1066–1081.

[264] A. B. Sullenger, *Nucleic Acid Ther.* **2016**, *26*, 119.

[265] E. J. Cho, J. W. Lee, A. D. Ellington, *Annu. Rev. Anal. Chem.* **2009**, *2*, 241–64.

[266] J. Liu, Z. Cao, Y. Lu, *Chem. Rev.* **2009**, *109*, 1948–1998.

[267] A. D. Keefe, S. Pai, A. Ellington, *Nat. Rev. Drug Discov.* **2010**, *9*, 537–550.

[268] W. Tan, H. Wang, Y. Chen, X. Zhang, H. Zhu, C. Yang, R. Yang, C. Liu, *Trends Biotechnol.* **2011**, *29*, 634–640.

[269] D. Xiang, S. Shigdar, G. Qiao, T. Wang, A. Z. Kouzani, S. F. Zhou, L. Kong, Y. Li, C. Pu, W. Duan, *Theranostics* **2015**, *5*, 23–42.

[270] Y. S. Kim, N. H. Ahmad Raston, B. M. Gu, *Biosens. Bioelectron.* **2016**, *76*, 2–19.

[271] H. Sun, W. Tan, Y. Zu, *Analyst* **2016**, *141*, 403–415.

[272] K. E. Maier, M. Levy, *Mol. Ther. Methods Clin. Dev.* **2016**, *5*, 16014–16023.

[273] R. E. Wang, H. Wu, Y. Niu, J. Cai, *Curr. Med. Chem.* **2011**, *18*, 4126–4138.

[274] M. Kuwahara, in *Chem. Biol. Nucleic Acids Fundam. Clin. Appl.* (Eds.: V.A. Erdmann, A. Volker, W.T. Markiewicz, J. Barciszewski), **2014**, pp. 243–270.

[275] M. M. Vu, N. E. Jameson, S. J. Masuda, D. Lin, R. Larralde-Ridaura, A. Lupták, *Chem. Biol.* **2012**, *19*, 1247–1254.

[276] Y. Fujimoto, Y. Nakamura, S. Ohuchi, *Biochimie* **2012**, *94*, 1900–1909.

[277] A. D. Keefe, S. T. Cload, *Curr. Opin. Chem. Biol.* **2008**, *12*, 448–456.

[278] L. Gold, D. Ayers, J. Bertino, C. Bock, A. Bock, E. N. Brody, J. Carter, A. B. Dalby, B. E. Eaton, T. Fitzwater, et al., *PLoS One* **2010**, *5*, e15004.

[279] V. B. Pinheiro, A. I. Taylor, C. Cozens, M. Abramov, M. Renders, S. Zhang, J. C. Chaput, J. Wengel, S. Y. Peak-Chew, S. H. McLaughlin, et al., *Science.* **2012**, *336*, 341–344.

[280] F. Tolle, G. M. Brändle, D. Matzner, G. Mayer, *Angew. Chem. - Int. Ed. Eng.* **2015**, *54*, 10971–10974.

[281] S. C. B. Gopinath, *Anal. Bioanal. Chem.* **2007**, *387*, 171–182.

[282] T. Schütze, B. Wilhelm, N. Greiner, H. Braun, F. Peter, M. Mörl, V. A. Erdmann, H. Lehrach, Z. Konthur, M. Menger, et al., *PLoS One* **2011**, *6*, e29604.

[283] E. W. M. Ng, D. T. Shima, P. Calias, E. T. Cunningham, D. R. Guyer, A. P. Adamis, *Nat. Rev. Drug Discov.* **2006**, *5*, 123–132.

[284] A. Vater, S. Klussmann, *Drug Discov. Today* **2015**, *20*, 147–155.

[285] B. Gatto, M. Palumbo, C. Sissi, *Curr. Med. Chem.* **2009**, *16*, 1248–1265.

[286] W. O. Tucker, K. T. Shum, J. A. Tanner, *Curr. Pharm. Des.* **2012**, *18*, 2014–2026.

[287] S. Neidle, S. Balasubramanian, *Quadruplex Nucleic Acids*, The Royal Society Of Chemistry, Cambridge, **2006**.

[288] L. Spindler, W. Fritzsche, *Guanine Quartets: Structure and Application*, The Royal Society Of Chemistry, Cambridge, **2012**.

[289] V. T. Mukundan, A. T. Phan, *J. Am. Chem. Soc.* **2013**, *135*, 5017–5028.

[290] P. L. Tran, A. De Cian, J. Gros, R. Moriyama, J. L. Mergny, *Top. Curr. Chem.* **2013**, *330*, 243–273.

[291] M. Malgowska, D. Gudanis, R. Kierzek, E. Wyszko, V. Gabelica, Z. Gdaniec, *Nucleic Acids Res.* **2014**, *42*, 10196–10207.

[292] X. M. Li, K. W. Zheng, J. Y. Zhang, H. H. Liu, Y. De He, B. F. Yuan, Y. H. Hao, Z. Tan, *Proc. Natl. Acad. Sci. U. S. A.* **2015**, *112*, 14581–14586.

[293] A. Virgilio, V. Esposito, G. Citarella, L. Mayol, A. Galeone, *ChemBioChem* **2012**, *13*, 2219–2224.

[294] A. T. Phan, V. Kuryavyi, J. B. Ma, A. Faure, M. L. Andréola, D. J. Patel, *Proc. Natl. Acad. Sci. U. S. A.* **2005**, *102*, 634–639.

[295] G. W. Collie, G. N. Parkinson, *Chem. Soc. Rev.* **2011**, *40*, 5867–5892.

[296] X. Ji, H. Sun, H. Zhou, J. Xiang, Y. Tang, C. Zhao, *Nucleic Acid Ther.* **2011**, *21*, 185–200.

[297] B. Santosh, P. K. Yadava, *Biomed Res. Int.* **2014**, *2014*, 50451–50464.

[298] J. Qu, S. Yu, Y. Zheng, Y. Zheng, H. Yang, J. Zhang, *Cell. Mol. Life Sci.* **2016**, *74*, 683–695.

[299] D. W. Drolet, L. S. Green, L. Gold, N. Janjic, *Nucleic Acid Ther.* **2016**, *26*, 127–146.

[300] Y. Yu, C. Liang, Q. Lv, D. Li, X. Xu, B. Liu, A. Lu, G. Zhang, *Int. J. Mol. Sci.* **2016**, *17*, 358–377.

[301] R. C. Becker, T. Povsic, C. G. Mauricio, C. P. Rusconi, B. Sullenger, *Thromb. Haemost.* **2010**, *103*, 586–595.

[302] V. Makwana, S. Simmons, S. Missailidis, in *Anticancer Ther.*, **2008**, pp. 331–345.

[303] H. P. Lassalle, S. Marchal, F. Guillemin, A. Reinhard, L. Bezdetnaya, *Curr. Drug Metab.* **2012**, *13*, 1130–1144.

[304] D. Musumeci, C. Riccardi, D. Montesarchio, *Molecules* **2015**, *20*, 17511–17532.

[305] E. Zavyalova, N. Ustinov, A. Golovin, G. Pavlova, A. Kopylov, *Curr. Med. Chem.* **2016**, *23*, 2230–2244.

[306] C. Platella, C. Riccardi, D. Montesarchio, G. N. Roviello, D. Musumeci, *Biochim. Biophys. Acta - Gen. Subj.* **2017**, http://dx.doi.org/10.1016/j.bbagen.2016.11.027.

[307] J. A. Huntington, T. P. Baglin, *Trends Pharmacol. Sci.* **2003**, *24*, 589–595.

[308] J. A. Huntington, *J. Thromb. Haemost.* **2005**, *3*, 1861–1872.

[309] A. S. Wolberg, *Blood Rev.* **2007**, *21*, 131–142.

[310] E. Di Cera, *Mol. Aspects Med.* **2008**, *29*, 203–254.

[311] L. G. Licari, J. P. Kovacic, *J. Vet. Emerg. Crit. Care* **2009**, *19*, 11–22.

[312] J. Hirsh, *Thromb. Res.* **2003**, *109*, S1–S8.

[313] T. E. Warkentin, A. Greinacher, *Ann. Thorac. Surg.* **2003**, *76*, 2121–31.

[314] S. Rangarajan, *Haemophilia* **2011**, *17*, 90–94.

[315] L. C. Bock, L. C. Griffin, J. A. Latham, E. H. Vermaas, J. J. Toole, *Nature* **1992**, *355*, 564–566.

[316] K. Padmanabhan, K. P. Padmanabhan, J. D. Ferrara, J. E. Sadler, A. Tulinsky, *J. Biol. Chem.* **1993**, *268*, 17651–17654.

[317] S. M. Nimjee, C. P. Rusconi, R. A. Harrington, B. A. Sullenger, *Trends Cardiovasc. Med.* **2005**, *15*, 41–45.

[318] I. Russo Krauss, A. Merlino, A. Randazzo, E. Novellino, L. Mazzarella, F. Sica, *Nucleic Acids Res.* **2012**, *40*, 8119–8128.

[319] R. F. Macaya, P. Schultze, F. W. Smith, J. A. Roet, J. Feigon, *Proc. Natl. Acad. Sci. U. S. A.* **1993**, *90*, 3745–3749.

[320] I. Smirnov, R. H. Shafer, *Biochemistry* **2000**, *39*, 1462–1468.

[321] T. Coppola, M. Varra, G. Oliviero, A. Galeone, G. D. Isa, L. Mayol, E. Morelli, M. Bucci, V. Vellecco, G. Cirino, et al., *Bioorg. Med. Chem.* **2008**, *16*, 8244–8253.

[322] M. C. R. Buff, F. Schäfer, B. Wulffen, J. Müller, B. Pötzsch, A. Heckel, G. Mayer, *Nucleic Acids Res.* **2010**, *38*, 2111–2118.

[323] T. Agarwal, S. Kumar, S. Maiti, *Biochimie* **2011**, *93*, 1694–1700.

[324] H. Dougan, D. M. Lyster, C. V. Vo, A. Stafford, J. I. Weitz, J. B. Hobbs, *Nucl. Med. Biol.* **2000**, *27*, 289–297.

[325] M. V. Yigit, D. Mazumdar, Y. Lu, *Bioconjugate Chem.* **2008**, *19*, 412–417.

[326] Y. C. Shiang, C. C. Huang, T. H. Wang, C. W. Chien, H. T. Chang, *Adv. Funct. Mater.* **2010**, *20*,

3175–3182.

[327] Y. C. Shiang, C. L. Hsu, C. C. Huang, H. T. Chang, *Angew. Chem. - Int. Ed. Eng.* **2011**, *50*, 7660–7665.

[328] C. L. Hsu, H. T. Chang, C. T. Chen, S. C. Wei, Y. C. Shiang, C. C. Huang, *Chem. Eur. J.* **2011**, *17*, 10994–11000.

[329] L. Gao, Y. Cui, Q. He, Y. Yang, J. Fei, J. Li, *Chem. Eur. J.* **2011**, *17*, 13170–13174.

[330] D. Musumeci, G. Oliviero, G. N. Roviello, E. M. Bucci, G. Piccialli, *Bioconjugate Chem.* **2012**, *23*, 382–391.

[331] C. L. Hsu, S. C. Wei, J. W. Jian, H. T. Chang, W. H. Chen, C. C. Huang, *RSC Adv.* **2012**, *2*, 1577–1584.

[332] E. Babu, P. M. Mareeswaran, S. Rajagopal, *J. Fluoresc.* **2013**, *23*, 137–146.

[333] Q. Yue, T. Shen, L. Wang, S. Xu, H. Li, Q. Xue, Y. Zhang, X. Gu, S. Zhang, J. Liu, *Biosens. Bioelectron.* **2014**, *56*, 231–236.

[334] J. M. Yu, L. R. Yang, X. F. Liang, T. T. Dong, H. Z. Liu, *Analyst* **2015**, *140*, 4114–4120.

[335] L. Martino, A. Virno, A. Randazzo, A. Virgilio, V. Esposito, C. Giancola, M. Bucci, G. Cirino, L. Mayol, *Nucleic Acids Res.* **2006**, *34*, 6653–6662.

[336] A. Virno, A. Randazzo, C. Giancola, M. Bucci, G. Cirino, L. Mayol, *Bioorg. Med. Chem.* **2007**, *15*, 5710–5718.

[337] I. Russo Krauss, A. Merlino, C. Giancola, A. Randazzo, L. Mazzarella, F. Sica, *Nucleic Acids Res.* **2011**, *39*, 7858–7867.

[338] A. Aviñó, C. Fàbrega, M. Tintoré, R. Eritja, *Curr. Pharm. Des.* **2012**, *18*, 2036–47.

[339] N. Borbone, M. Bucci, G. Oliviero, E. Morelli, J. Amato, V. D'Atri, S. D. D'Errico, V. Vellecco, G. Cirino, G. Piccialli, et al., *J. Med. Chem.* **2012**, *55*, 10716–10728.

[340] D. Musumeci, D. Montesarchio, *Pharmacol. Ther.* **2012**, *136*, 202–215.

[341] S. Nagatoishi, T. Nojima, B. Juskowiak, S. Takenaka, *Angew. Chem. - Int. Ed. Eng.* **2005**, *44*, 5067–5070.

[342] T. M. Lerga, C. K. O'Sullivan, *Anal. Chim. Acta* **2008**, *610*, 105–111.

[343] S. Takenaka, B. Juskowiak, *Anal. Sci.* **2011**, *27*, 1167–1172.

[344] S. De Tito, F. Morvan, A. Meyer, J. J. Vasseur, A. Cummaro, L. Petraccone, B. Pagano, E. Novellino, A. Randazzo, C. Giancola, et al., *Bioconjugate Chem.* **2013**, *24*, 1917–1927.

[345] J. Johnson, R. Okyere, A. Joseph, K. Musier-Forsyth, B. Kankia, *Nucleic Acids Res.* **2013**, *41*, 220–228.

[346] J. Szejtli, *Chem. Rev.* **1998**, *98*, 1743–1753.

[347] T. Ikunaga, H. Ikeda, A. Ueno, *Chem. Eur. J.* **1999**, *5*, 2698–2704.

[348] S. Matsumura, S. Sakamoto, A. Ueno, H. Mihara, *Chem. Eur. J.* **2000**, *6*, 1781–1788.

[349] S. Pagliari, R. Corradini, G. Galaverna, S. Sforza, A. Dossena, M. Montalti, L. Prodi, N. Zaccheroni, R. Marchelli, *Chem. Eur. J.* **2004**, *10*, 2749–2758.

[350] M. Montalti, L. Prodi, N. Zaccheroni, G. Battistini, S. Marcuz, F. Mancin, E. Rampazzo, U. Tonellato, *Langmuir* **2006**, *22*, 5877–5881.

[351] T. Loftsson, D. Duchêne, *Int. J. Pharm.* **2007**, *329*, 1–11.

[352] V. J. Stella, Q. He, *Toxicol. Pathol.* **2008**, *36*, 30–42.

[353] W. M. Leevy, G. M. Donato, R. Ferdani, W. E. Goldman, P. H. Schlesinger, G. W. Gokel, *J. Am. Chem. Soc.* **2002**, *124*, 9022–9023.

[354] L. You, G. W. Gokel, *Chem. Eur. J.* **2008**, *14*, 5861–5870.

[355] C. Coppola, A. Paciello, G. Mangiapia, S. Licen, M. Boccalon, L. De Napoli, L. Paduano, P. Tecilla, D. Montesarchio, *Chem. Eur. J.* **2010**, *16*, 13757–13772.

[356] P. C. Weber, D. H. Ohlendorf, J. J. Wendoloski, F. R. Salemme, *Science.* **1989**, *243*, 85–88.

[357] W. A. Hendrickson, A. Pähler, J. L. Smith, Y. Satow, E. A. Merritt, R. P. Phizackerley, *Proc. Natl. Acad. Sci. U. S. A.* **1989**, *86*, 2190–2194.

[358] E. P. Diamandis, T. K. Christopoulos, *Clin. Chem.* **1991**, *37*, 625–636.

[359] A. Holmberg, A. Blomstergren, O. Nord, M. Lukacs, J. Lundeberg, M. Uhlén, *Electrophoresis* **2005**, *26*, 501–510.

[360] S. V. Vinogradov, T. K. Bronich, A. V. Kabanov, *Adv. Drug Deliv. Rev.* **2002**, *54*, 135–147.

[361] H. S. Choi, W. Liu, P. Misra, E. Tanaka, J. P. Zimmer, B. Itty Ipe, M. G. Bawendi, J. V Frangioni, *Nat. Biotechnol.* **2007**, *25*, 1165–1170.

[362] L. Illum, S. S. Davis, C. G. Wilson, N. W. Thomas, M. Frier, J. G. Hardy, *Int. J. Pharm.* **1982**, *12*,

135–146.
[363] C. J. H. Porter, S. M. Moghimi, L. Illum, S. S. Davis, *FEBS Lett.* **1992**, *305*, 62–66.
[364] S. Mitragotri, J. Lahann, *Nat. Mater.* **2009**, *8*, 15–23.
[365] S. Barua, K. Rege, *Small* **2009**, *5*, 370–376.
[366] S. M. Moghimi, A. C. Hunter, J. C. Murray, *Pharmacol. Rev.* **2001**, *53*, 283–318.
[367] E. V. Piletska, S. A. Piletsky, *Langmuir* **2010**, *26*, 3783–3785.
[368] B. Silvestri, D. Guarnieri, G. Luciani, A. Costantini, P. A. Netti, F. Branda, *J. Mater. Sci. Mater. Med.* **2012**, *23*, 1697–1704.
[369] J. L. Vivero-Escoto, R. C. Huxford-Phillips, W. Lin, *Chem. Soc. Rev.* **2012**, *41*, 2673–2685.
[370] K. Wang, X. He, X. Yang, H. Shi, *Acc. Chem. Res.* **2013**, *46*, 1367–1376.
[371] C. Caltagirone, A. Bettoschi, A. Garau, R. Montis, *Chem. Soc. Rev.* **2014**, *44*, 4645–4671.
[372] J.-E. Kim, H. Kim, S. S. An, M. Kim, Y.-J. Song, *Int. J. Nanomedicine* **2014**, *9*, 235–241.
[373] M. Montalti, L. Prodi, E. Rampazzo, N. Zaccheroni, *Chem. Soc. Rev.* **2014**, *43*, 4243–4268.
[374] S. Cheng, B. Zheng, M. Wang, X. Ge, Q. Zhao, W. Liu, M. H. W. Lam, *Biosens. Bioelectron.* **2014**, *53*, 479–485.
[375] W. Q. Lim, S. Z. F. Phua, H. V. Xu, S. Sreejith, Y. Zhao, *Nanoscale* **2015**, *8*, 12510–12519.
[376] W. G. Lewis, F. G. Magallon, V. V. Fokin, M. G. Finn, *J. Am. Chem. Soc.* **2004**, *126*, 9152–9153.
[377] V. V. Rostovtsev, L. G. Green, V. V. Fokin, K. B. Sharpless, *Angew. Chem. - Int. Ed. Eng.* **2002**, *41*, 2596–2599.
[378] C. W. Tornøe, C. Christensen, M. Meldal, *J. Org. Chem.* **2002**, *67*, 3057–3064.
[379] J. Lietard, A. Meyer, J. J. Vasseur, F. Morvan, *J. Org. Chem.* **2008**, *73*, 191–200.
[380] C. Bouillon, A. Meyer, S. Vidal, A. Jochum, Y. Chevolot, J. Cloarec, J. Praly, J. Vasseur, F. Morvan, *J. Org. Chem.* **2006**, *71*, 4700–4702.
[381] W. Tang, S.-C. Ng, *Nat. Protoc.* **2008**, *3*, 691–697.
[382] R. Giraldo, M. Suzuki, L. Chapman, D. Rhodes, *Proc. Natl. Acad. Sci. U. S. A.* **1994**, *91*, 7658–7662.
[383] S. Paramasivan, I. Rujan, P. H. Bolton, *Methods* **2007**, *43*, 324–331.
[384] S. Masiero, R. Trotta, S. Pieraccini, S. De Tito, R. Perone, A. Randazzo, G. P. Spada, *Org. Biomol. Chem.* **2010**, *8*, 2683–2692.
[385] A. I. Karsisiotis, N. M. Hessari, E. Novellino, G. P. Spada, A. Randazzo, M. Webba da Silva, *Angew. Chem. - Int. Ed. Eng.* **2011**, *50*, 10645–10648.
[386] M. Malgowska, D. Gudanis, A. Teubert, G. Dominiak, Z. Gdaniec, *J. Biotechnol. Comput. Biol. Bionanotechnol.* **2012**, *93*, 381–390.
[387] A. Randazzo, G. P. Spada, M. Webba da Silva, *Top. Curr. Chem.* **2013**, *330*, 67–86.
[388] C. C. Hardin, T. Watson, M. Corregan, C. Bailey, *Biochemistry* **1992**, *31*, 833–841.
[389] N. V Hud, F. W. Smith, F. A. L. Anet, J. Feigon, *Biochemistry* **1996**, *35*, 15383–15390.
[390] S. Poniková, M. Antalík, T. Hianik, *Gen. Physiol. Biophys.* **2008**, *27*, 271–277.
[391] M. Vorlíčková, I. Kejnovská, J. Sagi, D. Renčiuk, K. Bednářová, J. Motlová, J. Kypr, *Methods* **2012**, *57*, 64–75.
[392] J. Mergny, A. Phan, L. Lacroix, *FEBS Lett.* **1998**, *435*, 74–78.
[393] J. Mergny, L. Lacroix, *Curr. Protoc. Nucleic Acid Chem.* **2009**, *37*, 17.1.1–17.1.15.
[394] M. Holzinger, M. Singh, S. Cosnier, *Langmuir* **2012**, *28*, 12569–12574.
[395] J. Tang, Y. Lu, Y. Wang, J. Zhou, W. Tang, *Talanta* **2014**, *128*, 460–465.
[396] C. P. Rusconi, E. Scardino, J. Layzer, G. a Pitoc, T. L. Ortel, D. Monroe, B. a Sullenger, *Nature* **2002**, *419*, 90–94.
[397] S. M. Nimjee, J. R. Keys, A. G. Pitoc, G. Quick, C. P. Rusconi, A. S. Bruce, *Mol. Ther.* **2006**, *14*, 408–415.
[398] P. J. Bates, E. M. Reyes-Reyes, M. T. Malik, E. M. Murphy, M. G. O'Toole, J. O. Trent, *Biochim. Biophys. Acta - Gen. Subj.* **2016**, http://dx.doi.org/10.1016/j.bbagen.2016.12.015.
[399] P. J. Bates, J. B. Kahlon, S. D. Thomas, J. O. Trent, D. M. Miller, *J. Biol. Chem.* **1999**, *274*, 26369–26377.
[400] V. Dapić, P. J. Bates, J. O. Trent, A. Rodger, S. D. Thomas, D. M. Miller, *Biochemistry* **2002**, *41*, 3676–3685.
[401] V. Dapić, V. Abdomerović, R. Marrington, J. Peberdy, A. Rodger, J. O. Trent, P. J. Bates, *Nucleic Acids Res.* **2003**, *31*, 2097–2107.
[402] P. J. Bates, D. A. Laber, D. M. Miller, S. D. Thomas, J. O. Trent, *Exp. Mol. Pathol.* **2009**, *86*, 151–164.

[403] E. W. Choi, L. V. Nayak, P. J. Bates, *Nucleic Acids Res.* **2009**, *38*, 1623–1635.

[404] M. M. Dailey, M. Clarke Miller, P. J. Bates, A. N. Lane, J. O. Trent, *Nucleic Acids Res.* **2010**, *38*, 4877–4888.

[405] M. C. Miller, J. O. Trent, *Curr. Protoc. nucleic acid Chem.* **2011**, *Chapter 17*, Unit 17.3.

[406] M. C. Miller, H. T. Le, W. L. Dean, P. A. Holt, J. B. Chaires, J. O. Trent, *Org. Biomol. Chem.* **2011**, *9*, 7633–7637.

[407] H. T. Le, M. C. Miller, R. Buscaglia, W. L. Dean, P. A. Holt, J. B. Chaires, J. O. Trent, *Org. Biomol. Chem.* **2012**, *10*, 9393–9404.

[408] M. C. Miller, C. J. Ohrenberg, A. Kuttan, J. O. Trent, *Curr. Protoc. Nucleic Acid Chem.* **2015**, *61*, 17.7.1–17.7.18.

[409] W. J. Chung, B. Heddi, E. Schmitt, K. W. Lim, Y. Mechulam, A. T. Phan, *Proc. Natl. Acad. Sci.* **2015**, *112*, 2729–2733.

[410] J. Ai, Y. Xu, B. Lou, D. Li, E. Wang, *Talanta* **2014**, *118*, 54–60.

[411] A. B. Chinen, C. M. Guan, C. A. Mirkin, *Angew. Chem. - Int. Ed. Eng.* **2015**, *54*, 527–531.

[412] D. H. M. Dam, J. H. Lee, P. N. Sisco, D. T. Co, M. Zhang, M. R. Wasielewski, T. W. Odom, *ACS Nano* **2012**, *6*, 3318–3326.

[413] D. Chen, B. Li, S. Cai, P. Wang, S. Peng, Y. Sheng, Y. He, Y. Gu, H. Chen, *Biomaterials* **2016**, *100*, 1–16.

[414] J. H. Choi, K. H. Chen, J. H. Han, A. M. Chaffee, M. S. Strano, *Small* **2009**, *5*, 672–675.

[415] D. H. M. Dam, H. Lee, R. C. Lee, K. H. Kim, N. L. Kelleher, T. W. Odom, *Bioconjugate Chem.* **2015**, *26*, 279–285.

[416] C. R. Ireson, L. R. Kelland, *Mol. Cancer Ther.* **2006**, *5*, 2957–62.

[417] F. Mongelard, P. Bouvet, *Curr. Opin. Mol. Ther.* **2010**, *12*, 107–114.

[418] G. Acton, *Sympathy for the Devil*, Troubador Publishing Ltd., **2013**.

[419] D. Laber, M. Choudry, B. Taft, L. Bhupalam, V. Sharma, F. Hendler, K. Barnhart, *ASCO Annu. Meet. Proc.* **2004**, 3112.

[420] D. Laber, V. Sharma, L. Bhupalam, B. Taft, F. Hendler, K. Barnhart, *ASCO Annu. Meet. Proc.* **2005**, 3064.

[421] Antisoma, *Annu. Rep. Accounts* **2011**.

[422] D. M. Miller, D. A. Laber, P. J. Bates, J. O. Trent, B. S. Taft, G. Kloecker, in *Ann. Oncol.*, Oxford Univ Press, Great Clarendon St, Oxford OX2 6DP, England, **2006**, pp. 147–148.

[423] D. Laber, B. Taft, G. Kloecker, G. Acton, D. Miller, *Mol. Cancer Ther.* **2007**, *6*, C147.

[424] D. Rizzieri, K. Stockerl-Goldstein, A. Wei, R. H. Herzig, F. Erlandsson, R. K. Stuart, *ASCO Annu. Meet. Abstr.* **2010**, *28*, 6557.

[425] J. E. Rosenberg, R. M. Bambury, E. M. Van Allen, H. A. Drabkin, P. N. Lara, A. L. Harzstark, N. Wagle, R. A. Figlin, G. W. Smith, L. A. Garraway, et al., *Invest. New Drugs* **2014**, *32*, 178–187.

[426] D. H. M. Dam, K. S. B. Culver, P. N. Sisco, T. W. Odom, *Ther. Deliv.* **2012**, *3*, 1263–1267.

[427] D. H. M. Dam, R. C. Lee, T. W. Odom, *Nano Lett.* **2014**, *14*, 2843–2848.

[428] D. H. M. Dam, K. S. B. Culver, T. W. Odom, *Mol. Pharm.* **2014**, *11*, 580–587.

[429] D. H. M. Dam, K. S. B. Culver, I. Kandela, R. C. Lee, K. Chandra, H. Lee, C. Mantis, A. Ugolkov, A. P. Mazar, T. W. Odom, *Nanomedicine Nanotechnology, Biol. Med.* **2015**, *11*, 671–679.

[430] M. T. Malik, M. G. O'Toole, L. K. Casson, S. D. Thomas, G. T. Bardi, E. M. Reyes-Reyes, C. K. Ng, K. A. Kang, P. J. Bates, *Oncotarget* **2015**, *6*, 22270–22281.

[431] K. Y. Lee, H. Kang, S. H. Ryu, D. S. Lee, J. H. Lee, S. Kim, *J. Biomed. Biotechnol.* **2010**, *2010*, 168306.

[432] Y. Takafuji, J. I. Jo, Y. Tabata, *J. Biomater. Sci. Polym. Ed.* **2011**, *22*, 1179–1195.

[433] Y. Cho, Y. Bin Lee, J. H. Lee, D. H. Lee, E. J. Cho, S. J. Yu, Y. J. Kim, J. I. Kim, J. H. Im, J. H. Lee, et al., *PLoS One* **2016**, *11*, 1–14.

[434] X. Fan, L. Sun, Y. Wu, L. Zhang, Z. Yang, *Sci. Rep.* **2016**, *6*, 25799.

[435] O. Gissberg, E. M. Zaghloul, K. E. Lundin, C. H. Nguyen, C. Landras-Guetta, J. Wengel, R. Zain, C. I. E. Smith, *Nucleic Acid Ther.* **2016**, *26*, 183–189.

[436] J. Schuemann, R. Berbeco, D. B. Chithrani, S. H. Cho, R. Kumar, S. J. McMahon, S. Sridhar, S. Krishnan, *Int. J. Radiat. Oncol. Biol. Phys.* **2016**, *94*, 189–205.

[437] M. H. Ko, S. Kim, W. J. Kang, J. H. Lee, H. Kang, S. H. Moon, D. W. Hwang, H. Y. Ko, D. S. Lee, *Small* **2009**, *5*, 1207–1212.

[438] Z. Cao, R. Tong, A. Mishra, W. Xu, G. C. L. Wong, J. Cheng, Y. Lu, *Angew. Chem. - Int. Ed. Eng.*

2009, *48*, 6494–6498.

[439] Y. A. Shieh, S. J. Yang, M. F. Wei, M. J. Shieh, *ACS Nano* **2010**, *4*, 1433–1442.

[440] J. Guo, X. Gao, L. Su, H. Xia, G. Gu, Z. Pang, X. Jiang, L. Yao, J. Chen, H. Chen, *Biomaterials* **2011**, *32*, 8010–8020.

[441] J. Zhang, R. Chen, F. Chen, M. Chen, Y. Wang, *J. Control. Release* **2015**, *213*, e8–e152.

[442] H. Gao, J. Qian, S. Cao, Z. Yang, Z. Pang, S. Pan, L. Fan, Z. Xi, X. Jiang, Q. Zhang, *Biomaterials* **2012**, *33*, 5115–5123.

[443] W. Tao, X. Zeng, J. Wu, X. Zhu, X. Yu, X. Zhang, J. Zhang, G. Liu, L. Mei, *Theranostics* **2016**, *6*, 470–484.

[444] G. Xu, X. Yu, J. Zhang, Y. Sheng, G. Liu, W. Tao, L. Mei, *Int. J. Nanomedicine* **2016**, *11*, 2953–2965.

[445] H. Xing, L. Tang, X. Yang, K. Hwang, W. Wang, Q. Yin, N. Y. Wong, L. W. Dobrucki, N. Yasui, J. A. Katzenellenbogen, et al., *J. Mater. Chem. B. Mater. Biol. Med.* **2013**, *1*, 5288–5297.

[446] H. Zhang, L. Hou, X. Jiao, J. Yandan, X. Zhu, L. Hongji, X. Chen, J. Ren, Y. Xia, Z. Zhang, *Curr Pharm Biotechnol* **2014**, *14*, 1105–1117.

[447] B. Zhang, Z. Luo, J. Liu, X. Ding, J. Li, K. Cai, *J. Control. Release* **2014**, *192*, 192–201.

[448] X. Li, Y. Yu, Q. Ji, L. Qiu, *Nanomedicine Nanotechnology, Biol. Med.* **2015**, *11*, 175–184.

[449] L. H. Peng, Y. H. Zhang, L. J. Han, C. Z. Zhang, J. H. Wu, X. R. Wang, J. Q. Gao, Z. W. Mao, *ACS Appl. Mater. Interfaces* **2015**, *7*, 18628–18637.

[450] T. Le Trinh, G. Zhu, X. Xiao, W. Puszyk, K. Sefah, Q. Wu, W. Tan, C. Liu, *PLoS One* **2015**, *10*, 1–17.

[451] Z. X. Liao, E. Y. Chuang, C. C. Lin, Y. C. Ho, K. J. Lin, P. Y. Cheng, K. J. Chen, H. J. Wei, H. W. Sung, *J. Control. Release* **2015**, *208*, 42–51.

[452] X. Li, X. Zhu, L. Qiu, *Acta Biomater.* **2016**, *35*, 269–279.

[453] S. M. Taghdisi, N. M. Danesh, M. Ramezani, P. Lavaee, S. H. Jalalian, R. Y. Robati, K. Abnous, *Eur. J. Pharm. Biopharm.* **2016**, *102*, 152–158.

[454] W. Y. Lai, W. Y. Wang, Y. C. Chang, C. J. Chang, P. C. Yang, K. Peck, *Biomaterials* **2014**, *35*, 2905–2914.

[455] L. Li, J. Hou, X. Liu, Y. Guo, Y. Wu, L. Zhang, Z. Yang, *Biomaterials* **2014**, *35*, 3840–3850.

[456] K. Roy, R. K. Kanwar, J. R. Kanwar, *Biomaterials* **2015**, *71*, 84–99.

[457] D. W. Hwang, H. Y. Ko, J. H. Lee, H. Kang, S. H. Ryu, I. C. Song, D. S. Lee, S. Kim, *J. Nucl. Med.* **2010**, *51*, 98–105.

[458] J. K. Kim, K. J. Choi, M. Lee, M. H. Jo, S. Kim, *Biomaterials* **2012**, *33*, 207–217.

[459] L. Tang, X. Yang, L. W. Dobrucki, I. Chaudhury, Q. Yin, C. Yao, S. Lezmi, W. G. Helferich, T. M. Fan, J. Cheng, *Angew. Chem. - Int. Ed. Eng.* **2012**, *51*, 12721–12726.

[460] H. Hu, A. Dai, J. Sun, X. Li, F. Gao, L. Wu, Y. Fang, H. Yang, L. An, H. Wu, et al., *Nanoscale* **2013**, *5*, 10447–10454.

[461] T. Kuo, W. Lai, C. Li, Y. Wun, H. Chang, J. Chen, P. Yang, C. Chen, *Nano Res.* **2014**, *7*, 658–669.

[462] J. Li, H. Zheng, P. J. Bates, T. Malik, X. F. Li, J. O. Trent, C. K. Ng, *Nucl. Med. Biol.* **2014**, *41*, 179–185.

[463] H. Ma, Z. Gao, P. Yu, S. Shen, Y. Liu, B. Xu, *Biochem. Biophys. Res. Commun.* **2014**, *449*, 44–48.

[464] C. H. Li, T. R. Kuo, H. J. Su, W. Y. Lai, P. C. Yang, J. S. Chen, D. Y. Wang, Y. C. Wu, C. C. Chen, *Sci. Rep.* **2015**, *5*, 15675.

[465] Z. Noaparast, S. J. Hosseinimehr, M. Piramoon, S. M. Abedi, *J. Drug Target.* **2015**, *23*, 497–505.

[466] X. Zhao, L. Xu, M. Sun, W. Ma, X. Wu, H. Kuang, L. Wang, C. Xu, *Small* **2016**, *12*, 4662–4668.

[467] K. Abdelmohsen, M. Gorospe, *RNA Biol.* **2012**, *9*, 799–808.

[468] M. Koutsioumpa, E. Papadimitriou, *Recent Pat. Anticancer. Drug Discov.* **2014**, *9*, 137–152.

[469] H. Fujiki, T. Watanabe, M. Suganuma, *J. Cancer Res. Clin. Oncol.* **2014**, *140*, 689–699.

[470] A. G. Hovanessian, C. Soundaramourty, D. El Khoury, I. Nondier, J. Svab, B. Krust, *PLoS One* **2010**, *5*, e15787.

[471] T. Konishi, Y. Karasaki, M. Nomoto, H. Ohmori, K. Shibata, T. Abe, K. Shimizu, H. Itoh, K. Higashi, *J. Biochem.* **1995**, *117*, 1170–1177.

[472] Y. Wang, J. Guan, H. Wang, Y. Wang, D. Leeper, G. Iliakis, *J. Biol. Chem.* **2001**, *276*, 20579–20588.

[473] C. Yang, D. A. Maiguel, F. Carrier, *Nucleic Acids Res.* **2002**, *30*, 2251–2260.

[474] K. Kim, D. D. Dimitrova, K. M. Carta, M. Daras, J. A. Borowiec, A. Saxena, **2005**, *25*, 2463–2474.

[475] A. G. Hovanessian, F. Puvion-Dutilleul, S. Nisole, J. Svab, E. Perret, J. S. Deng, B. Krust, *Exp. Cell*

Res. **2000**, *261*, 312–328.
[476] C. A. Balinsky, H. Schmeisser, S. Ganesan, K. Singh, T. C. Pierson, K. C. Zoon, *J. Virol.* **2013**, *87*, 13094–13106.
[477] M. Métifiot, S. Amrane, J. L. Mergny, M. L. Andreola, *Biochimie* **2015**, *118*, 173–175.
[478] R. Perrone, E. Butovskaya, S. Lago, A. Garzino-Demo, C. Pannecouque, G. Palù, S. N. Richter, *Int. J. Antimicrob. Agents* **2016**, *47*, 311–316.
[479] X. Xu, F. Hamhouyia, S. D. Thomas, T. J. Burke, A. C. Girvan, W. G. McGregor, J. O. Trent, D. M. Miller, P. J. Bates, *J. Biol. Chem.* **2001**, *276*, 43221–43230.
[480] A. C. Girvan, Y. Teng, L. K. Casson, S. D. Thomas, S. Juliger, M. W. Ball, J. B. Klein, W. M. Pierce, S. S. Barve, P. J. Bates, *Mol. Cancer Ther.* **2006**, *5*, 1790–1799.
[481] B. Scaggiante, B. Dapas, G. Grassi, G. Manzini, *FEBS J.* **2006**, *273*, 1350–1361.
[482] Y. Teng, A. C. Girvan, L. K. Casson, W. M. Pierce, M. Qian, S. D. Thomas, P. J. Bates, *Cancer Res.* **2007**, *67*, 10491–10500.
[483] S. Soundararajan, W. Chen, E. K. Spicer, N. Courtenay-Luck, D. J. Fernandes, *Cancer Res.* **2008**, *68*, 2358–2365.
[484] K. Farin, S. Schokoroy, R. Haklai, I. Cohen-Or, G. Elad-Sfadia, M. E. Reyes-Reyes, P. J. Bates, A. D. Cox, Y. Kloog, R. Pinkas-Kramarski, *Cancer Res.* **2011**, *71*, 2140–2151.
[485] F. Pichiorri, D. Palmieri, L. De Luca, J. Consiglio, J. You, A. Rocci, T. Talabere, C. Piovan, A. Lagana, L. Cascione, et al., *J. Exp. Med.* **2013**, *210*, 951–968.
[486] Y. Goldshmit, S. S. Trangle, Y. Kloog, R. Pinkas-Kramarski, *Oncotarget* **2014**, *5*, 8602–8613.
[487] N. Shen, F. Yan, J. Pang, L. C. Wu, A. Al-Kali, M. R. Litzow, S. Liu, *Oncotarget* **2014**, *5*, 5494–5509.
[488] N. Zhang, T. Bing, X. Liu, C. Qi, L. Shen, L. Wang, D. Shangguan, *Chem. Sci.* **2015**, *6*, 3831–3838.
[489] E. Wolfson, M. Goldenberg, S. Solomon, A. Frishberg, R. Pinkas-Kramarski, *Oncotarget* **2016**, *7*, 65320–65334.
[490] E. M. Reyes-Reyes, Y. Teng, P. J. Bates, *Cancer Res.* **2010**, *70*, 8617–8629.
[491] E. M. Reyes-Reyes, F. R. Šalipur, M. Shams, M. K. Forsthoefel, P. J. Bates, *Mol. Oncol.* **2015**, *9*, 1392–1405.
[492] G. J. Doherty, H. T. McMahon, *Annu. Rev. Biochem.* **2009**, *78*, 857–902.
[493] A. Wittrup, S. Sandgren, J. Lilja, C. Bratt, N. Gustavsson, M. Mörgelin, M. Belting, *J. Biol. Chem.* **2007**, *282*, 27897–27904.
[494] S. Fumoto, J. Nishi, H. Ishii, X. Wang, H. Miyamoto, N. Yoshikawa, M. Nakashima, J. Nakamura, K. Nishida, *Mol. Pharm.* **2009**, *6*, 1170–1179.
[495] D. Yu, Y. Zhang, Z. Mao, C. Gao, *Macromol. Biosci.* **2013**, *13*, 1413–1421.
[496] C. Liang, B. Guo, H. Wu, N. Shao, D. Li, J. Liu, L. Dang, C. Wang, H. Li, S. Li, et al., *Nat. Med.* **2015**, *21*, 288–294.
[497] M. J. Piña, A. Girotti, M. Santos, J. C. Rodríguez-Cabello, F. J. Arias, *Mol. Pharm.* **2016**, *13*, 795–808.
[498] K. D. Ha, S. M. Bidlingmaier, B. Liu, *Front. Physiol.* **2016**, *7*, 381.
[499] H. Gao, Z. Yang, S. Zhang, Z. Pang, X. Jiang, *J. Drug Target.* **2014**, *22*, 450–459.
[500] E. Kočišová, P. Praus, J. Bok, S. Bonneau, F. Sureau, *J. Fluoresc.* **2015**, *25*, 1245–1250.
[501] J. W. Kotula, E. D. Pratico, X. Ming, O. Nakagawa, R. L. Juliano, B. a. Sullenger, *Nucleic Acid Ther.* **2012**, *22*, 187–195.
[502] A. Saci, L. C. Cantley, C. L. Carpenter, *Mol. Cell* **2011**, *42*, 50–61.
[503] P. P. Hsu, S. A. Kang, J. Rameseder, Y. Zhang, K. A. Ottina, D. Lim, T. R. Peterson, Y. Choi, N. S. Gray, M. B. Yaffe, et al., *Science* **2011**, *332*, 1317–1322.
[504] Y. Yu, S. O. Yoon, G. Poulogiannis, Q. Yang, X. M. Ma, J. Villén, N. Kubica, G. R. Hoffman, L. C. Cantley, S. P. Gygi, et al., *Science* **2011**, *332*, 1322–1326.
[505] H. B. Pang, G. B. Braun, T. Friman, P. Aza-Blanc, M. E. Ruidiaz, K. N. Sugahara, T. Teesalu, E. Ruoslahti, *Nat. Commun.* **2014**, *5*, 4904.
[506] S. Yoshida, R. Pacitto, Y. Yao, K. Inoki, J. A. Swanson, *J. Cell Biol.* **2015**, *211*, 159–172.
[507] S. Sung, J. Choi, H. Cheong, *Oncotarget* **2015**, *6*, 40405–40417.
[508] W. Palm, Y. Park, K. Wright, N. N. Pavlova, D. A. Tuveson, C. B. Thompson, *Cell* **2015**, *162*, 259–270.
[509] Y. Kim, C. H. Jung, M. Seo, E. K. Kim, J. M. Park, S. S. Bae, D. H. Kim, *Mol Cell.* **2015**, *57*, 207–218.

[510] J. Lin, S. S. Shi, J. Q. Zhang, Y. J. Zhang, L. Zhang, Y. Liu, P. P. Jin, P. F. Wei, R. H. Shi, W. Zhou, et al., *Small* **2016**, *12*, 5759–5768.

[511] Z. Bagheri, B. Ranjbar, H. Latifi, M. I. Zibaii, T. T. Moghadam, A. Azizi, *Int. J. Biol. Macromol.* **2015**, *72*, 806–811.

[512] P. Balagurumoorthy, S. K. Brahmachari, D. Mohanty, M. Bansal, V. Sasisekharan, *Nucleic Acids Res.* **1992**, *20*, 4061–4067.

[513] A. Ambrus, D. Chen, J. Dai, T. Bialis, R. A. Jones, D. Yang, *Nucleic Acids Res.* **2006**, *34*, 2723–2735.

[514] L. Petraccone, C. Spink, J. O. Trent, N. C. Garbett, C. S. Mekmaysy, C. Giancola, J. B. Chaires, *J. Am. Chem. Soc.* **2011**, *133*, 20951–20961.

[515] A. N. U. Puri, R. Blumenthal, *Acc. Chem. Res.* **2011**, *44*, 1071–1079.

[516] N. Grimaldi, F. Andrade, N. Segovia, L. Ferrer-Tasies, S. Sala, J. Veciana, N. Ventosa, *Chem. Soc. Rev.* **2016**, *45*, 6520–6545.

[517] O. Paecharoenchai, L. Teng, B. C. Yung, L. Teng, P. Opanasopit, R. J. Lee, *Nanomedicine* **2013**, *8*, 1865–1873.

[518] R. M. Handjani-Vila, A. Ribier, B. Rondot, G. Vanlerberghie, *Int. J. Cosmet. Sci.* **1979**, *1*, 303–314.

[519] G. P. Kumar, P. Rajeshwarrao, *Acta Pharm. Sin. B* **2011**, *1*, 208–219.

[520] C. Marianecci, L. Di Marzio, F. Rinaldi, C. Celia, D. Paolino, F. Alhaique, S. Esposito, M. Carafa, *Adv. Colloid Interface Sci.* **2014**, *205*, 187–206.

[521] R. Rajera, K. Nagpal, S. K. Singh, D. N. Mishra, *Biol. Pharm. Bull.* **2011**, *34*, 945–953.

[522] S. Moghassemi, A. Hadjizadeh, *J. Control. Release* **2014**, *185*, 22–36.

[523] V. B. Junyaprasert, V. Teeranachaideekul, T. Supaperm, *AAPS PharmSciTech* **2008**, *9*, 851–859.

[524] S. Moghassemi, E. Parnian, A. Hakamivala, M. Darzianiazizi, M. M. Vardanjani, S. Kashanian, B. Larijani, K. Omidfar, *Mater. Sci. Eng. C* **2015**, *46*, 333–340.

[525] L. Redondo-Morata, M. I. Giannotti, F. Sanz, *Langmuir* **2012**, *28*, 12851–12860.

[526] J. Y. Fang, C. T. Hong, W. T. Chiu, Y. Y. Wang, *Int. J. Pharm.* **2001**, *219*, 61–72.

[527] C. Marianecci, D. Paolino, C. Celia, M. Fresta, M. Carafa, F. Alhaique, *J. Control. Release* **2010**, *147*, 127–135.

[528] S. Hua, *Front. Pharmacol.* **2015**, *6*, 1–5.

[529] E. Ojeda, G. Puras, M. Agirre, J. Zarate, S. Grijalvo, R. Eritja, G. Martinez-Navarrete, C. Soto-Sánchez, A. Diaz-Tahoces, M. Aviles-Trigueros, et al., *Biomaterials* **2016**, *77*, 267–279.

[530] G. P. Ochoa, J. Z. Sesma, M. A. Díez, A. Díaz-Tahoces, M. Avilés-Trigeros, S. Grijalvo, R. Eritja, E. Fernández, J. L. Pedraz, *Pharm. Res.* **2014**, *31*, 1665–1675.

[531] S. Grijalvo, A. Alagia, G. Puras, J. Zárate, J. L. Pedraz, R. Eritja, *Colloids Surfaces B Biointerfaces* **2014**, *119*, 30–37.